# **Failure Mode Classification for Life Prediction Modeling of Solid-State Lighting**

by

Peter Joseph Sakalaukus Jr.

A dissertation submitted to the Graduate Faculty of
Auburn University
in partial fulfillment of the
requirements for the degree of
Doctor of Philosophy

Auburn, Alabama
August 1, 2015

Keywords: Solid-State Lighting, Kalman, Accelerated Life Testing, Aluminum Electrolytic Capacitors, Electrical Connectors, LEDs



Approved by

Pradeep Lall, Chair, John and Anne MacFarlane Professor of Mechanical Engineering
and Director, NSF Center for Advanced Vehicle Electronics
Jeffrey C. Suhling, Quina Distinguished Professor and Chair of Mechanical Engineering
Bart Prorok, Professor of Mechanical Engineering
John Hung, Professor of Electrical Engineering

Lynn Davis, Research Triangle Institute Fellow

## Abstract

Since the passing of the Energy Independence and Security Act of 2007, the U.S. government has mandated greater energy independence which has acted as a catalyst for accelerating and facilitating research efforts toward the development and deployment of market-driven solutions for energy-saving homes, buildings and manufacturing, as well as sustainable transportation and renewable electricity generation. As part of this effort, an emphasis toward advancing solid-state lighting technology through research, development, demonstration, and commercial applications is assisting in the phase out of the common incandescent light bulb, as well as developing a more economical lighting source that is less toxic than compact fluorescent lighting. This has led lighting manufacturers to pursue SSL technologies for a wide range of consumer lighting applications.

An SSL luminaire’s lifetime can be characterized in terms of lumen maintenance life. Lumen maintenance or lumen depreciation is the percentage decrease in the relative luminous flux from that of the original, pristine luminous flux value. Lumen maintenance life is the estimated operating time, in hours, when the desired failure threshold is projected to be reached at normal operating conditions. One accepted failure threshold of SSL luminaires is lumen maintenance of 70% -- a 30% reduction in the light output of the luminaire. Currently, the only approved lighting standard that puts forth a recommendation for long-term luminous flux maintenance projections towards a specified failure threshold of an SSL luminaire is the IES TM-28-14 (TM28) standard.

TM28 was derived as a means to compare luminaires that have been tested at different facilities, research labs or companies. TM28 recommends the use of the Arrhenius equation to determine SSL device specific reaction rates from thermally driven failure mechanisms used to characterize a single failure mode – the relative change in the luminous flux output or “light power” of the SSL luminaire. The use of the Arrhenius equation necessitates two different temperature conditions, 25°C and 45°C are suggested by TM28, to determine the SSL lamp specific activation energy. One principal issue with TM28 is the lack of additional stresses or parameters needed to characterize non-temperature dependent failure mechanisms. Another principal issue with TM28 is the assumption that lumen maintenance or lumen depreciation gives an adequate comparison between SSL luminaires. Additionally, TM28 has no process for the determination of acceleration factors or lifetime estimations.

Currently, a literature gap exists for established accelerated test methods for SSL devices to assess quality, reliability and durability before being introduced into the marketplace. Furthermore, there is a need for Physics-of-Failure based approaches to understand the processes and mechanisms that induce failure for the assessment of SSL reliability in order to develop generalized acceleration factors that better represent SSL product lifetime.

This and the deficiencies in TM28 validate the need behind the development of acceleration techniques to quantify SSL reliability under a variety of environmental conditions. The ability to assess damage accrual and investigate reliability of SSL components and systems is essential to understanding the life time of the SSL device itself. The methodologies developed in this work increases the understanding of SSL devices through the investigation of component and device reliability under a variety of accelerated test conditions. The approaches for suitable lifetime predictions through the development of novel generalized acceleration factors, as well as a prognostics and health management framework, will greatly reduce the time and effort needed to produce SSL acceleration factors for the development of lifetime predictions.

# Acknowledgments

My sincerest thanks to my research advisor and mentor, Dr. Pradeep Lall, for all of his guidance which was provided to me during my tenure at Auburn University. A special thanks to Dr. Lynn Davis for his role in shaping my understanding of solid-state lighting and for agreeing to be a part of my dissertation committee. I would also like to thank Dr. John Hung, Dr. Bart Prorok and Dr. Jeff Suhling for supporting me in the completion of this dissertation and acting as my dissertation committee. Special thanks to my fellow researchers and friends for contributing in some form or another to the success of this work. I would also like to thank the staff and students of the Mechanical Engineering Department for offering assistance when needed. I would like to acknowledge the Department of Energy and Research Triangle Institute for funding my research. Many thanks to my parents, Peter and Tammy, for their support and encouragement during my studies and throughout my life. A very special thanks to my beautiful wife, Sarah, for being there when my stress level was at the max and for taking on extra duties at home. I love you and would not have succeeded without you. This work is dedicated to our children, Gloria, Violet and Peter, in hopes that they achieve greatness in their lives.

Table of Contents

## List of Figures

## List of Tables

# 1. Introduction

Since the passing of the Energy Independence and Security Act of 2007 (EISA), the United States (U.S.) has mandated greater energy independence through the increased production of clean renewable fuels, an increase in the efficiency of domestic products, buildings, and vehicles, as well as improvements in the nation's energy performance (Congress, 2007). This has acted as a catalyst for the U.S. Department of Energy's (DOE) Office of Energy Efficiency & Renewable Energy (EERE). EERE is currently accelerating and facilitating research efforts toward the development and deployment of market-driven solutions for energy-saving homes, buildings and manufacturing, as well as sustainable transportation and renewable electricity generation (EERE, 2006). As part of this effort, EERE's Building Technologies Office is working toward advancing solid-state lighting (SSL) technology through research, development, demonstration, and commercial applications (EERE, 2006) in order to aid in the phase out of the common incandescent light bulb, as well as develop a more economical lighting source that is less toxic than compact fluorescent lighting (CFL). This has led lighting manufacturers to pursue SSL technologies for a wide range of consumer lighting applications.

Two major roadblocks are hindering the transition process to SSL lighting: cost and quality. In order to cut cost, manufactures are moving toward less expensive packaging materials and a variety of package construction techniques which may potentially erode the quality of the lighting device and reduce its survival rate in everyday applications.

Conversely, should manufactures focus solely on quality, cost conscious consumers would then refrain from purchasing expensive SSL technologies.

An SSL luminaire's lifetime is typically characterized in terms of lumen maintenance life. Lumen maintenance or lumen depreciation is the percentage decrease in the relative luminous flux from that of the original, pristine luminous flux value. Lumen maintenance life is the estimated operating time, in hours, when the desired failure threshold is projected to be reached at normal operating conditions. One predominately used failure threshold of an SSL luminaire is lumen maintenance Lp in hours. This is the predicted time an SSL device will reach percent "p" or a 100 minus "p" percent reduction in the light output of the luminaire. Lp is useful at denoting a perceptible change in luminous flux. The percentage choice as a reduction of luminous flux failure criteria is application or manufacturer specific, such as L50, L70, and L90. One commonly accepted failure threshold of an SSL luminaire is a 30% reduction in the luminous flux output of the device, called L70 (IES, 2014b). TM28 utilizes the Arrhenius equation to determine SSL device specific reaction rates from thermally driven failure mechanisms used to characterize a single failure mode – the relative change in the luminous flux output or "light power" of the SSL luminaire. TM28 requires a minimum of 6000 hours of testing with a recommended sampling period less than or equal to 1000 hours. Additionally, it necessitates two different temperature conditions, 25°C and 45°C are suggested, to determine the SSL lamp specific activation energy.

One principal issue with TM28 is the lack of additional stresses or parameters needed to characterize non-temperature dependent failure mechanisms. Another principal issue with TM28 is the assumption that lumen maintenance or lumen depreciation gives an adequate comparison between SSL luminaires. Additionally, TM28 has no process for the determination of acceleration factors or lifetime estimations. The use of TM28 yields lumen maintenance projections that can be useful in the determination of acceleration factors, as shown in this work. In order to completely comprehend the inherent problems with TM28, it is important to fully understand how TM28 works, as well as what an SSL device is and how it works.

## 1.1. Solid-State Lighting

Traditional consumer lighting, such as incandescent bulbs and CFLs, has relied on the use of an electrical filament or plasma to produce illumination. Due to lack of efficiency, a government mandated phase out of incandescent bulbs has recently taken place. Consumer lighting has since turned to CFLs and SSL devices. The lighting industry has steadily increased its focus to the implementation of SSL technologies over CFLs. Highly toxic mercury used in the illumination process of CFLs, there susceptibility to vibration, drop and shock, as well as their propensity to fail when repeatedly power cycled on and off, made the phase out and transition an easy decision. SSL technology is fundamentally different from traditional lighting technologies in terms of the materials used for illumination, the power requirements of the device and the vastly different architecture schemes used in the construction of SSL devices.

SSL devices can be divided into two fundamental components: the light engine (LE) and the electrical driver (ED). The LE is composed of a massive heat sink and an array of light-emitting diodes (LEDs) that produce light in response to an electrical excitation supplied by a constant current source. In order to utilize LEDs in lighting applications, an ED is required to convert the standard AC current source to a DC current source to produce the small, constant current needed to illuminate each LED.

These fundamental components can be housed together to form a lamp, or lightbulb, for omnidirectional lighting similar to CFLs. Conversely, the lighting system and electrical system can also be kept separate for use in a downward directional light, or a downlight, where the ED is connected to the LE by way of an electrical connector (EC). In the following sections, the ED and LE will be discussed in greater detail so as to increase the reader's understanding of these two fundamental components.

### 1.1.1. Electrical Driver

In order to promote consumer adoption of SSL, the existing lighting architecture which utilizes AC power, has been used as a basis for SSL devices. This requires the ED to be designed as a rectifier circuit to convert AC power to DC power so the current requirement of the LED can be met. In addition to being a rectifier, EDs are typically designed with a pulse-width modulated (PWM) IC controller to produce better efficiency and a lower LED junction temperature. This is achieved by pulsing the LED on and off at a flicker rate greater than the human eye can detect. A general schematic of an SSL ED is depicted in Figure 1.

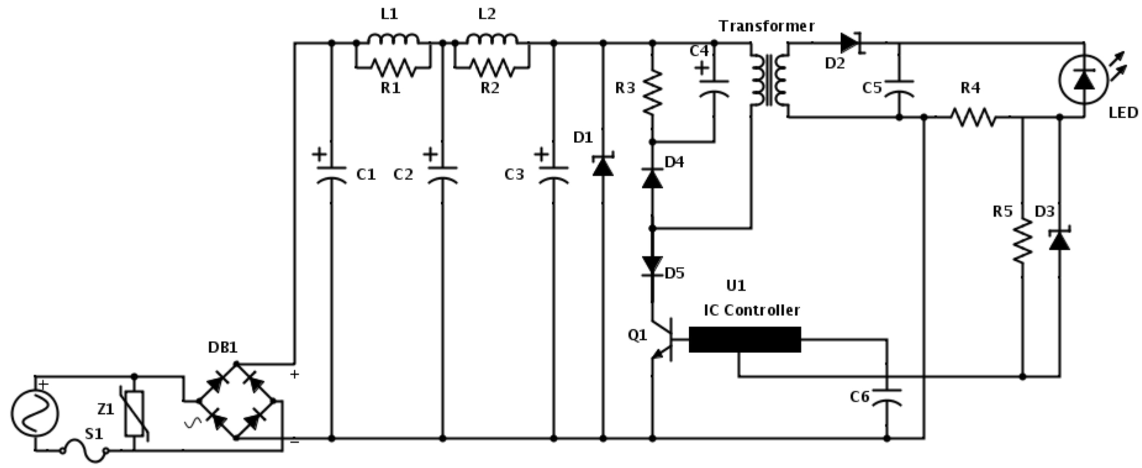


Figure 1: Schematic of an LED ED.

SSL EDs, like any other electronic device, are composed of a variety of surface mount components such as resistors, capacitors, and diodes, as well as consist of an IC controller and MOSFETs. They also contain plated-through-hole (PTH) components such as varistors, inductors and aluminum electrolytic capacitors (AECs). It is important to note that AECs have been reported to experience the highest failure rate when compared to other components inside of an ED (Kulkarni C. S., 2012) (Imam, 2005) (Kulkarni C. S., 2012) (Lan, 2012). For this reason, AECs were investigated as a potential indication of failure for a portion of this work. Therefore, it is important to discuss the design of AECs.

#### 1.1.1.1. Aluminum Electrolytic Capacitors

As previously mentioned, AECs typically have the highest failure rate compared to the other components that compromise an ED and are considered the "weakest-link" (Kulkarni C. S., 2012) (Imam, 2005) (Kulkarni C. S., 2012) (Lan, 2012). AEC degradation may cause EDs to fail completely due to a current surge or produce an undesirable light output of the LED array. An AEC is a type of capacitor that uses an electrolyte to achieve a larger capacitance per unit volume compared to traditional capacitors. They are used in high current – low frequency electrical circuits, such as an SSL ED, and are needed to help convert AC power to DC power (Georgiev, 1945). An AEC is composed of a cathode aluminum foil, electrolytic paper, liquid electrolyte and a dielectric (Rubycon Corporation, 2013) (Nichicon Inc., 2002). Figure 2 depicts the components that make up an AEC.

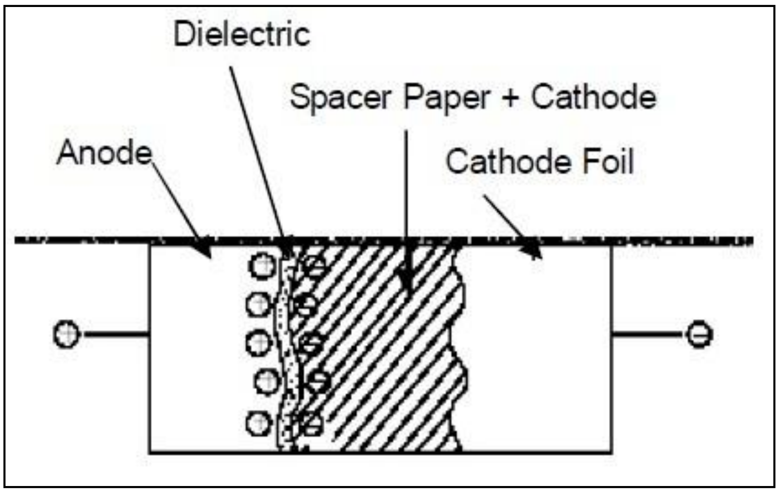


Figure 2: Construction of an AEC (Rubycon Corporation, 2013).

There are two intrinsic quantities used to describe an AEC: capacitance (CAP) and equivalent series resistance (ESR). The CAP can be calculated by knowing the dielectric constant, surface area of the dielectric and the thickness of the dielectric (Rubycon Corporation, 2013) (Nichicon Inc., 2002) (Albertsen, 2012). The ESR can be estimated by summing the electrolytic resistance, dielectric loss and the electrode resistance (Rubycon Corporation, 2013) (Han, 2009) (Harada, 1993). In this work, the ESR and CAP were measured directly using a handheld LCR meter instead of using an estimation technique to determine the ESR and CAP values.

### 1.1.2. LIGHT ENGINE

The LE is the component of SSL that emits light through the process of electroluminescence which is the emission of light from a material that exceeds blackbody radiation when an electrical field excitation is applied (Zukauskas, 2002). This process occurs in SSL devices through the use of LEDs. A brief introduction of LEDs is given in the succeeding section.

The LE is designed to produce artificial white light through either color mixing or phosphor conversion by producing tristimulus values that are in the center of the chromaticity diagram as shown in Figure 3. The tristimulus values correspond to the intensity required to produce proper excitation of the three cones within the human eye in order for the emitted light to be perceived as “white” (Schubert, 2006) (CREE, 2013). The correlated color temperature (CCT) of white light, measured in degrees Kelvin, describes the perceived hue the human eye detects. A CCT value between 2700K – 3000K describes a warm-white emission, while values of 4500K – 5500K describe a cool-white or daylight emission. The CCT value is characterized in relation to the temperature of an ideal black-body radiator line or Planckian locus with a comparable hue. The isotemperature line that denotes the CCT of the light source is perpendicular to the Planckian locus which can also be seen in Figure 3 (Hernandez-Andres, 1999) (Hsieh, 2012). Greater detail pertaining to the creation of artificial white light can be found further in the chapter.

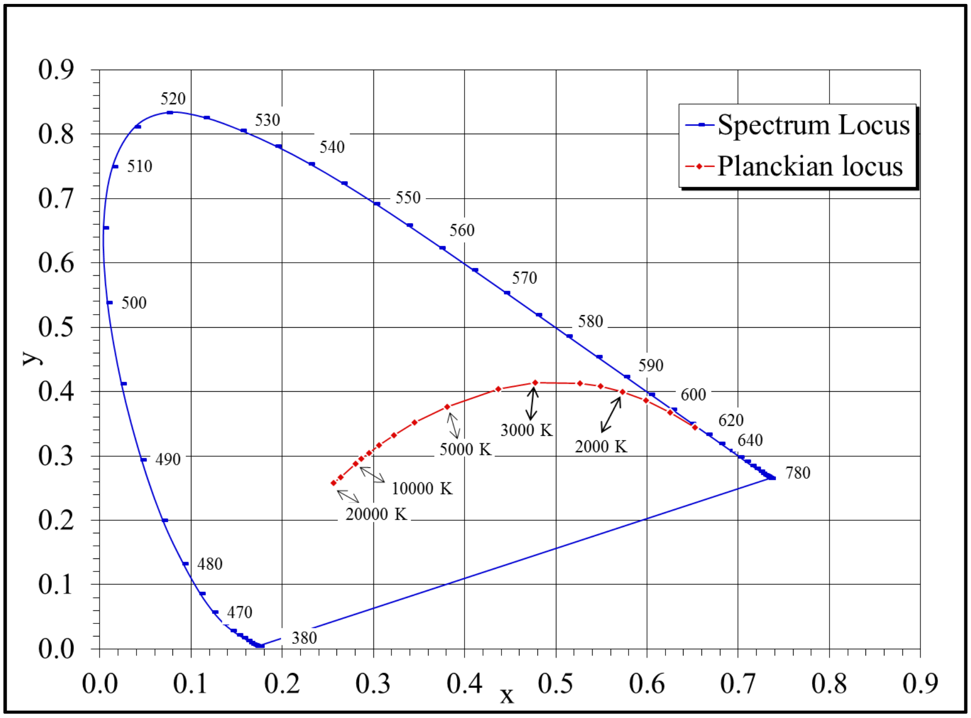


Figure 3: CIE 1931 x-y Chromaticity Diagram.

#### 1.1.2.1. LIGHT-EMITTING DIODE

An LED is a p-n junction diode that uses a two-lead semiconductor material as its light source. When the p-n junction experiences a forward bias, the electrons originating from the n-side have a sufficient amount of energy to move across the boundary layer to recombine with the p-side, while the electron holes from the p-side are distributed across the active layer of the semiconductor to diffuse with the n-side. The result is the depletion of free carriers in an area near the p-n junction known as the depletion region or activation region. The activation area releases energy in the form of photons producing light. (Zukauskas, 2002) (Schubert, 2006) (Chang, 2012)

LEDs are characteristically monochromatic emitters exhibiting a narrow band of wavelengths of a single hue. The monochromatic color of the LED is determined by the band gap energy of the semiconductor material. LEDs are commonly constructed from bare wafers made out of materials such as sapphire, Gallium Nitride (GaN), Silicon Carbide (SiC), Silicon (Si) and Gallium Arsenide (GaAs) (Chang, 2012). Epitaxial wafers (epiwafer) are grown atop of the bare wafers to produce the finished form of the semiconductor material. The color an LED emits is determined by the type of epiwafer used. The various types used in LED construction are Indium Gallium Nitride (InGaN) or Aluminum Gallium Nitride (AlGaN) for producing blue, green, and ultra-violet light; Aluminum Gallium Indium Phosphide (AlGaInP) for producing red or yellow light; and Aluminum Gallium Arsenide (AlGaAs) for producing red or infrared light (Chang, 2012) (Schubert, 2006). An example of a blue LED package typical of SSL devices can be seen in Figure 4.

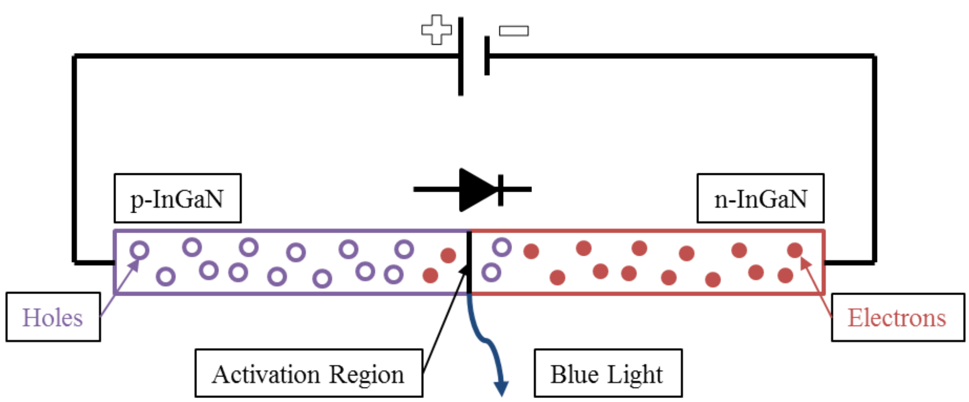


Figure 4: Schematic of a Blue LED Package.

#### 1.1.2.2. COLOR MIXING

As previously mentioned, an LED is a monochromatic emitter that cannot produce white light on its own. One solution is to use the process of color mixing which combines color LEDs that have a different spectral power distribution (SPD) over the visible spectrum. When the SPD of each LED is combined, the spectral wavelengths produce what is perceived by the human eye as “white” light. Figure 5 depicts the CIE color matching functions that are the numerical description of the chromatic response of the CIE 2° standard colorimetric observer (CIE, 2004a) (Wyszecki, 1982) (CREE, 2013). This corresponds to the band-pass filtered chromaticity response of the three cones in the human eye and allows for the chromaticity coordinates of a perceived hue or color to be shown as a simple locus on a 2-D unit plane (CREE, 2013). The color matching functions are used to produce tristimulus values, when combined, give the perception of “white” light. This approach can be accomplished using a dichromatic (two LEDs), trichromatic (three LEDs), tetrachromatic (four LEDs) or pentachromatic (five LEDS) light source which can be classified in terms of their luminous efficacy of radiation, luminous source efficiency, and color-rendering index (CRI) properties. (Schubert, 2006)

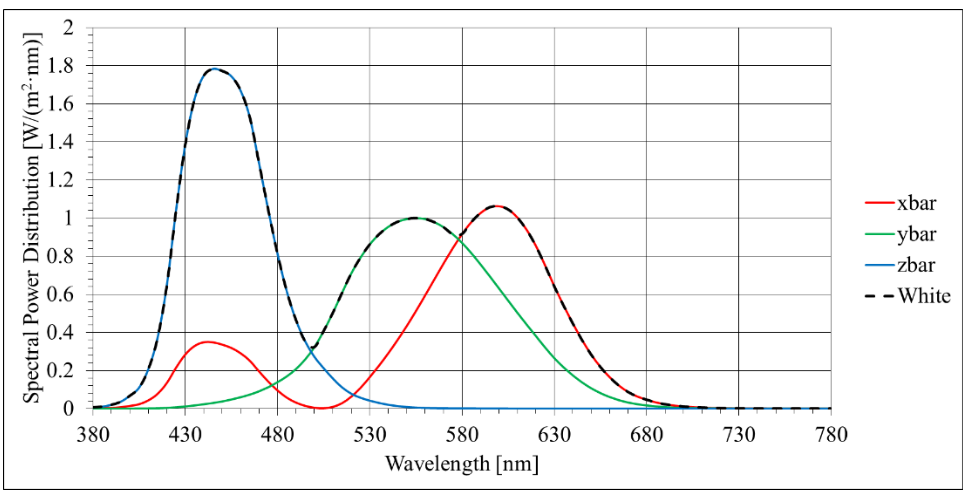


Figure 5: SPD of the CIE Color Matching Functions.

A dichromatic light source uses two complementary colors or complementary wavelengths at a specific power ratio to produce white light. Typically, blue and yellow wavelengths are used in a dichromatic light source. In some cases, a monolithic dichromatic LED is used to produce white light instead of two individual LEDs. A monolithic dichromatic LED is constructed with two different semiconductor materials stacked together. The bottom semiconductor material radiates photons toward the top semiconductor layer which absorbs those protons and combines them with its own protons to produce white light. This construction of a dichromatic source has two activation regions used in the production of white light through the process of photoluminescence. Dichromatic sources produce a very high luminous efficacy and source efficiency, but the lowest CRI values. (Schubert, 2006)

High-quality white light uses the three additive primary colors of blue, green and red to produce a trichromatic light source. Trichromatic sources have better CRI values compared to dichromatic sources, but have a lower luminous efficacy and source efficiency. Unfortunately, optical output power of trichromatic light sources is extremely temperature dependent. The temperature dependency issue arises from the changes in the emission power, peak wavelength, and spectral width of the emitted light. This causes a chromaticity shift of the light source toward a higher CCT or a lower spectral wavelength, i.e. blue light, due to the increased temperature of the device. (Schubert, 2006)

Though not typically used, tetrachromatic and pentachromatic light sources use either four and five LEDs, respectively, to produce white light. The increase in the number of light sources produces a higher CRI value, but will produce a lower luminous efficacy and source efficiency. (Schubert, 2006)

#### 1.1.2.3. PHOSPHOR CONVERSION

Phosphor conversion is the most common method used in SSL lamps to generate white light. Phosphor conversion utilizes short-wavelength LEDs (blue or ultraviolet) that excite phosphors to produce white light through a process called down conversion. The phosphor is either placed directly onto the LED semiconductor material or remotely away from the LED. Phosphors are an inorganic host material that have been doped with an optically active element. Typically, a phosphor is constructed of garnets. The optical elements used in the construction of phosphors are rare-earth elements, rare-earth oxides or any other rare-earth compound. (Schubert, 2006)

The most commonly used materials for phosphor converted light are a cerium (Ce) doped yttrium aluminum garnet (YAG) or a Ce-YAG phosphor and blue LEDs. This material combination yields white light through the mixing of the unabsorbed blue emission and the down converted emissions from the yellow Ce-YAG phosphor (Oh, 2010) (Lunia, 2014). This process produces two peaks on the SPD, one being the blue peak through luminescence and the other being the yellow peak through phosphorescence. The magnitude of these two peaks is dependent on many factors, such as the desired CCT of the white light emitted (i.e. warm-white or cool-white), and not on the position of the phosphor. The position of the phosphor is demonstrated for SSL lamps that are warm-white and cool-white in Figure 6. This comparison illustrates that the position of the phosphor, remote or proximate, doesn’t affect the peaks of the SPD for SSL lamps.

A)
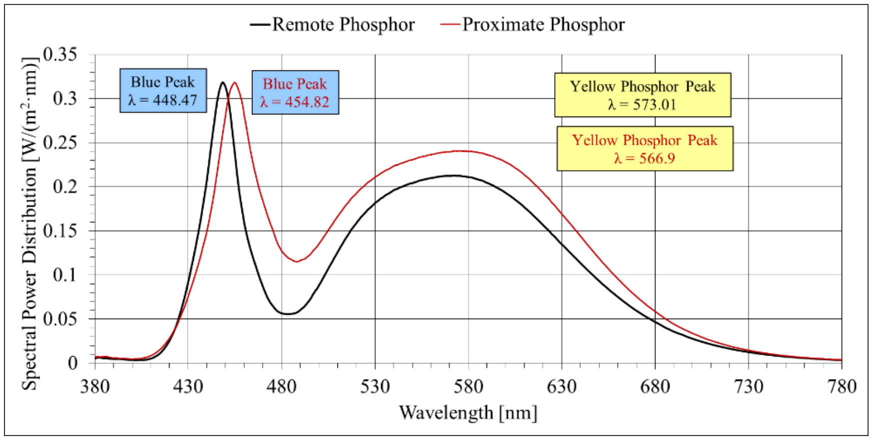


B)
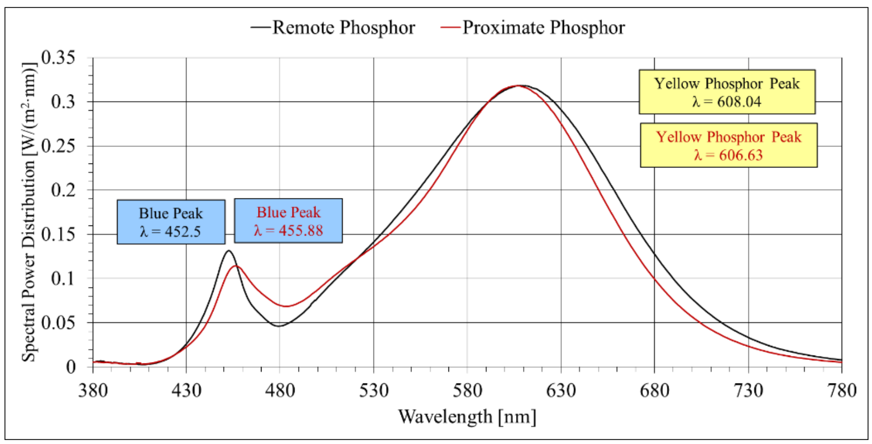


Figure 6: A) SPD of Phosphor Converted Cool-White Lamps; B) SPD of Phosphor Converted Warm-White Lamps.

Similar to color mixing, the phosphor converted light source can be classified as dichromatic, trichromatic or tetrachromatic. Likewise, a phosphor converted dichromatic light source has the highest luminous efficacy of radiation and luminous source efficiency with the CRI values being the lowest. (Schubert, 2006)

## 1.2. Lumen Maintenance Life

As previously mentioned, SSL lifetime is characterized in terms of lumen maintenance life. Lumen maintenance life for LEDS and SSL lamps is based of relative luminous flux projections using the IES TM-21-11 (TM21) and IES TM-28-14 (TM28) standards, respectively. (IES, 2011) (IES, 2014b)

The TM21 and TM28 standards are the only “approved methods” for the projection of lumen maintenance for LEDs and SSL lamps, respectively. Photometric measurements for all SSL devices follows the LM-79-08 (LM79) measurement standard (IES, 2008a). The LM-80-08 (LM80) and LM-84-14 (LM84) testing standards outline recommended operating temperatures and sampling periods (IES, 2008b) (IES, 2014a). This is currently the only IES approved criteria used by lighting manufactures to give rated product lifetimes.

The TM28 projection standard recommends two operating temperatures, 25°C and 45°C, with a sampling period of at most 1000 hours for SSL lamps under test. Additionally, it dictates the elimination of the first 1000 hours of test data with a minimum of five measurement points, i.e. 1000 hours to 6000 hours. The TM28 projection standard requires the use of the relative luminous flux (RLF), $\Phi$, which is the measured luminous flux divided by its original, pristine value. In this work, the RLF has been used in the form of percentages, where 100% is the pristine value instead of the industrial standard of one as pristine. This is a deviation from the TM28 method of producing RLF and was used to give more insight and understanding of the RLF of the SSL devices. A log-linear relationship between RLF and time is used to determine each temperature dependent decay rate, $\alpha$, as shown in equations (1) and (2). The natural log of RLF is plotted against time, t, and a linear curve-fit is used to determine the slope of the plot or the decay rate constant and projected initial constant or y-intercept, $\beta$, at each temperature condition. An example of how to determine the decay rate constant can be seen for the same SSL lamp, PWW, in Figure 7 and Figure 8 for an operating temperature of 25°C and 85°C, respectively.

$$\Phi(t) = \beta \cdot \exp(-\alpha \cdot t) \tag{1}$$

$$\ln(\Phi) = \ln(\beta) - \alpha \cdot t \tag{2}$$

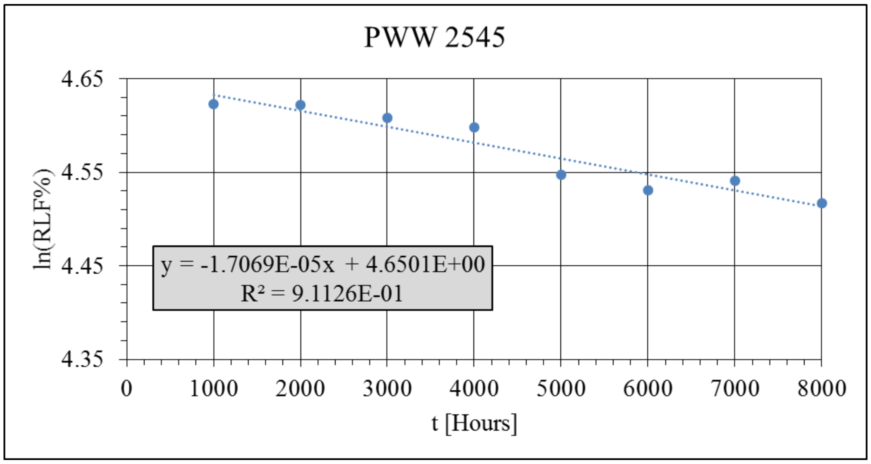


Figure 7: Determination of the Decay Rate and Projected Initial Constants for the SSL Lamp PWW with an operating temperature of 25°C.

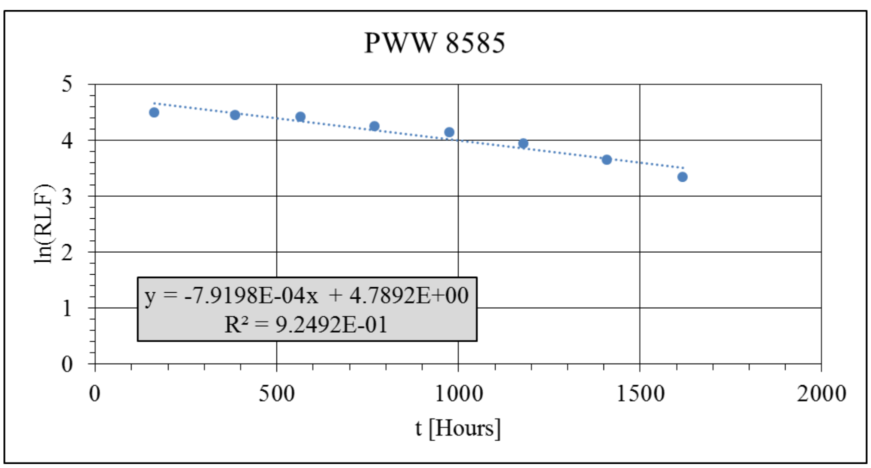


Figure 8: Determination of the Decay Rate and Projected Initial Constants for the same SSL Lamp PWW at a different operating temperature of 85°C.

The two decay rate constants and temperature conditions are then used to determine the SSL lamp specific activation energy ($E_a$) using equation (3), where $k_b$ is the Boltzmann's constant. Additionally, the pre-exponential factor, A, is determined using either decay rate with its corresponding temperature condition.

$$E_a = k_b \cdot \frac{\ln(\alpha_1) - \ln(\alpha_2)}{\frac{1}{T_2} - \frac{1}{T_1}} \tag{3}$$

$$A = \alpha_1 \cdot \exp\left(\frac{E_a}{k_b \cdot T_1}\right) = \alpha_2 \cdot \exp\left(\frac{E_a}{k_b \cdot T_2}\right) \tag{4}$$

By using the previously determined quantities of activation energy and pre-exponential factor with the absolute in-situ temperature or recommended operating temperature, the in-situ decay rate constant, $\alpha_i$, can be determined using the form of the Arrhenius equation shown in equation (5).

$$\alpha_i = A \cdot \exp\left(\frac{-E_a}{k_b \cdot T_i}\right) \tag{5}$$

Lastly, the in-situ projected initial constant, $\beta_0$, is determined in order to calculate the in-situ RLF, $\Phi_i$, in order to produce lumen maintenance projections

$$\beta_0 = \sqrt{\beta_{55°C} \cdot \beta_{85°C}} \tag{6}$$

$$\Phi_i(t) = \beta_0 \cdot \exp(-\alpha_i \cdot t) \tag{7}$$

The RLF taken at the failure criteria of 70% is used to estimate the operating time in hours until the SSL device reaches L70.

$$L_{70} = \frac{\ln\left(\frac{\beta_0}{70}\right)}{\alpha_i} \tag{8}$$

### 1.3. RESEARCH OBJECTIVE

The equations for the TM28 projection standard have been outlined in the aforementioned section to illustrate the simplistic nature of lifetime projections currently used for SSL luminaires. One principal issue with TM28 is the lack of additional stresses or parameters needed to characterize non-temperature dependent failure mechanisms. Another principal issue is the assumption that one particular failure mode, lumen depreciation, is an adequate comparison of SSL luminaires. Furthermore, it will be demonstrated that TM28 does not adequately account for failure modes and mechanisms associated with the EDs used to power the LEDs or the ECs used to connect the ED and LE.

Currently, there are no established accelerated test methods for SSL devices to assess quality, reliability and durability before being introduced into the marketplace. Additionally, there is a need for Physics-of-Failure (PoF) based approaches to understand the processes and mechanisms that induce failure for the assessment of SSL reliability in order to develop suitable AFs that better represent SSL product lifetime. This and the deficiencies in TM28 validate the need behind the development of acceleration techniques to quantify SSL reliability under a variety of operational conditions. The ability to assess damage accrual in SSL devices is essential to understanding the lifetime of the SSL device itself.

This work will chronical the investigation of a large sample set of SSL lamps at different acceleration conditions and sampling times. This investigation demonstrates the deficiencies with TM28, as well as puts forth a robust model for the determination of acceleration factors (AFs) for lifetime characterization outside the scope of TM28. Additionally, an examination of an off-the-shelf ED in a harsh environment with the LE held in a pristine state will demonstrate the inability of TM28 to properly characterize failure of this SSL system due to no observed degradation in the LE and degradation only occurring in the ED. Lastly, degradation data from the AECs located inside the EDs and the ECs used to connect the electrical driver to the LE will be used to produce a prognostic framework for end of life predictions as a solution to the deficiencies of TM28 for SSL devices that do not include the LE.

The methodologies developed in this work increases the understanding of SSL lamps and devices through the investigation of lamp, driver and connector reliability which will enhance quality and reduce cost. This body of work will confirm the deficiencies with TM28 and demonstrate validated improvements over the current state-of-the-art used for SSL lifetime projections through the development of novel generalized acceleration factors, as well as a prognostics and health management (PHM) framework that can be tailored for use with non-thermally induced failure mechanisms.

# 2. Literature Review

This chapter will illustrate the current state-of-the-art with SSL devices, SSL components and lifetime characterization techniques. The SSL light engine reliability section will summarize previously reported failure modes and mechanisms encountered in SSL devices with specific focus on issues surrounding the components of the LE. SSL component level reliability will emphasize previously published research regarding ECs and AECs. The lifetime characterization section will discuss the proposed methods and techniques for the development of AFs, lifetime predictions, and PHM.

## 2.1. SSL LIGHT ENGINE RELIABILITY

An SSL lamp architecture is designed with performance factors in mind. Architectural integrity of SSL devices also takes into account some of the known and published LED related failure mechanisms, such as carbonization of the encapsulant material, delamination, encapsulant yellowing, lens cracking, and phosphor thermal quenching (Chang, 2012). Each failure mechanism ultimately produces a similar failure mode of lumen degradation. This is predominately due to two contributing factors: high junction temperature and moisture ingress. Literature is available on a wide variety of SSL component level investigations, such as the encapsulation materials, phosphors and LEDs. However, there is no published literature that investigates the entire SSL system which is essential to understanding the long-term reliability of these devices.

Excessive temperatures inside the LED package or the ingress of moisture can produce thermal-mechanical and hydro-mechanical stresses between the various material layers of LED packages causing delamination (Chang, 2012). Elevated temperatures and humidity can produce delamination between the die and silicone encapsulant (Philips Lumileds Lighting Company, 2006) and between the encapsulant and packaging lead frame (Luo, 2010). The stresses can also produce a number of small hairline cracks which is known as lens cracking. Lens cracking occurs with the introduction of thermal expansion at various operating temperatures (Hsu, 2008) (Philips Lumileds Lighting Company, 2006), as well as when a long-term exposure to moisture is experienced (Hewlett Packard, 1997).

### 2.1.1. Encapsulation Material

This makes material selection for the encapsulant material of an LED package extremely important in order to improve the efficiency of LEDs. Using the improper material will produce thermal stresses due to CTE mismatches and reduce the rate of heat transfer from the semiconductor causing a high junction temperature. The majority of high-power and mid-power LEDs use an epoxy or silicone based system as an encapsulant material.

Pure epoxy as an encapsulant material tends to degrade quickly when exposed to high temperatures and/or ultraviolet light. Consequently, this degradation promotes the ingress of moisture and air, as well as discoloration of the LEDs which will shorten the lifetime of white and blue LEDs. A higher refractive index and lower absorption coefficient has been shown to increase the light extraction efficiency of epoxy as shown in Figure 9. (Lin, 2006)

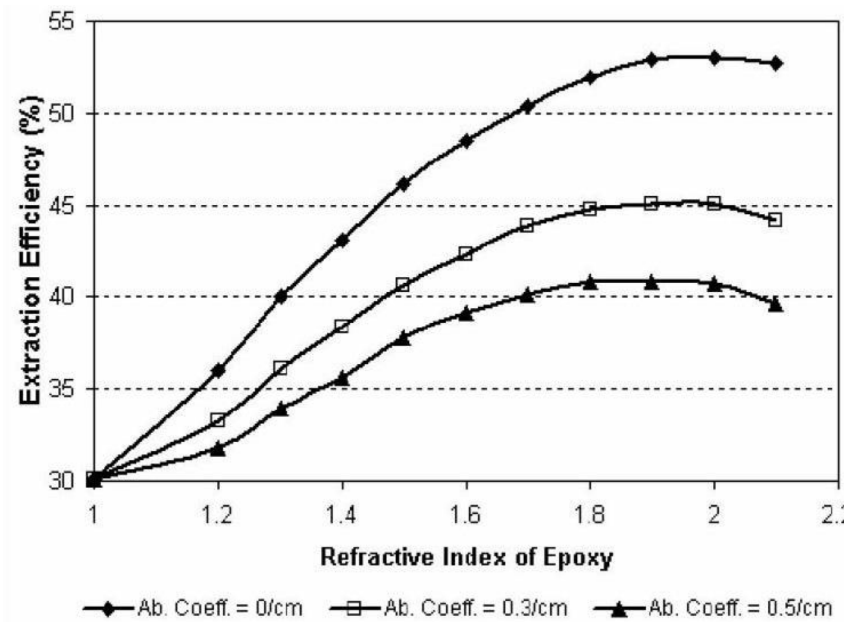


Figure 9: Extraction efficiency as a function of epoxy RI and absorption coefficient. (Lin, 2006)

Silicone as an encapsulant material is also used for high power LEDs and outdoor applications because of its good thermal stability and UV resistance (Lin, 2006). Some predominant issues of silicone are its poor physical properties and moisture resistance, as well as the need for an outer layer of protection (Lin, 2006).

Plastic encapsulation materials (PEMs) encounter degradation through large junction temperatures causing the attenuation of the light output (Narendran, 2004) (Baillot, 2010). Additionally, carbonization of the PEM on the diode surface can occur when excessive ambient temperatures are encountered. Large temperatures can cause formations of conductive paths across the LED which will ultimately lead to complete failure (Chang, 2012). Research has shown that PEM at elevated temperatures for prolonged periods of time start to degrade causing growth between the intermetallic layers, reduction of insulated electrical pathways, the initiation of thermal runaway processes and instantaneous combustion (McCluskey P. M., 2000) (McCluskey P. M., 2000). PEMs on the diode can also experience chain scission and discoloration known as encapsulant yellowing from an increase in the junction temperature and the presence of phosphors (Chang, 2012).

Thermal and UV characteristics of encapsulant materials can be enhanced by adding anti-oxidants and UV stabilizers or absorbers. The pure epoxy resins of diglycidyl ether of bisphenol-A and cycloaliphatic, as well as a novel formulation of an enhanced epoxy resin, have been investigated by thermally aging the encapsulants to explore the UV and thermal performance of each material is shown in Figure 10. (Lin, 2006) From Figure 10, the performance of an encapsulation material that has been enhanced fares better than the pure epoxy encapsulation materials.

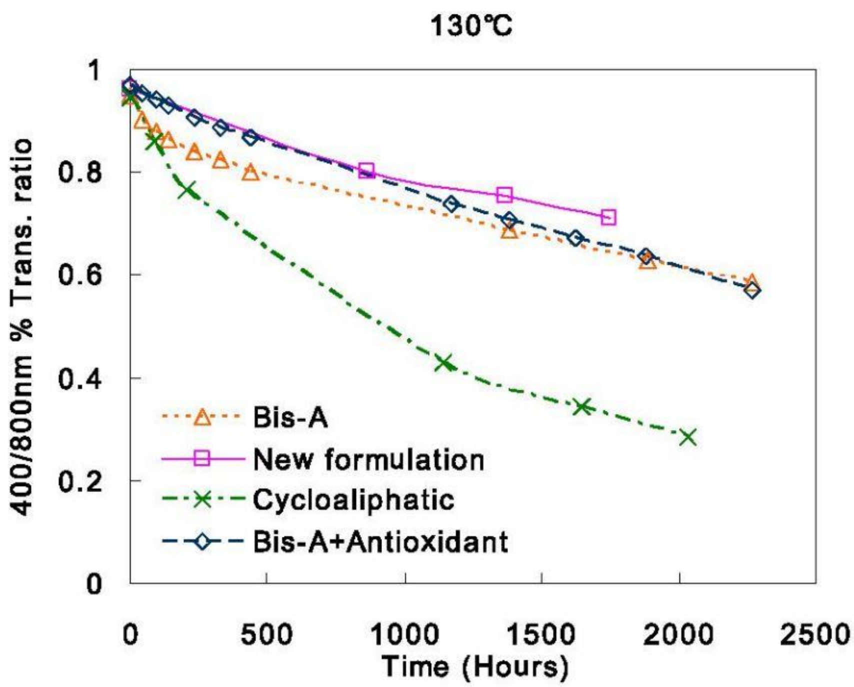


Figure 10: Thermal aging results of different epoxy encapsulation materials. (Lin, 2006)

Bisphenol-A polycarbonate (BPA-PC) plastic lens used as an encapsulation material has also been studied as a suitable choice for LEDs. One analysis demonstrated the effects of blue light radiation at high temperatures has on BPA-PC (Mehr M. Y., 2013b). The transmission spectra of light through photo-aged BPA-PC plates demonstrated little effect on the transmission between the wavelengths of 500nm and 700nm. However, it was observed that for wavelengths below 500nm, there was a significant decrease in transmission as shown in Figure 11. Additionally, at higher exposure times, the lower the transmission at 450nm which is an indication of encapsulant yellowing as shown in Figure 12.

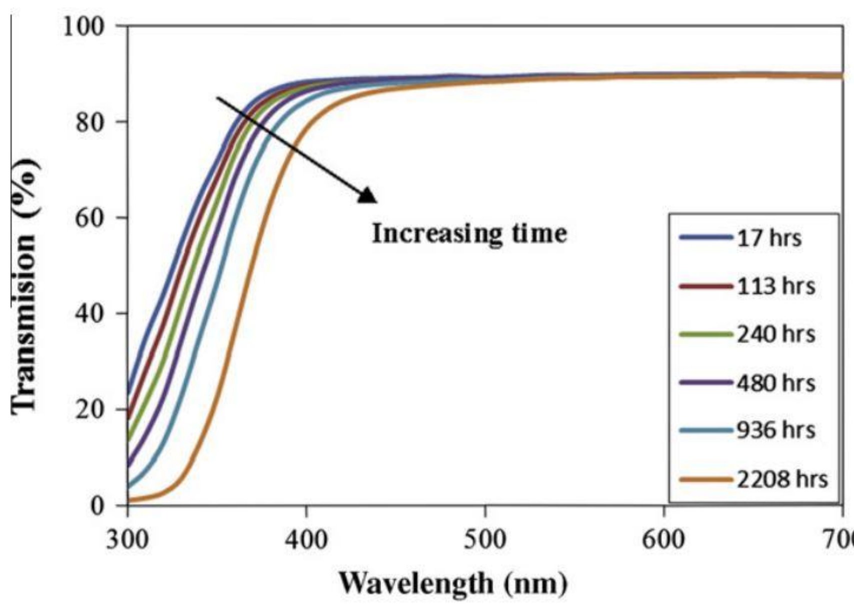


Figure 11: Transmission Spectra of Photoaged BPA-PC Plates with Irradiation Time. (Mehr M. Y., 2013b)

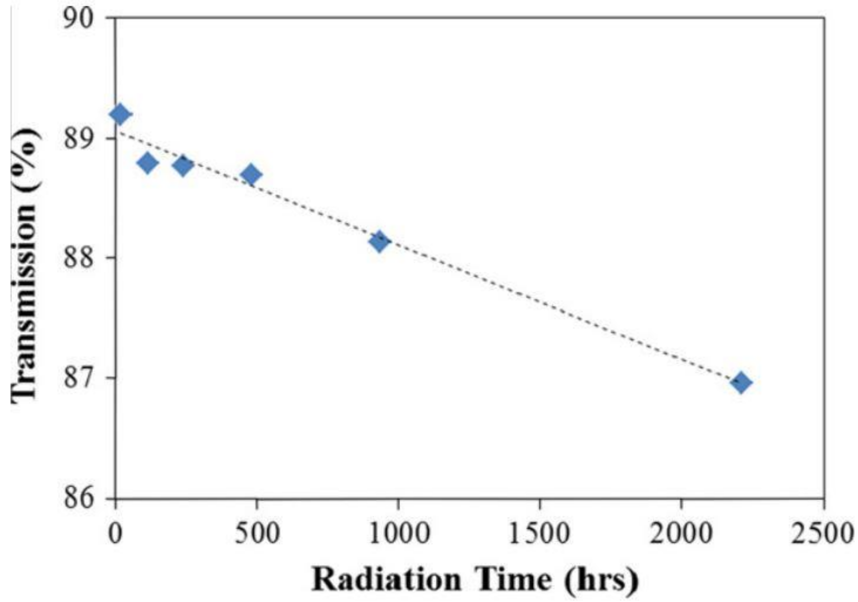


Figure 12: Transmission at 450nm of Photo-Aged BPA-PC Plates with Irradiation Time. (Mehr M. Y., 2013b)

Upon further investigation, the SPD of a LED chip place behind thermally aged BPA-PC plates and its corresponding maximum relative radiant power showed a decrease over radiation time. (Mehr M. Y., 2013b).

The yellowing index (YI) was of the BPA-PC plates as a function of exposure time for this work can be seen in Figure 13. From this analysis, there were two stages in the discoloration observed in both thermally-aged and photo-aged samples. The first stage is called the “induction regime” where there is no major change in the YI with relatively slow rate of yellowing. The second stage called the “accelerated regime” experiences a highly accelerated rate of yellowing. The transition between both regimes took place after 500 hours and 1500 hours for photo-aged and thermally-aged BPA-PC plates, respectively. The end results indicated that under blue radiation, the yellowing mechanism is the combination of photo-Fries and photo-oxidation with photo-Fries having the largest impact as ageing time increased (Mehr M. Y., 2013b).

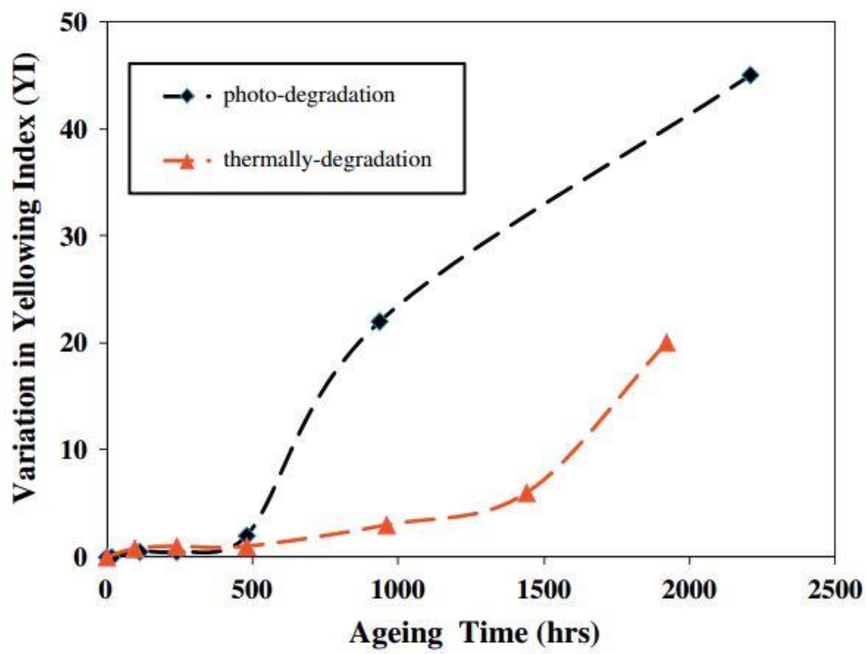


Figure 13: Variation in Yellowing Index of Thermal-Aged and Photo-Aged BPA-PC Plates Exposed to Blue Light at Different Ageing Times. (Mehr M. Y., 2013b)

Corrosion and depolymerization characteristics are also important in material selection. Encapsulants such as silicone resins, used to create water tight seals, may out-gas from excessive temperatures or the introduction of moisture releasing acetic acid which is highly corrosive to the packaging elements of LEDs (Dow Corning Corporation, 1997). The catalysts used to prepare silicones can also prove to be detrimental to the reliability of LEDs. When moisture and elevated temperatures are introduced, the compounds used to prepare silicone will start to catalyze producing depolymerization and a reduction in its thermal stability (Dow Corning Corporation, 1997). Furthermore, chromophores in the phosphors can catalyze reactions, such as polymerization and depolymerization of the encapsulants. Such reactions can result in clouding of otherwise transparent systems or unexpected changes in viscosity of the encapsulant during processing.

A high refractive index (RI) of the encapsulant is an essential parameter that needs to be accounted for since it impacts the light extraction efficiency of an LED. When light exits an LED with a remote phosphor configuration, light is scattered into a mixing chamber before it exits through the remote phosphor. A portion of the light is backscattered toward the LEDs. This will cause the internal temperature of the luminaire to increase, as well as cause the failure mechanism of encapsulant yellowing on the diode itself. The effect of short-wavelength radiation due to backscattering has been investigated for a group of white LED arrays which had a similar junction temperature of 95°C but produced different relative short-wavelength amplitudes, A, ranging between 0.89 – 1.24 as shown in Figure 14. (Narendran, 2004)

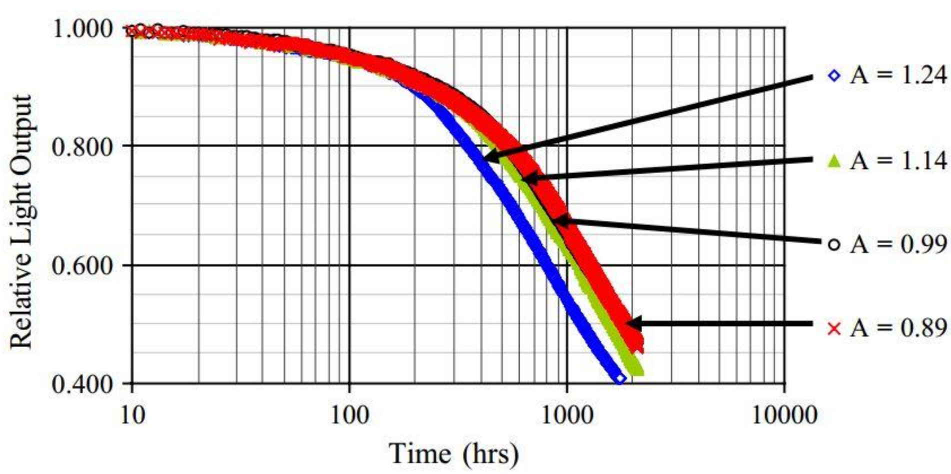


Figure 14: Relative Light output variation as a function of logarithmic time for an array of white LEDs. (Narendran, 2004)

As Figure 14 illustrates, larger short-wavelength amplitudes cause lumen degradation much faster than smaller short-wavelength amplitudes. This means that the encapsulant material must also be highly transparent with a large RI and is further enhanced by using a dome-shaped encapsulant (Schubert, 2006). A mismatch in the RI reduces the efficiency of light extraction. Also, the encapsulant material should be designed with an angle of incidence smaller than the critical angle. When the critical angle is exceeded, photons no longer escape the semiconductor and are reflected internally. The critical angle and the RI of the optical components in a luminaire provide design constraints that will prevent unintended reflections within the luminaire during both the absorption and emission steps of the phosphor down conversion process (Chang, 2012) (Lin, 2006). As shown in Figure 14, exposure to high temperatures due to UV absorption will reduce the RI of encapsulants which leads to the reduction of the luminous output. Additionally, the effect of junction temperature on the light output has been investigated for a group of white LED arrays with similar short-wavelength amplitudes of 1.14 and different junction temperature, Tj, between 69°C – 115°C. In addition to smaller short-wavelength amplitudes, Figure 15 demonstrates that the junction temperature of the LED also plays an important role in lumen degradation of LEDs. (Narendran, 2004)

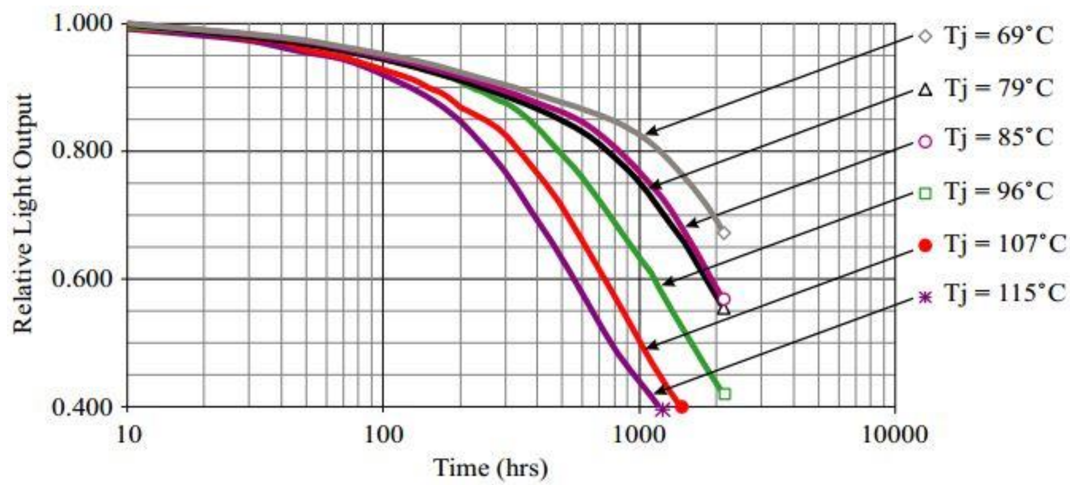


Figure 15: Light output variation as a function of logarithmic time at different junction temperatures. (Narendran, 2004)

### 2.1.2. PHOSPHOR

In addition to using a proper encapsulation material, another essential component in SSL applications is the use of phosphor to convert the light of a blue or UV LED to the desired white color. Unfortunately, the presence of phosphor produces a substantial decrease in reliability (Meneghini, 2008). When phosphor is in direct contact with the die, 60% of the phosphor emission is backscattered toward the LED chip and absorbed directly causing encapsulant yellowing. Using a remote phosphor technique decreases the amount of phosphor emissions absorbed by the encapsulation material. An LED package with lower concentrations of backscattered phosphor emissions and higher phosphor thicknesses has a higher luminous efficacy (Chang, 2012).

Phosphor thermal quenching occurs at elevated temperatures when the luminescence efficiency begins to decrease rapidly. This causes the thermal vibrations from the semiconductor to become intensive enough to decrease the quantum efficiency of the LED producing energy levels that intersect that of the phosphor deterring luminescence (Lakshmanan, 2011). This will degrade the phosphor and decrease the light output due to thermally driven temperature dependent phosphorescence decay (Philips Lumileds Lighting Company, 2006). Typical phosphors used in white LEDs can be divided into sulfides, aluminates, nitrides, and silicates with each having its own strengths and weaknesses. The phosphors used to produce white LEDs must be able to absorb a high amount of blue or UV light; have a high conversion efficiency; and have a high resistance to chemicals, oxygen, carbon dioxide, and moisture (Xie R. J., 2007).

The current state of research focused on solving the phosphor thermal quenching problem utilizes and develops new phosphor materials mixed with a variety of color LEDs to generate white light. Investigations have been conducted already into several combinations of a phosphorus/LED mix to produce some variation of white light. Chang et al. developed a robust list of previous research into phosphor configurations to combat thermal quenching with some notable contributions found in Table 1. (Chang, 2012)

Table 1: Notable Phosphor Combinations to Combat Thermal Quenching.

| **Phosphor Configuration** | **Type of LED** |
|---|---|
| Yellow YAG: $Ce^{3+}$ | Blue |
| Red $Sr_2SiN_8:Eu^{2+}$ & Green $SrSi_2O_2N_2:Eu^{2+}$ | Blue InGaN & GaN |
| Red CaAl-$SiN_3:Eu^{2+}$ | Blue & Violet |

The remote phosphor approach of luminaire design frequently utilizes an indium gallium nitride (InGaN) LED or blue LED and a yellow emitting cerium doped yttrium aluminum garnet (YAG: Ce) phosphor. This can be seen in existing consumer LED light bulbs such as the Philips LPrize bulb. The phosphor is positioned away from the LED rather than directly on the LED as is done for the production of white LEDs today. Blue light combines with the yellow phosphor inside of a mixing chamber before exiting the luminaire as white light. By increasing the distance between the blue LED and the phosphor, the color stability of the SSL system can be enhanced. An increase in the luminaire’s ability to perform at high operating temperatures can also be achieved with remote phosphor.

Research has shown that a luminaire using a yellow emitting YAG:Ce remote phosphor and a blue LED to generate white light degrades less when compared to one that uses white LEDs. Narendran et al. investigated three groups of LED arrays at two different currents: white LEDs with a phosphor layer on the LED, blue LEDs with a remote phosphor configuration and blue LEDs with no phosphor. It was shown that white LEDs degraded much quicker than blue LEDs with and without a remote phosphor configuration as shown in Figure 16. (Narendran, 2004)

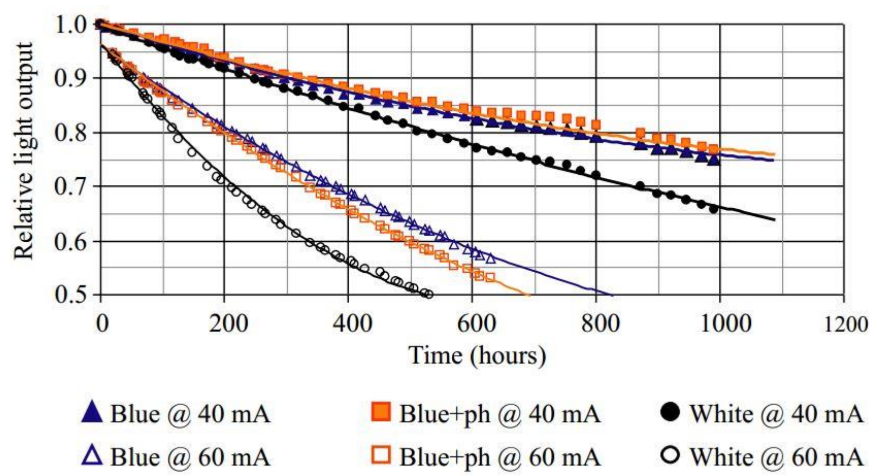


Figure 16: Lumen degradation for different types of LED arrays. (Narendran, 2004)

Remote phosphor also has an additional advantage of reducing heat accumulation inside the mixing chamber of the luminaire used to produce white light. Insertion of a low-index air-layer between the remote phosphor layer and the blue LED, as well as the distance between the phosphor and LED, will reduce degradation of the phosphor due to a lower temperature inside the mixing chamber. When phosphor thermal quenching occurs, failure modes of lumen degradation, color shift and the broadening of full width at half maximum (FWHM) due to thermally driven temperature dependent phosphorescence decay are produced (Chang, 2012). These failure modes have been researched and can be seen in Figure 17. Figure 17 shows degradation beginning to occur at a temperature of 80°C. Measurements were taken at different intervals as the luminaire was heated. It is shown that after 80°C, thermal quenching begins to take effect producing a decrease in the light output along with the broadening of FWHM initiating a drift of the perceived color of the white light.

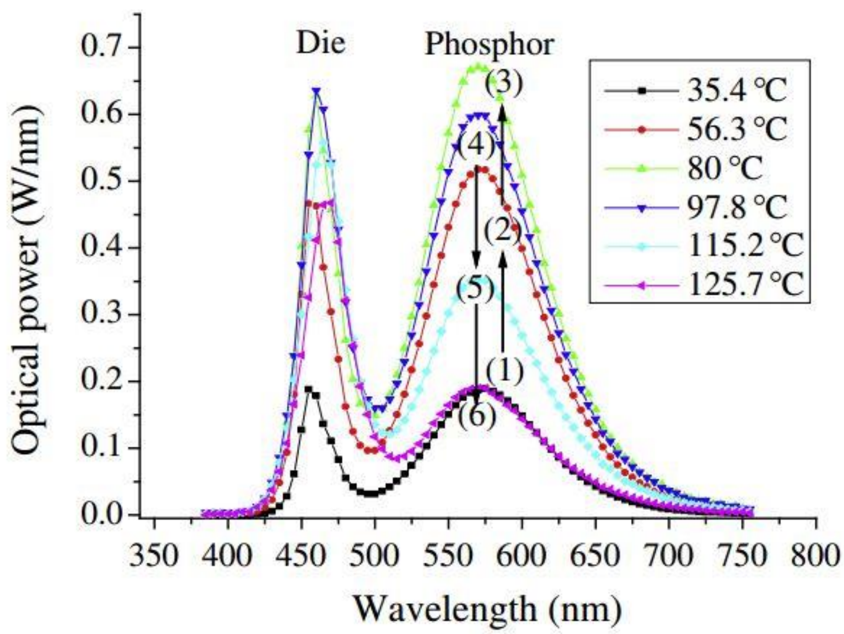


Figure 17: Optical power change with temperature rise. (Chang, 2012)

Proximate phosphor is used with "white" LEDs. In this case, the phosphor is placed directly onto the chip. A comparison study of the effects degraded BPA-PC and Poly-methl methacrylate (PMMA) has on a commercially available mid-power proximate phosphor LED has recently been published in literature (Lu, 2015).

The effects of thermally aged at 85°C for 3000 hours and non-thermally aged BPA-PC encapsulants with a pristine proximate phosphor LED demonstrated a relative luminous intensity decrease in both the blue wavelength range and the yellow wavelength range as shown in Figure 18. The thermally aged BPA-PC decreased at the blue peak and remained stable at the yellow peak when compared to the non-aged BPA-PC (Lu, 2015)

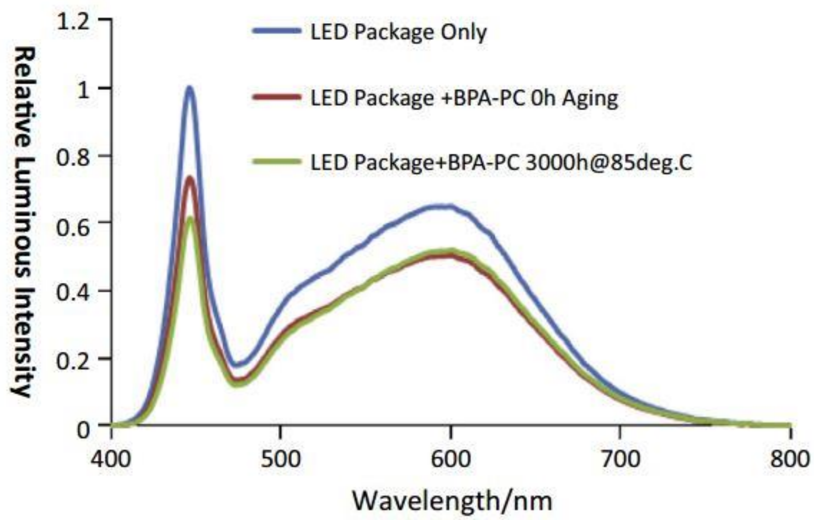


Figure 18: Spectral Power Distribution of a Proximate Phosphor LED Alone, with Non-Aged PBA-PC and Thermal-Aged BPA-PC. (Lu, 2015)

A similar study was conducted on PMMA using the same ALT condition of 85°C for 3000 hours with the inclusion of the ALT condition 85°C for 3000 hours with blue radiation and the ALT condition 85°C for 3000 hours with 85% RH. The results demonstrated no significant change in the relative luminous intensity of the proximate LED with the inclusion of PMMA or aged PMMA. (Lu, 2015)

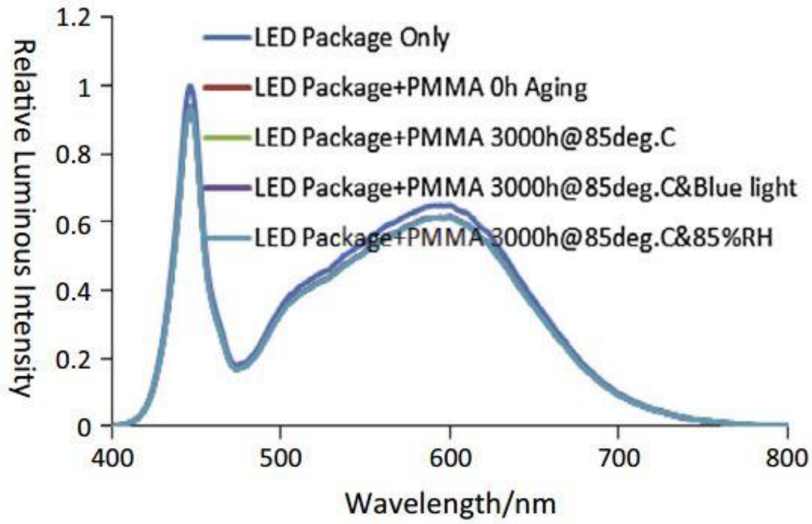


Figure 19: Spectral Power Distribution of a Proximate Phosphor LED PMMA Configurations. (Lu, 2015)

To further investigate the BPA-PC and PMMA specimens, the transmittance spectra over the visible spectrum was measured and is shown for BPA-PC and PMMA in Figure 20 and Figure 21, respectively. Figure 20 shows a decrease in peak wavelength of blue light after thermal aging. Additionally, for non-aged BPA-PC, transmittance varies with wavelength. Figure 21 depicts the transmittance spectra of PMMA and produced values almost identical. (Lu, 2015) From this analysis, the selection of the encapsulation material is an important parameter to account for when investigating proximate phosphor LEDs.

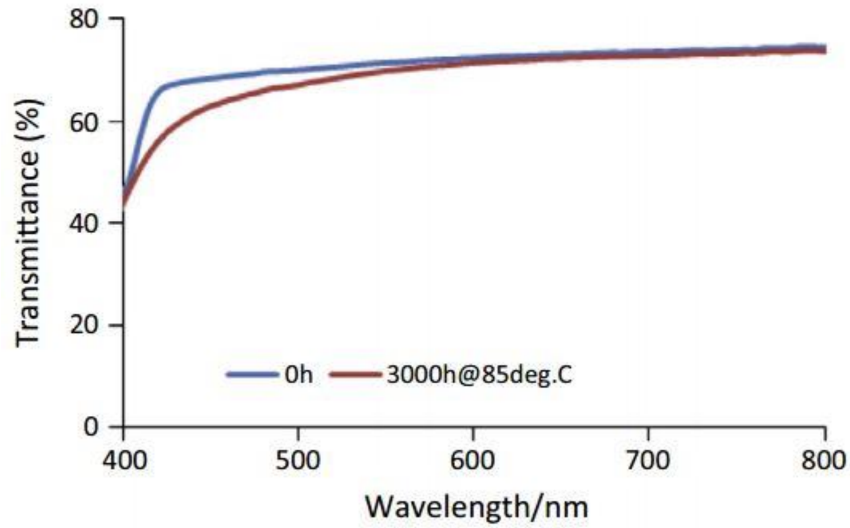


Figure 20: Transmittance Spectra of BPA-PC. (Lu, 2015)

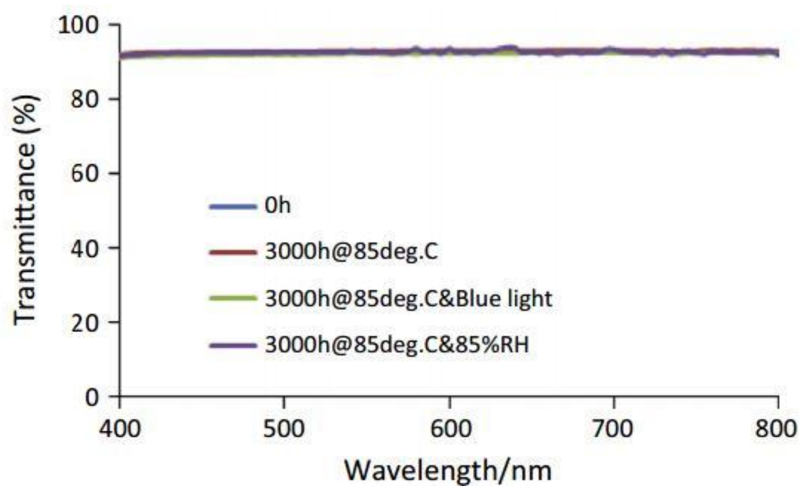


Figure 21: Transmittance Spectra of the PMMA Configurations. (Lu, 2015)

The majority of research into SSL devices has focused on the LEDs, phosphors and encapsulation materials. The investigation of these components together, in the form of an operational SSL lamp in order to determine the overall interactions of the combined failure mechanisms, is a novel approach. It is essential to understand the synergism between these failure mechanisms to produce meaningful lifetime characterizations of SSL devices.

## 2.2. COMPONENT LEVEL RELIABILITY

### 2.2.1. ALUMINUM ELECTROLYTIC CAPACITORS

The predominant failure mechanism of the AEC is loss of liquid electrolyte through dissipation and decomposition. Liquid electrolyte loss can be attributed to an elevated ambient temperature, electrochemical reactions at the dielectric layer, moisture ingress or diffusion through the seal (Albertsen, 2012) (Han, 2009). This will lead to a drift of the electrical parameters of the AEC. If an AEC is kept at an elevated ambient temperature for a prolonged period of time causing liquid electrolyte degradation, then the CAP will decrease and the ESR will increase (Rubycon Corporation, 2013) (Nichicon Inc., 2002) (Albertsen, 2012) (Han, 2009) (Harada, 1993) (Gasperi, 1996) (BHC Components, 2002) (Sankaran, 1997) (Stevens, 2002) (Panasonic Industrial Company, 2008) (Cornell Dubilier Electronics Inc., 2000) (Celaya, 2011) (Ma, 2005). Literature has shown that CAP and ESR are excellent leading indications of failure for prognostic and health management techniques (Kulkarni C. S., 2012) (Imam, 2005) (Kulkarni C. S., 2012), as well suitable parameters to investigate LED driver reliability (Lan, 2012).

### 2.2.2. ELECTRICAL CONNECTORS

ECs are extensively used in a wide variety of electronics ranging from mission critical systems to consumer grade products. Connectors exposed to dynamic operating conditions may experience vibration resulting in fretting corrosion and degradation in the contact resistance over time. Fretting corrosion is due to mechanical stresses and is defined as accelerated damage at the interface of two contacting surfaces that are subject to oscillatory movements (Xie F. , 2007). Connector degradation may lead to premature electrical failure during use, or prior to, which can potentially be catastrophic.

EC fretting corrosion has been studied experimentally using a variety of test setups. The effects of frequencies, vibration levels and tie off lengths for a range of vibration profiles have been previously investigated for tin coated, rectangular-pin and socket ECs (Flowers G. T., 2006) (Flowers G. T., 2005) (Flowers G. T., 2004) and for single tin plated blade/receptacle connector pairs (Xie F. F., 2009). Other more realistic test configurations take into consideration humidity, temperature, and pressure to produce a more robust data set on connector degradation (Jedrzejczyk, 2009) (Lam, 2006). Additionally, experimental work on ECs has focused on the effects that different intermetallic compounds (Noel, 2011) (Daniel, 2004) and polymers (Swingler J. , 2009) (Swingler J. L., 2010) have on fretting deterioration when used as a protective coating.

Simulations have been published that attempt to predict the contact resistance or wear of a connector during deterioration. One predictive model for contact resistance incorporated contact wipe, fretting vibration amplitude and frequency, contaminant chemistry, material properties, plating thickness, asperity deformations, normal loads, electrical loads and surface topography (Bryant, 1994). Another simulation model related early stage fretting corrosion to the threshold vibration levels for the connector, the dynamic characteristics of the connector/wire configuration and the vibration profile (Flowers G. T., 2005). Furthermore, additional published connector degradation models include a multi-scale asperity model to predict electrical resistance of a connector (Jackson, 2007), a finite element model of the connector system to relate the actual dynamics of the contact interface to the threshold vibration levels required for the onset of fretting and the relative motion transfer function (Xie F. F., 2009), and a finite element model that takes into account the mechanical, electrical and thermal interactions of a pin and connector to perform a realistic performance analysis to provide predictions of the contact forces and the electrical and thermal contact resistances on the contact regions (Angadi, 2008). The aforementioned finite element model also provided stresses, strains, heat effects, current flow, electrical potential and temperature distributions in the spring and pin parts of a connector (Angadi, 2008).

The use of electrical degradation data due to fretting corrosion with a PHM framework has not been discovered in the literature review. This is a novel approach for lifetime predictions of an EC through in-situ measurements for real-time health monitoring.

### 2.3. LIFETIME CHARACTERIZATION

PHM is a useful tool to monitor and assess degradation of "products" for reliability assessment and lifetime predictions. PHM is a proven technique and has been used for the correlation of damage initiation, damage progression and residual life in the pre-failure space using damage based proxies, time dependent feature vectors and time-frequency characteristics with a variety of electronic components, accelerated testing methods and recursive algorithms to prognosticate life (Lall P. B., 2008d) (Lall P. C., 2006a) (Lall P. C., 2007a) (Lall P. C., 2008a) (Lall P. G., 2007b) (Lall P. H., 2007e) (Lall P. H., 2008c) (Lall P. H., 2007c) (Lall P. H., 2006b) (Lall P. I., 2005a) (Lall P. I., 2004a) (Lall P. I., 2006c) (Lall P. I., 2004b) (Lall P. I., 2006d) (Lall P. I., 2004c) (Lall P. I., 2008f) (Lall P. L., 2011a) (Lall P. L., 2011c) (Lall P. L., 2011b) (Lall P. L., 2010a) (Lall P. L., 2009b) (Lall P. L., 2010b) (Lall P. L., 2009a) (Lall P. P., 2008b) (Lall P. P., 2005b) (Lall P. P., 2004d) (Lall P. P., 2006e) (Lall P. P., 2007d) (Lall P. W., 2012a) (Lall P. S., 2013a) (Lall P. Z., 2013b) (Lall P. S., 2012b). Literature is sparse to nonexistent with the implementation of PHM techniques to accurately assess and predict reliability of ECs, AECs and SSL.

Some work has been published on the use of PHM techniques with AECs. Celaya et al. has demonstrated the effects of electrical overstress accelerated aging on AECs. The ESR and capacitance values were estimated from the capacitor impedance frequency response and a lump parameter model, respectively, and used in conjunction with a Kalman filter to determine the remaining useful life (RUL) (Celaya, 2011). Zhou et al. investigated three components of a switch-mode power supply, MOSFETs, diodes and AECs, using a PoF approach. The values of each component were estimated using equations outlined in literature and were used with a linear regression model to make RUL predictions (Zhou, 2012). Abdennadher et al. examined the ESR and capacitance of AECs in an uninterruptible power supply. The values were estimated using current and voltage measurements of the power supply and used in conjunction with a Least-Squares curve-fit to extrapolate the RUL of the AECs (Abdennadher, 2010).

Fan et al. used a PoF based PHM approach for high-power LEDs by identifying the failure modes and potential failure mechanisms to establish a useful model to quantify degradation through the evaluation of material type, geometry and published LM-80 data from the manufacturer. Specifically, focus was placed on the construction of two different models to assess the degradation of the two “critical failure mechanisms” of thermal-induced lumen degradation and solder interconnect fatigue (Fan, 2011). Sutharssan et al. also used a PoF data driven approach on single LEDs that were aged with an accelerated voltage condition. The Euclidean and Mahalanobis distance measuring techniques were used to correlate changes in the current through the p-n junction and the temperature of the p-n junction to degradation in the luminous flux for the assessment of the RUL (Sutharssan, 2011).

Mehr et al. investigated lifetime of BPA-PC plastic lens used in LEDs in terms of acceleration factors. Two commercially available BPA-PC plates, A and B, where aged at three different temperatures of 100°C, 120°C and 140°C for 3000 hours at each temperature condition (Mehr M. Y., 2013a). Relative luminous flux calculations were carried out for a pristine light source for the thermally-aged plates A and B. This degradation data was then used with the Arrhenius equation to produce temperature dependent reaction rates for both A and B. The reaction rates were used to produce acceleration factors for BPA-PC plastic degradation in a range of 2.2 to 4.3. (Mehr M. Y., 2013a)

Long-term testing in normal operating conditions is being conducted by the DOE and the Pacific Northwest National Lab (PNNL) for LED luminaires on the I-35 West Bridge, Minneapolis, Minnesota (DOE: EERE, 2014a), LED parking structure lighting (DOE: EERE, 2013b), LED street lighting (DOE EERE, 2013c), a University of Florida performing arts building (Miller N. K., 2014a) and for pedestrian friendly outdoor lighting (Miller N. M., 2013). In each of these cases, the goal is long-term data collection under use conditions. The DOE through PNNL and the Research Triangle Institute (RTI) have begun the process of developing accelerated testing methods and analysis of PAR38 lamps (DOE: EERE, 2013d) and six inch recessed downlights (DOE: EERE, 2013a), respectively.

Proposed methods and algorithms for lifetime characterization of SSL devices does not yet exist in the current body of literature for an SSL device at accelerated conditions. It has been shown the Arrhenius equation can produce acceleration factors for encapsulation materials with no generalized acceleration factor model put forth. In the work outlined in this dissertation, an investigation of the degradation of an entire SSL device is shown, as well as a generalized acceleration factor model. This is a novel approach that has not been demonstrated in the literature before. Additionally, while PHM has been implemented with AECs and LEDs in separate instances, an investigation between the interactions of AECs and LEDs for a prognostic framework has not been found in literature.

## 2.4. IES Approved Methods and Standards

Since a number of approved IES standards are mentioned throughout the manuscript, it is important to discuss the scope and intentions of each standard.

### 2.4.1. IES LM-79-08

The IES LM-79-08 (LM79) is the only approved method for electrical and photometric measurements of SSL products. LM79 describes the procedures to follow and precautions to be observed in order to obtain reproducible measurements of total luminous flux, electrical power, luminous intensity distribution and chromaticity for SSL products under a standard operating condition of 25°C with less than 65% RH. (IES, 2008a)

LM79 has been used extensively in this work in order to accurately and precisely measure the spectral radiant flux of SSL lamps using a $4\pi$ integrating sphere configuration as described in the standard. Additionally, the self-absorption factor needed to correct differences between the NIST standard calibration lamp and the SSL lamp under test follows the procedures outlined in LM79.

### 2.4.2. IES LM-80-08 & LM-84-14

The IES LM-80-08 (LM80) was developed as the approved method for measuring lumen maintenance of LEDs. LM80 requires the testing of LEDs operating between photometric measurements per LM79 to be at a minimum of three nominal case temperatures of 55°C, 85°C and a case temperature selected by the manufacturer (IES, 2008b). This standard lead to the development of LM-84-14 (LM84) method for measuring luminous flux and color maintenance of LED lamps, light engines and luminaires. LM84 outlines the methods for luminous flux and color maintenance of SSL devices, but does not provide any guidance or recommendations regarding sampling, predictive estimations or extrapolation of luminous flux maintenance beyond the final measurement (IES, 2014a). Both methods do not outline acceleration techniques or lifetime predictions.

### 2.4.3. IES TM-21-11 &TM-28-14

Both the IES TM-21-11 (TM21) and TM-28-14 (TM28) are standards for the projection of long-term luminous flux maintenance for LEDs and SSL luminaires, respectively. Both methods outline a similar technique to produce luminous flux projections using the Arrhenius equation at normal operating conditions of 25°C with less than 65% RH. Each method outlines an appropriate sampling time and guidelines for using the relative luminous flux measurements obtained from LM79. (IES, 2011) (IES, 2014b)

These methods do not outline acceleration techniques, acceleration factors or lifetime predictions. They are simply used make lumen maintenance projects based off of collected degradation data.

## 2.5. CONCLUSIONS

The investigation of a complete SSL system in terms of temperature and humidity has not previously been reported and validates the necessity for acceleration techniques and algorithms to describe degradation in SSL devices. Additionally, the direct measurement of AECs, the interactions between the AECs with the EDs and LEs and the creation of a PHM framework to quantify degradation is a novel approach for SSL luminaires. Lastly, ECs used to connect the ED and the LE has never been investigated for use with PHM techniques.

# 3. Experimental Plan & Procedure

This chapter will outline the different test vehicles, the ALT conditions used to accelerate degradation, the techniques used to collect degradation data and the steps used to process the raw collected data into meaningful results for a robust generalized AF model and PHM framework that corrects the deficiencies with TM28.

## 3.1. Test Vehicles

### 3.1.1. Solid-State Lighting Lamps

A large sample set of SSL lamps tested at different acceleration conditions and sampling times has been used in this work. The test vehicles used in the SSL lamp analysis are off-the-shelf SSL 60W replacement lamps of various shapes, sizes and rated characteristics as shown in Table 2.

Table 2: Rated Parameters of SSL Lamps.

| SSL Lamp | CCW | CHWW | CWW | PCW | PLP | PSL | PWW |
|---|---|---|---|---|---|---|---|
| Luminous Flux [lm] | 800 | 800 | 800 | 830 | 800 | 800 | 830 |
| CCT [K] | 5000 | 3000 | 2700 | 5000 | 2700 | 2700 | 2700 |
| Power [W] | 9 | 9 | 9.5 | 12 | 12.5 | 10.5 | 11 |
| Efficacy [lm/W] | 88.9 | 88.9 | 84.2 | 69.1 | 64 | 76.2 | 75 |
| Power Factor | 1 | 0.63 | 0.9 | 0.9 | 0.7 | 0.9 | 0.7 |
| Length [mm] | 111.1 | 125 | 112.7 | 104.6 | 106.68 | 111.7 | 105 |
| Diameter [mm] | 60.3 | 69.6 | 60.3 | 61.2 | 58.42 | 68.9 | 60 |
| Weight [g] | 113 | 148 | 113 | 132 | 176 | 56 | 132 |
| Remote Phosphor | | | | X | X | | X |
| Proximate Phosphor | X | X | X | | | X | |
| Warm-White | | X | X | | X | X | X |
| Cool-White | X | | | X | | | |

The SSL lamps were used to confirm the deficiencies with using the Arrhenius equation, as with TM28, to properly model the failure modes of an SSL system and to develop a suitable model to produce generalized AFs. Table 3 lists the SSL lamp groups, denoted as 85CG#, used to investigate the Arrhenius model which focuses on temperature dependent failure mechanisms only. This set of SSL lamps utilized the same temperature condition with varied combinations of humidity and power to illustrate the need to account for additional stresses to properly model the failure mechanisms and modes of SSL lamps.

Table 3: SSL Lamp Groups Used for the TM28 Defficiency Analysis.

| **SSL Lamp Group** | **SSL Lamp** | **# Samples** |
|---|---|---|
| 85CG1 | PLP | 10 |
| 85CG2 | PSL | 5 |
| 85CG3 | PWW | 10 |

Table 4: SSL Lamp Groups Used for Generalized Acceleration Factors.

| **SSL Lamp Group** | **SSL Lamp** | **# Samples** |
|---|---|---|
| SSLG1 | CHWW | 10 |
| | CWW | 10 |
| | PWW | 10 |
| SSLG2 | CCW | 10 |
| | PCW | 10 |
| | PSL | 10 |
| SSLG3 | CCW | 1 |
| | CHWW | 1 |
| | CWW | 1 |
| | PCW | 1 |
| | PLP | 1 |
| | PSL | 1 |
| | PWW | 1 |

Table 4 lists the SSL groups, denoted as SSLG#, that underwent three different ALT conditions to compile a robust dataset needed to develop a suitable generalized AF model. The degradation of the lamps has been characterized as the relative change of the photometric and colorimetric measurements taken for of each lamp at each sampling period. The ALT conditions and the photometric and colorimetric quantities for the SSL lamps is discussed in greater detail further in this chapter.

### 3.1.2. LED ELECTRICAL DRIVER

The test vehicle used to investigate ED reliability was an off-the-shelf SSL device which consisted of an LED downlight module, an ED (boost PWM half-bridge rectifier) and wired connections to attach the two components, as well as to connect the ED to the main power supply. The EDs were separated into two groups which underwent different ALT conditions. Group1 (EDG1) consisted of five EDs intact and five EDs with the AECs removed. Group 2 (EDG2) consisted of ten EDs with the AECs removed from each unit. A single, pristine LE was used with the EDs from ALT to monitor the overall health of the SSL system. This approach facilitates assignment of any observed changes in lumen maintenance caused by the degradation of the EDs. Figure 22 illustrates how each component of the SSL system is incorporated.

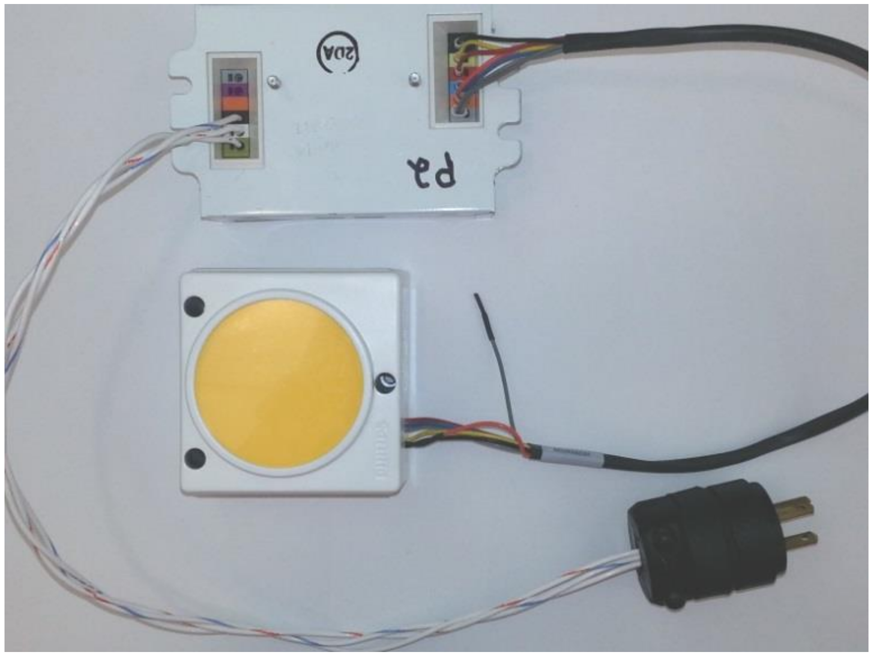

Figure 22: The SSL System Used to Investiagtate ED Reliability.

Four specific AECS inside each ED were monitored as leading indications of failure in the “pre-failure space” for the SSL system. Each ED contained four AECs of three different types that were removed to take electrical measurements of CAP and ESR for each AEC directly. Once the measurements on the AECs were taken, the AECs were connected back to the ED to investigate the effects on the SSL system due to the degradation of the ED and AECs. Figure 23 depicts an ED removed from its protective casing, as well as the removed AECs with their corresponding location inside of the ED. Table 5 lists the useful characteristics of the AECs located inside the ED.

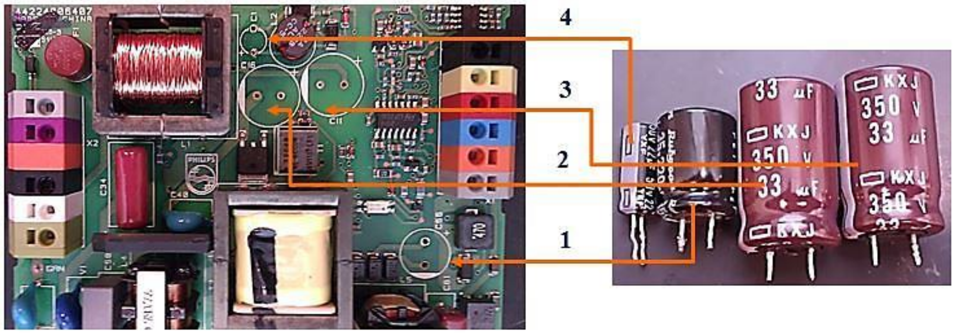


Figure 23: The removed AECs and their corresponding location inside the EDs.

Table 5: AEC Manufacturer Characteristics. (Rubycon Corporation, 2013) (Nippon Chemi-Con, 2013)

| AEC # | Endurance [Hrs.] | $T_o$ [°C] | $V_o$ [Vdc] | $C_o$ [µF] |
|---|---|---|---|---|
| 1 | 8000 to 10000 | -40 to +105 | 35 | 220 |
| 2 | 10000 to 12000 | -40 to +105 | 350 | 33 |
| 3 | 10000 to 12000 | -40 to +105 | 350 | 33 |
| 4 | 4000 to 5000 | -40 to +105 | 50 | 22 |

### 3.1.3. ELECTRICAL CONNECTORS

A group of five tin coated, rectangular-pin and socket ECs used to connect an SSL LE and its accompanying ED were investigated in order to obtain information on the reliability of this SSL component due to vibration induced fretting degradation which lacks a temperature dependent reaction rate needed to use TM28. The degradation of the ECs was accelerated using an electrodynamic shaker system in order to monitor the change in the electrical contact resistance of a pair of daisy chained pins for the development of a PHM framework. An example of this test vehicle can be seen in Figure 24.

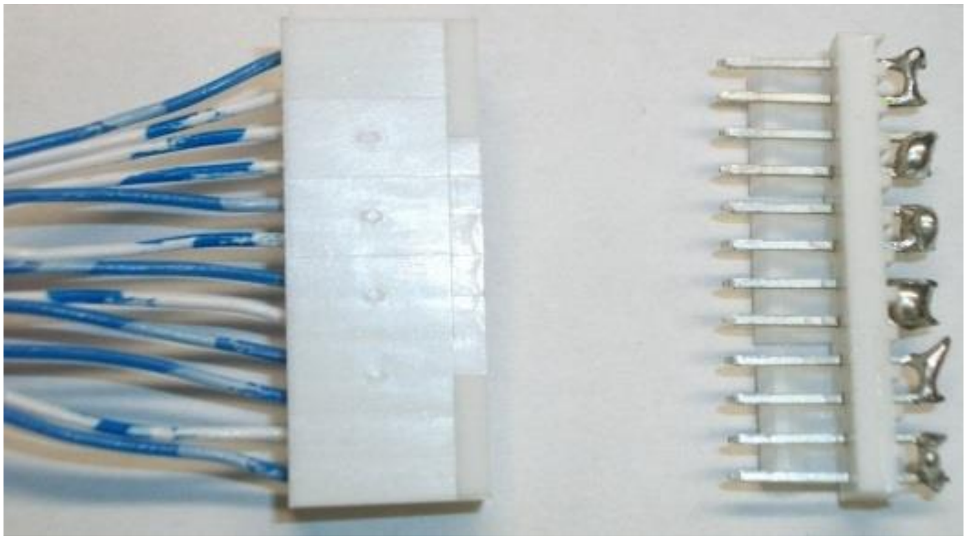

Figure 24: The EC Test Vehicle.

### 3.2. ACCELERATED LIFE TESTING

ALT has been used to accelerate the degradation of each test vehicle in order to capture failure data for the determination of failure modes and mechanisms to develop suitable acceleration models and a PHM framework.

#### 3.2.1. VIBRATION PROFILE

Each EC, as shown in Figure 24, was subjected to random vibrations using an out-of-plane electrodynamic shaker system. The male portion of the EC was rigidly attached to the vibration table to coincide with the male pins inside the LE that is separate from the ED as shown in Figure 22. The female portion was allowed to oscillate during the random vibration profile to accelerate fretting degradation on the pins. Figure 25 depicts the vibration profile with the vibration parameters shown in Table 6.

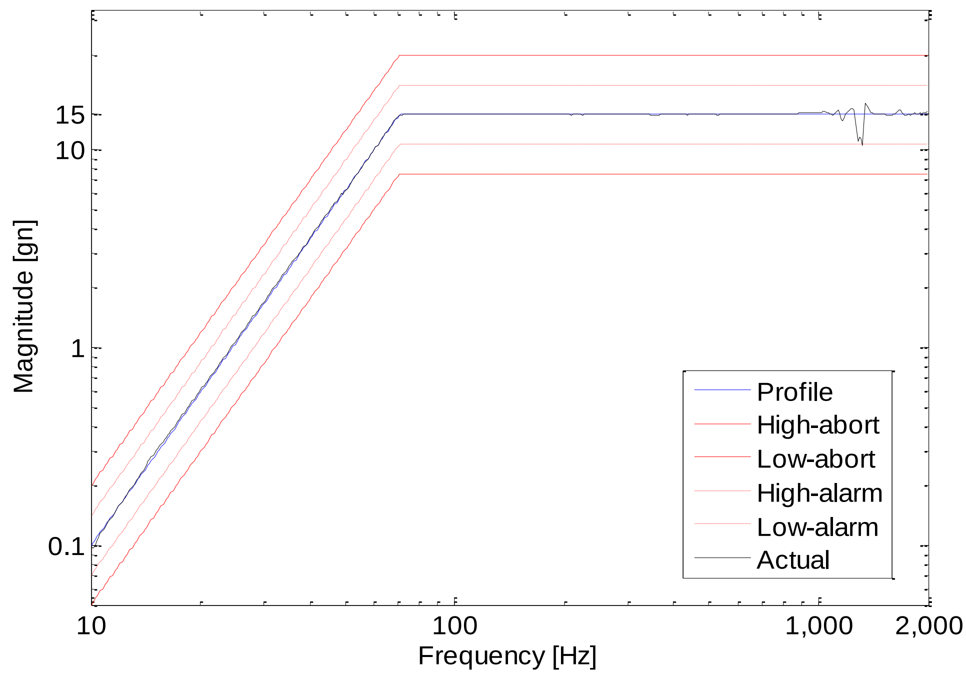


Figure 25: The Random Vibration Acceleration Profile.

Table 6: Out-of-Plane Vibration Characteristics.

| **Component** | **Value** |
|---|---|
| Peak-to-Peak Displacement [in] | 0.279 |
| Velocity [in/s] | 21.202 |
| Vibration Loading [grms] | 10 |
| Frequency Range [Hz] | 65 – 2000 |

### 3.2.2. High Temperature Storage Life Profile

High temperature storage life (HTSL) testing was used to determine the effects of high temperature over time in order to investigate thermally activated failure mechanisms on EDG1, with specific focus on the degradation of the AECs. The test vehicles underwent a steady-state high temperature soak with appropriate measurement intervals as described in the JEDEC Standard 22-A103D. (JEDEC, 2010) The HTSL profile can be seen in Figure 26, where $\Delta t$ is the sampling period at interval i = 0, 1, 2...

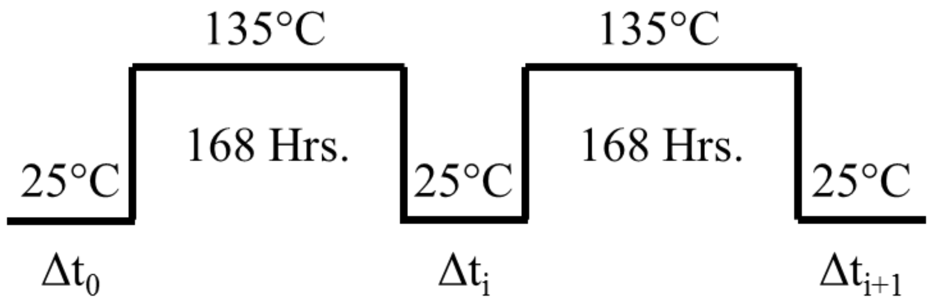


Figure 26: HTSL Acceleration Profile for EDG1.

### 3.2.3. STEADY-STATE TEMPERATURE BIAS PROFILE

A steady-state temperature bias (TB) life test was used with 85CG2 to illustrate the effects of temperature with no humidity. This has been investigated to demonstrate that thermally activated failure mechanisms alone are insufficient at quantifying the reliability of SSL lamps as stated with TM28. The TB profile can be seen in Figure 27 , where Δt is the sampling period at interval i = 0, 1, 2...

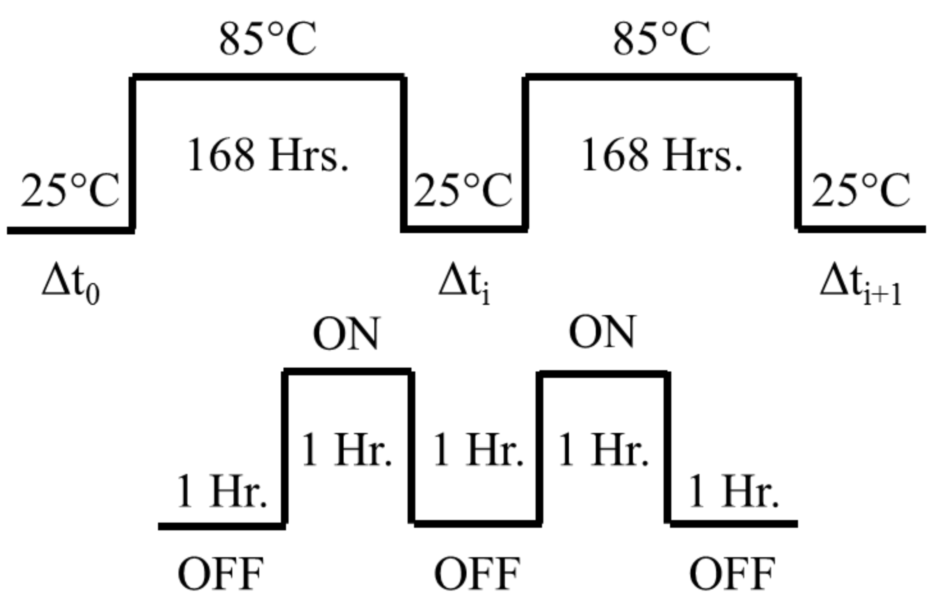


Figure 27: TB Acceleration Profile for 85CG2.

### 3.2.4. Steady-State Temperature-Humidity Soak Profile

A steady-state temperature-humidity soak (THS) life test was utilized to investigate the reliability of the group EDG2 in a humid environment. This ALT environment consisted of high humidity with a moderate temperature to hasten the ingress of moisture inside the EDs in order to investigate humidity related failure mechanisms of the AECs.

Additionally, THS life testing on group 85CG1 was explored as a suitable criterion to accelerate degradation in SSL lamps. This was completed in order to compare nonbiased life testing to biased life testing of the SSL lamps, as well as demonstrate lumen degradation as a function of humidity is more detrimental than that of only temperature. Subsequently, nonbiased life testing did not facilitate corrosion and humidity ingress quickly enough and was replaced with bias life testing. The specimens were removed approximately every 168 hours in order to conduct photometric and colorimetric testing using methods described in the IES LM-79-08 standard (IES, 2008a). The THS profile can be seen in Figure 28, where $\Delta t$ is the sampling period at interval i = 0, 1, 2...

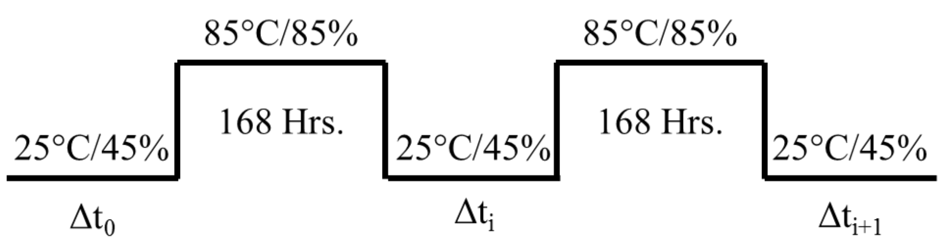


Figure 28: THS Acceleration Profile for EDG2 and 85CG1.

### 3.2.5. Steady-State Temperature-Humidity Bias Profile

A steady-state temperature-humidity bias (THB) life test was performed with an applied electrical bias to accelerate the ingress of moisture in order to facilitate corrosion and determine the reliability of SSL lamps in humid environments (JEDEC, 2009). The THB life test of for SSLG1 followed the JEDEC standard JESD22-A101C with electrical bias cycled on/off every hour (JEDEC, 2009). Groups SSLG2 and SSLG3 underwent the same electrical bias cycle as SSLG1 but were accelerated at different temperature-humidity profiles and sampling periods. The THB profiles can be seen in Figure 29 - Figure 31, where Δt is the sampling period at interval i = 0, 1, 2...

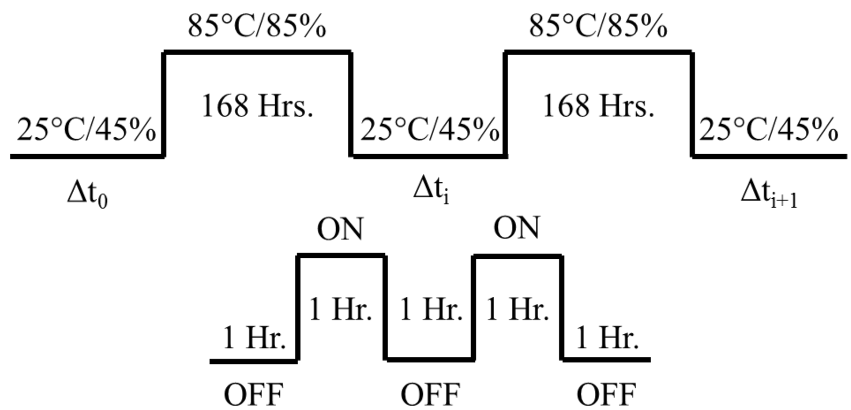


Figure 29: THB Acceleration Profile for SSLG1.

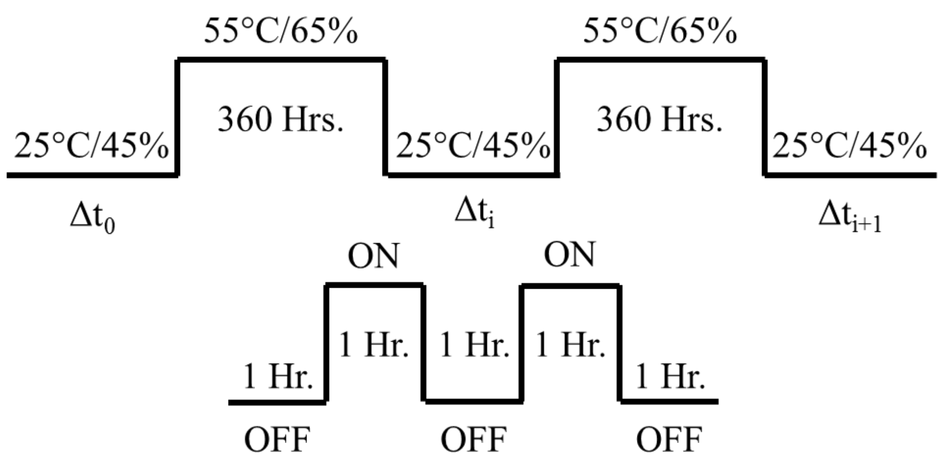


Figure 30: THB Acceleration Profile for SSLG2.

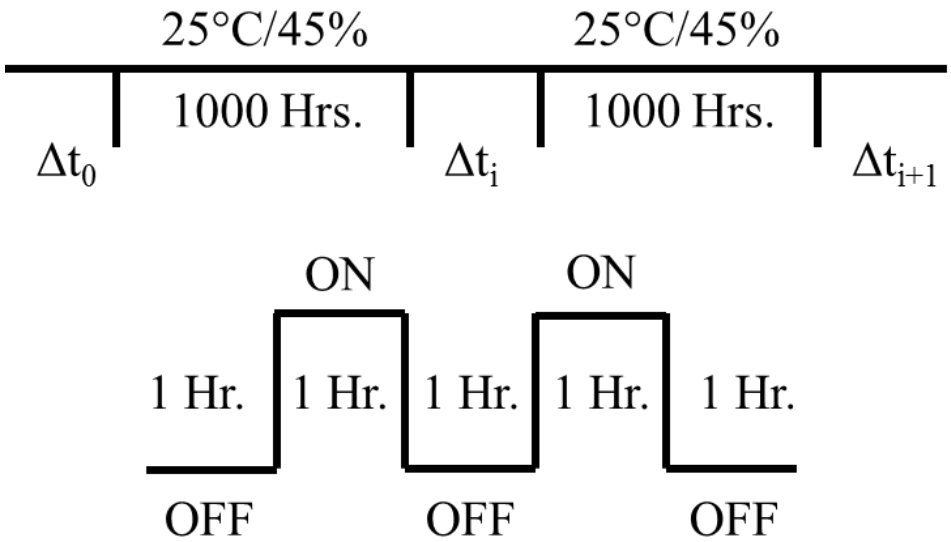


Figure 31: THB Acceleration Profile for SSLG3.

### 3.3. MEASUREMENT PROCEDURE

Two distinct measurement schemes were employed to collect the majority of the data for the test vehicles in this work, one dealing with resistance change and the other dealing with photometric and colorimetric measurements. The SSL lamp groups and the EDs followed the same process outlined in the IES LM-79-08 testing standard for the collection of photometric data, as well as additional standards and methods for the determination of the colorimetric quantities in order to monitor the overall health of the systems. The ECs underwent a random vibration profile to accelerate fretting degradation which required the ability to collect infinitesimally small changes in resistance across a set of daisy chained pins. To complete this task, the method of resistance spectroscopy (RS) was used along with the vibration measurement setup to detect the small changes of resistance. The AECs were measured directly using a handheld LCR meter which required no setup nor data collection methods to acquire the changes in CAP and ESR; therefore, it will only be discussed briefly at the end of this section.

### 3.3.1. SSL DATA COLLECTION

Photometric measurements were carried out for both ED groups and for all the SSL lamps following the IES LM-79-08 measurement standard (IES, 2008a). In order to measure the overall health of the EDs, the AECs were connected to their corresponding ED through a bread board and then connected to the pristine LE that resided inside the integrating sphere through another set of leads. A lamp holder and connection cord where constructed to attach the downlight module to the lamp port which is designed for the standard Edison style base used with today's lightbulbs. The SSL lamps where connected directly to the integrating sphere.

Photometry is the science of measuring light in terms of light output (DeCusatis, 1997). Figure 32 illustrates the measurement setup used to acquire the photometric data for the EDs and SSL lamps. The photometric measurements were conducted at room temperature with a spectrometer, lighting software and an integrating sphere to accurately obtain the spectral radiant flux of each test vehicle. The spectral radiant flux gives the information needed to determine the luminous flux or light power, as well as the many colorimetric parameters used to classify different characteristics of the SSL devices.

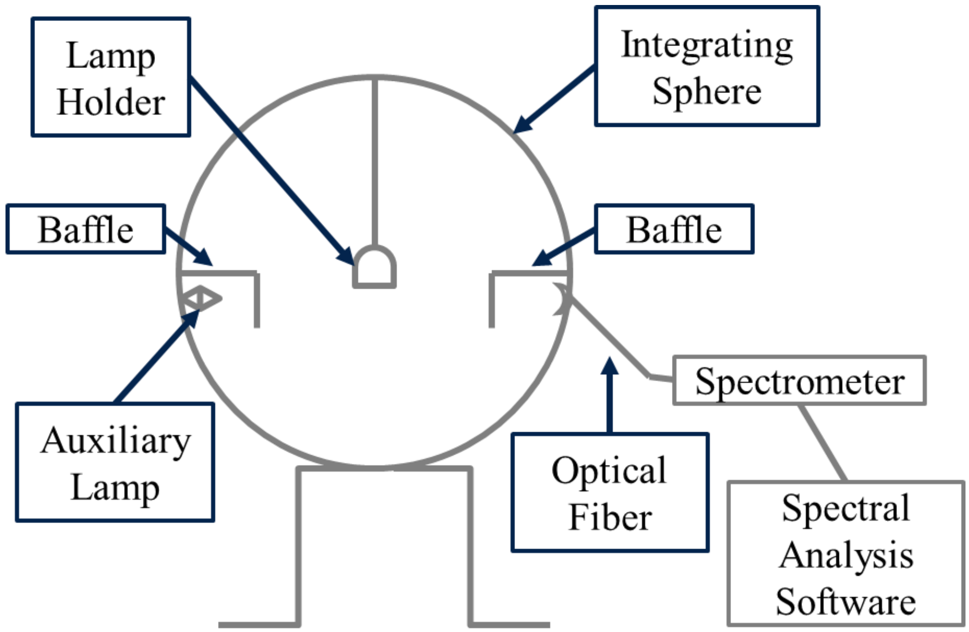


Figure 32: The SSL Photometric Measurement System.

The integrating sphere uses what is called 4π geometry for SSL devices that emit light omnidirectional or forward directional by utilizing the entire surface of the integrating sphere. The IES LM-79-08 standard states that the total spectral radiant flux, $\Phi_{test}(\lambda)$ [W/nm], of an SSL product under test can be obtained by comparing it to a known reference or calibration standard's, $\Phi_{ref}(\lambda)$, spectral radiant flux (IES, 2008a). It is determined using equation (9), where $y_{test}(\lambda)$ and $y_{ref}(\lambda)$ are the spectrometer readings of the lamp under test and the reference lamp found using the integrating sphere, respectively.

$$\Phi_{test}(\lambda) = \left[ \Phi_{ref}(\lambda) \cdot \frac{y_{test}(\lambda)}{y_{ref}(\lambda)} \right] \cdot \alpha_{CCF} = \Phi_m(\lambda) \cdot \alpha_{CCF} \tag{9}$$

$$\alpha_{CCF}(\lambda) = \frac{y_{aux,REF}(\lambda)}{y_{aux,TEST}(\lambda)} \tag{10}$$

Once the integrating sphere has been calibrated with the known calibration standard, the bracketed term in (9) is calculated internally by the SpectraSuite software with the measured spectral radiant flux, $\Phi_m(\lambda)$, of the test lamp becoming the output of the software. An example of this output can be seen in Figure 33.

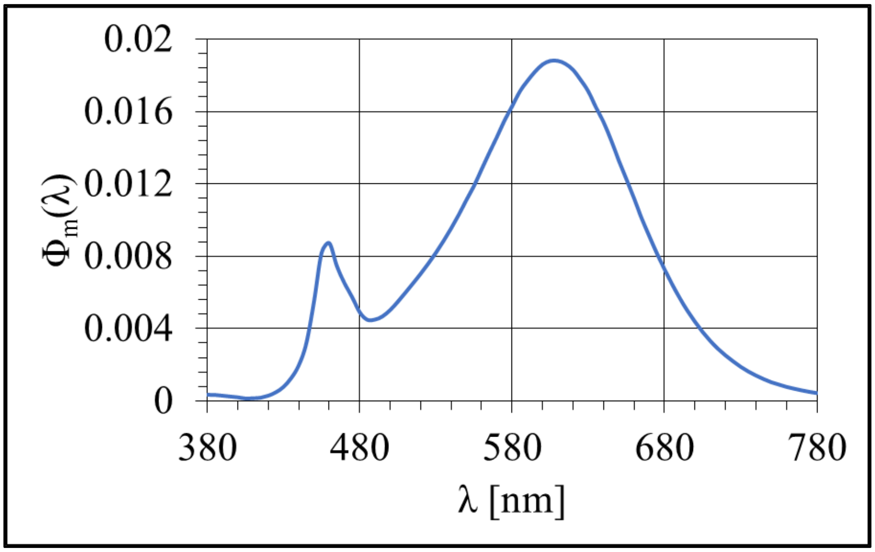


Figure 33: The Measured Spectral Radiant Flux.

The self-absorption correction factor, $\alpha_{CCF}$, can be found through a comparison of an auxiliary lamp measurement with the test lamp inside the integrating sphere, $y_{aux,Test}(\lambda)$, and an auxiliary lamp measurement with the calibration lamp standard inside the sphere, $y_{aux,REF}(\lambda)$ (IES, 2008a). Both the test lamp and calibration lamp standard are off during the auxiliary measurements. The self-absorption factor is a critical parameter since SSL devices typically have a different physical size, shape and absorption characteristic when compared to the calibration lamp standard used to calibrate the integrating sphere and the spectrometer. The self-absorption correction factor needed to correct the measured spectral radiant flux shown in Figure 33 is depicted in Figure 34.

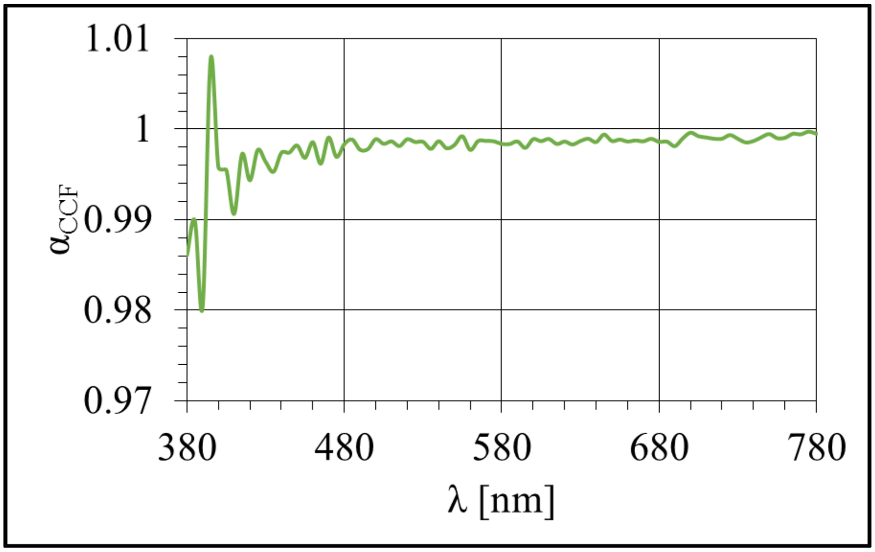


Figure 34: The Self-Absoprtion Correction Factor for Figure 33.

The total spectral radiant flux for the SSL device under test can now be determined by multiplying the measured spectral radiant flux with the self-absorption correction factor and is shown in Figure 35.

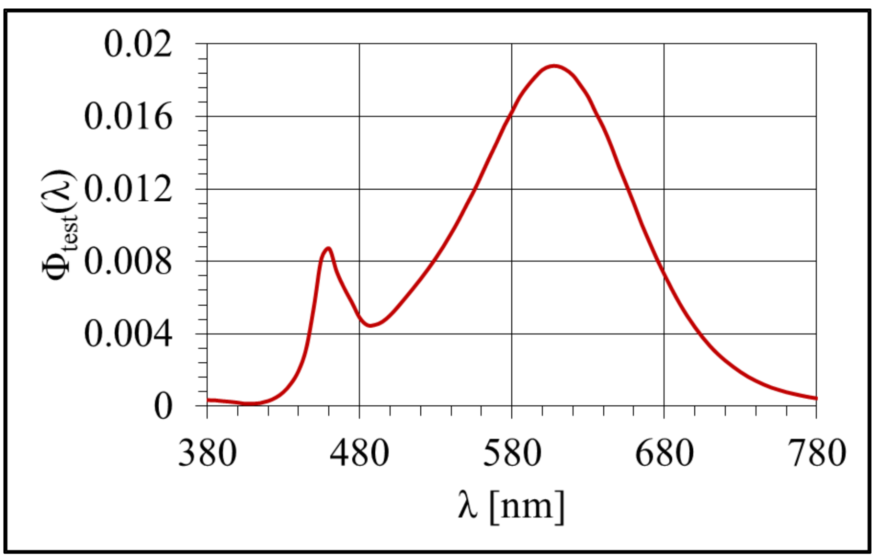


Figure 35: The Total Spectral Radiant Flux.

The total luminous flux, $\Phi_{test}$, in lumens [lm] of the SSL product under test can now be determined by multiplying the wavelength dependent spectral radiant flux found using equation (9) and shown in Figure 35 with the wavelength dependent spectral luminous efficiency function for photopic vision, V (λ), as shown in Figure 36. This wavelength dependent vector is then integrated over the visible spectrum using equation (11), where $K_m$ is the maximum spectral luminous efficacy. (DeCusatis, 1997) (IES, 2008a) (Wyszecki, 1982)

$$\Phi_{test} = K_m \cdot \int_{380}^{780} \Phi_{test}(\lambda) \cdot V(\lambda) \cdot d\lambda \tag{11}$$

$$K_m = 683\, lm/W \tag{12}$$

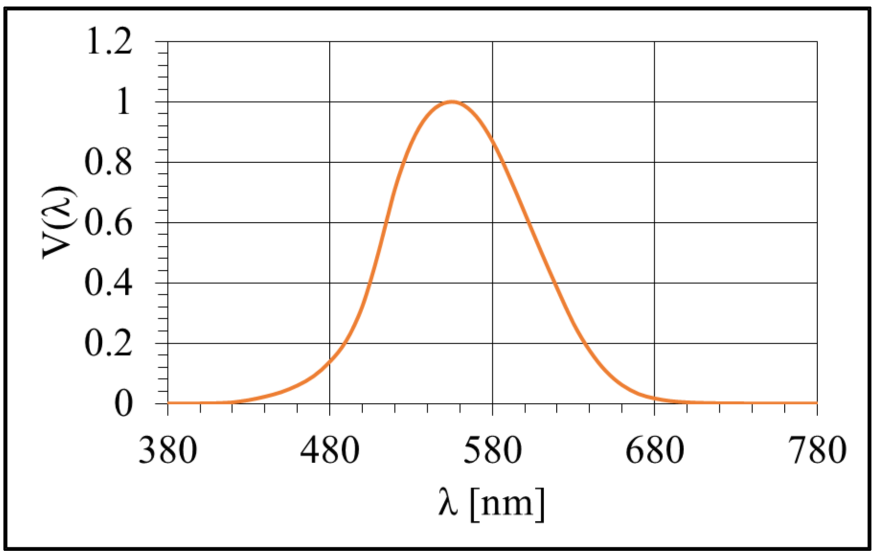


Figure 36: The Total Spectral Luminous Efficiency Function for Photopic Vision.

### 3.3.2. Vibration Data Collection

In order to induce fretting degradation on the ECs, a novel test setup was developed. The construction of this setup allowed the male portion of the connector pin to be held rigid with the out-of-plane vibration table by clamping it between the red blocks that are secured to the shaker as shown in Figure 37. The female portion was allowed to “rock” up and down during vibration. To ensure fretting degradation occurred, the leads to the connector were pulled taunt at the beginning of the experiment and clamped to the wooden table at a tie-off length of about 13.5 cm. The leads of the pins to be measured where then connected to a modified Wheatstone bridge along with a signal generator that produced a sinusoidal AC signal at one volt and 95 kHz. This was used along with a lock-in amplifier (LIA) and phase sensitive detection (PSD) to acquire the magnitude of the voltage across the Wheatstone bridge without a phase dependency in order to determine the infinitesimal changes in contact resistance of the ECs. This measurement technique is known as Resistance Spectroscopy (RS).

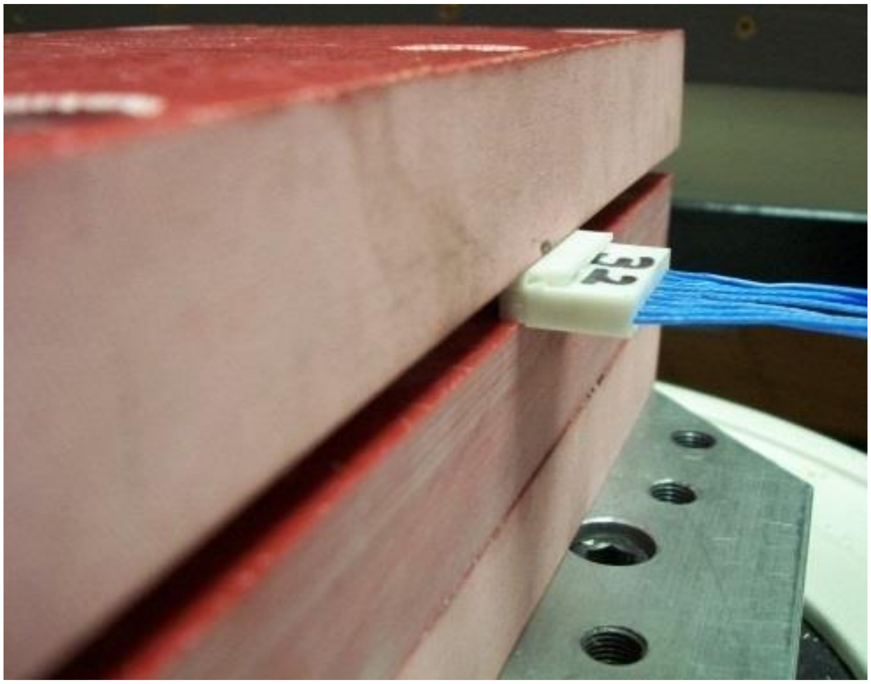


Figure 37: The EC with the Male Portion Held Rigid with the Vibration Table.

#### 3.3.2.1. RESISTANCE SPECTROSCOPY

Continuity measurements typically use measurement devices, such as an oscilloscope, and a traditional DC Wheatstone Bridge to measure changes in voltage (Hambley, 2005). This measurement setup does not have the adequate resolution required to determine very minute changes in the contact resistance (Lall P. S., 2012b) (Lall P. L., 2011a) (Lall P. L., 2011b) (Lall P. L., 2011c) (Lall P. L., 2010a) (Lall P. L., 2010b) (Lall P. L., 2009a) (Lall P. L., 2009b). RS is capable of capturing high precision measurements, as low as 1 nano-volt. The schematic of the RS measurement setup can be seen in Figure 38.

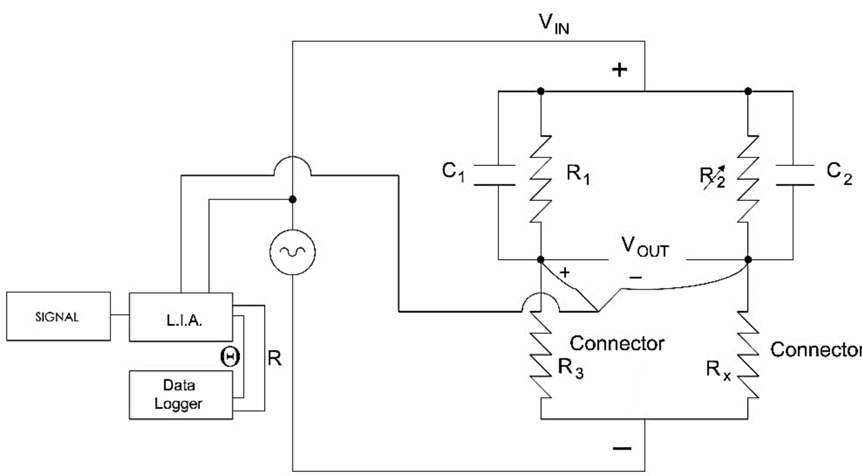


Figure 38: Schematic of the Resistance Spectroscopy Measurement Setup.

The AC signal generator produces a sinusoidal signal that supplies power to the entire system. The capacitors, $C_1$ and $C_2$, are used to eliminate any possible fluctuations from inductance produced by wires running through the measurement system. The resistor, $R_1$, is a static resistor and the resistor, $R_3$, is a daisy chained connector that acts as a static resistor. $R_2$ is a variable resistor used to balance the modified Wheatstone bridge similar to a traditional Wheatstone bridge. The connector subjected to vibration is $R_x$. The outputs of the LIA are the magnitude, R, and phase, Θ, of the response signal. The quantities are recorded with a data acquisition unit for the length of the experiment. The change in resistance of the connector can be calculated using the measured voltages, resistances and capacitances from the bridge in the same fashion as a traditional Wheatstone bridge. Impedances are needed to incorporate the capacitors in order to accurately solve for the unknown resistance of the connector. The values of the modified Wheatstone bridge, as well as the impedance values are shown in Table 7. The impedance equation for the AC Wheatstone Bridge is analogous to the resistance equation for the DC Wheatstone Bridge as shown in equation (13) and the corresponding equations used to calculate impedance values are shown in equations (14) – (17).

$$V_{out} = V_{in}\left(\frac{z_1 \cdot z_x - z_2 \cdot z_3}{(z_1 + z_3)(z_2 + z_x)}\right) \tag{13}$$

$$z_1 = \sqrt{R_1^2 + \frac{1}{4.\pi^2.\omega^2.c_1^2}} \tag{14}$$

$$z_2 = \sqrt{R_2^2 + \frac{1}{4.\pi^2.\omega^2.c_2^2}} \tag{15}$$

$$z_3 = R_3 \tag{16}$$

$$z_x = R_x \tag{17}$$

Table 7: The Modified Wheatstone Bridge Components with Impedance Values.

| **Component** | **Value** | **Impedance** | **Value** |
|---|---|---|---|
| R1 [Ω] | 10.02 | Z1 [Ω] | 162.71 |
| R2 [Ω] | 12.76 | Z2 [Ω] | 172.65 |
| R3 [Ω] | 0.22 | Z3 [Ω] | 0.22 |
| C1 [nF] | 10.316 | N/A | N/A |
| C2 [nF] | 9.73 | N/A | N/A |

Equation (13) can be re-arranged algebraically to solve for the unknown resistance of the EC. The exact form of the equation used to find the change in contact resistance of the ECs is shown in equation (18).

$$R_x = \left( \frac{z_1 \cdot z_2 \left( \frac{v_{out}}{v_{in}} \right) + z_2 \cdot z_3 \left( \frac{v_{out}}{v_{in}} \right) + z_2 \cdot z_3}{z_1 - z_1 \cdot \left( \frac{v_{out}}{v_{in}} \right) - z_3 \cdot \left( \frac{v_{out}}{v_{in}} \right)} \right) \tag{18}$$

### 3.3.2.2. PHASE SENSITIVE DETECTION

Before the change in contact resistance of the EC can be found, the infinitesimal change of voltage across the modified Wheatstone bridge must be measured with a high degree of accuracy and precision. The AC signal generator excites the modified Wheatstone bridge with a sinusoidal wave at a fixed external frequency, $\omega_1$, which is detected by the LIA. The LIA generates an internal reference signal from the response signal at the internal reference frequency, $\omega_2$, using a phase-locked-loop. The response and internal signals are represented by equations (19) and (20), respectively. (Lall P. S., 2012b) (Lall P. L., 2011a) (Lall P. L., 2011b) (Lall P. L., 2011c) (Lall P. L., 2010a) (Lall P. L., 2010b) (Lall P. L., 2009a) (Lall P. L., 2009b) (Stanford Research Systems)

$$V_1 = V_{out} \cdot \sin(\omega_1 \cdot t + \theta_1) \tag{19}$$

$$V_2 = V_{ref} \cdot \sin(\omega_2 \cdot t + \theta_2) \tag{20}$$

The LIA amplifies the response signal and then multiplies it by the internal reference signal using PSD as shown in equation (21).

$$\begin{aligned} V_{PSD} &= V_1 \cdot V_2 = V_{out} \cdot V_{ref} \sin(\omega_1 \cdot t + \theta_1) \cdot \sin(\omega_2 \cdot t + \theta_2) \\ V_{PSD} &= \frac{V_{out} \cdot V_{ref}}{2} \begin{Bmatrix} \cos[(\omega_1 - \omega_2) \cdot t + (\theta_1 - \theta_2)] \\ - \cos[(\omega_1 + \omega_2) \cdot t + (\theta_1 + \theta_2)] \end{Bmatrix} \end{aligned} \tag{21}$$

The PSD outputs two AC signals, one at the difference of the frequencies and one at the sum of the frequencies. The PSD output goes through a low pass filter to eliminate the AC signal producing the in-phase component of the signal vector. The in-phase component is a DC signal proportional to the response signal amplitude and the cosine of the phase difference of the response and internal signals. (Lall P. S., 2012b) (Lall P. L., 2011a) (Lall P. L., 2011b) (Lall P. L., 2011c) (Lall P. L., 2010a) (Lall P. L., 2010b) (Lall P. L., 2009a) (Lall P. L., 2009b) (Stanford Research Systems)

$$\begin{aligned} V_{psd1} &= \frac{V_{out} \cdot V_{ref}}{2} \cdot \cos(\theta_1 - \theta_2) = \frac{V_{out} \cdot V_{ref}}{2} \cdot \cos(\Delta\theta) \\ V_{psd1} &\propto V_{out} \cdot \cos(\Delta\theta) \end{aligned} \tag{22}$$

In order to eliminate the phase dependency, a second PSD is used. The second PSD multiplies the amplified response signal by the reference signal that has been shifted by 90°. The output also goes through a low pass filter producing the quadrature component of the signal vector. The quadrature component is also a DC signal that is proportional to the response signal amplitude and the sine of the phase difference of the response and internal signals. (Lall P. S., 2012b) (Lall P. L., 2011a) (Lall P. L., 2011b) (Lall P. L., 2011c) (Lall P. L., 2010a) (Lall P. L., 2010b) (Lall P. L., 2009a) (Lall P. L., 2009b) (Stanford Research Systems)

$$V_{psd2} = \frac{V_{out} \cdot V_{ref}}{2} \cdot \sin\left(\theta_1 - \theta_2\right) = \frac{V_{out} \cdot V_{ref}}{2} \cdot \sin\left(\Delta\theta\right)$$
$$V_{psd2} \propto V_{out} \cdot \sin\left(\Delta\theta\right) \tag{23}$$

By using the outputs of the two PSDs to find the magnitude of the response vector, the phase dependency is removed. The amplitude of the response signal is equivalent to the output of the modified Wheatstone bridge. (Lall P. S., 2012b) (Lall P. L., 2011a) (Lall P. L., 2011b) (Lall P. L., 2011c) (Lall P. L., 2010a) (Lall P. L., 2010b) (Lall P. L., 2009a) (Lall P. L., 2009b) (Stanford Research Systems)

$$R = \sqrt{\left(V_{out} \cdot \cos(\Delta\theta)\right)^2 + \left(V_{out} \cdot \sin(\Delta\theta)\right)^2} = V_{out} \tag{24}$$

### 3.3.3. AEC DATA COLLECTION

As previously mentioned, the AECs were measured directly using a handheld LCR meter. The ESR parameter can be estimated by summing the electrolytic resistance, dielectric loss and the electrode resistance using equations outlined in the literature (Han, 2009) (Harada, 1993) (Rubycon Corporation, 2013). In this work, CAP and ESR were measured directly instead of using the typical lumped parameter approach to estimate the ESR (Han, 2009). This measurement scheme is a novel approach not previously seen in literature.

## 3.4. DATA PROCESSING

### 3.4.1. COLORIMETRY

Colorimetry is the science used to describe and quantify the perception of light by the human eye in terms of color (Schanda, 2007). The tristimulus values for the lamp under test are computed using the spectral radiant flux obtained from equation (9) and the CIE

1931 color matching functions from a standard 2° observer as previously shown in Figure 5. The tristimulus values are analogous to the intensity required to produce the proper excitation of the three cones in the retina of the human eye in order for the emitted light to be perceived as “white”. (Schubert, 2006) (CREE, 2013) (DeCusatis, 1997) (Schanda, 2007) (Westland, 2004) (CIE, 2004a) (Wyszecki, 1982)

$$X = k \cdot \int_{380}^{780} \Phi_{test}(\lambda) \cdot \bar{x}(\lambda) \cdot d\lambda = k \cdot \sum_{\lambda} \Phi_{test}(\lambda) \cdot \bar{x}(\lambda) \cdot \Delta\lambda \tag{25}$$

$$Y = k \cdot \int_{380}^{780} \Phi_{test}(\lambda) \cdot \bar{y}(\lambda) \cdot d\lambda = k \cdot \sum_{\lambda} \Phi_{test}(\lambda) \cdot \bar{y}(\lambda) \cdot \Delta\lambda \tag{26}$$

$$Z = k \cdot \int_{380}^{780} \Phi_{test}(\lambda) \cdot \bar{z}(\lambda) \cdot d\lambda = k \cdot \sum_{\lambda} \Phi_{test}(\lambda) \cdot \bar{z}(\lambda) \cdot \Delta\lambda \tag{27}$$

The color matching functions ($\bar{x}(\lambda)$, $\bar{y}(\lambda)$, and $\bar{z}(\lambda)$) are provided with seven significant figures by the CIE in tabular form at 1 nm intervals over the visible light spectrum (Westland, 2004) (CIE, 2004a). The variable k is known as the normalizing factor and is shown in equation (28). (Schanda, 2007) (Westland, 2004) (Wyszecki, 1982)

$$k = \frac{100}{\int_{380}^{780} E(\lambda) \cdot \bar{y}(\lambda) \cdot d\lambda} \tag{28}$$

In this equation, E (λ) is the relative spectral power distribution of a CIE standard illuminant. For this work, the CIE standard illuminant A was chosen due to its ability to be used with SSL devices below a CCT value of 4000K (CIE, 2004a) (Wyszecki, 1982). Additionally, the CIE standard illuminant D65 was used since this standard pertains to SSL devices with a CCT range of 4000K – 7000K (CIE, 2004a) (Wyszecki, 1982). Once the tristimulus values are obtained, the various color coordinate systems and colorimetric parameters can be determined to describe the color characteristics of the SSL device.

#### 3.4.1.1. 2-D Colorimetric Systems

The original color space coordinate system is the CIE 1931 x-y coordinate system which can be found from the tristimulus values. (DeCusatis, 1997) (Schanda, 2007) (Westland, 2004) (CIE, 2004a) (Wyszecki, 1982)

$$x = \frac{X}{X+Y+Z} \tag{29}$$

$$y = \frac{Y}{X+Y+Z} \tag{30}$$

Traditionally, only two coordinates, x and y, are used to describe this color space due to the relationship between the x and y coordinates with the z coordinate. The sum of the three coordinates is equal to one. This relationship prohibits the use of a 3-D color space diagram to describe the SSL device. Figure 39 illustrates the chromaticity diagram for this color space in terms of perceived color by the human eye with the black circle denoting the white point at (1/3, 1/3).

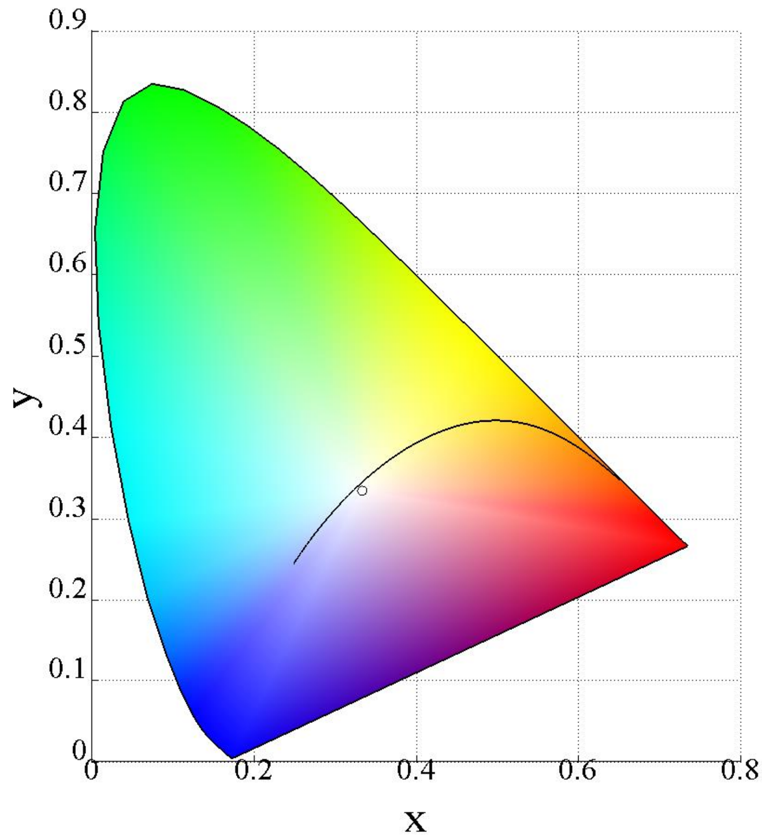


Figure 39: CIE 1931 x-y Chromaticity Diagram.

The inability to suitably investigate Colorimetry and industrial color-control problems led to the development of new chromaticity coordinates to produce a uniform color space (UCS). The first adopted UCS was the CIE 1960 u-v color space. (Wyszecki, 1982)

$$u = \frac{2x}{6y - x + 1.5} \tag{31}$$

$$v = \frac{3y}{6y - x + 1.5} \tag{32}$$

This UCS was eventually replaced and is currently only used to determine the color rendering index (CRI), as well as the correlated color temperature (CCT) of SSL devices.

The obsolete CIE 1960 coordinate system was replaced with the CIE 1976 u`-v` color space since the chromaticity of this space is perceptually more uniform than the CIE 1931 color space. (Hsieh, 2012) (CIE, 2004a) (CIE, 2004b) (CIE, 1995) (Wyszecki, 1982)

$$u` = u = \frac{2x}{6y - x + 1.5} \tag{33}$$

$$v` = \frac{3}{2} \cdot v = \frac{4.5y}{6y - x + 1.5} \tag{34}$$

A third chromaticity coordinate for the CIE 1960 and CIE 1976 color space can be determined in the same fashion as the z-coordinate for the CIE 1931 color space. Due to the similar relationship between the CIE 1960 and CIE 1976 coordinates as mentioned for the CIE 1931 color space, a 3-D color space using these coordinate systems does not accurately describe the SSL device. The chromaticity diagram for this space, shown in Figure 40, is intended to be used for comparisons between the colors of lamps that have similar size and shape with a negligible difference of luminance ($\Delta Y < 0.5$) (CIE, 2004a) (Wyszecki, 1982). It is also plotted in terms of perceived color with the black circle denoting the white point in this color space (0.2105, 0.4737).

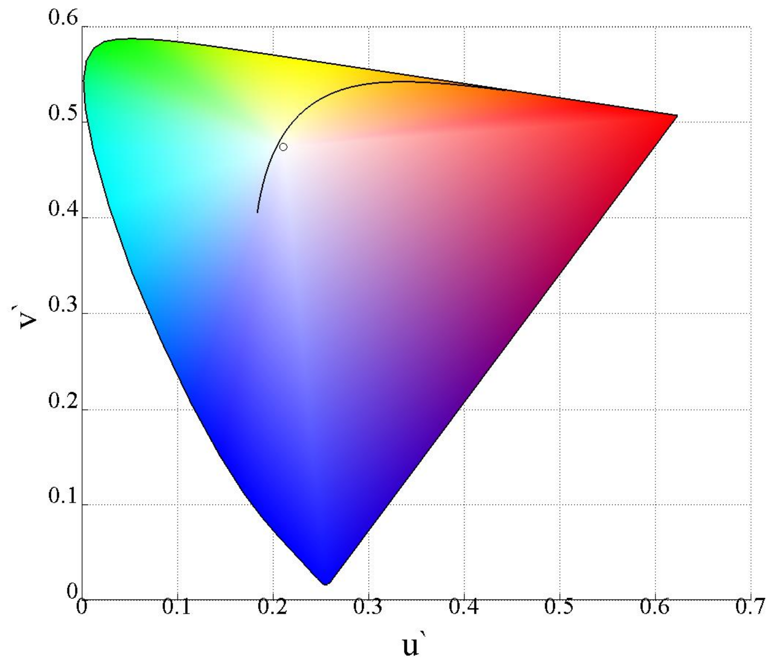


Figure 40: CIE 1976 u`-v` Chromaticity Diagram.

The color shift or color difference of the SSL lamp in 2-D color space is determined using the u`-v` coordinate system. Color shift gives insight into the magnitude of the color change in the u`-v` color space for a SSL device under test from its original pristine values at time zero to the measured value at each sampling period. This is determined using the Euclidean distance between the u`-v` coordinates. (CIE, 2004a) (Wyszecki, 1982)

$$\Delta E_{u`v`} = \sqrt{(u`-u`_0)^2 + (v`-v`_0)^2} = \sqrt{(\Delta u`)^2 + (\Delta v`)^2} \qquad (35)$$

### 3.4.1.2. 3-D COLORIMETRIC SYSTEMS

In order to investigate a 3-D, approximately uniform, color spacing of the lighting device, either the CIE 1976 L*-a*-b* (CIELAB) or the CIE L*-u*-v* (CIELUV) color space must be used to produce color shifts that are in rectangular coordinates, as well as for the determination of the lightness, colorfulness and hue of the SSL device. The CIELAB color space is shown in equations (36) - (41). (CIE, 2004a) (Wyszecki, 1982)

$$L^* = 116 \cdot f\left(\frac{Y}{Y_n}\right) - 16 \tag{36}$$

$$a^* = 500 \cdot \left[ f\left(\frac{X}{X_n}\right) - f\left(\frac{Y}{Y_n}\right) \right] \tag{37}$$

$$b^* = 200 \cdot \left[ f\left(\frac{Y}{Y_n}\right) - f\left(\frac{Z}{Z_n}\right) \right] \tag{38}$$

$$f\left(\frac{X}{X_n}\right) = \begin{Bmatrix} \left(\frac{X}{X_n}\right)^{1/3} if \left(\frac{X}{X_n}\right) > \left(\frac{24}{116}\right)^3 \\ \left(\left(\frac{841}{108}\right) \cdot \left(\frac{X}{X_n}\right) + \frac{16}{116}\right) if \left(\frac{X}{X_n}\right) \le \left(\frac{24}{116}\right)^3 \end{Bmatrix} \tag{39}$$

$$f\left(\frac{Y}{Y_n}\right) = \begin{Bmatrix} \left(\frac{Y}{Y_n}\right)^{1/3} if \left(\frac{Y}{Y_n}\right) > \left(\frac{24}{116}\right)^3 \\ \left(\left(\frac{841}{108}\right) \cdot \left(\frac{Y}{Y_n}\right) + \frac{16}{116}\right) if \left(\frac{Y}{Y_n}\right) \le \left(\frac{24}{116}\right)^3 \end{Bmatrix} \tag{40}$$

$$f\left(\frac{Z}{Z_n}\right) = \begin{Bmatrix} \left(\frac{Z}{Z_n}\right)^{1/3} if \left(\frac{Z}{Z_n}\right) > \left(\frac{24}{116}\right)^3 \\ \left(\left(\frac{841}{108}\right) \cdot \left(\frac{Z}{Z_n}\right) + \frac{16}{116}\right) if \left(\frac{Z}{Z_n}\right) \le \left(\frac{24}{116}\right)^3 \end{Bmatrix} \tag{41}$$

The CIELAB color space utilizes the tristimulus values of an SSL device to produce the 3-D color mapping. The subscript, n, denotes the tristimulus values of a specified white object stimulus that is light reflected from a perfect reflecting diffuser illuminated by the same SSL device. The white object stimulus will have a luminance value of 100. Therefore, by normalizing the tristimulus values of the SSL device by luminance times 100, then the white object stimulus can be determined. The CIELUV color space uses the same lightness, L*, as CIELAB with the additional parameters relying on the knowledge of the white object stimulus's u`-v` coordinates denoted with subscript, n. (CIE, 2004a) (Wyszecki, 1982)

$$u^* = 13 \cdot L^* \cdot (u` - u_n`) \tag{42}$$

$$v^* = 13 \cdot L^* \cdot (v` - v_n`) \tag{43}$$

Lightness, L*, describes the brightness of an illuminated area relative to an equivalent illuminated area that appears white. Similarly, the computation of chroma for the CIELAB and CIELUV color spaces describes the colorfulness of the illuminated area compared to an equivalent area that appears white. (CIE, 2004a) (Wyszecki, 1982)

$$C^*_{ab} = \sqrt{a^{*2} + b^{*2}} \tag{44}$$

$$C^*_{uv} = \sqrt{u^{*2} + v^{*2}} \tag{45}$$

The hue of an SSL device is described in terms of its hue angle ranging from 0° to 360°. The hue angle relates the illuminated area to one of the perceived colors of red, yellow, green or blue, or a combination of two of these colors. (CIE, 2004a) (Wyszecki, 1982)

$$\begin{aligned} &h_{ab} = \arctan\left(\frac{b^*}{a^*}\right) \\ &0° < h_{ab} > 90° \Rightarrow (\uparrow a^* \,\&\, \uparrow b^*) \\ &90° < h_{ab} < 180° \Rightarrow (\downarrow a^* \,\&\, \uparrow b^*) \\ &180° < h_{ab} < 270° \Rightarrow (\downarrow a^* \,\&\, \downarrow b^*) \\ &270° < h_{ab} < 360° \Rightarrow (\uparrow a^* \,\&\, \downarrow b^*) \end{aligned} \tag{46}$$

$$h_{uv} = \arctan\left(\frac{u*}{v*}\right)$$
$$0° < h_{uv} > 90° \Rightarrow (\uparrow u* \& \uparrow v*)$$
$$90° < h_{uv} < 180° \Rightarrow (\downarrow u* \& \uparrow v*) \tag{47}$$
$$180° < h_{uv} < 270° \Rightarrow (\downarrow u* \& \downarrow v*)$$
$$270° < h_{uv} < 360° \Rightarrow (\uparrow u* \& \downarrow v*)$$

The change in hue of an SSL device under test from its original pristine hue can be determined from knowledge of the chroma values and hue angles at each sampling period and the initial, pristine values. (CIE, 2004a) (Wyszecki, 1982)

$$\Delta H_{ab} = \sqrt{\left(C_{ab}*|_t \cdot C_{ab}*|_0\right)} \cdot \sin\left(\frac{\Delta h_{ab}}{2}\right) \tag{48}$$

$$\Delta H_{uv} = \sqrt{\left(C_{uv}*|_t \cdot C_{uv}*|_0\right)} \cdot \sin\left(\frac{\Delta h_{uv}}{2}\right) \tag{49}$$

The saturation of the SSL lamp can only be determined in the CIELUV color space due to CIELAB not having a corresponding chromaticity diagram. Saturation describes the colorfulness of the illuminated area in proportion to its lightness. (CIE, 2004a) (Wyszecki, 1982)

$$s_{uv} = \frac{C*_{uv}}{L*} \tag{50}$$

Similar to the 2-D color space, the color difference in 3-D space can be determined using the Euclidean distance between the initial, pristine value and the one obtained at each sampling period. (CIE, 2004a) (Wyszecki, 1982) The color difference will be the same using either CIELAB or CIELUV and can be determined using either one of the equations in (51) - (54).

$$\Delta E_{a*b*} = \sqrt{(\Delta L*)^2 + (\Delta a*)^2 + (\Delta b*)^2} \tag{51}$$

$$\Delta E_{a*b*} = \sqrt{(\Delta L*)^2 + (\Delta C_{ab}*)^2 + (\Delta H_{ab})^2} \tag{52}$$

$$\Delta E_{u*v*} = \sqrt{(\Delta L*)^2 + (\Delta u*)^2 + (\Delta v*)^2} \tag{53}$$

$$\Delta E_{u*v*} = \sqrt{(\Delta L*)^2 + (\Delta C_{uv}*)^2 + (\Delta H_{uv})^2} \tag{54}$$

### 3.4.1.3. CORRELATED COLOR TEMPERATURE

The CCT of white light, measured in degrees Kelvin, is calculated from the isotemperature lines that are perpendicular to the temperature of the Planckian locus or ideal black-body radiator with a comparable hue using the CIE 1960 u-v coordinate system. This is accomplished by searching for the closest point on the Planckian locus to that of the test lamp's u-v coordinates. The u-v coordinates of the Planckian locus are derived from Planck's formula for spectral radiant existence as shown in equation (55). (CIE, 2004a) (Wyszecki, 1982)

$$M_e(\lambda, T_b) = \frac{2 \cdot \pi \cdot c^2}{\lambda^5} \cdot \left( \exp\left( \frac{h \cdot c}{k \cdot \lambda \cdot T_b} \right) - 1 \right)^{-1} \tag{55}$$

In equation (55), c is the speed of light (2.998 x $10^8$ m/s), h is the Planck constant (6.626 x $10^{-34}$ J·s), k is the Boltzmann constant (1.381 x $10^{-23}$ J/K), λ is wavelength ranging from 300 to 830 nm, and $T_b$ is the absolute temperature of the blackbody. The first step is to formulate a table of u-v coordinates at different blackbody temperatures with the blackbody temperature increasing by 1% from the previous value. The blackbody tristimulus values are determined by integrating the spectral radiant existence with the color matching functions over the interval of (0, ∞]. (Ohno, 2014) (Wyszecki, 1982)

$$X(T_b) = \int_0^{\infty} M_e(\lambda, T_b) \cdot \bar{x}(\lambda) \cdot d\lambda \tag{56}$$

$$Y(T_b) = \int_0^{\infty} M_e(\lambda, T_b) \cdot \bar{y}(\lambda) \cdot d\lambda \tag{57}$$

$$Z(T_b) = \int_0^{\infty} M_e(\lambda, T_b) \cdot \bar{z}(\lambda) \cdot d\lambda \tag{58}$$

Once the temperature dependent tristimulus values have been determined, the temperature dependent u-v coordinates are calculated. To better illustrate the Planckian u-v table, an example portion of the tabulated Planckian u-v table is shown in Table 8. (Ohno, 2014) (Wyszecki, 1982)

$$u(T_b) = \frac{4 \cdot X(T_b)}{X(T_b) + 15 \cdot Y(T_b) + 3 \cdot Z(T_b)} \tag{59}$$

$$v(T_b) = \frac{6 \cdot Y(T_b)}{X(T_b) + 15 \cdot Y(T_b) + 3 \cdot Z(T_b)} \tag{60}$$

The second step is to determine which Planckian u-v coordinates produce the smallest Euclidean distance from the SSL device u-v coordinates as shown in equation (61). (Ohno, 2014)

$$\Delta E_i = \sqrt{\left(u(T_b)_i - u_x\right)^2 + \left(v(T_b)_i - v_x\right)^2} \tag{61}$$

$$\Delta E_{i=m} = \min(\Delta E_i) \tag{62}$$

A triangle can now be formed from the u-v chromaticity coordinates of the SSL device ($u_x$, $v_x$) and the two u-v chromaticity coordinates at Tm+1 and Tm-1 as shown in Figure 41. Assuming a linear line between the two Planckian u-v coordinates, the blackbody temperature that is closest to the u-v coordinates of the SSL device is determined by solving the triangle. (Ohno, 2014)

$$CCT = (T_b)_x = (T_b)_{m-1} + \left((T_b)_{m+1} - (T_b)_{m-1}\right) \cdot \frac{\Delta x}{L} \tag{63}$$

$$\Delta x = \frac{\Delta E_{m-1}^2 - \Delta E_{m+1}^2 + L^2}{2 \cdot L} \tag{64}$$

$$L = \sqrt{\left(u(T_b)_{m+1} - u(T_b)_{m-1}\right)^2 + \left(v(T_b)_{m+1} - v(T_b)_{m-1}\right)^2} \tag{65}$$

Table 8: Planckian u-v Table Example.

| $(T_b)_i$ [K] | $u(T_b)_i$ | $v(T_b)_i$ | $\Delta E_i$ | i |
|---|---|---|---|---|
| 1000 | 0.448005849 | 0.354625418 | 0.039028926 | 1 |
| 1002.5 | 0.447421125 | 0.354676063 | 0.038799097 | 2 |
| 1005.00625 | 0.446836496 | 0.354726602 | 0.038569993 | 3 |
| 1007.518766 | 0.446251968 | 0.354777034 | 0.038341615 | 4 |
| 1010.037563 | 0.445667546 | 0.354827358 | 0.038113966 | 5 |
| ⋮ | ⋮ | ⋮ | ⋮ | ⋮ |
| 2992.563587 | 0.250832165 | 0.347689361 | 7.72059E-08 | m-1 |
| 3000.044996 | 0.250566684 | 0.347588409 | 5.38099E-11 | m |
| 3007.545109 | 0.250302021 | 0.347487156 | 8.38595E-08 | m+1 |
| ⋮ | ⋮ | ⋮ | ⋮ | ⋮ |
| 5946.31953 | 0.203652773 | 0.314547385 | 0.003293202 | 715 |
| 5961.185329 | 0.203556215 | 0.314427589 | 0.003310203 | 716 |
| 5976.088292 | 0.20346006 | 0.31430792 | 0.003327204 | 717 |
| 5991.028513 | 0.203364304 | 0.314188379 | 0.003344207 | 718 |
| 6006.006084 | 0.203268948 | 0.314068968 | 0.00336121 | 719 |

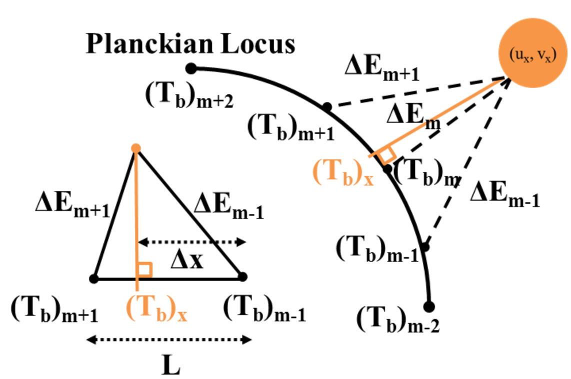


Figure 41: Triangular Solution Principles for the Determination of CCT.

### 3.4.1.4. COLOR RENDERING INDEX

The color rendering index (CRI) of an SSL device relates the effect the lighting source has on the color appearance of a set of 14 standard CIE test color samples and a 15th defined by the Japanese Industrial Standard JIS-Z872 that pertains to Japanese complexion under daylight conditions. These samples are defined in Table 9. (CIE, 1995) (CIE, 2004a) (CIE, 2004b) (Schanda, 2007) (Zukauskas, 2002) (Schubert, 2006) (Wyszecki, 1982)

Table 9: CIE and JIS Test Color Samples.

| **Test Color # ($TC_i$)** | **Munsell Notation (Hue/Lightness/Chroma)** | **Color Appearance under Daylight** |
|---|---|---|
| 1 | 7.5R 6/4 | Light Greyish Red |
| 2 | 5Y 6/4 | Dark Greyish Yellow |
| 3 | 5GY 6/8 | Strong Yellow Green |
| 4 | 2.5G 6/8 | Moderate Yellowish Green |
| 5 | 10BG 6/4 | Light Bluish Green |
| 6 | 5PB 6/8 | Light Blue |
| 7 | 2.5P 6/8 | Light Violet |
| 8 | 10P 6/8 | Light Reddish Purple |
| 9 | 4.5R 4/13 | Strong Red |
| 10 | 5Y 8/10 | Strong Yellow |
| 11 | 4.5G 5/8 | Strong Green |
| 12 | 3PB 3/11 | Strong Blue |
| 13 | 5YR 8/4 | Light Yellowish Pink (Human Complexion) |
| 14 | 5GY 4/4 | Moderate Olive Green (Leaf Green) |
| 15 | 1YR 6/4 | Japanese Complexion (JIS Only) |

The first step to acquire the CRI values of an SSL device is to calculate the SPD or reference illuminate for the previously determined CCT of the test vehicle in question normalized by the SPD value at the wavelength of 560 nm which corresponds to the peak value the human eye can detect. The calculation of the relative SPD is dependent upon the value of the CCT. The simplest form of the SPD is Planck's equation for CCT values less than 4000K. (CIE, 1995) (CIE, 2004a) (CIE, 2004b) (Wyszecki, 1982)

$$(CCT < 4000K)$$

$$S(\lambda) = \frac{\frac{2\cdot\pi\cdot c^2}{\lambda^5}\cdot\left(\exp\left(\frac{h\cdot c}{k\cdot\lambda\cdot CCT}\right)-1\right)^{-1}}{\frac{2\cdot\pi\cdot c^2}{(560nm)^5}\cdot\left(\exp\left(\frac{h\cdot c}{k\cdot(560nm)\cdot CCT}\right)-1\right)^{-1}} \tag{66}$$

When CCT values are larger than or equal to 4000K, a different process must be used to calculate the relative SPD. This process requires the calculation of the x-y chromaticity coordinates in terms of daylight ($x_D$, $y_D$) using the previously determined CCT. (CIE, 1995) (CIE, 2004a) (CIE, 2004b) (Wyszecki, 1982)

$$y_D = -3.000\cdot {x_D}^2 + 2.870\cdot x_D - 0.275 \tag{67}$$

$$(4000K \le CCT \le 7000K)$$

$$x_D = \frac{-4.6070x10^9}{CCT^3} + \frac{2.9678x10^6}{CCT^2} + \frac{0.09911x10^3}{CCT} + 0.244063 \tag{68}$$

$$(CCT > 7000K)$$

$$x_D = \frac{-2.0064x10^9}{CCT^3} + \frac{1.9018x10^6}{CCT^2} + \frac{0.24748x10^3}{CCT} + 0.237040 \tag{69}$$

Once the daylight chromaticity coordinates have been determined, the relative SPD for the larger CCT values can be determined using equation (70), where $S_0(\lambda)$, $S_1(\lambda)$, and $S_2(\lambda)$ are tabulated CIE components for daylight illuminates. (CIE, 1995) (CIE, 2004a) (CIE, 2004b) (Wyszecki, 1982)

$$S(\lambda) = S_0(\lambda) + M_1\cdot S_1(\lambda) + M_2\cdot S_2(\lambda) \tag{70}$$

$$M_1 = \frac{-1.3515 - 1.7703\cdot x_D + 5.9114\cdot y_D}{0.0241 + 0.256\cdot x_D - 0.7341\cdot y_D} \tag{71}$$

$$M_2 = \frac{0.0300 - 31.4424\cdot x_D + 30.071\cdot y_D}{0.0241 + 0.256\cdot x_D - 0.7341\cdot y_D} \tag{72}$$

With the SPD known for each CCT value, the next step is to determine the tristimulus values of the SSL device under test (denoted with subscript n) and for the SPD (denoted with subscript SPD) normalized by their respective luminance values with the normalized luminance as 100. (CIE, 1995) (CIE, 2004a) (CIE, 2004b) (Wyszecki, 1982)

$$X_n = \frac{X}{Y} \cdot 100 \tag{73}$$

$$Y_n = 100 \tag{74}$$

$$Z_n = \frac{Z}{Y} \cdot 100 \tag{75}$$

$$X_{SPD} = \frac{\int_{380}^{780} S(\lambda) \cdot \bar{x}(\lambda) \cdot d\lambda}{\int_{380}^{780} S(\lambda) \cdot \bar{y}(\lambda) \cdot d\lambda} \cdot 100 \tag{76}$$

$$Y_{SPD} = 100 \tag{77}$$

$$Z_{SPD} = \frac{\int_{380}^{780} S(\lambda) \cdot \bar{z}(\lambda) \cdot d\lambda}{\int_{380}^{780} S(\lambda) \cdot \bar{y}(\lambda) \cdot d\lambda} \cdot 100 \tag{78}$$

Next, the tristimulus values for each CIE Test Color ($TC_i$) illuminated by the SPD and by the SSL device are normalized with the illuminance values of the SPD and the SSL device, respectively, to account for adaptive color shift due to different states of chromatic adaptation. The tristimulus values for $TC_i$ illuminated by the SPD, where i = 1, 2…15, are shown in equations (79) – (81). (CIE, 1995) (CIE, 2004a) (CIE, 2004b) (Wyszecki, 1982)

$$\left(X_{SPD}\right)_{TC_i} = \frac{\int_{380}^{780} S(\lambda)\cdot \bar{x}(\lambda)\cdot TC_i(\lambda)\cdot d\lambda}{\int_{380}^{780} S(\lambda)\cdot \bar{y}(\lambda)\cdot d\lambda}\cdot 100 \tag{79}$$

$$\left(Y_{SPD}\right)_{TC_i} = \frac{\int_{380}^{780} S(\lambda)\cdot \bar{y}(\lambda)\cdot TC_i(\lambda)\cdot d\lambda}{\int_{380}^{780} S(\lambda)\cdot \bar{y}(\lambda)\cdot d\lambda}\cdot 100 \tag{80}$$

$$\left(Z_{SPD}\right)_{TC_i} = \frac{\int_{380}^{780} S(\lambda)\cdot \bar{z}(\lambda)\cdot TC_i(\lambda)\cdot d\lambda}{\int_{380}^{780} S(\lambda)\cdot \bar{y}(\lambda)\cdot d\lambda}\cdot 100 \tag{81}$$

The tristimulus values for $TC_i$ illuminated by the test vehicle, where i = 1, 2…15, are shown in equations (82) – (84).

$$\left(X_n\right)_{TC_i} = \frac{\int_{380}^{780} \Phi_{test}(\lambda)\cdot \bar{x}(\lambda)\cdot TC_i(\lambda)\cdot d\lambda}{\int_{380}^{780} \Phi_{test}(\lambda)\cdot \bar{y}(\lambda)\cdot d\lambda}\cdot 100 \tag{82}$$

$$\left(Y_n\right)_{TC_i} = \frac{\int_{380}^{780} \Phi_{test}(\lambda)\cdot \bar{y}(\lambda)\cdot TC_i(\lambda)\cdot d\lambda}{\int_{380}^{780} \Phi_{test}(\lambda)\cdot \bar{y}(\lambda)\cdot d\lambda}\cdot 100 \tag{83}$$

$$\left(Z_n\right)_{TC_i} = \frac{\int_{380}^{780} \Phi_{test}(\lambda)\cdot \bar{z}(\lambda)\cdot TC_i(\lambda)\cdot d\lambda}{\int_{380}^{780} \Phi_{test}(\lambda)\cdot \bar{y}(\lambda)\cdot d\lambda}\cdot 100 \tag{84}$$

The CIE 1960 u-v coordinates are now determined using the new tristimulus values with equations (59) and (60). A summary table of the calculated tristimulus and u-v coordinates in variable form for each TC, the SPD and the test vehicle are given in Table 10 to better illustrate the parameters that have been calculated thus far.

Table 10: Summary Table I of Calculated CRI Parameters.

| **$TC_i$** | **X** | **Y** | **Z** | **u** | **v** |
|---|---|---|---|---|---|
| $TC_1$ | $(X_{SPD})_{TC1}$ | $(Y_{SPD})_{TC1}$ | $(Z_{SPD})_{TC1}$ | $(u_{SPD})_{TC1}$ | $(v_{SPD})_{TC1}$ |
| | $(X_n)_{TC1}$ | $(Y_n)_{TC1}$ | $(Z_n)_{TC1}$ | $(u_n)_{TC1}$ | $(v_n)_{TC1}$ |
| $TC_2$ | $(X_{SPD})_{TC2}$ | $(Y_{SPD})_{TC2}$ | $(Z_{SPD})_{TC2}$ | $(u_{SPD})_{TC2}$ | $(v_{SPD})_{TC2}$ |
| | $(X_n)_{TC2}$ | $(Y_n)_{TC2}$ | $(Z_n)_{TC2}$ | $(u_n)_{TC2}$ | $(v_n)_{TC2}$ |
| $TC_3$ | $(X_{SPD})_{TC3}$ | $(Y_{SPD})_{TC3}$ | $(Z_{SPD})_{TC3}$ | $(u_{SPD})_{TC3}$ | $(v_{SPD})_{TC3}$ |
| | $(X_n)_{TC3}$ | $(Y_n)_{TC3}$ | $(Z_n)_{TC3}$ | $(u_n)_{TC3}$ | $(v_n)_{TC3}$ |
| $TC_4$ | $(X_{SPD})_{TC4}$ | $(Y_{SPD})_{TC4}$ | $(Z_{SPD})_{TC4}$ | $(u_{SPD})_{TC4}$ | $(v_{SPD})_{TC4}$ |
| | $(X_n)_{TC4}$ | $(Y_n)_{TC4}$ | $(Z_n)_{TC4}$ | $(u_n)_{TC4}$ | $(v_n)_{TC4}$ |
| $TC_5$ | $(X_{SPD})_{TC5}$ | $(Y_{SPD})_{TC5}$ | $(Z_{SPD})_{TC5}$ | $(u_{SPD})_{TC5}$ | $(v_{SPD})_{TC5}$ |
| | $(X_n)_{TC5}$ | $(Y_n)_{TC5}$ | $(Z_n)_{TC5}$ | $(u_n)_{TC5}$ | $(v_n)_{TC5}$ |
| $TC_6$ | $(X_{SPD})_{TC6}$ | $(Y_{SPD})_{TC6}$ | $(Z_{SPD})_{TC6}$ | $(u_{SPD})_{TC6}$ | $(v_{SPD})_{TC6}$ |
| | $(X_n)_{TC6}$ | $(Y_n)_{TC6}$ | $(Z_n)_{TC6}$ | $(u_n)_{TC6}$ | $(v_n)_{TC6}$ |
| $TC_7$ | $(X_{SPD})_{TC7}$ | $(Y_{SPD})_{TC7}$ | $(Z_{SPD})_{TC7}$ | $(u_{SPD})_{TC7}$ | $(v_{SPD})_{TC7}$ |
| | $(X_n)_{TC7}$ | $(Y_n)_{TC7}$ | $(Z_n)_{TC7}$ | $(u_n)_{TC7}$ | $(v_n)_{TC7}$ |
| $TC_8$ | $(X_{SPD})_{TC8}$ | $(Y_{SPD})_{TC8}$ | $(Z_{SPD})_{TC8}$ | $(u_{SPD})_{TC8}$ | $(v_{SPD})_{TC8}$ |
| | $(X_n)_{TC8}$ | $(Y_n)_{TC8}$ | $(Z_n)_{TC8}$ | $(u_n)_{TC8}$ | $(v_n)_{TC8}$ |
| $TC_9$ | $(X_{SPD})_{TC9}$ | $(Y_{SPD})_{TC9}$ | $(Z_{SPD})_{TC9}$ | $(u_{SPD})_{TC9}$ | $(v_{SPD})_{TC9}$ |
| | $(X_n)_{TC9}$ | $(Y_n)_{TC9}$ | $(Z_n)_{TC9}$ | $(u_n)_{TC9}$ | $(v_n)_{TC9}$ |
| $TC_{10}$ | $(X_{SPD})_{TC10}$ | $(Y_{SPD})_{TC10}$ | $(Z_{SPD})_{TC10}$ | $(u_{SPD})_{TC10}$ | $(v_{SPD})_{TC10}$ |
| | $(X_n)_{TC10}$ | $(Y_n)_{TC10}$ | $(Z_n)_{TC10}$ | $(u_n)_{TC10}$ | $(v_n)_{TC10}$ |
| $TC_{11}$ | $(X_{SPD})_{TC11}$ | $(Y_{SPD})_{TC11}$ | $(Z_{SPD})_{TC11}$ | $(u_{SPD})_{TC11}$ | $(v_{SPD})_{TC11}$ |
| | $(X_n)_{TC11}$ | $(Y_n)_{TC11}$ | $(Z_n)_{TC11}$ | $(u_n)_{TC11}$ | $(v_n)_{TC11}$ |
| $TC_{12}$ | $(X_{SPD})_{TC12}$ | $(Y_{SPD})_{TC12}$ | $(Z_{SPD})_{TC12}$ | $(u_{SPD})_{TC12}$ | $(v_{SPD})_{TC12}$ |
| | $(X_n)_{TC12}$ | $(Y_n)_{TC12}$ | $(Z_n)_{TC12}$ | $(u_n)_{TC12}$ | $(v_n)_{TC12}$ |
| $TC_{13}$ | $(X_{SPD})_{TC13}$ | $(Y_{SPD})_{TC13}$ | $(Z_{SPD})_{TC13}$ | $(u_{SPD})_{TC13}$ | $(v_{SPD})_{TC13}$ |
| | $(X_n)_{TC13}$ | $(Y_n)_{TC13}$ | $(Z_n)_{TC13}$ | $(u_n)_{TC13}$ | $(v_n)_{TC13}$ |
| $TC_{14}$ | $(X_{SPD})_{TC14}$ | $(Y_{SPD})_{TC14}$ | $(Z_{SPD})_{TC14}$ | $(u_{SPD})_{TC14}$ | $(v_{SPD})_{TC14}$ |
| | $(X_n)_{TC14}$ | $(Y_n)_{TC14}$ | $(Z_n)_{TC14}$ | $(u_n)_{TC14}$ | $(v_n)_{TC14}$ |
| $TC_{15}$ | $(X_{SPD})_{TC15}$ | $(Y_{SPD})_{TC15}$ | $(Z_{SPD})_{TC15}$ | $(u_{SPD})_{TC15}$ | $(v_{SPD})_{TC15}$ |
| | $(X_n)_{TC15}$ | $(Y_n)_{TC15}$ | $(Z_n)_{TC15}$ | $(u_n)_{TC15}$ | $(v_n)_{TC15}$ |
| SPD | $(X_{SPD})$ | $(Y_{SPD})$ | $(Z_{SPD})$ | $(u_{SPD})$ | $(v_{SPD})$ |
| Test Vehicle | $(X_n)$ | $(Y_n)$ | $(Z_n)$ | $(u_n)$ | $(v_n)$ |

After finding the u-v coordinates for the SPD, test vehicle and each TC illuminated by the test vehicle, the adaptive color shift due to the different chromaticities of the SPD and test vehicle can be accounted for. (CIE, 1995) (CIE, 2004a) (CIE, 2004b) (Wyszecki, 1982)

$$(u_k)_{TC_i} = \frac{10.872 + 0.404 \cdot \frac{c_{SPD}}{c_n} \cdot (c_n)_{TC_i} - 4 \cdot \frac{d_{SPD}}{d_n} \cdot (d_n)_{TC_i}}{16.518 + 1.481 \cdot \frac{c_{SPD}}{c_n} \cdot (c_n)_{TC_i} - \frac{d_{SPD}}{d_n} \cdot (d_n)_{TC_i}} \tag{85}$$

$$(v_k)_{TC_i} = \frac{5.520}{16.518 + 1.481 \cdot \frac{c_{SPD}}{c_n} \cdot (c_n)_{TC_i} - \frac{d_{SPD}}{d_n} \cdot (d_n)_{TC_i}} \tag{86}$$

$$c = \frac{1}{v} \cdot (4 - u - 10 \cdot v) \tag{87}$$

$$d = \frac{1}{v} \cdot (1.708 \cdot v + 0.404 - 1.481 \cdot u) \tag{88}$$

In equations (87) and (88), the variables c and d are calculated using the u-v coordinates for the test vehicle, SPD and each TC illuminated by the test vehicle. A summary table to illustrate calculated terms is shown in variable form in Table 11.

Table 11: Summary Table II of Calculated CRI Parameters.

| **$TC_i$** | **$u_k$** | **$v_k$** | **c** | **d** |
|---|---|---|---|---|
| $TC_1$ | $(u_k)_{TC1}$ | $(v_k)_{TC1}$ | $(c_n)_{TC1}$ | $(d_n)_{TC1}$ |
| $TC_2$ | $(u_k)_{TC2}$ | $(v_k)_{TC2}$ | $(c_n)_{TC2}$ | $(d_n)_{TC2}$ |
| $TC_3$ | $(u_k)_{TC3}$ | $(v_k)_{TC3}$ | $(c_n)_{TC3}$ | $(d_n)_{TC3}$ |
| $TC_4$ | $(u_k)_{TC4}$ | $(v_k)_{TC4}$ | $(c_n)_{TC4}$ | $(d_n)_{TC4}$ |
| $TC_5$ | $(u_k)_{TC5}$ | $(v_k)_{TC5}$ | $(c_n)_{TC5}$ | $(d_n)_{TC5}$ |
| $TC_6$ | $(u_k)_{TC6}$ | $(v_k)_{TC6}$ | $(c_n)_{TC6}$ | $(d_n)_{TC6}$ |
| $TC_7$ | $(u_k)_{TC7}$ | $(v_k)_{TC7}$ | $(c_n)_{TC7}$ | $(d_n)_{TC7}$ |
| $TC_8$ | $(u_k)_{TC8}$ | $(v_k)_{TC8}$ | $(c_n)_{TC8}$ | $(d_n)_{TC8}$ |
| $TC_9$ | $(u_k)_{TC9}$ | $(v_k)_{TC9}$ | $(c_n)_{TC9}$ | $(d_n)_{TC9}$ |
| $TC_{10}$ | $(u_k)_{TC10}$ | $(v_k)_{TC10}$ | $(c_n)_{TC10}$ | $(d_n)_{TC10}$ |
| $TC_{11}$ | $(u_k)_{TC11}$ | $(v_k)_{TC11}$ | $(c_n)_{TC11}$ | $(d_n)_{TC11}$ |
| $TC_{12}$ | $(u_k)_{TC12}$ | $(v_k)_{TC12}$ | $(c_n)_{TC12}$ | $(d_n)_{TC12}$ |
| $TC_{13}$ | $(u_k)_{TC13}$ | $(v_k)_{TC13}$ | $(c_n)_{TC13}$ | $(d_n)_{TC13}$ |
| $TC_{14}$ | $(u_k)_{TC14}$ | $(v_k)_{TC14}$ | $(c_n)_{TC14}$ | $(d_n)_{TC14}$ |
| $TC_{15}$ | $(u_k)_{TC15}$ | $(v_k)_{TC15}$ | $(c_n)_{TC15}$ | $(d_n)_{TC15}$ |
| SPD | N/A | N/A | $(c_{SPD})$ | $(d_{SPD})$ |
| Test Vehicle | N/A | N/A | $(c_n)$ | $(d_n)$ |

Now that adaptive color shift has been accounted for, the CIE 1964 UCS W*-U*-V* coordinates can be determined for each TC illuminated by the SPD, equations (89) – (91), and the test vehicle, equations (92) – (94), using the variables listed in each of the two summary tables. (CIE, 2004a) (CIE, 1995) (CIE, 2004b) (Wyszecki, 1982)

$$\left(W_{SPD}*\right)_{TC_i} = 25 \cdot \left(\left(Y_{SPD}\right)_{TC_i}\right)^{\frac{1}{3}} - 17 \tag{89}$$

$$\left(U_{SPD}*\right)_{TC_i} = 13 \cdot \left(W_{SPD}*\right)_{TC_i} \cdot \left(\left(u_{SPD}\right)_{TC_i} - u_n\right) \tag{90}$$

$$\left(V_{SPD}*\right)_{TC_i} = 13 \cdot \left(W_{SPD}*\right)_{TC_i} \cdot \left(\left(v_{SPD}\right)_{TC_i} - v_n\right) \tag{91}$$

$$\left(W_n*\right)_{TC_i} = 25 \cdot \left(\left(Y_n\right)_{TC_i}\right)^{\frac{1}{3}} - 17 \tag{92}$$

$$\left(U_n*\right)_{TC_i} = 13 \cdot \left(W_n*\right)_{TC_i} \cdot \left(\left(u_k\right)_{TC_i} - u_n\right) \tag{93}$$

$$\left(V_n*\right)_{TC_i} = 13 \cdot \left(W_n*\right)_{TC_i} \cdot \left(\left(v_k\right)_{TC_i} - v_n\right) \tag{94}$$

Now that the colorimetric data has been transformed into the W*-U*-V* color space, the CRI values of R1 – R15 and the general CRI value of Ra can be determined using the resultant color shift, $\Delta E_i$. (CIE, 1995) (CIE, 2004a) (CIE, 2004b) (Wyszecki, 1982)

$$\Delta E_i = \sqrt{\begin{array}{l}\left(\left(W_{SPD}*\right)_{TC_i} - \left(W_n*\right)_{TC_i}\right)^2 + \\ \left(\left(U_{SPD}*\right)_{TC_i} - \left(U_n*\right)_{TC_i}\right)^2 + \\ \left(\left(V_{SPD}*\right)_{TC_i} - \left(V_n*\right)_{TC_i}\right)^2\end{array}} \tag{95}$$

$$Ri = 100 - 4.6 \cdot \Delta E_i \tag{96}$$

$$Ra = \frac{1}{8} \cdot \sum_{i=1}^{8} Ri \tag{97}$$

### 3.4.1.5. DOMINANT WAVELENGTH

An additional colorimetric quantity that gives greater insight in understanding the color characteristics of SSL lamps is the dominant (or complementary) wavelength. SSL devices have either a dominant wavelength or complementary wavelength. The CIE definition for dominant wavelength is: “Wavelength of the monochromatic stimulus that, when additively mixed in suitable proportions with the specified achromatic stimulus, matches the color stimulus considered” (Schanda, 2007). This is visually explained in Figure 42.

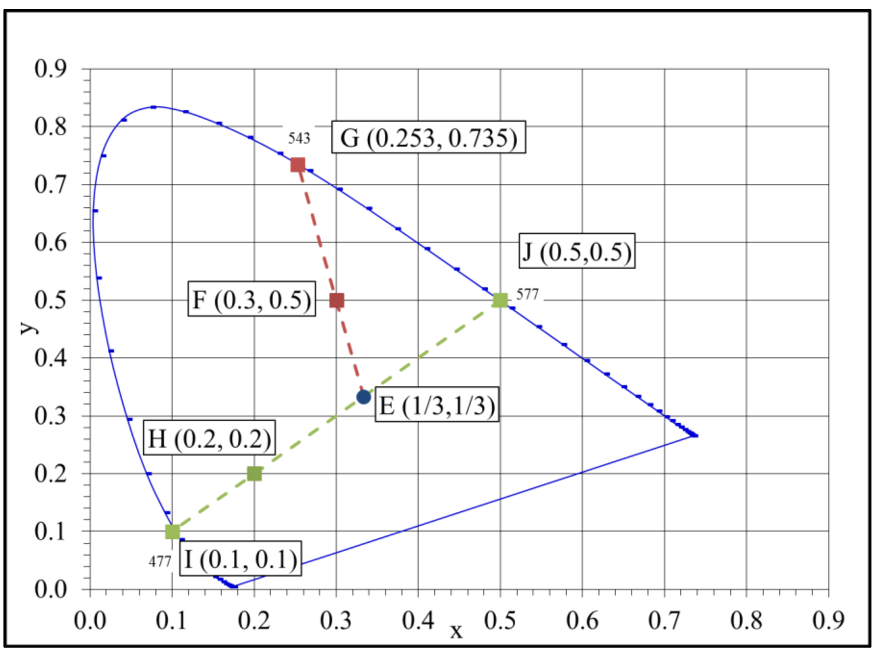


Figure 42: CIE Chromaticity Diagram with Dominant and Complementary Wavelengths.

Looking at Figure 42, chromaticity E is the specified achromatic stimulus. Chromaticity E is the white point of CIE Illuminate E with chromaticity coordinates (1/3, 1/3). CIE Illuminate E is an equal-energy radiator that has a constant SPD inside the visible spectrum and gives equal weight to all wavelengths. Chromaticities F and H are arbitrarily chosen chromaticity coordinates for two different monochromatic stimuli or SSL lamps. Chromaticities G, J, and I are pseudo monochromatic stimuli used to match the color of chromaticities F and H. (CIE, 2004a) (Schanda, 2007) (Wyszecki, 1982)

If the achromatic stimulus E is additively mixed with the pseudo monochromatic stimulus G with monochromatic radiation of wavelength 543 nm, then the chromaticity point F is reached when a straight-line is drawn between points E and G. Thus, chromaticity G is the dominant wavelength of chromaticity F. Conversely, if the same reasoning is applied for the achromatic stimulus E and the pseudo monochromatic stimulus I with monochromatic radiation of wavelength 477 nm, then chromaticity H is reached. However, chromaticity I is not the dominate wavelength due to its chromaticity coordinates being below the achromatic stimulus E. In this case, chromaticity H does not have a dominate wavelength, but will have a complementary wavelength. If the line that crosses chromaticity H is extended toward the spectrum locus to chromaticity J, a larger monochromatic radiation of wavelength 577 nm is reached. Since 577 nm is larger than 477 nm, chromaticity H has a complementary wavelength at chromaticity J.

#### 3.4.1.6. EXCITATION PURITY

The excitation purity of the monochromatic stimulus indicates how far the chromaticity point is from the achromatic stimulus towards the spectrum locus or the "purple" line at the bottom of the spectrum locus. The excitation purity is determined using the dominant wavelength or complementary wavelength depending on the chromaticity of the SSL device. Equations (98) and (99) detail the two forms of the equation to calculate excitation purity of the SSL device with chromaticity coordinates (x, y), where the subscript "w" denotes the chromaticity coordinates of the achromatic stimulus and the subscript "b" denotes the chromaticity coordinates of the dominate (or complementary) wavelength. (CIE, 2004a) (Schanda, 2007) (Wyszecki, 1982)

$$p_e = \frac{x - x_w}{x_b - x_w} \tag{98}$$

$$p_e = \frac{y - y_w}{y_b - y_w} \tag{99}$$

The correct form of the excitation purity equation to obtain greater precision is recommend to be determined as the equation that gives the largest numerator (Schanda, 2007) or the equation that gives the least amount of computational rejection error (Wyszecki, 1982).

The excitation purity and dominant (or complementary) wavelength together give a complete understanding of the chromaticity coordinates of the monochromatic stimulus being tested.

#### 3.4.1.7. CIE WHITENESS AND TINT

The CIE has developed standard formulas to evaluate the perceived whiteness, W, and tint, T, of SSL devices to promote uniformity among manufacturers (CIE, 2004a).

$$W = 100 + 800 \cdot (x_n - x) + 1700 \cdot (y_n - y) \tag{100}$$

$$T = 1000 \cdot (x_n - x) - 650 \cdot (y_n - y) \quad (101)$$

The chromaticity coordinates (x, y) refer to those of the SSL device being tested and the chromaticity coordinates ($x_n$, $y_n$) refer to the perfect diffuser or standard illuminate D65. D65 is used to compare the SSL device to a chromaticity of neutral hue used to describe cool-white light or daylight. The whiteness and tint of the perfect diffuser is equal to 100 and 0, respectively. As the whiteness value increases, the indicated whiteness becomes larger. Positive values of tint denote a greener tint, while negative values indicate a redder tint. (CIE, 2004a) (Schanda, 2007) (Wyszecki, 1982)

The linear whiteness formula is only applicable for SSL devices that are called "white" commercially and provides a relative measure of whiteness, not an absolute one. Additionally, these formulas are only valid within a restricted volume that lies between the limits of $40 < W < 220$ and $-4 < T < 2$. Furthermore, equal differences between whiteness of D65 and the SSL device do not always represent equal perceptual differences in whiteness, nor do equal differences in tint always represent equal perceptual differences in the greenishness or reddishness of the white light. Measures that correlate with perceptual difference are currently beyond present knowledge. (CIE, 2004a)

#### 3.4.1.8. YELLOW-TO-BLUE RATIO

An additional parameter was developed through the course of this research to characterize the shift in the yellow phosphor peak and/or the blue LED peak. To better illustrate this, the SPD graphs of a cool-white SSL lamp and a warm-white SSL lamp are given in Figure 43 and Figure 44, respectively.

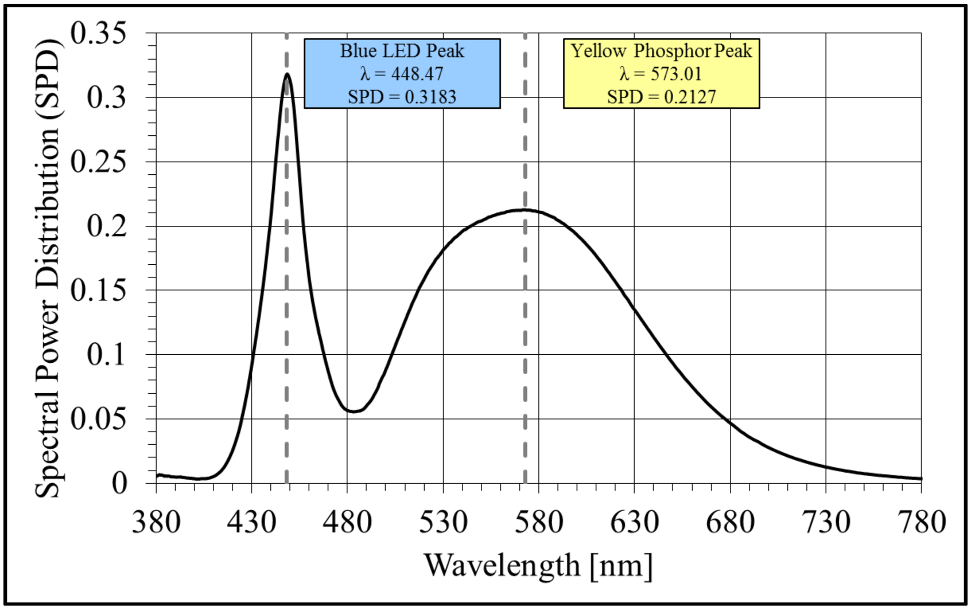


Figure 43: SPD of a Cool-White SSL Lamp.

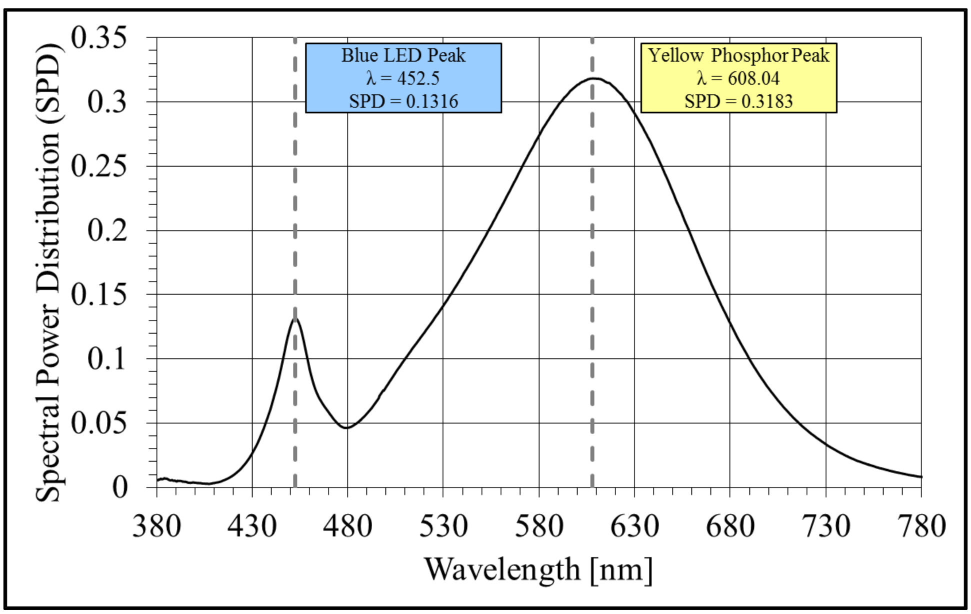


Figure 44: SPD of a Warm-White SSL Lamp.

The yellow-to-blue (yb) ratio is determined using the SPD values at each peak as shown in equation (102).

$$yb = \frac{SPD(\lambda_{yellow})}{SPD(\lambda_{blue})} \quad (102)$$

If the yb ratio is greater than one or less than one, then this ratio describes a warm white SSL lamp or a cool-white SSL lamp, respectively. Table 12 lists the values from Figure 43 and Figure 44, as well as the yb ratio of each figure.

Table 12: Yellow-to-Blue Ratio Example.

| **Figure** | **$\lambda_y$ [nm]** | **SPD($\lambda_y$) [W/(m$^2$·nm)]** | **$\lambda_b$ [nm]** | **SPD($\lambda_b$) [W/(m$^2$·nm)]** | **yb** |
|---|---|---|---|---|---|
| Figure 43 | 573.01 | 0.2127 | 448.47 | 0.3183 | 0.6682 |
| Figure 44 | 608.04 | 0.3183 | 452.5 | 0.1316 | 2.4182 |

### 3.4.2. PHM ALGORITHMS

#### 3.4.2.1. KALMAN FILTERING

The Kalman filter (KF) is a recursive estimator that produces a statistically optimal estimate of the instantaneous state of a linear dynamic system's output that is perturbed by noise (Balakrishnan, 1987) (Grewal, 2001) (Zarchan, 2000). The system dynamics of the KF are described in state space form using the feature vector or system state, as well as a known input. Since the feature vector usually cannot be accurately describe as a single constant or with a linear fit, a second order system was used to represent the evolution of the system state during the onset of damage accrual. The choice of the second order filter was also influenced by the general observation that feature vectors evolve non-linearly and generally accelerate towards the end of life. The second order continuous form of the system dynamics is shown in equations (103) and (104).

$$\dot{x} = A \cdot x + B \cdot u + w \Rightarrow \begin{bmatrix} \dot{x} \\ \ddot{x} \\ \dddot{x} \end{bmatrix} = \begin{bmatrix} 0 & 1 & 0 \\ 0 & 0 & 1 \\ 0 & 0 & 0 \end{bmatrix} \cdot \begin{Bmatrix} x \\ \dot{x} \\ \ddot{x} \end{Bmatrix} + \begin{bmatrix} 0 \\ 0 \\ 1 \end{bmatrix} \cdot u + \begin{bmatrix} 0 \\ 0 \\ w \end{bmatrix} \tag{103}$$

$$y = C \cdot x + v = \begin{bmatrix} 1 & 0 & 0 \end{bmatrix} \cdot \begin{Bmatrix} x \\ \dot{x} \\ \ddot{x} \end{Bmatrix} + v \tag{104}$$

The variables ẋ and ẍ are the first and second time derivatives of the feature vector x, respectively. The parameters u and y are the input vector and output vector, respectively. The matrices A, B, and C are the system dynamic matrix, input matrix and measurement matrix, respectively. The process noise, w, is assumed to be a zero mean multivariate normal distribution with a covariance, Q, called the process noise matrix. The measurement noise or white noise, v, is assumed to be a zero mean Gaussian white noise normal distribution with a covariance, R, called the measurement noise matrix. These parameters are usually unknown and are sometimes used to "tune" the filter. (Balakrishnan, 1987) (Grewal, 2001) (Zarchan, 2000)

$$Q = E[w \cdot w^T] = \begin{bmatrix} 0 & 0 & 0 \\ 0 & 0 & 0 \\ 0 & 0 & \Phi_s \end{bmatrix} \tag{105}$$

$$R = E[v \cdot v^T] = \sigma_{noise}^2 \tag{106}$$

In order to discretize the continuous form of the KF, the discrete fundamental matrix, $\Phi_k$, must be determined from the system dynamics matrix A. The fundamental matrix can be computed from the Taylor series expansion of the system dynamics matrix as shown in equations (107) - (109). Also, the discrete input matrix, $G_k$, can be determined by integrating the product of the discrete fundamental matrix and the continuous input matrix as shown in equation (110).

$$\Phi(t) = e^{A\cdot t} = I + A\cdot t + \frac{(A\cdot t)^2}{2!} + \ldots + \frac{(A\cdot t)^n}{n!} \tag{107}$$

$$\Phi(t) = \begin{bmatrix} 1 & 0 & 0 \\ 0 & 1 & 0 \\ 0 & 0 & 1 \end{bmatrix} + \begin{bmatrix} 0 & 1 & 0 \\ 0 & 0 & 1 \\ 0 & 0 & 0 \end{bmatrix} \cdot t + \begin{bmatrix} 0 & 0 & 1 \\ 0 & 0 & 0 \\ 0 & 0 & 0 \end{bmatrix} \cdot \frac{t^2}{2!} \tag{108}$$

$$\Phi_k = \Phi(T_s) = \begin{bmatrix} 1 & T_s & \frac{T_s}{2} \\ 0 & 1 & T_s \\ 0 & 0 & 1 \end{bmatrix} \tag{109}$$

$$G_k = \int_0^{T_s} (\Phi(\tau) \cdot B) d\tau \tag{110}$$

Therefore, the discrete form of the system dynamics is shown below, where $z_k$ is the actual measured output vector of the system at time step k and the discrete measurement matrix, H, is identical to the continuous measurement matrix, C.

$$x_{k+1} = \Phi_k \cdot x_k + G_k \cdot u_k + w_k \tag{111}$$

$$z_k = H \cdot x_k + v_k \tag{112}$$

The discrete process noise, $w_k$, has the same assumptions as the continuous process noise. The covariance of the discrete process noise, $Q_k$, is called the discrete process noise matrix and requires knowledge of the continuous process noise matrix. The discrete measurement noise covariance, $R_k$, is assumed to be identical to the continuous measurement matrix. (Balakrishnan, 1987) (Grewal, 2001) (Zarchan, 2000)

$$Q_k = \int_0^{T_s} \left(\Phi(\tau) \cdot Q \cdot \Phi^T(\tau)\right) d\tau \tag{113}$$

$$R_k = E[v_k \cdot v_k^{\ T}] \tag{114}$$

Since the internal dynamics cannot be measured, the feature vectors must be estimated using the KF. The estimated state and output are assumed to have some unknown process and measurement noise intertwined within the signal itself. The first step is to project the state space using the discrete fundamental matrix.

$$\overline{x_k} = \Phi_k \cdot \hat{x}_k + G_k \cdot u_k \tag{115}$$

$$\overline{z_k} = H \cdot \overline{x_k} \tag{116}$$

The variable $\bar{x}_k$ is the projection of the feature vector at the k^th time step from the estimated state $\hat{x}_k$ and input $u_k$ used to estimate the output $\hat{z}_k$. Next, the Kalman gains are computed from a set of recursive matrix equations called the Riccati equations (Balakrishnan, 1987) (Grewal, 2001) (Zarchan, 2000). The Riccati equations are shown in equations (117) - (119).

$$M_k = \Phi_k \cdot P_{k-1} \cdot \Phi_k{}^T + Q_k \tag{117}$$

$$K_k = M_k \cdot H^T \cdot (H \cdot M_k \cdot H^T + R_k)^{-1} \tag{118}$$

$$P_k = (I - K_k \cdot H) \cdot M_k \tag{119}$$

$M_k$ is the predicted (*a priori*) estimate of the error covariance matrix, $K_k$ is the Kalman gain which minimizes the error between the estimated state and actual state and $P_k$ is the updated (*a posteriori*) estimate of the error covariance matrix. The diagonal elements of $P_k$ represent the variance of the true state minus the estimated state. Once the Kalman gains have been computed, the estimated state is updated using the previous estimate as shown in equation (120). (Balakrishnan, 1987) (Grewal, 2001) (Zarchan, 2000) The block diagram of the KF can be seen in Figure 45.

$$\hat{x}_k = \overline{x}_k + K_k \cdot (z_k - H \cdot \overline{x}_k) \tag{120}$$

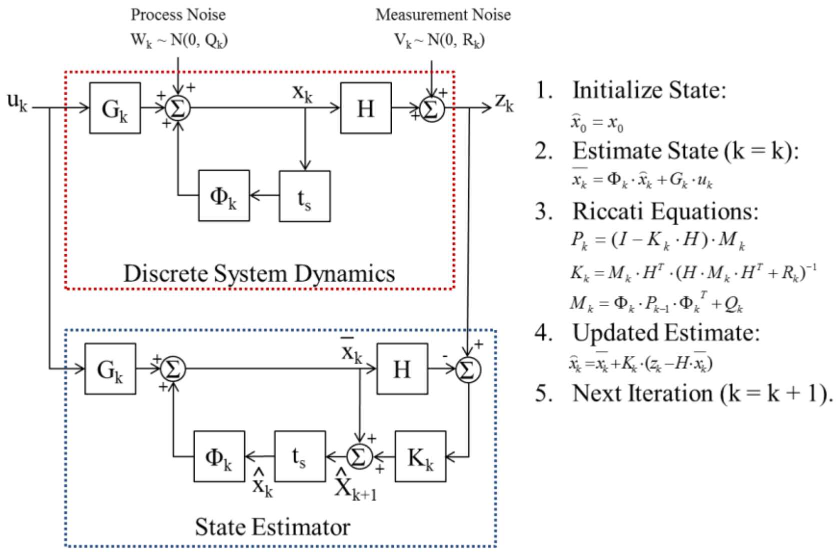


Figure 45: Block Diagram of the Kalman Filter.

A simulation was constructed as a verification tool for proper implementation of the KF and is shown in. The simulation was designed as a ground based radar tracking a falling object with a measurement standard deviation of 300 m.

Table 13: KF Simulation Parameters.

| **Parameter** | $\mathbf{u_k}$ |
|---|---|
| Initial Position [km] | 122 |
| Velocity [m/s] | -2400 |
| Acceleration [m$^2$/s] | -9.81 |
| time [s] | 30 |
| Sampling Period [s] | 0.1 |
| σ [m] | 300 |

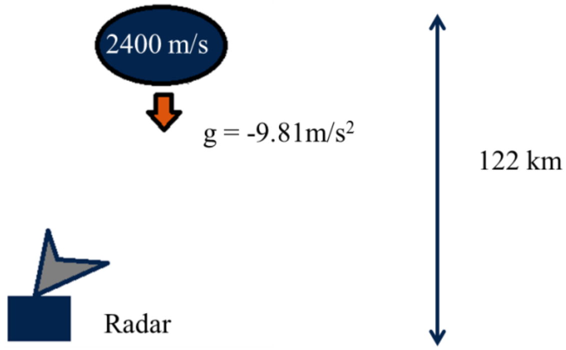


Figure 46: Simulation Diagram for KF Example.

By applying the kinematic equation for linear motion, the theoretical position after 30 s of the falling object was determined to be 45585.5 m.

$$y = x_0 + v \cdot t + \frac{1}{2} \cdot g \cdot t^2 \tag{121}$$

Since the radar will have a certain amount of noise in the measurement, additive white Gaussian noise was included in the simulated signal to demonstrate the measurement of a noisy signal.

$$y_{star} = awgn(y, snr) \tag{122}$$

Equation (122) utilizes a built-in Matlab command specifically designed to add white Gaussian noise to the vector signal, y, with a signal-to-noise ratio (snr) in decibels. For this simulation a snr of 50db was arbitrarily chosen. Process noise was simulated using a zero mean multivariate normal distribution command to produce the process noise matrix.

$$w_k = mvnrnd(0, \sigma) \tag{123}$$

Equation (123) produces a random vector using zero mean and the standard deviation, σ, from the multivariate normal distribution. The error between the theoretical position and the simulated position with white Gaussian noise at each time step is shown below to illustrate the capture of a noisy input signal.

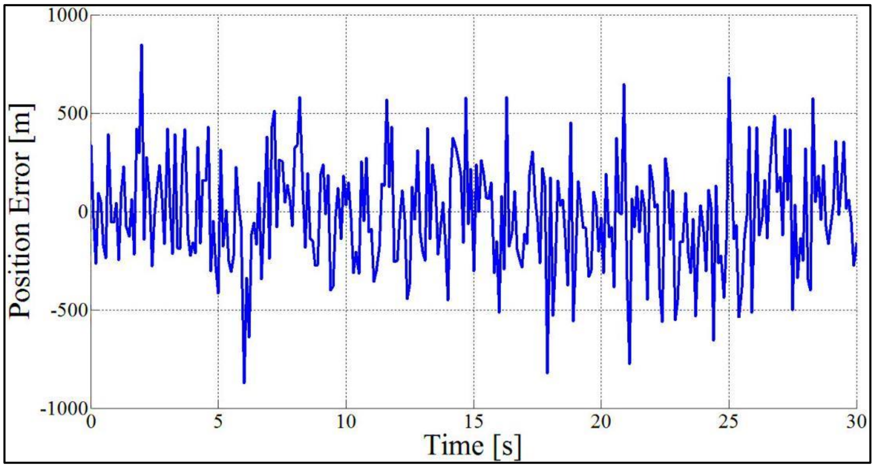


Figure 47: Position Error between Theoretical and Simulation for the Falling Object.

In order to use the KF, the covariance matrix and initial state had to be initialized. Since the initial covariance matrix was unknown, it has been initialized to an arbitrarily large value of a 3x3 identity matrix multiplied by a scalar of 10^15. It has been shown that the polynomial Kalman filter is insensitive to the initial value of the covariance matrix and that a large initial covariance matrix is a suitable choice because it will take into account any uncertainties in the initial measurements (Zarchan, 2000). The initial state at time zero was taken as zero for each state variable. Figure 48 shows the position error between the KF tracking result and the theoretical position which illustrates the successfully filtered noisy signal.

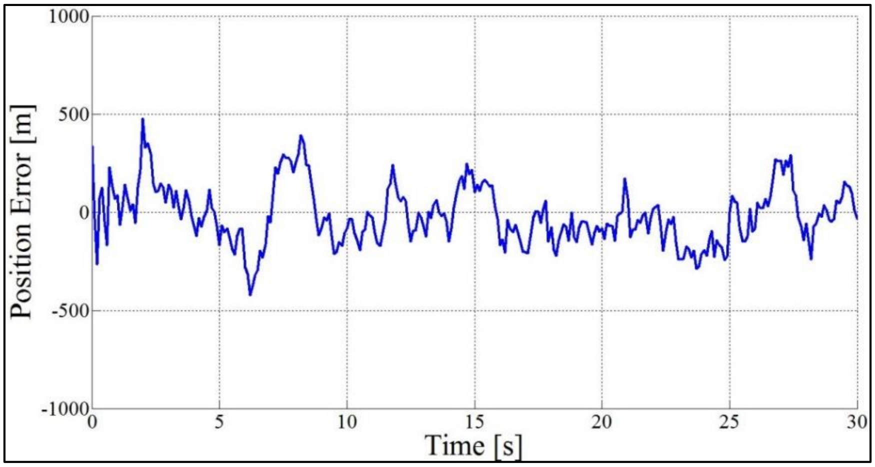


Figure 48: Position Error between Theoretical and KF for the Falling Object.

The settling time, overshoot, undershoot and root mean square error (RMSE) of the state variables is given in Table 14. This validates the KF's ability to accurately track the object's position with a RMSE of 0.14%.

Table 14: Validation Parameters for KF.

| **Parameter** | $x$ | $\dot{x}$ | $\ddot{x}$ |
|---|---|---|---|
| Settling Time [ms] | 294.862 | 286.8696 | 10.0997 |
| Overshoot | 167.5167 | 63.5347 | 9396.2 |
| Undershoot | 0 | 441.2713 | 74528 |
| RMSE | 0.14% | 1.29% | 4.46% |

The forecast of the estimated feature vector into the future to determine the RUL was accomplished using the state evolution equation to iteratively solve the intersection of the underlying physics model. The Newton-Raphson method was used in conjunction with the state evolution equation from the KF to determine the estimated time for the end of life ($t_{eol}$) of the feature vector (Lall P. W., 2012a).

$$f(t_k) = \hat{x}_k + \hat{\dot{x}}_k \cdot t_k + \frac{1}{2} \cdot \hat{\ddot{x}}_k \cdot t_k{}^2 - x(t_{eol}) \tag{124}$$

$$t_{k+1} = t_k - \frac{f(t_k)}{f`(t_k)} \tag{125}$$

In this work, a pre-described model based on the accrued plastic work in interconnects of the system has not been used because the inputs to the system are not always known or measurable and cannot be assumed to always be constant or known in advance. In order to adequately capture the degradation in the EC, the KF used the feature vector of resistance change acquired from RS to describe the underlying plastic work to prognosticate the RUL. Similarly, the change in ESR and CAP of the AECs were used as two separate feature vectors to deduce which is a better candidate for a PHM framework.

#### 3.4.2.2. EXTENDED KALMAN FILTER

The extended Kalman filter (EKF) is a nonlinear version of the KF and is generally more robust due to the use of linear approximations over small ranges of state space and the assumption of linearity over the range of estimation errors (Grewal, 2001). The EKF allows the relationship between the system state and output to be nonlinear. This allows for a better description of the evolution of the system state during the onset of damage accrual when no prior knowledge of the system is known. Similarly to the KF, the system dynamics of the EKF are described in state space form using the feature vector or system state, as well as a known input. The second order continuous form of the system dynamics is shown in equations (126) and (127).

$$\dot{x} = A(x)\cdot x + w \Rightarrow \begin{bmatrix} \dot{x} \\ \ddot{x} \\ \dddot{x} \end{bmatrix} = \begin{bmatrix} \frac{\partial \dot{x}}{\partial x} & \frac{\partial \dot{x}}{\partial \dot{x}} & \frac{\partial \dot{x}}{\partial \ddot{x}} \\ \frac{\partial \ddot{x}}{\partial x} & \frac{\partial \ddot{x}}{\partial \dot{x}} & \frac{\partial \ddot{x}}{\partial \ddot{x}} \\ \frac{\partial \dddot{x}}{\partial x} & \frac{\partial \dddot{x}}{\partial \dot{x}} & \frac{\partial \dddot{x}}{\partial \ddot{x}} \end{bmatrix} \cdot \begin{Bmatrix} x \\ \dot{x} \\ \ddot{x} \end{Bmatrix} + \begin{bmatrix} 0 \\ 0 \\ w \end{bmatrix} \tag{126}$$

$$y = C(x)\cdot x + v = \begin{bmatrix} \frac{\partial x}{\partial x} & \frac{\partial x}{\partial \dot{x}} & \frac{\partial x}{\partial \ddot{x}} \end{bmatrix} \cdot \begin{Bmatrix} x \\ \dot{x} \\ \ddot{x} \end{Bmatrix} + v \tag{127}$$

The variables ẋ and ẍ are the first and second time derivatives of the feature vector x. The parameters u and y are the input vector and output vector, respectively. The matrices A (x) and C (x) are the Jacobian matrices used to linearize the nonlinear system and describe the system dynamics matrix and measurement matrix, respectively. The same assumptions for the process noise, process noise matrix, measurement noise and measurement noise matrix used with the KF hold true for the EKF. The exponential function is generally used as the nonlinear function that describes the state evolution equation as shown in equations (128) - (130). (Grewal, 2001) (Zarchan, 2000)

$$x = A \cdot e^{B\cdot t} \tag{128}$$

$$\dot{x} = B\cdot A\cdot e^{B\cdot t} = B\cdot x \tag{129}$$

$$\ddot{x} = B^2 \cdot A\cdot e^{B\cdot t} = B^2 \cdot x = B\cdot \dot{x} \tag{130}$$

Using the system model, the system dynamic and measurement matrix can be determined.

$$A(x) = \begin{bmatrix} \frac{\partial \dot{x}}{\partial x} & \frac{\partial \dot{x}}{\partial \dot{x}} & \frac{\partial \dot{x}}{\partial b} \\ \frac{\partial \ddot{x}}{\partial x} & \frac{\partial \ddot{x}}{\partial \dot{x}} & \frac{\partial \ddot{x}}{\partial b} \\ \frac{\partial \dot{b}}{\partial x} & \frac{\partial \dot{b}}{\partial \dot{x}} & \frac{\partial \dot{b}}{\partial b} \end{bmatrix} = \begin{bmatrix} B & 1 & x \\ B^2 & B & 2\cdot B\cdot x \\ 0 & 0 & 0 \end{bmatrix} \tag{131}$$

$$C(x)=\begin{bmatrix}\frac{\partial x}{\partial x} & \frac{\partial x}{\partial \dot{x}} & \frac{\partial x}{\partial \ddot{x}}\end{bmatrix}=\begin{bmatrix}1 & 0 & 0\end{bmatrix} \tag{132}$$

In order to discretize the continuous form of the EKF, the discrete fundamental matrix, $\Phi_k$, and discrete process noise matrix, $Q_k$, are determined from the system dynamics matrix as was previously done with the KF. (Grewal, 2001) (Zarchan, 2000)

$$\Phi(t)=e^{A(x)\cdot t}=I+A(x)\cdot t+\frac{(A(x)\cdot t)^2}{2!}+\ldots+\frac{(A(x)\cdot t)^n}{n!} \tag{133}$$

$$\Phi(t)=\left\{\begin{array}{l}\begin{bmatrix}B & 1 & x\\ B^2 & B & 2\cdot B\cdot x\\ 0 & 0 & 0\end{bmatrix}+\begin{bmatrix}B & 1 & x\\ B^2 & B & 2\cdot B\cdot x\\ 0 & 0 & 0\end{bmatrix}\cdot t\\ +\begin{bmatrix}B & 1 & x\\ B^2 & B & 2\cdot B\cdot x\\ 0 & 0 & 0\end{bmatrix}\cdot\frac{t^2}{2!}\end{array}\right\} \tag{134}$$

$$\Phi_k=\Phi(T_s)=\begin{bmatrix}B & 1 & x\\ B^2 & B & 2\cdot B\cdot x\\ 0 & 0 & 0\end{bmatrix}\cdot\left(\frac{1}{2}\cdot T_s^{\,2}+T_s+1\right) \tag{135}$$

The discrete process noise matrix:

$$Q=\begin{bmatrix}0 & 0 & 0\\ 0 & 0 & 0\\ 0 & 0 & \Phi_k\end{bmatrix} \tag{136}$$

$$Q_k=\int_0^{Ts}\left(\Phi(\tau)\cdot Q\cdot\Phi^T(\tau)\right)d\tau \tag{137}$$

The internal dynamics for the EKF has been modeled using Euler integration in order to produce projections of the feature vector.

$$\overline{x_k}=\hat{x}_k+T_s\cdot\overline{\dot{x}_{k-1}} \tag{138}$$

$$\bar{\dot{x}}_k = \hat{\dot{x}}_k + T_s \cdot \overline{\ddot{x}_{k-1}} \tag{139}$$

$$\bar{\ddot{x}}_k = \hat{\ddot{x}}_k \tag{140}$$

The discretized system dynamics matrix and process matrix are used with the Riccati equations as outlined in the previous section to determine the feature vectors. The Newton-Raphson method was used in conjunction with the state evolution equation from the EKF to determine the estimated time for the end of life ($t_{eol}$) of the feature vector (Lall P. W., 2012a).

$$f(t_k) = A \cdot e^{B \cdot t} - x(t_{eol}) \tag{141}$$

$$t_{k+1} = t_k - \frac{f(t_k)}{f`(t_k)} \tag{142}$$

In this work, the EKF has been used with the same feature vectors as the KF in order to determine the "best" algorithm to describe the degradation of the components. A simulation was not run using the EKF due to the large similarity with the KF.

### 3.4.3. PREDICTIVE MODELING

Since the adoption of EISA, the consumer lighting industry has largely shifted towards SSL devices. SSL devices have vastly different failure modes and mechanisms when compared to traditional lighting. Traditional lighting "burns-out" after the tungsten filament evaporates producing locations with smaller surface areas to radiate heat. This large temperature gradient in the thinner portion of the filament produces a large enough thermal stress that breaks the filament. Traditional lighting is also highly vulnerable to shock and vibration, as well as not susceptible to environmental conditions. Conversely, SSL lamps do not rely on thermal radiation to produce light. Instead, SSL uses the process of electroluminescence which eliminates the filament allowing for a higher survivability when exposed to shock and vibration. However, SSL lamps experience a whole host of failure modes not encountered by traditional lighting, such as phosphor degradation, short circuits or electrostatic discharge. TM28 does not account for any of these failure modes and only utilizes temperature dependent failure mechanisms. This makes the development of suitable generalized AFs for lifetime predictive modeling of SSL lamps that accounts for thermally driven and humidity based stresses essential in order to understand the long-term survivability of these devices.

#### 3.4.3.1. PECK'S MODEL

As previously mentioned, the lighting industry has adopted the TM28 projection standard that uses the Arrhenius relationship to develop acceleration techniques for SSL lamps as a function of temperature only. This does not account for other stresses that SSL devices potentially encounter. In order to introduce additional stresses with the Arrhenius relationship, the generalized Eyring relationship is used. (Nelson, 1990) (Ohring, 1998) (Viswanadham, 1998) (JEDEC, 2006)

$$t_f = A_0 \cdot T^{\alpha} \cdot \exp\left[\begin{array}{l} \dfrac{E_a}{k_b \cdot T} + (A_1 + \dfrac{A_2}{T}) \cdot S_1 + \cdots \\ + (A_{n-1} + \dfrac{A_n}{T}) \cdot S_{n-1} \end{array}\right] \tag{143}$$

The generalized Eyring relationship corrects stress and synergism issues with the Arrhenius model by allowing for the inclusion of additional stresses. This is the basis for the Arrhenius model, as well as corrosion models that include stresses due to moisture ingress. Most corrosion models utilize two additional stresses, a function of humidity and unknown function of voltage, to predict the time to failure. (Nelson, 1990) (Ohring, 1998) (Viswanadham, 1998) (JEDEC, 2006)

$$t_f = A_0 \cdot T^{\alpha} \cdot \exp\left( \begin{array}{l} \dfrac{E_a}{k_b \cdot T} + \dfrac{A_1 \cdot T + A_2}{T} \cdot f(RH) \\ + \dfrac{A_3 \cdot T + A_4}{T} \cdot f(V) \end{array} \right) \tag{144}$$

A well-known and highly used corrosion model is Peck's Power Law. Typically, the unknown-function of voltage is considered a constant with no impact on the time-to-failure predictions. This form is simply referred to as Peck's model. (Nelson, 1990) (JEDEC, 2006) (Hallberg, 1991) (Peck, 1986)

$$t_f = A_0 \cdot f(V) \cdot RH^{-N} \cdot \exp\left[ \frac{E_a}{k_b \cdot T} \right] \tag{145}$$

$$t_f = A_0 \cdot RH^{-N} \cdot \exp\left[ \frac{E_a}{k_b \cdot T} \right] \tag{146}$$

Peck's model was originally designed around failure due to electrolytic corrosion of aluminum interconnect metallization on epoxy molded encapsulants used in semiconductor devices (Hallberg, 1991) (Peck, 1986). Table 15 shows the various temperature & humidity conditions used to produce the unknown parameters that are highlighted at the bottom of the table. (Nelson, 1990) (JEDEC, 2006) (Hallberg, 1991) (Peck, 1986)

Table 15: Temperature-Humidity Conditions for Peck's Model Parameter Selection.

| **Temperature [°C]** | **Relative Humidity [%]** |
|---|---|
| 85 | 85 |
| 100 | 85 |
| 110 | 85 |
| 120 | 85 |
| 130 | 85 |
| 140 | 85 |
| 130 | 90 |
| **N** | **2.7** |
| **Ea [eV]** | **0.7-0.8** |

Peck's model with the parameters listed in Table 15 are widely used in industry for lifetime predictions of aluminum corrosion with a high degree of accuracy. Since SSL lamps potentially encounter different failure mechanisms than what Peck's original model was designed for, it becomes imperative to produce SSL lamp specific parameters for Peck's corrosion model. Additionally, the use of an unknown voltage function in Peck's Power Law may not fully characterize the failure mechanisms found in SSL lamps. Therefore, the assumptions in Peck's Power Law pertaining to f (V) were used to produce a generic additional stress function, f (Ψ), to account for the variety of stresses SSL lamps encounter. Peck's model and Peck's Power Law have been used in the form of AFs for the determination of the unknown SSL lamp specific parameters needed to produce generalized AFs for SSL lamps, where the subscripts "o" and "a" denote the operating condition and acceleration condition, respectively.

$$AF = \frac{(t_f)_o}{(t_f)_a} = \left(\frac{RH_o}{RH_a}\right)^{-N} \cdot \exp\left(\frac{E_a}{k_b} \cdot \left(\frac{1}{T_o} - \frac{1}{T_a}\right)\right) \cdot F(\Psi) \tag{147}$$

$$AF = \frac{(t_f)_o}{(t_f)_a} = \left(\frac{RH_o}{RH_a}\right)^{-N} \cdot \exp\left(\frac{E_a}{k_b} \cdot \left(\frac{1}{T_o} - \frac{1}{T_a}\right)\right) \tag{148}$$

The log-linear relationship of RLF and time used in the TM28 projection standard has been used to determine the rate of decay each lamp experiences at the different operating conditions. This relationship does not take into account the environmental conditions the SSL lamps experienced, but does give valuable information pertaining to luminous flux degradation as a function of time. Hence, the rate of decay from both environmental conditions is a suitable choice to determine SSL lamp specific AFs.

$$AF = \frac{(\alpha)_a}{(\alpha)_o} \tag{149}$$

The lamp specific AFs are used to determine the unknown parameters in Peck's model or Peck's Power Law in order to produce generalized AFs. This was accomplished through the use of the log-linear form of the AF equations and multiple linear regression.

$$\ln(AF) = -N \cdot \ln\left(\frac{RH_o}{RH_a}\right) + \left(\frac{E_a}{k_b} \cdot \left(\frac{1}{T_o} - \frac{1}{T_a}\right)\right) + F(\Psi) \tag{150}$$

$$\ln(AF) = N \cdot \ln\left(\frac{RH_o}{RH_a}\right) + \left(\frac{E_a}{k_b} \cdot \left(\frac{1}{T_o} - \frac{1}{T_a}\right)\right) \tag{151}$$

### 3.4.3.2. PRINCIPAL COMPONENTS REGRESSION

In order to solve for the unknown parameters in equations (150) and (151), a multivariate analysis was performed. Multiple linear regression methods assume the model's predictor variables to be linearly independent and the response variable to be linearly dependent on the predictor variables. Linear dependency produces numerical predictions that are erroneous due to multi-collinearity, instability and variability. Since each SSL lamp population consists of a variety of different parameters with repeated observations, the multivariate technique of principal component regression (PCR) has been applied to eliminate linear dependency. PCR is a multivariate technique that uses eigenvectors to transform a set of standardized dependent variables to a new set of linearly independent variables. The new orthogonal principal components are ranked in order of importance to decrease the number of variables needed to explain most of the variance in the model. This is accomplished by looking at the proportion of total variance explained by each principal component from a Scree plot of the eigenvalues. (Lall P. S., 2008e) (Fekedulegen, 2002) (Everitt, 1992) (Mukhopadhyay, 2009) (Kleinbaum, 1978) (Rawlings, 1988)

The predictor and response variables for all datasets are combined and placed in a linear form of a general regression model with a dataset span of “n-sets” with “j” predictor variables. (Lall P. S., 2008e) (Fekedulegen, 2002) (Everitt, 1992) (Mukhopadhyay, 2009) (Kleinbaum, 1978) (Rawlings, 1988)

$$y_i = b_0 + b_1 \cdot x_{i1} + b_2 \cdot x_{i2} + \ldots + b_j \cdot x_{ij} \tag{152}$$

For this work, the regression model consists of at least two predictor column vectors with additional column vectors added depending on which form of Peck’s model is used. Table 16 summarizes the predictor and response variables used with PCR.

Table 16: PCR Variables.

| **Model** | **y** | $\mathbf{X_1}$ | $\mathbf{X_2}$ | $\mathbf{X_{3:j}}$ |
|---|---|---|---|---|
| Peck’s Model | ln(AF) | $RH_o/RH_a$ | $1/T_o-1/T_a$ | N/A |
| Peck’s Power Law | ln(AF) | $RH_o/RH_a$ | $1/T_o-1/T_a$ | $F(\Psi)_{3:j}$ |

Since the collected data for each SSL lamp has been placed together as a response vector and predictor matrix, the experimental data must be centered and scaled in order to compare the different studies properly, as well as to obtain the proper form of the regression equation. Centering and scaling requires the mean and standard deviation of each column vector from the predictor matrix. (Lall P. S., 2008e) (Fekedulegen, 2002) (Everitt, 1992) (Mukhopadhyay, 2009) (Kleinbaum, 1978) (Rawlings, 1988)

$$x_{ij}^* = \frac{x_{ij} - \mu_j}{\sigma_j} \tag{153}$$

The regression equation can now transformed using equations (152) and (153) into the final matrix form in equation (157).

$$y_i - \bar{y} = \left\{ \begin{array}{l} b_1 \cdot \left[ \dfrac{x_{i1} - \mu_1}{\sigma_1} \right] + b_2 \cdot \left[ \dfrac{x_{i2} - \mu_2}{\sigma_2} \right] + \\ \ldots + b_j \cdot \left[ \dfrac{x_{ij} - \mu_j}{\sigma_j} \right] \end{array} \right\} \tag{154}$$

$$y_i = \left\{ \begin{array}{l} \left[ \bar{y} - \left[ \dfrac{b_1}{\sigma_1} + \dfrac{b_2}{\sigma_2} + \ldots + \dfrac{b_j}{\sigma_j} \right] \right] + b_1^* \cdot x_{i1}^* \\ + b_2^* \cdot x_{i2}^* + \ldots + b_j^* \cdot x_{ij}^* \end{array} \right\} \tag{155}$$

$$y_i = 1 \cdot b_0^* + b_1^* \cdot x_{i1}^* + b_2^* \cdot x_{i2}^* + \ldots + b_j^* \cdot x_{ij}^* \tag{156}$$

$$\{y\} = \{1\} \cdot b_0^* + \left[ X^* \right] \cdot \left\{ b^* \right\} \tag{157}$$

The transformed set of predictor vectors are now a set of orthogonal, uncorrelated vectors. The j x j correlation matrix, C, gives a measure of the linear relationship between the variables with the coefficients residing between -1 to 1. Large positive and negative values indicate highly correlated variables. (Everitt, 1992)

$$[C] = [X^*]^T \cdot [X^*] \tag{158}$$

The correlation matrix eigenvalues, λ, and eigenvectors, V, are determined in rank order.

$$\left| [C] - \lambda \cdot [I] \right| \cdot \vec{V} = 0 \tag{159}$$

With the orthogonal eigenvectors solved, the standardized predictor matrix in equation (157) can be transformed into principal components. (Lall P. S., 2008e) (Fekedulegen, 2002) (Everitt, 1992) (Mukhopadhyay, 2009) (Kleinbaum, 1978) (Rawlings, 1988)

$$\{y\} = \{1\} \cdot b_0^* + [X^*] \cdot [I] \cdot \{b^*\} \tag{160}$$

$$\{y\} = \{1\} \cdot b_0^* + [X^*] \cdot [V] \cdot [V]^T \cdot \{b^*\} \tag{161}$$

$$\{y\} = \{1\} \cdot b_0^* + \left\langle [X^*] \cdot [V] \right\rangle \cdot \left\langle [V]^T \cdot \{b^*\} \right\rangle \tag{162}$$

$$\{y\} = \{1\} \cdot b_0^* + [Z] \cdot \{a\} \tag{163}$$

From equation (163), [Z] is an (i x j) matrix of principal components and {a} is column vector of new regression coefficients. Principal components associated with small eigenvalues are eliminated due to the insignificant impact on the total variance of the predictions. The approach used to eliminate principal components investigated the cumulative percentage contribution of the eigenvalues. Variables are selected based off the largest eigenvalues, “r” contributors, until a pre-selected percentage contribution is obtained. The remaining principal components are used to determine the regression coefficients {a} using a multiple linear regression technique.

$$\{a\} = \left[[Z]^T \cdot [Z]\right]^{-1} \cdot [Z]^T \cdot \{y\} \tag{164}$$

After the regression coefficients are solved, the values are transformed back into the natural variables from equation (152).

$$\{b\} = [V] \cdot \{a\} \tag{165}$$

$$b_0 = \bar{y} - \left[ \frac{b_1}{\sigma_1} + \frac{b_2}{\sigma_2} + \ldots + \frac{b_j}{\sigma_j} \right] \tag{166}$$

# 4. Experimental Results & Analysis

This culmination of the results illustrate the lack of accuracy and precision in lumen maintenance life estimations obtained using TM28. This chapter will detail the findings of this research in three different sections: SSL Lamps, SSL Electrical Drivers, and SSL Electrical Connectors.

## 4.1. SSL LAMPS

### 4.1.1. ACCELERATED LIFE TESTING COMPARISON

Some principal issues with TM28 is the lack of additional stresses or parameters needed to characterize non-temperature dependent failure mechanisms, as well as the lack of accelerated testing condition needed for reliability testing. To demonstrate these issues, multiple SSL lamp groups have undergone different ALT conditions with a temperature condition of 85°C held constant between the groups. In this case, the TM28 projection standard does not work due to the large ambient temperature. Also, this analysis illustrates the need for a model other than the Arrhenius equation, used with TM28, to properly characterize the failure modes of each SSL lamp group due to the contribution of other stresses, such as humidity and power.

Five sampling periods of 168 hours for a total of 840 hours or five weeks of accelerated aging was conducted for each ALT condition. The relative luminous flux, relative CCT, relative yellow-to-blue ratio and the u`-v` chromaticity shift for groups

85CG1 (85°C/85%), 85CG2 (85°C) and 85CG3 (85°C/85%/Bias) are shown in Figure 49 - Figure 52.

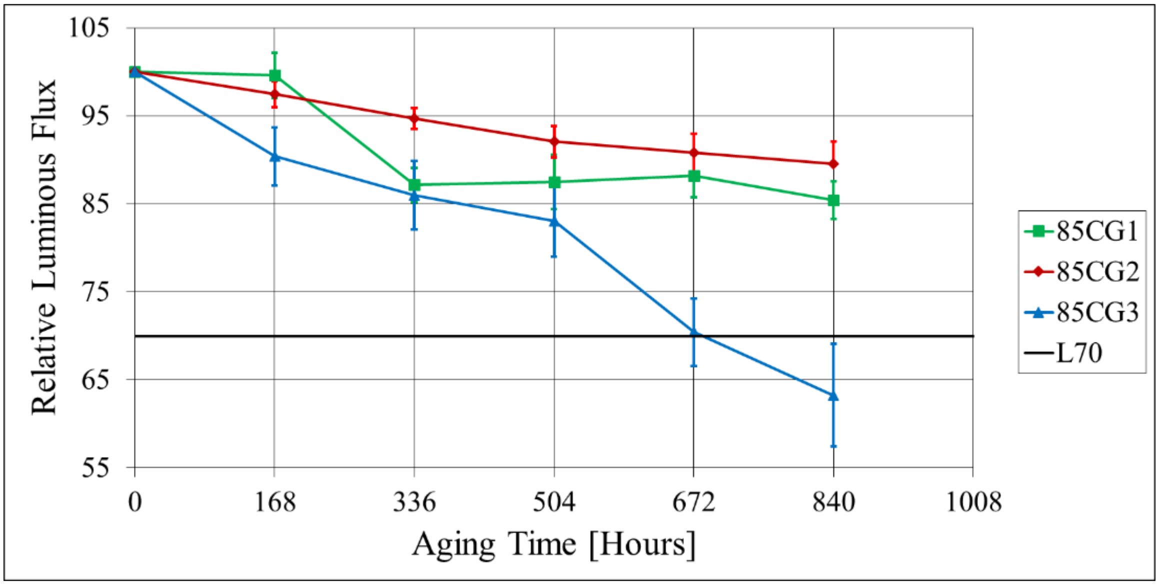


Figure 49: The Relative Luminous Flux Comparison of Groups 85CG1 (85°C/85%), 85CG2 (85°C) and 85CG3 (85°C/85%/Bias).

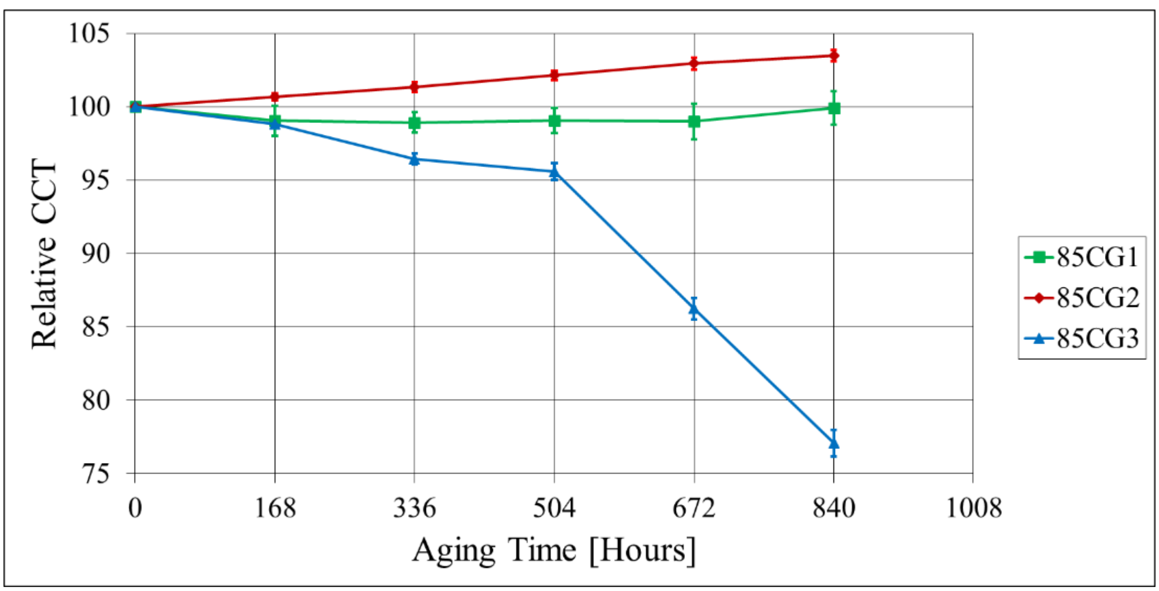


Figure 50: The Relative CCT Comparison of Groups 85CG1 (85°C/85%), 85CG2 (85°C) and 85CG3 (85°C/85%/Bias).

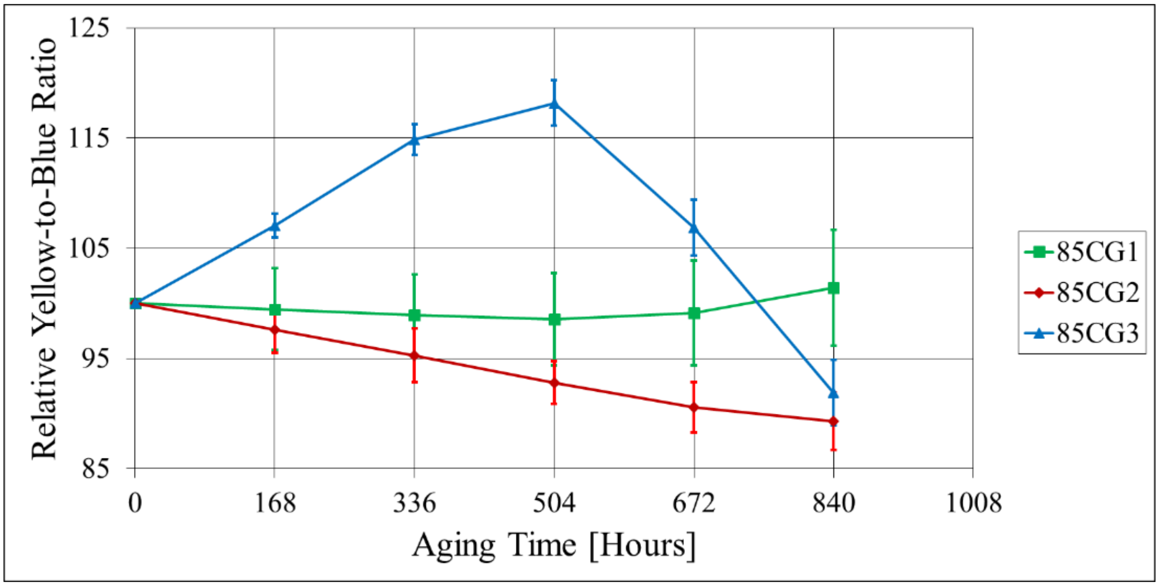


Figure 51: The Relative Yellow-to-Blue Ratio Comparison of Groups 85CG1 (85°C/85%), 85CG2 (85°C) and 85CG3 (85°C/85%/Bias).

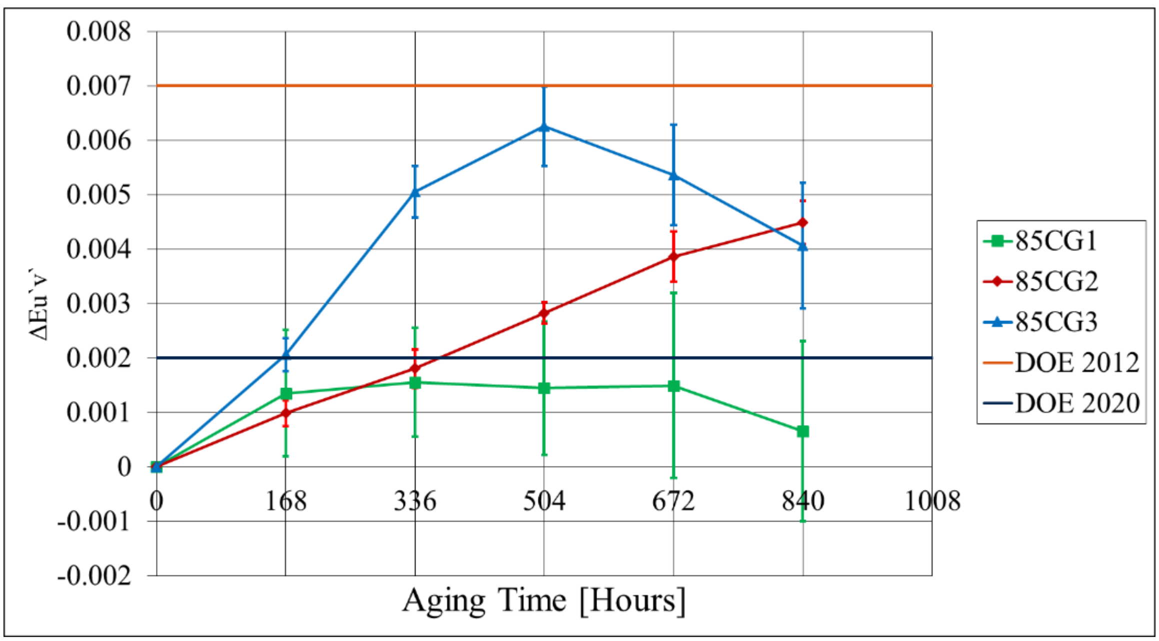


Figure 52: The u`-v` Chromaticity Shift Comparison of Groups 85CG1 (85°C/85%), 85CG2 (85°C) and 85CG3 (85°C/85%/Bias).

From Figure 49, 85CG2, which was only exposed to the temperature condition, experienced the least amount of degradation viewed in terms of RLF as used with TM28.

Additionally, a linear degradation trend is observed with 85CG2 compared to 85CG1 and 85CG3 illustrating less variance between RLF measurements. 85CG1, which included the humidity condition, produced a similar reduction in RLF as 85CG2, but began to exhibit an accelerated degradation rate towards the last sampling period compared to that of 85CG2 with a similar standard deviation. When an electrical bias is applied in addition to the humidity, as is the case with 85CG3, the rate of degradation greatly surpasses both 85CG1 and 85CG2 with an increasing amount of standard deviation as shown with the error bars. 85CG3 crossed the failure criteria of 70% at 672 hours of aging while 85CG1 and 85CG2 reached an RLF of 89.52% and 85.42%, respectively, at 840 hours of aging.

Figure 50 shows a similar degradation pattern as RLF with 85CG1 and 85CG2 both experiencing little to no reduction in relative CCT while 85CG3 demonstrated a reduction of 20% with the inclusion of an electrical bias. The standard deviation for 85CG1 is highest with 85CG2 as the lowest. The relative yellow-to-blue ratio in Figure 51 is inadequate at determining which ALT condition was more detrimental to the SSL lamps. From Figure 52, the u`-v` chromaticity shift for 85CG3 shows a larger non-uniform increase in the color shift before decreasing to a chromaticity shift that was lower at 840 hours than that of 85CG2. 85CG2 shows the least amount of variation after investigating the standard deviation, while 85CG1 & 85CG3 are an order of magnitude larger. As previously observed in Figure 49, the chromaticity shift of 85CG2 was linear showing a more uniform drift in the color coordinates.

From this analysis, it has been demonstrated that the addition of humidity and an electrical bias will have a large effect on the degradation of SSL lamps. To continue forward with this study, three groups of SSL lamps, SSLG1, SSLG2, and SSLG3, have undergone steady-state temperature humidity bias accelerated testing with different temperature/humidity combinations and an identical electrical bias.

### 4.1.2. Generalized Acceleration Factor Model

The results in the previous section illustrates the detrimental effects of applying humidity and an electrical bias to SSL lamps in terms of RLF reduction. This leads to an inherent problem with the choice of the Arrhenius model for acceleration factor determination. Additional parameters should be accounted for instead of only considering temperature induced failure mechanisms and modes. Also, the inability to account for additional stresses and accelerated operating temperatures limits TM28's ability to accurately compare SSL devices under different operating conditions.

To further investigate a generalized acceleration factor model, the RLF of the lamps from groups SSLG1 (85/85), SSLG2 (55/65) and SSLG3 (25/45) were used with the methods outlined in TM28 for the determination of SSL lamp specific decay rates to produce AFs, as well as determine the L70 at each ALT condition for a failure threshold of 30% reduction in RLF. All of the SSL lamps from SSLG1 surpassed the failure threshold and ultimately failed catastrophically. The last operational SSL lamp for CHWW, CWW and PWW failed at 1008 hours, 2016 hours and 1512 hours, respectively. All of the SSL lamps from SSLG2 and SSLG3 never crossed the failure threshold after 2520 hours and 10000 hours, respectively. However, two lamps from SSLG3, CCW and CWW, experienced complete failure at normal operating conditions prior to the next measurement period at 5000 hours and 4000 hours, respectively. The RLF for the SSL lamps from each group can be seen in Figure 53 - Figure 58.

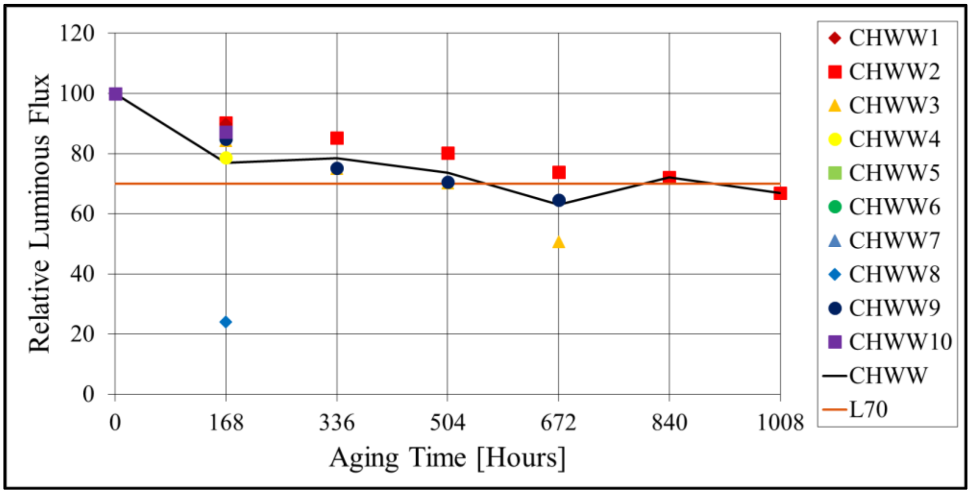


Figure 53: SSLG1 – RLF of CHWW at 85°C/85%.

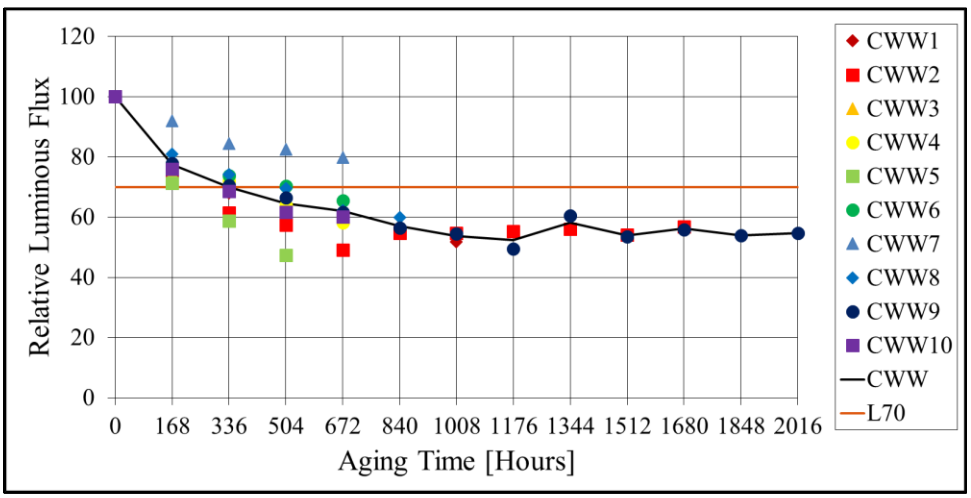


Figure 54: SSLG1 – RLF of CWW at 85°C/85%.

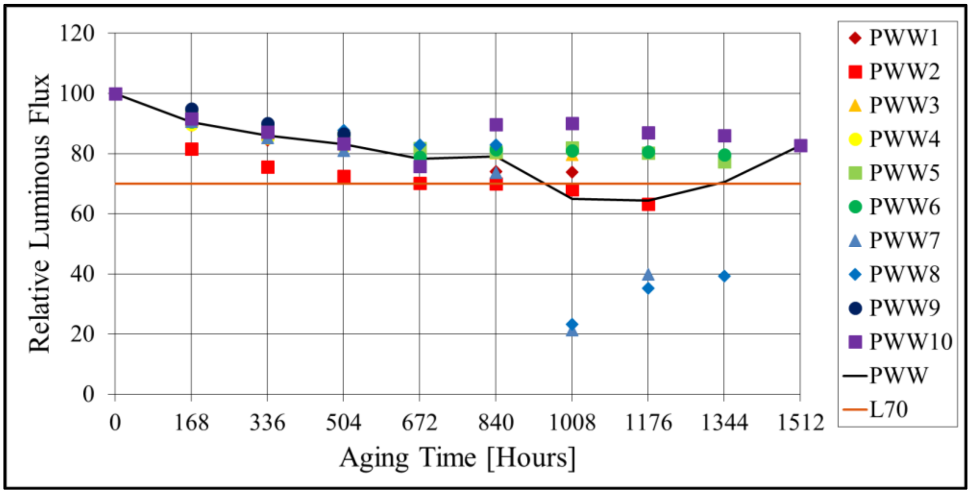


Figure 55: SSLG1 – RLF of PWW at 85°C/85%.

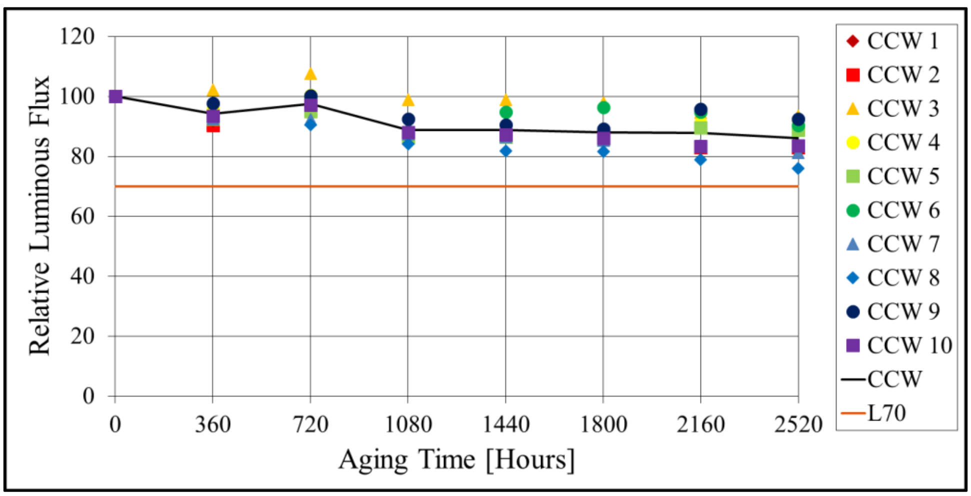


Figure 56: SSLG2 – RLF of CCW at 55°C/65%.

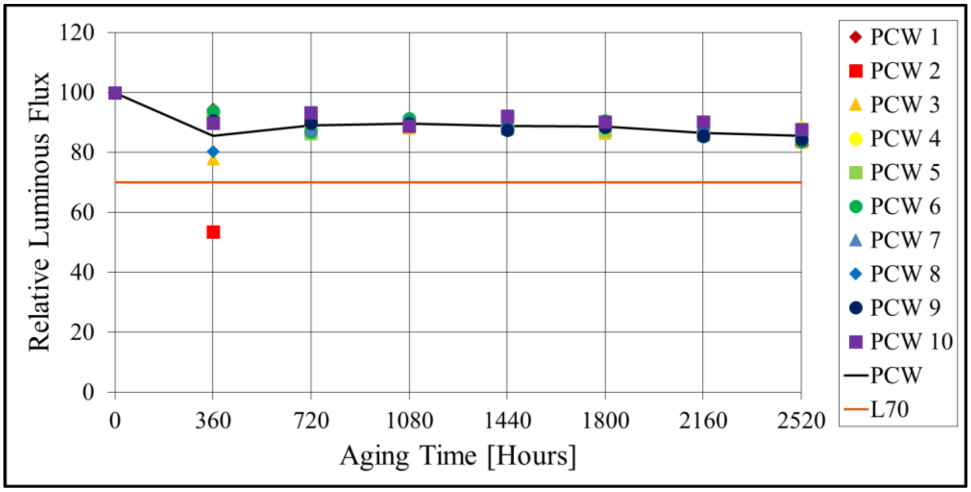


Figure 57: SSLG2 – RLF of PCW at 55°C/65%.

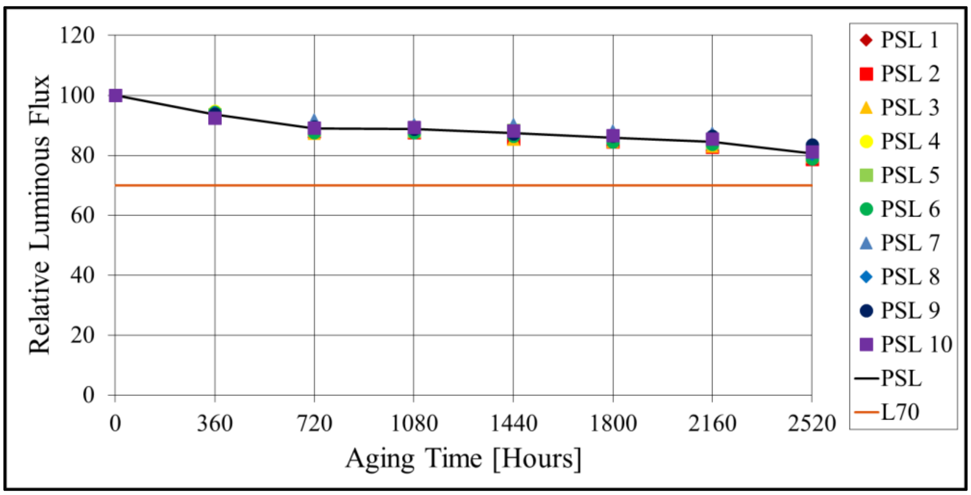


Figure 58: SSLG2 – RLF of PSL at 55°C/65%.

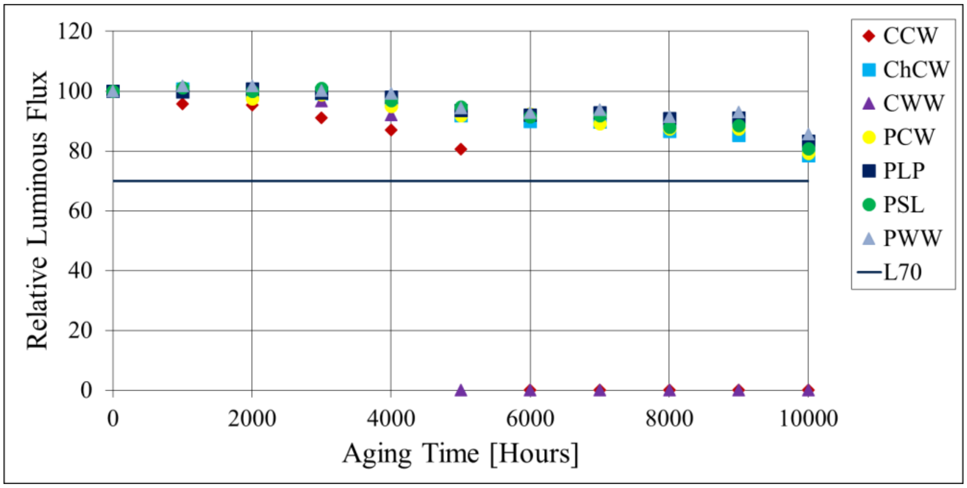


Figure 59: SSLG3 RLF at 25°C/45%.

The log-linear relationship between RLF, in the form of percentage, and time in hours has been used to determine each SSL lamp dependent decay rate as shown in Figure 60 - Figure 66. This is the same method put forth with TM28 and does not require knowledge of the ALT conditions each SSL lamp experienced.

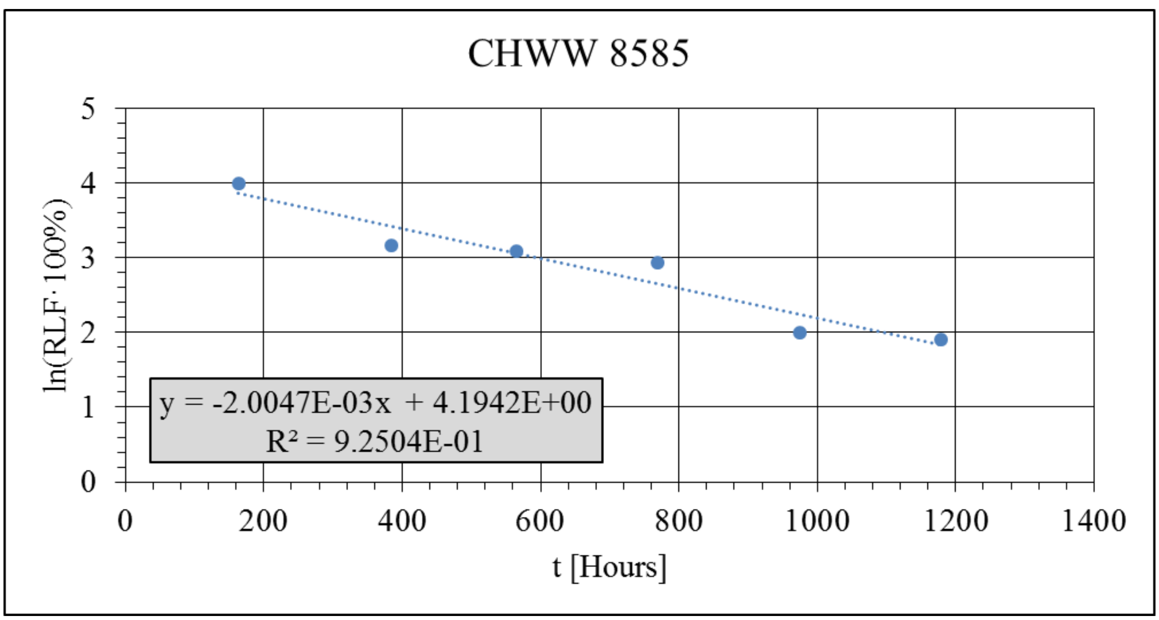


Figure 60: SSLG1 – Log-Linear Curvefit of CHWW.

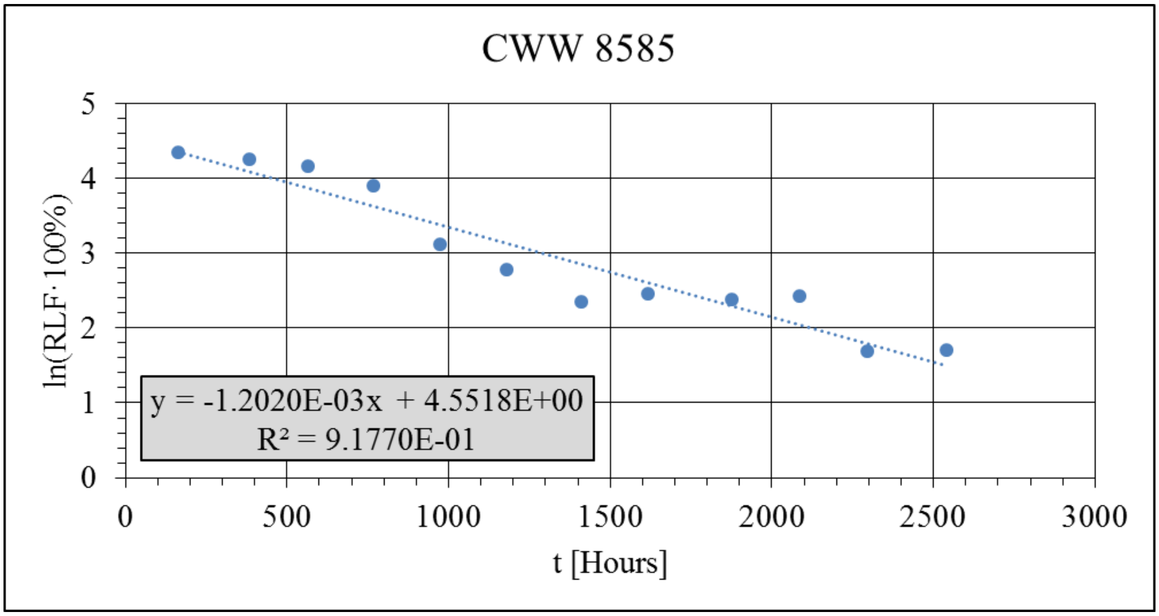


Figure 61: SSLG1 – Log-Linear Curvefit of CWW.

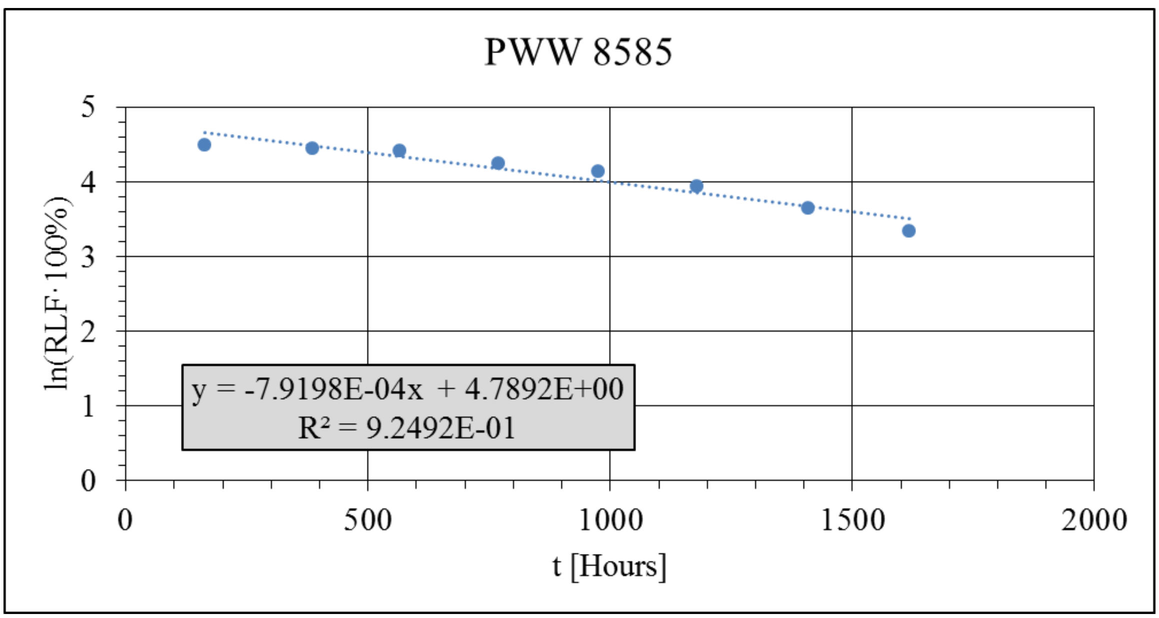


Figure 62: Log-Linear Curvefit of PWW.

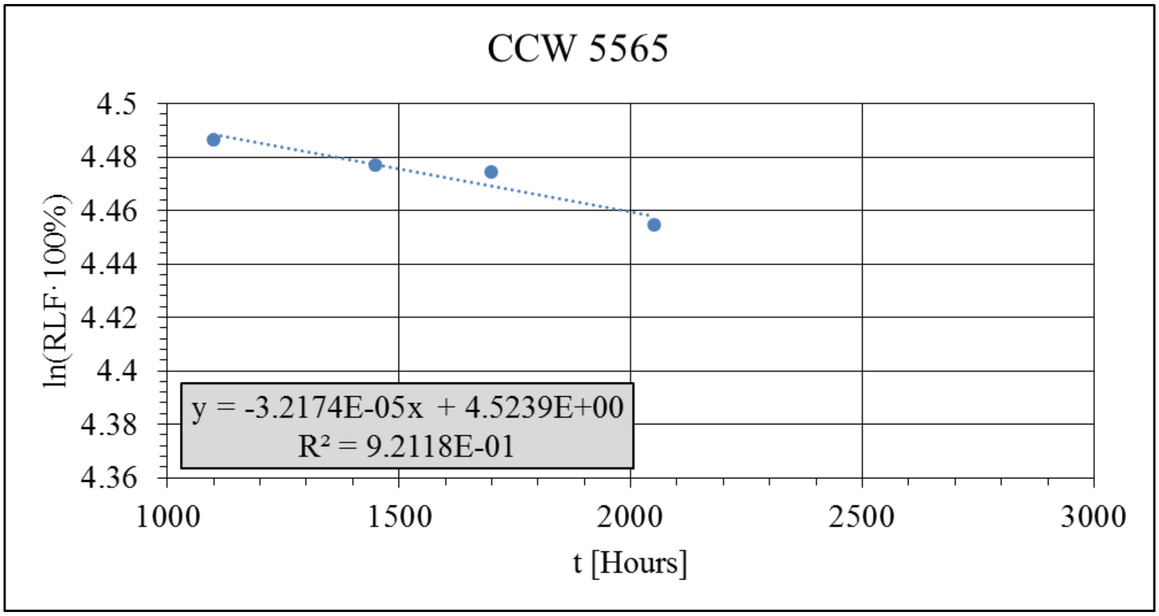


Figure 63: SSLG2 – Log-Linear Curvefit of CCW.

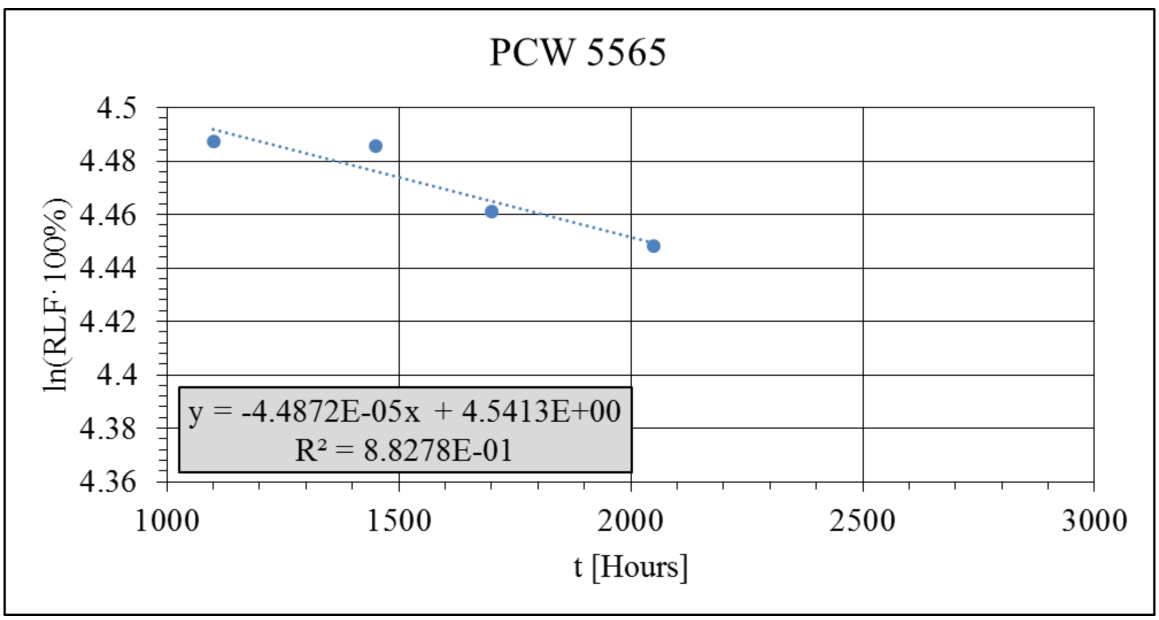


Figure 64: SSLG2 – Log-Linear Curvefit of PCW.

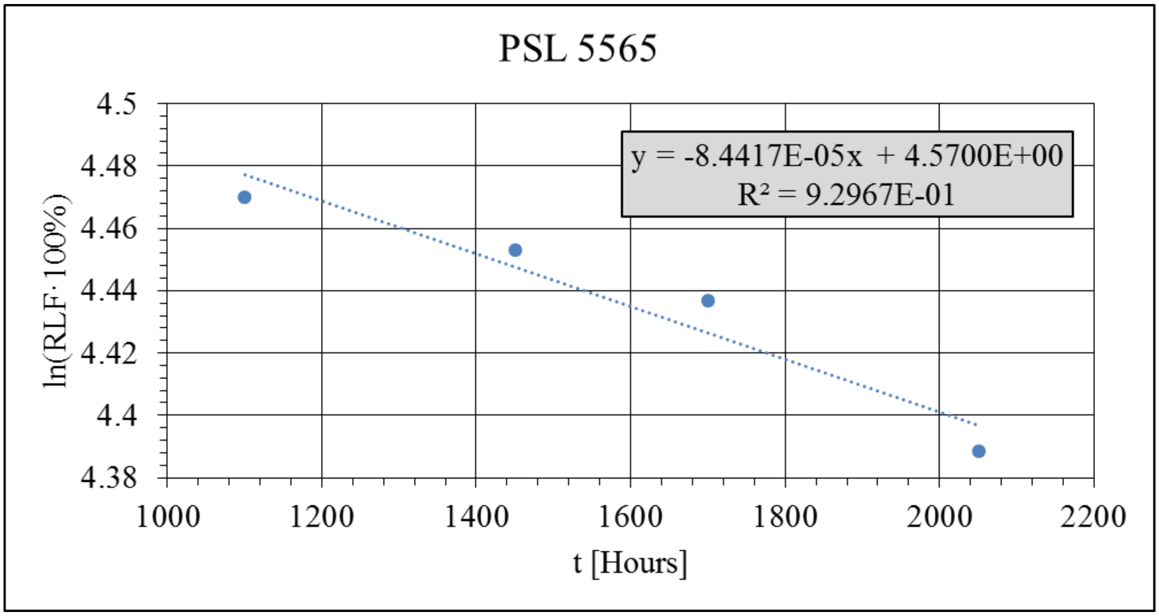


Figure 65: SSLG2 – Log-Linear Curvefit of PSL.

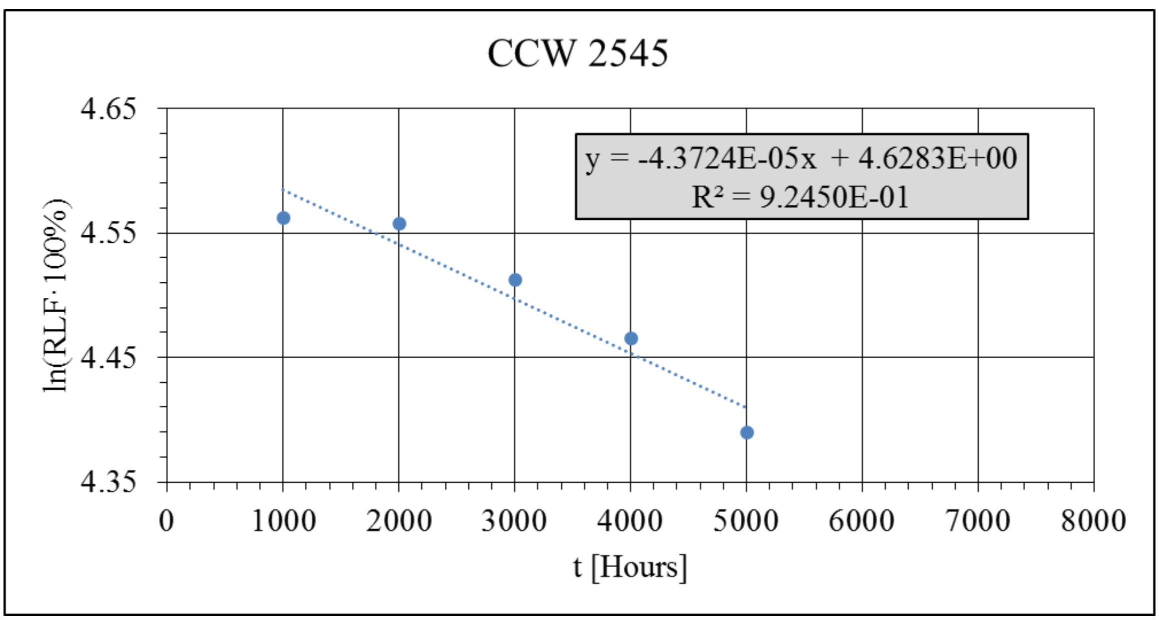


Figure 66: SSLG3 – Log-Linear Curvefit of CCW.

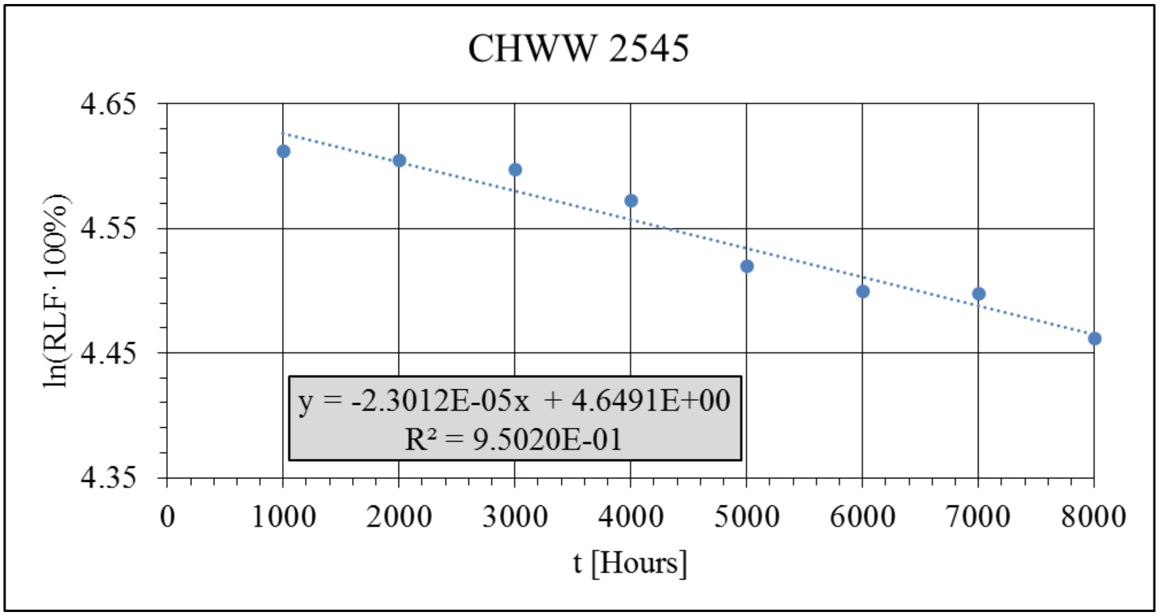


Figure 67: SSLG3 – Log-Linear Curvefit of CHWW.

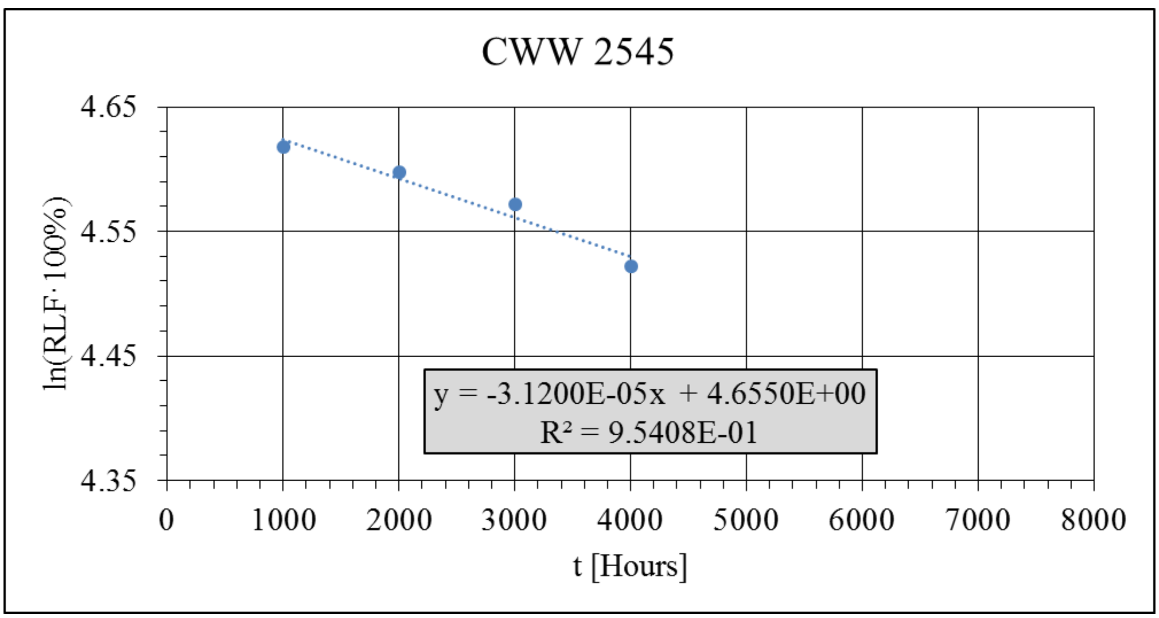


Figure 68: SSLG3 – Log-Linear Curvefit of CWW.

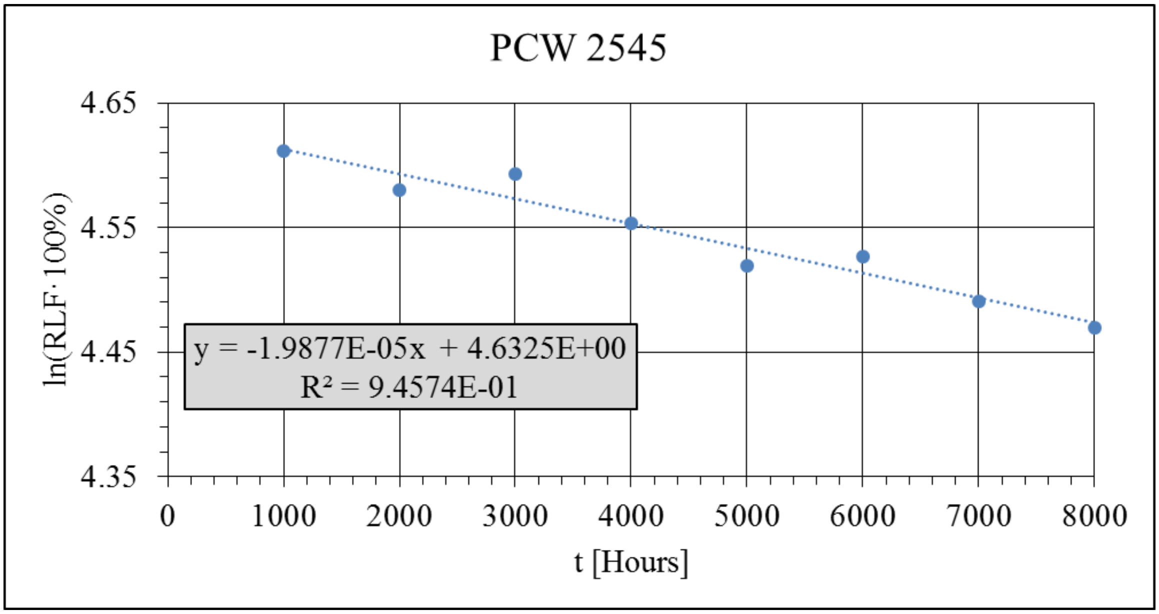


Figure 69: SSLG3 – Log-Linear Curvefit of PCW.

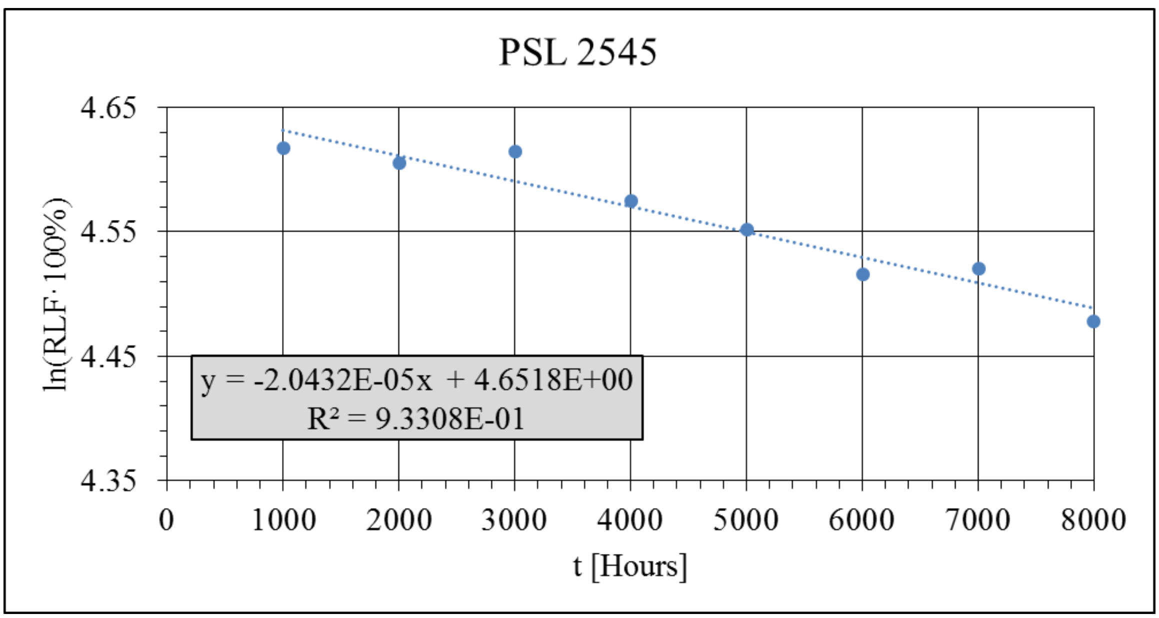


Figure 70: SSLG3 – Log-Linear Curvefit of PSL.

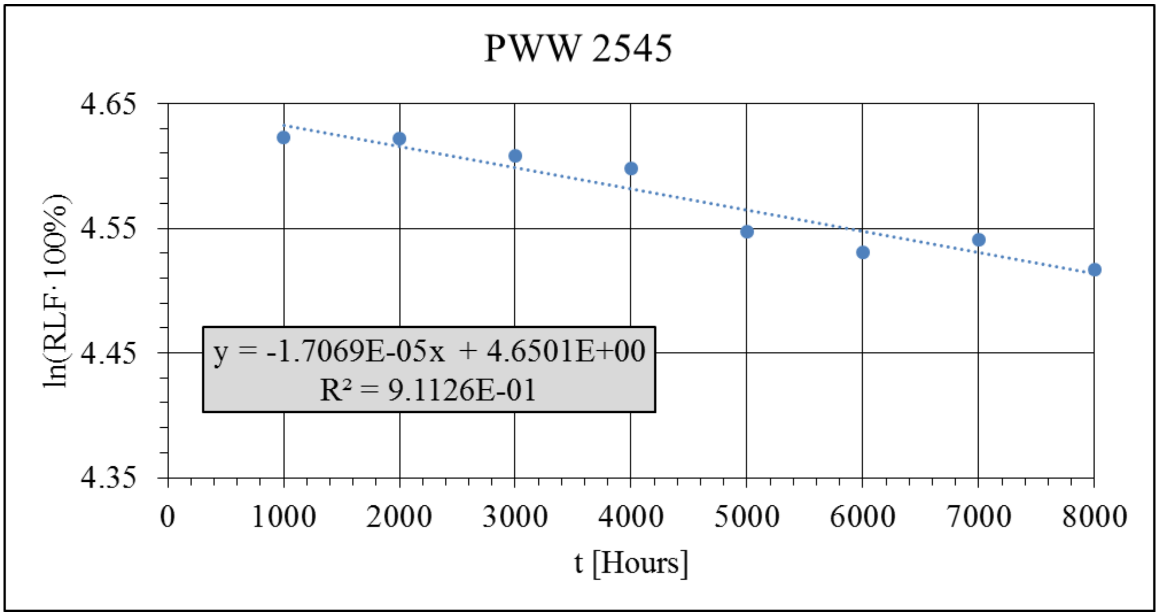


Figure 71: SSLG3 – Log-Linear Curvefit of PWW.

The log-linear plots give valuable information regarding the rate of degradation for each SSL lamp in terms of relative luminous flux with the decay rate and the natural log form of the projected initial constant listed in Table 17.

Table 17: Summary of the SSL Lamp Log-Linear Curvefit.

| **Parameter** | **CCW** | **CHWW** | **CWW** | **PCW** | **PSL** | **PWW** |
|---|---|---|---|---|---|---|
| T1°C/%RH1 | 25/45 | 25/45 | 25/45 | 25/45 | 25/45 | 25/45 |
| α1 | -4.37E-05 | -2.30E-05 | -3.12E-05 | -1.98E-05 | -2.04E-05 | -1.71E-05 |
| ln(β1) | 4.6283 | 4.6491 | 4.655 | 4.6325 | 4.6518 | 4.6501 |
| T2°C/%RH2 | 55/65 | 85/85 | 85/85 | 55/65 | 55/65 | 85/85 |
| α2 | -3.22E-05 | -2.00E-03 | -1.20E-03 | -4.49E-05 | -8.44E-05 | -7.92E-04 |
| ln(β2) | 4.5239 | 4.1942 | 4.5518 | 4.5413 | 4.57 | 4.7892 |

Using the SSL lamp specific decay rates and the projected initial constants, the lumen maintenance life was determined for the SSL lamps in each group similarly to what is outlined in TM28 for normal operating conditions. The L70 values for the SSL lamps from SSLG1 have been found experimentally, while the L70 values for the SSL lamps in

SSLG2 and SSLG3 are still unknown. Table 18 summarizes the lumen maintenance life values in hours for the SSL lamps from each group based of the method in TM28. This is an extension of the TM28 standard and has been completed to demonstrate the deficiencies with using the Arrhenius model for lifetime calculations.

Table 18: Experimental and Estimated Lumen Maintenance Life [Hrs.].

| **Group** | **CCW** | **CHWW** | **CWW** | **PCW** | **PSL** | **PWW** |
|---|---|---|---|---|---|---|
| SSLG1 Estimate | N/A | -27.08 | 252.33 | N/A | N/A | 682.73 |
| SSLG1 Actual | N/A | 106.11 | 385.36 | N/A | N/A | 780.7 |
| SSLG2 Estimate | 8560 | N/A | N/A | 6525 | 3809 | N/A |
| SSLG2 Actual | N/A | N/A | N/A | N/A | N/A | N/A |
| SSLG3 | 8686 | 17409 | 13029 | 19319 | 19739 | 23528 |
| SSLG3 Actual | N/A | N/A | N/A | N/A | N/A | N/A |

From Table 18, a few important observations were made. First, the L70 estimation for CCW from groups SSLG2 and SSLG3 are almost identical even though these groups had a temperature difference of 30°C and humidity difference of 20% RH. This is attributed to the premature failure of CCW in group SSLG3 which was at the normal operating condition. Second, using the Arrhenius equation, like TM28, produced a negative L70 value for CHWW in group SSLG1 and is attributed to the fact that 40% of the lamps failed before the first sample period of 168 hours. Last, the estimated L70 for lamps CWW and PWW from group SSLG1 differed from the actual L70 by 35.52% and 12.55%, respectively. From the L70 analysis, it is apparent that the use of the Arrhenius equation lacks the ability to accurately and precisely predict lumen maintenance life when compared to actual L70 values found experimentally.

The SSL lamp specific AFs were determined by dividing the reaction rate of the accelerated condition, $\alpha 2$, by the reaction rate of the operational condition, $\alpha 1$, as shown in

Table 19, where the values in "blue" and "red" are from the ALT conditions of 55°C/65% and 85°C/85%, respectively. The reasoning for using AFs is twofold. First, the use of AFs incorporates the degradation of the relative luminous flux as a function of time. Second, this removes the "time dependency" of the model. This allows for the use of regression techniques to predict AFs that do not have to account for the variations in time.

Table 19: The SSL Lamp Specific AFs.

| **Lamp** | **α2/α1** |
|---|---|
| CCW | 0.7358 |
| PCW | 2.2575 |
| PSL | 4.1316 |
| CHWW | 87.1154 |
| CWW | 38.5256 |
| PWW | 46.3987 |

The AFs for CCW, PCW and PSL range from 0.7358 – 4.1316 at the ALT condition of 55°C/65% and the AFs for CHWW, CWW and PWW range from 38.5256 – 87.1154 at the ALT condition of 85°C/85%. Each SSL lamp specific AF, which was determined from the log-linear relationship of RLF and time, has been used with the simplest form of Peck's equation to investigate the possibility of a generalized AF model that uses temperature and humidity as the only stresses. The log-linear form of Peck's model from equation (151), along with Principal Component Regression (PCR) has been used to determine the unknown parameters in Peck's model. Table 20 list the values used with the log-linear form of Peck's model and PCR to determine the unknown SSL specific Peck's model parameters.

Table 20: The Input Values of Peck's Model.

| Lamp | RHa | Ta [K] | RHo | To [K] | AF | RHo/RHa | 1/To - 1/Ta |
|---|---|---|---|---|---|---|---|
| CCW | 65 | 328.15 | 45 | 298.15 | 0.74 | 0.6923 | 3.06E-4 |
| PCW | 65 | 328.15 | 45 | 298.15 | 2.26 | 0.6923 | 3.06E-4 |
| PSL | 65 | 328.15 | 45 | 298.15 | 4.13 | 0.6923 | 3.06E-4 |
| CHWW | 85 | 358.15 | 45 | 298.15 | 87.12 | 0.5294 | 5.62E-4 |
| CWW | 85 | 358.15 | 45 | 298.15 | 38.53 | 0.5294 | 5.62E-4 |
| PWW | 85 | 358.15 | 45 | 298.15 | 46.40 | 0.5294 | 5.62E-4 |

Table 21 lists the SSL lamp specific parameters determined for Peck's model using PCR. The AFs from Peck's model are in the range of the SSL lamp specific AFs and the linear comparison between the natural log form of the predicted AF from Peck's model and the actual SSL specific AF produces a linear curve-fit with an $R^2$ value of 0.90, as shown in Figure 72. However, this does not mean success in the development of a generalized AF model. Upon a closer look, it was observed that the AFs from Peck's model for 55°C/65% produced a percentage error between the actual and estimated AF in the range of 19% to 117%. Likewise, the percentage error between the actual and estimated AF for 85°C/85% was in the range of 13% to 42%. Therefore, the simplest form of Peck's model does not accurately produce generalized AFs suitable for each SSL lamp in this study.

Table 21: The SSL Lamp Specific AFs.

| Peck's Parameters | α2/α1 |
|---|---|
| Ea [eV] | 0.59 |
| -N | -6.48 |
| $AF_p$ (55°C/65%) | 1.90 |
| $AF_p$ (85°C/85%) | 61.56 |

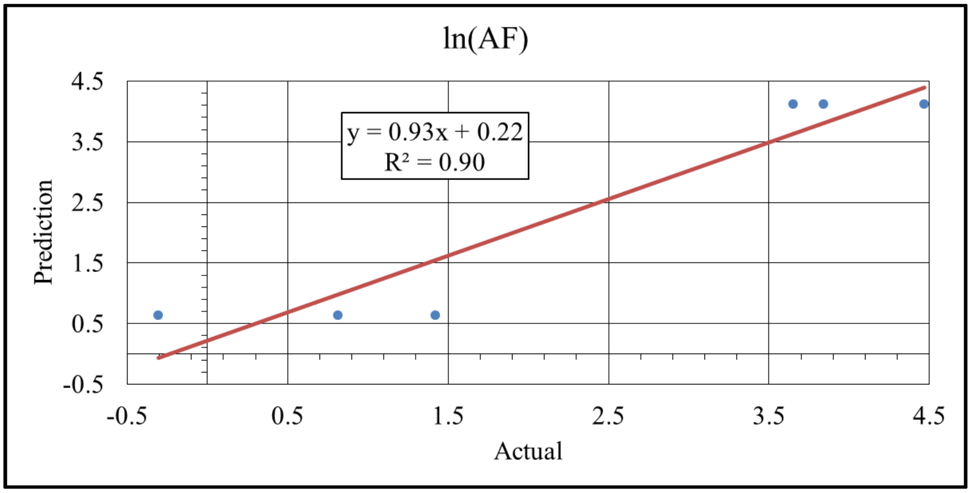


Figure 72: Self-Validation of Peck's Model.

Since Peck's model did not work properly, Peck's Power Law was used to determine a suitable generalized AF model. In order to properly determine additional unknown stresses to accurately characterize the SSL lamps in terms of AFs, some of the colorimetric quantities discussed in chapter three were investigated for possible inclusion into the AF model as part of the function f (Ψ). The colorimetric quantities used in the development of the AF model are the relative values of X, Y, Z, R9, R10, R11, R12, and yb.

The X, Y and Z tristimulus values were included in the model since these values correspond to the band-pass filtered chromaticity response of the three cones in the human eye and allows for the chromaticity coordinates of a perceived hue or color to be shown as a simple locus on a 2-D unit plane (CREE, 2013). The tristimulus values are the fundamental parameters needed to quantify the perceived color and are used with most colorimetric calculations.

The CRI values of R9, R10, R11, and R12, correspond to saturated solids of a strong red, strong yellow, strong green and strong blue, respectively. These values were included to account for the importance each color represents in the illumination process of LEDs. These values describe a test source's color rendering capabilities of properly illuminating an object (Schubert, 2006).

The yellow-to-blue ratio was selected because this value gives information pertaining to the type of SSL lamp under test and the degradation characteristics of the phosphor (yellow peak) and the LED (blue peak), such as a shift in the peak values or a reduction in their magnitude.

The colorimetric values for each lamp used in this analysis are graphically depicted in Figure 73 through Figure 120. The function f (Ψ) in this version of Peck's Power Law also included the manufacturer rated parameters of power, power factor, length, diameter, weight and efficacy to aid in the delineation between the SSL lamps and are listed in Table 22. Additionally, the entire dataset for PWW from SSLG1 was withheld from this analysis in order to cross-validate the results of the generalized AF model.

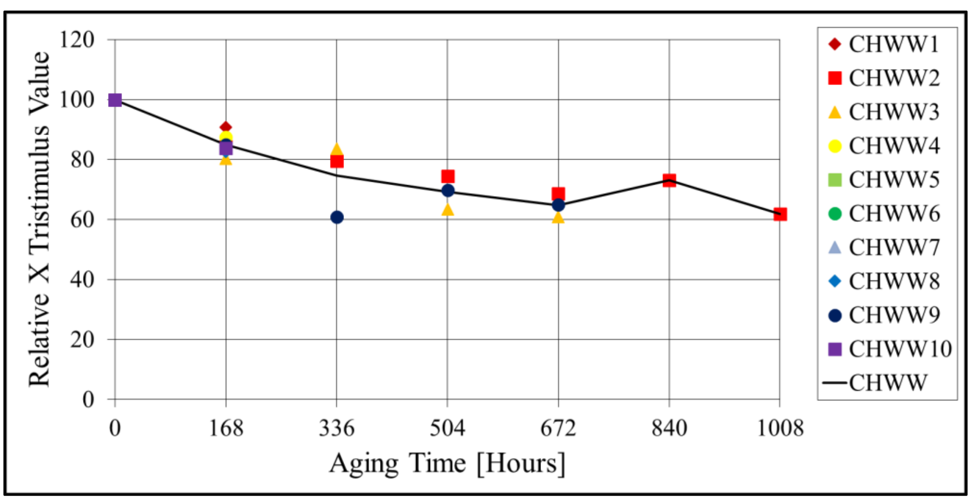


Figure 73: SSLG1 – Relative X Tristimulus Value of CHWW at 85°C/85%.

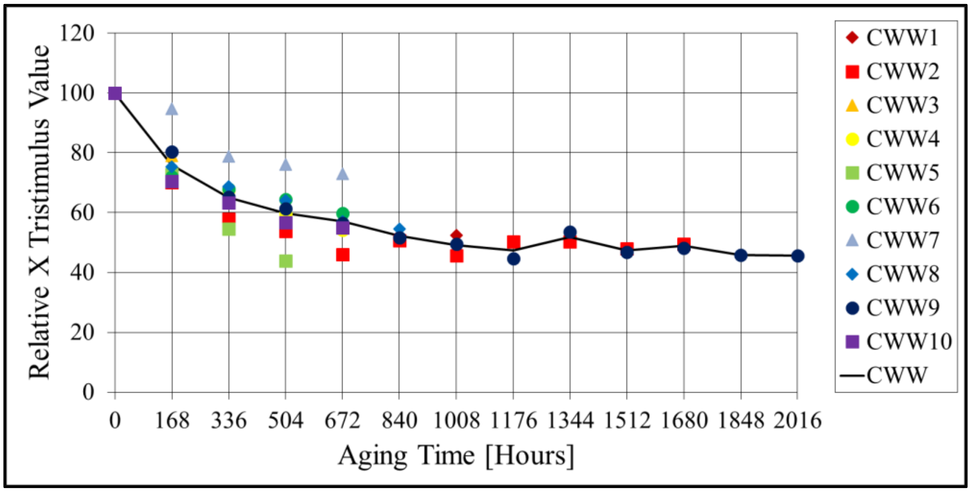


Figure 74: SSLG1 – Relative X Tristimulus Value of CWW at 85°C/85%.

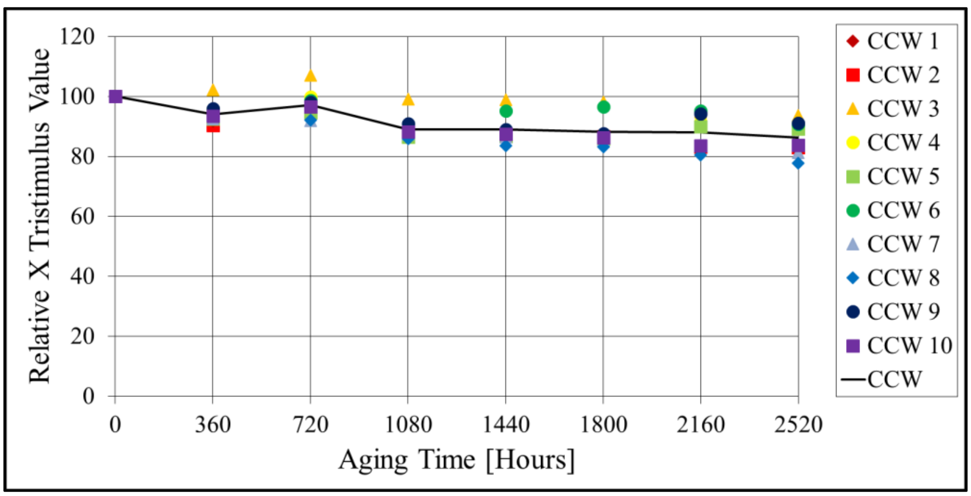


Figure 75: SSLG2 – Relative X Tristimulus Value of CCW at 55°C/65%.

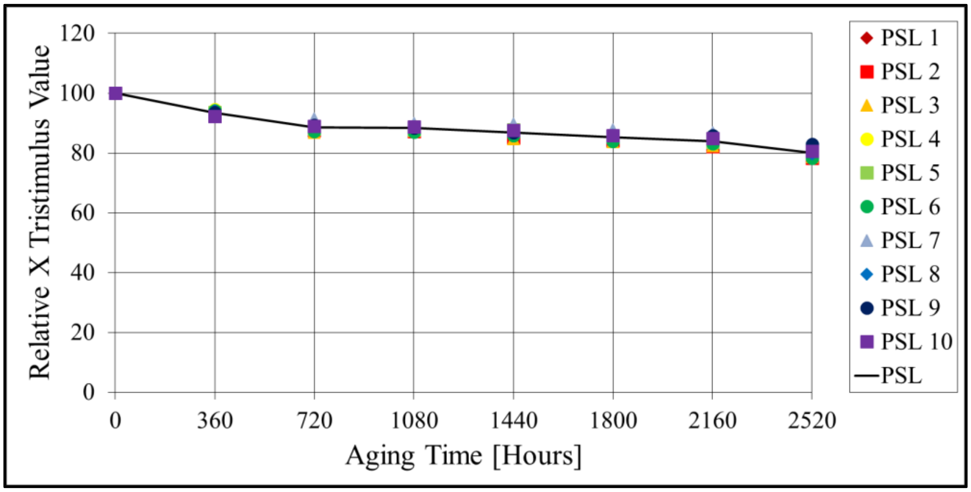


Figure 76: SSLG2 – Relative X Tristimulus Value of PSL at 55°C/65%.

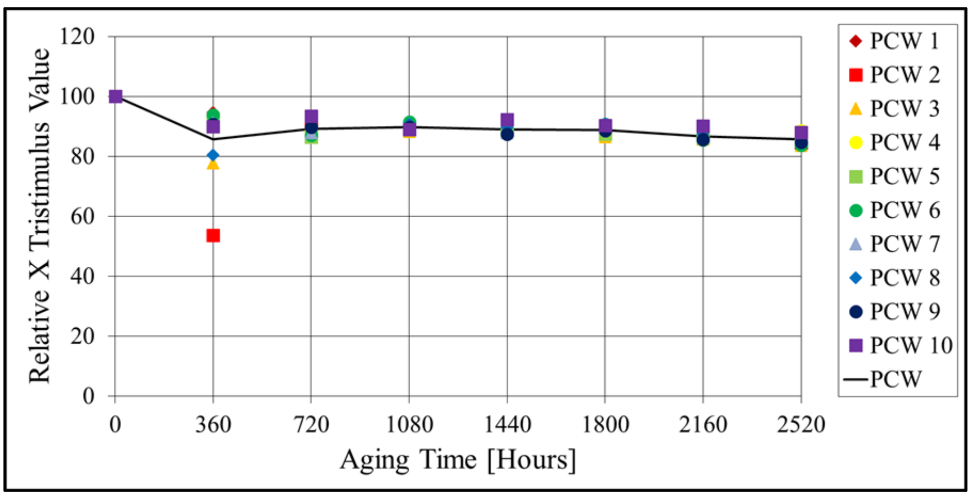


Figure 77: SSLG2 – Relative X Tristimulus Value of PCW at 55°C/65%.

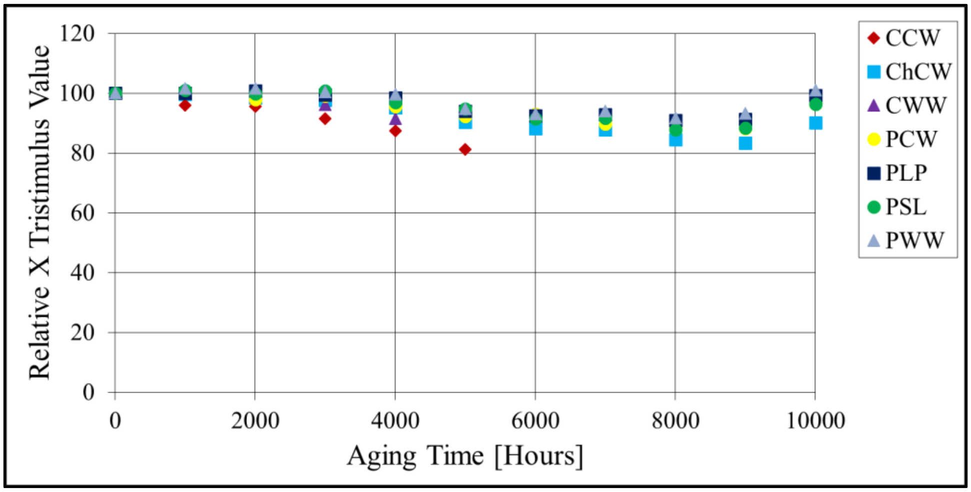


Figure 78: SSLG3 – Relative X Tristimulus Value at 25°C/45%.

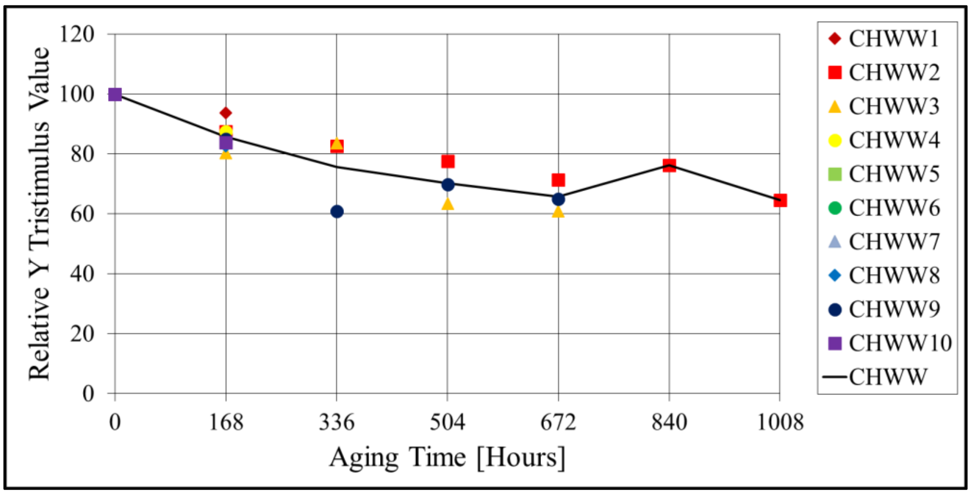


Figure 79: SSLG1 – Relative Y Tristimulus Value of CHWW at 85°C/85%.

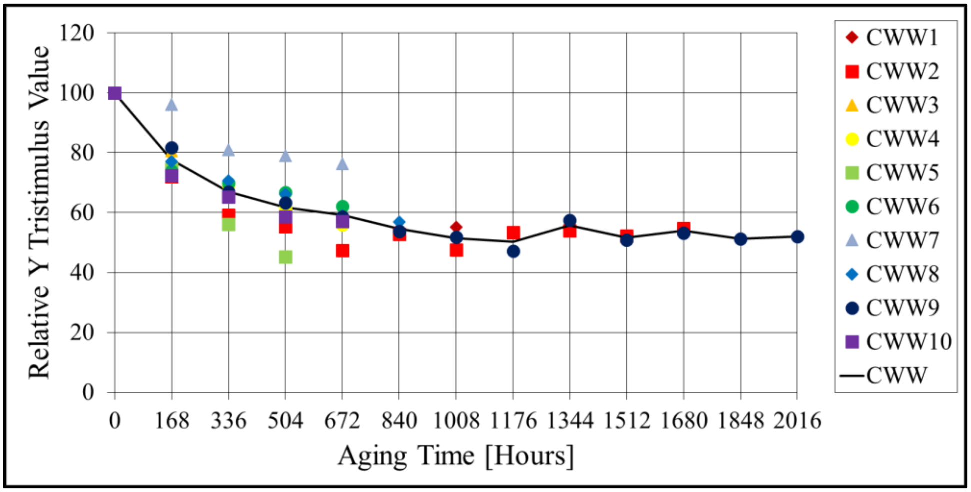


Figure 80: SSLG1 – Relative Y Tristimulus Value of CWW at 85°C/85%.

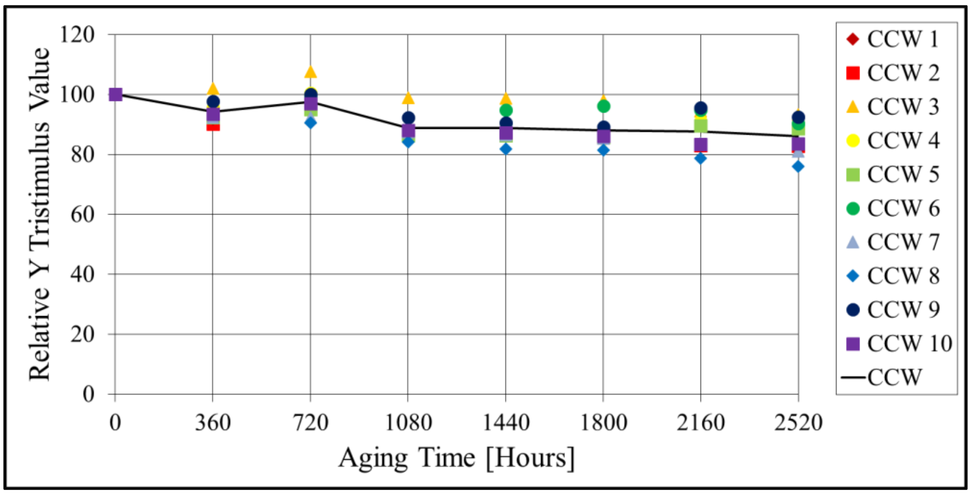


Figure 81: SSLG2 – Relative Y Tristimulus Value of CCW at 55°C/65%.

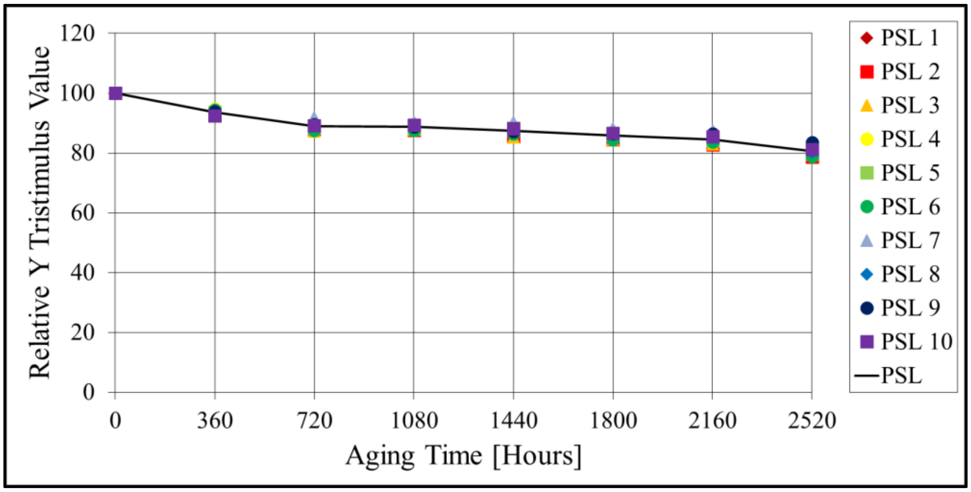


Figure 82: SSLG2 – Relative Y Tristimulus Value of PSL at 55°C/65%.

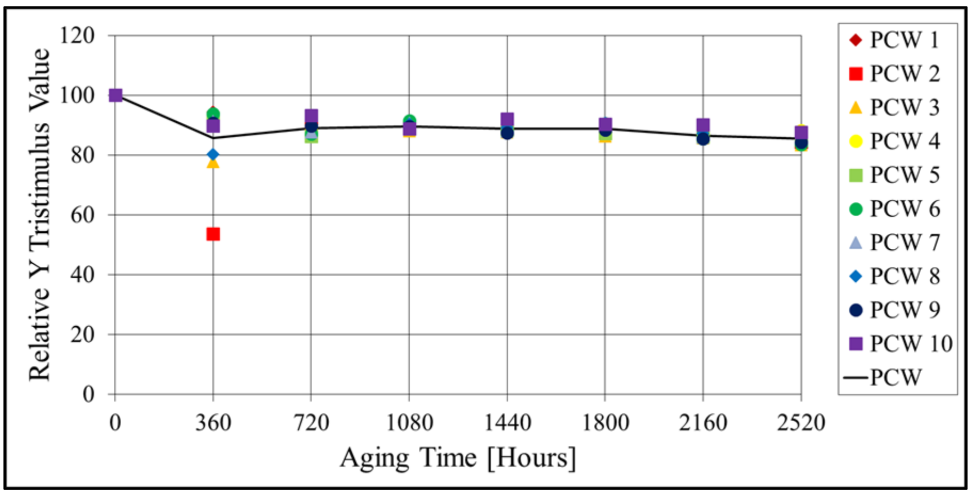


Figure 83: SSLG2 – Relative Y Tristimulus Value of PCW at 55°C/65%.

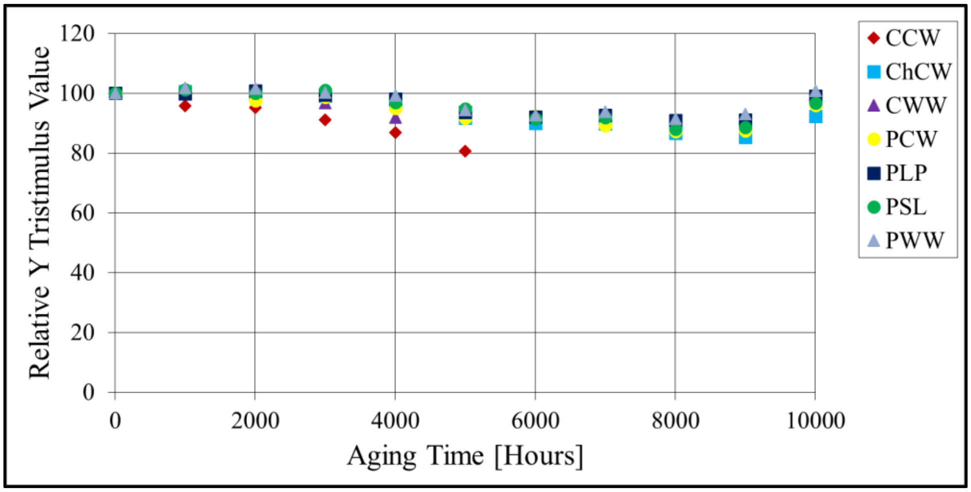


Figure 84: SSLG3 – Relative Y Tristimulus Value at 25°C/45%.

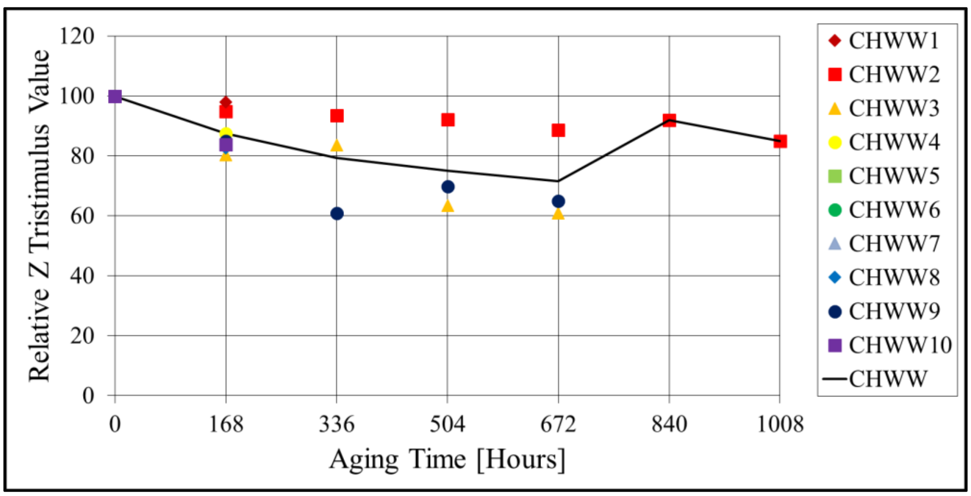


Figure 85: SSLG1 – Relative Z Tristimulus Value of CHWW at 85°C/85%.

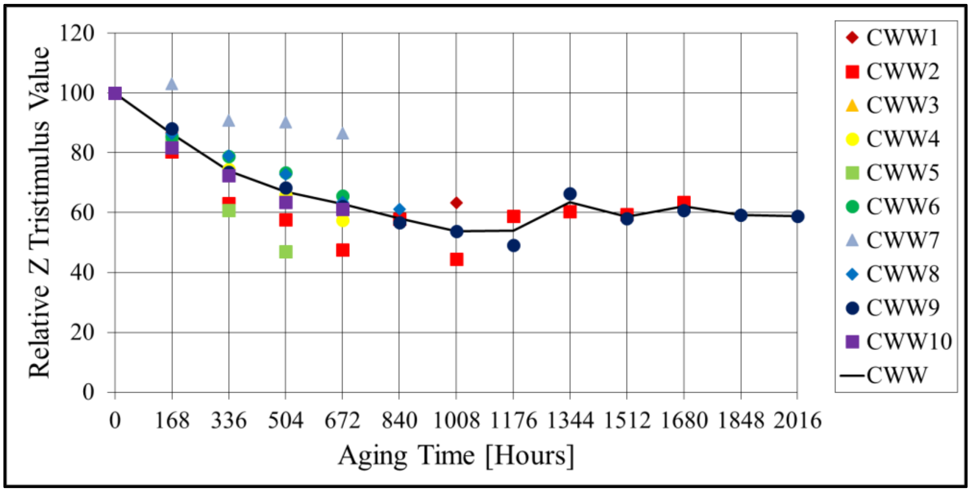


Figure 86: SSLG1 – Relative Z Tristimulu Value of CWW at 85°C/85%.

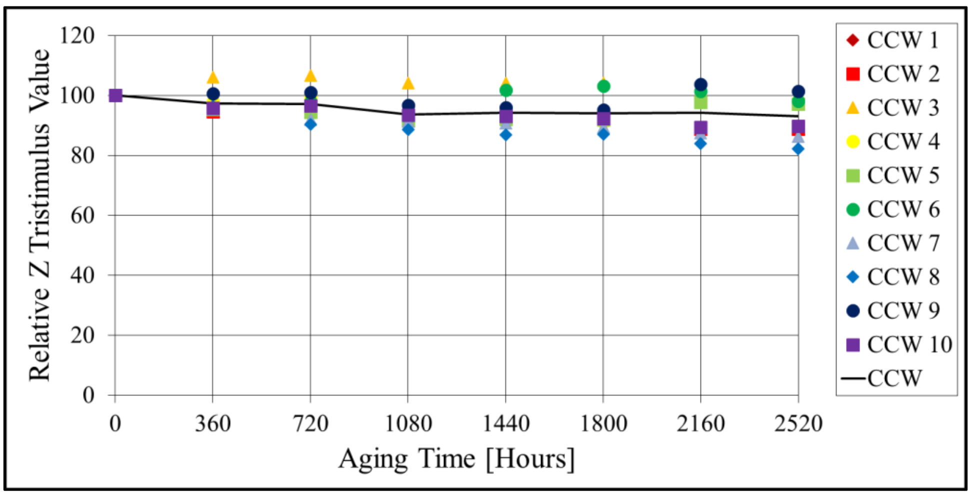


Figure 87: SSLG2 – Relative Z Tristimulus Value of CCW at 55°C/65%.

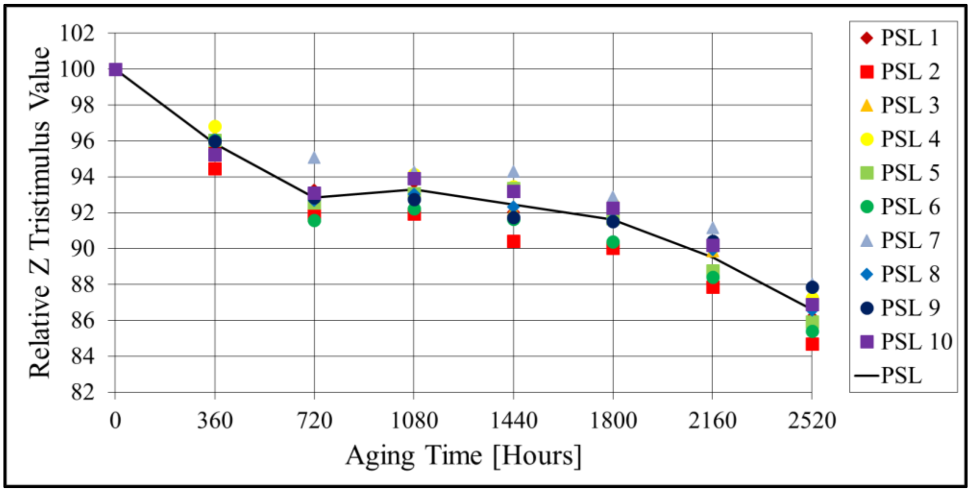


Figure 88: SSLG2 – Relative Z Tristimulus Value of PSL at 55°C/65%.

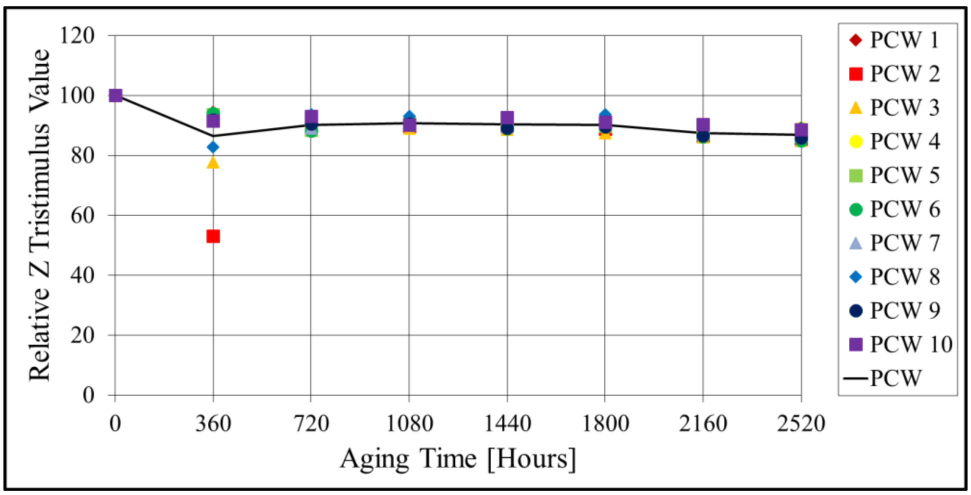


Figure 89: SSLG2 – Relative Z Tristimulus Value of PCW at 55°C/65%.

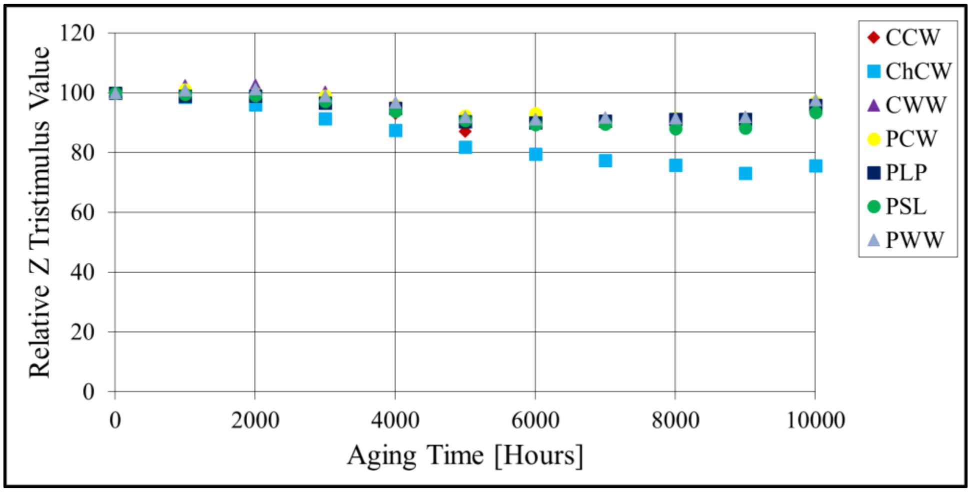


Figure 90: SSLG3 – Relative Z Tristimulus Value at 25°C/45%.

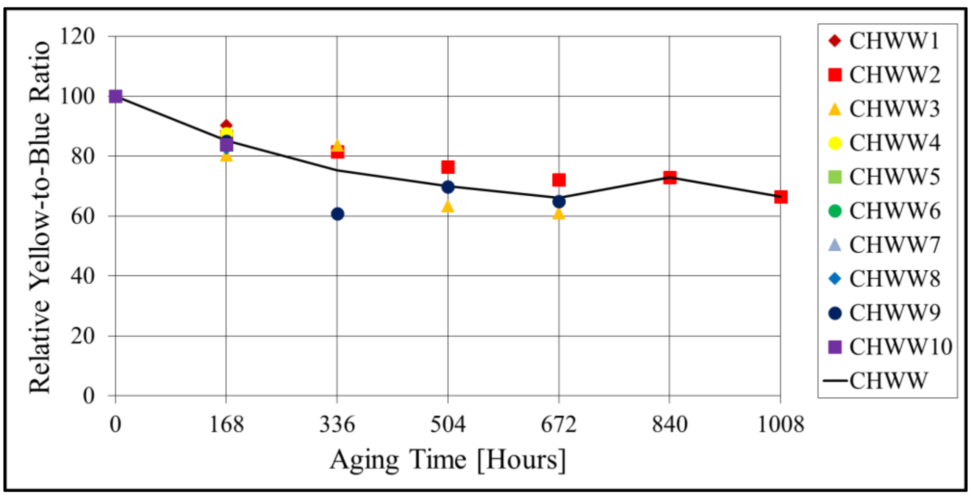


Figure 91: SSLG1 – Relative Yellow-to-Blue Ratio of CHWW at 85°C/85%.

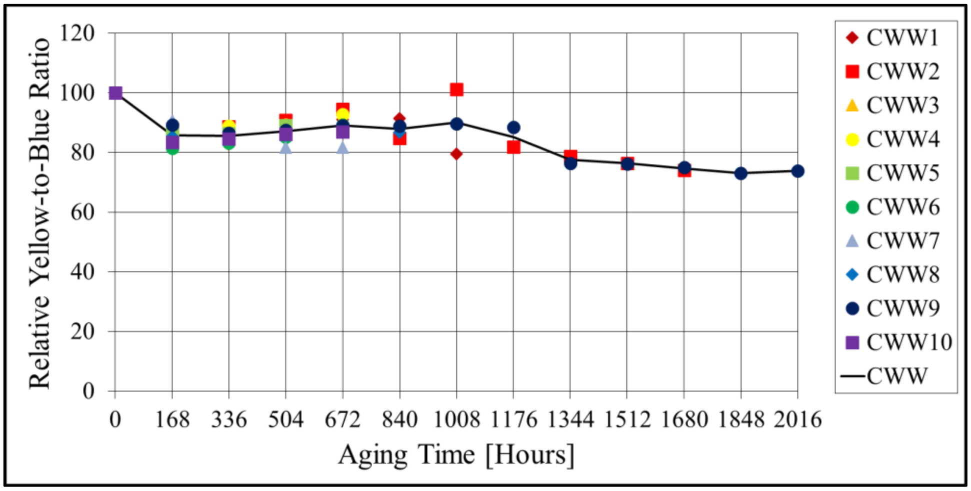


Figure 92: SSLG1 – Relative Yellow-to-Blue Ratio of CWW at 85°C/85%.

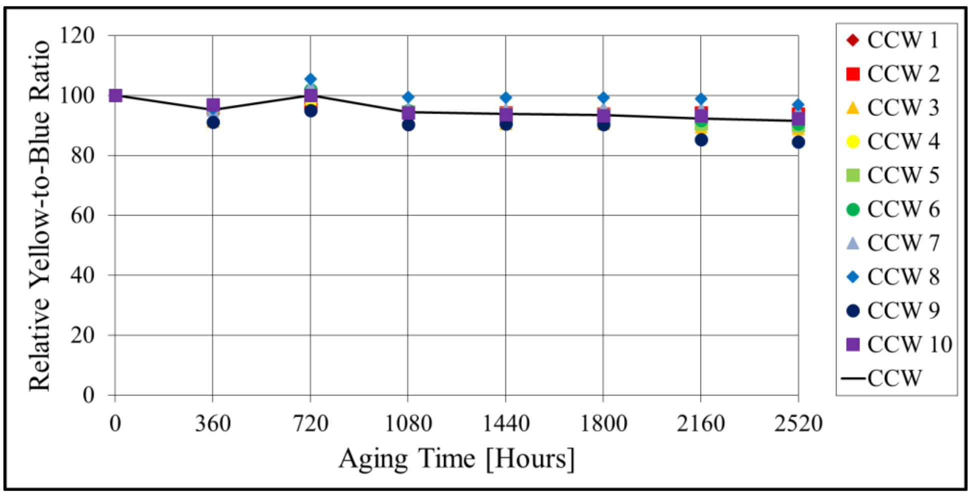


Figure 93: SSLG2 – Relative Yellow-to-Blue Ratio of CCW at 55°C/65%.

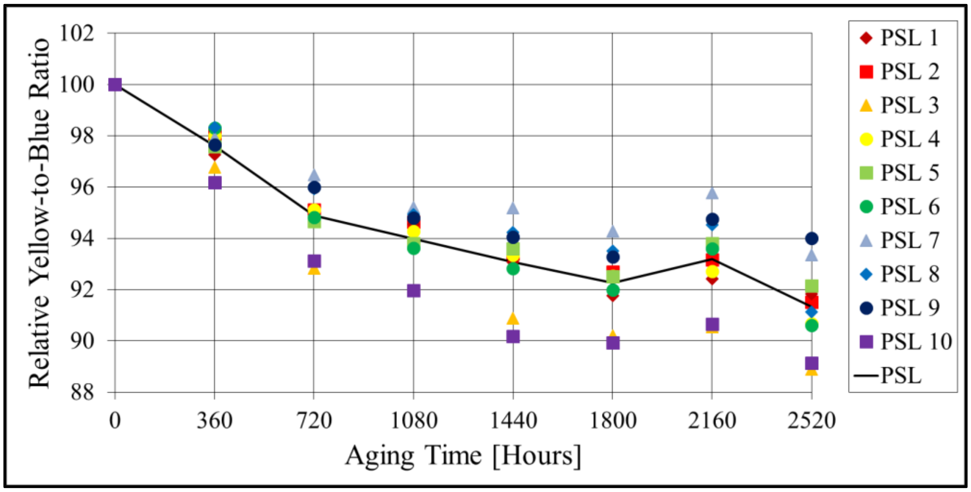


Figure 94: SSLG2 – Relative Yellow-to-Blue Ratio of PSL at 55°C/65%.

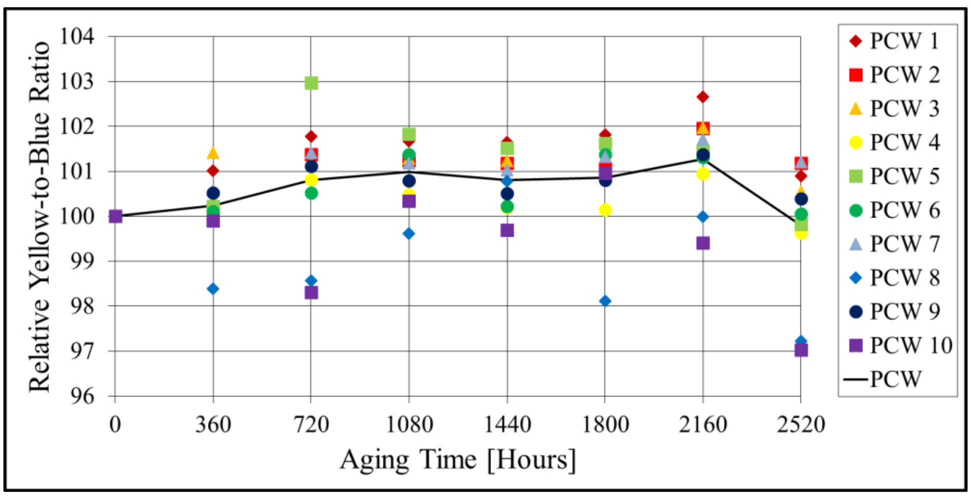


Figure 95: SSLG2 – Relative Yellow-to-Blue Ratio of PCW at 55°C/65%.

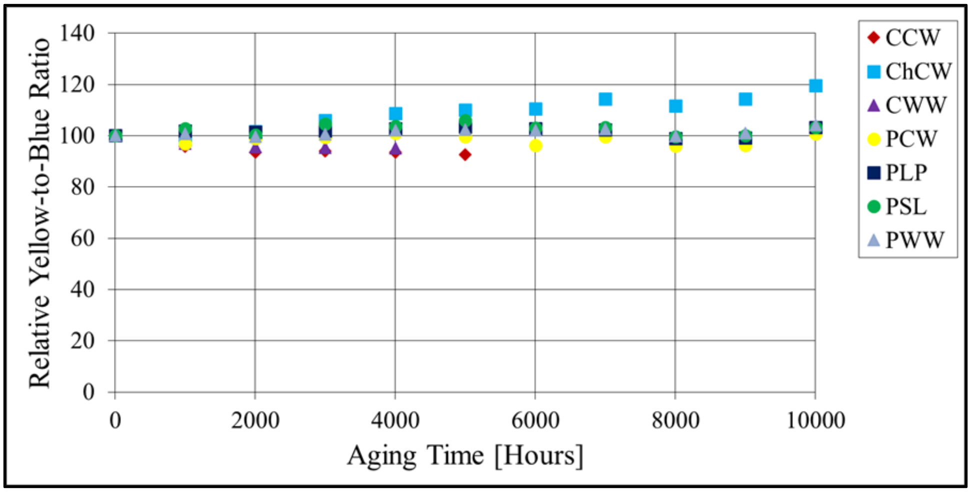


Figure 96: SSLG3 – Relative Yellow-to-Blue Ratio at 25°C/45%.

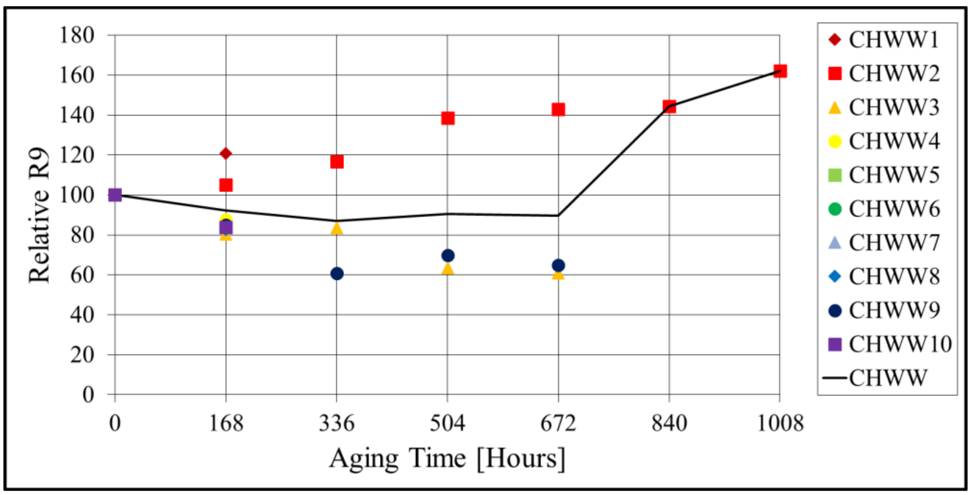


Figure 97: SSLG1 – Relative R9 of CHWW at 85°C/85%.

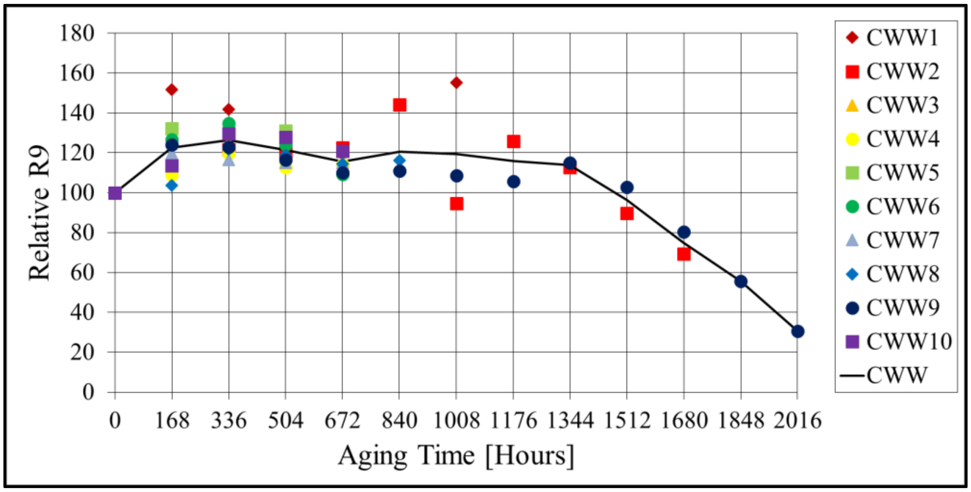


Figure 98: SSLG1 – Relative R9 of CWW at 85°C/85%.

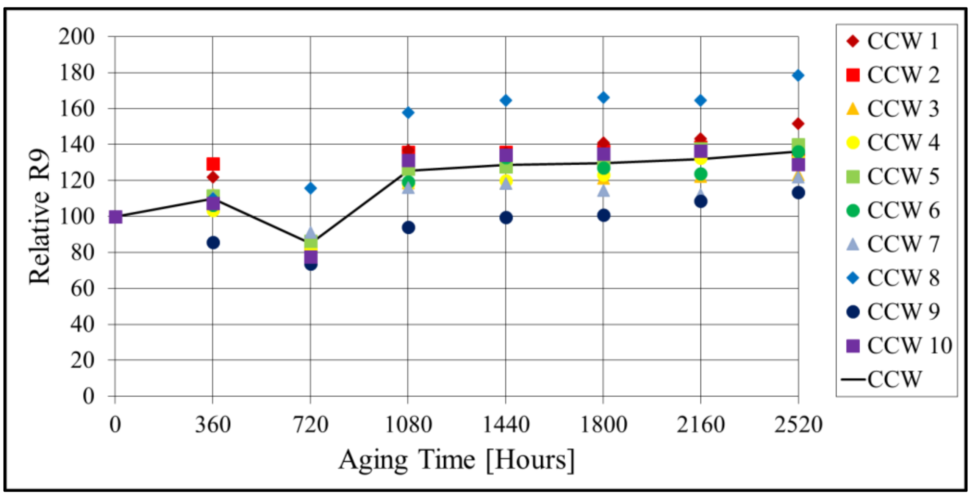


Figure 99: SSLG2 – Relative R9 of CCW at 55°C/65%.

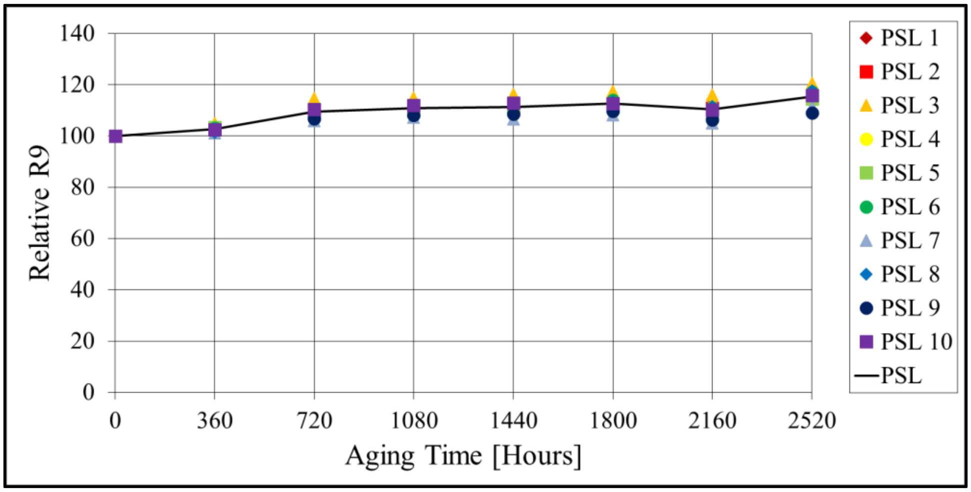


Figure 100: SSLG2 – Relative R9 of PSL at 55°C/65%.

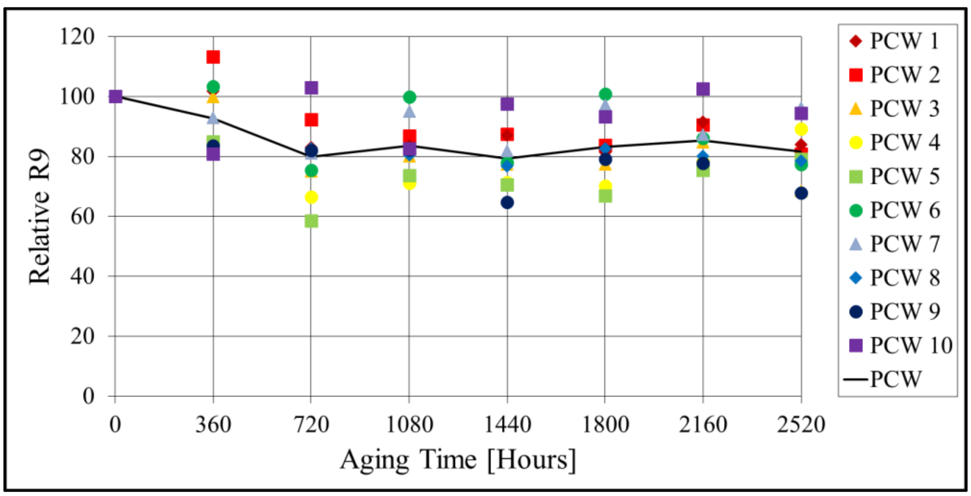


Figure 101: SSLG2 – Relative R9 of PCW at 55°C/65%.

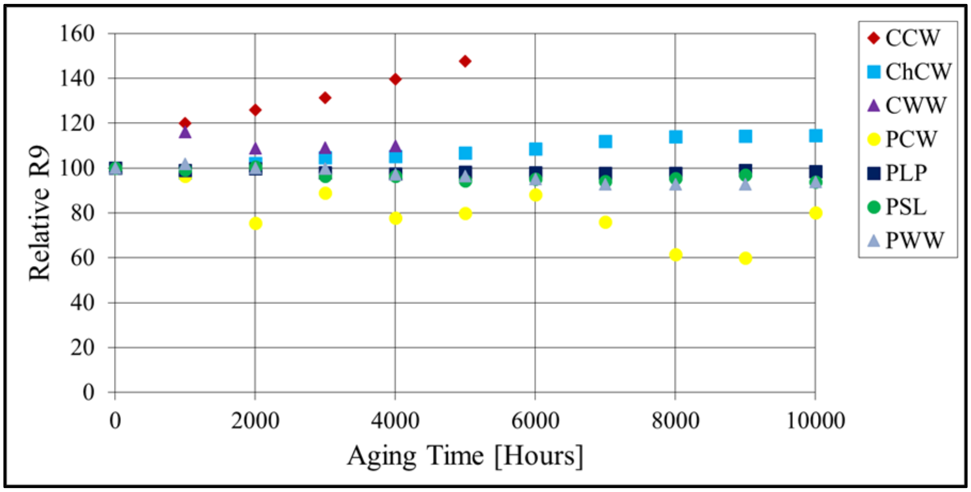


Figure 102: SSLG3 – Relative R9 at 25°C/45%.

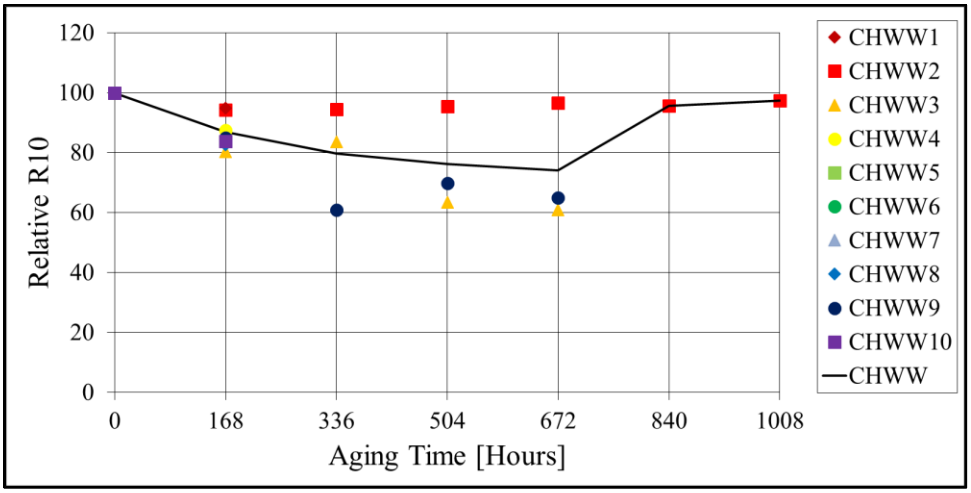


Figure 103: SSLG1 – Relative R10 of CHWW at 85°C/85%.

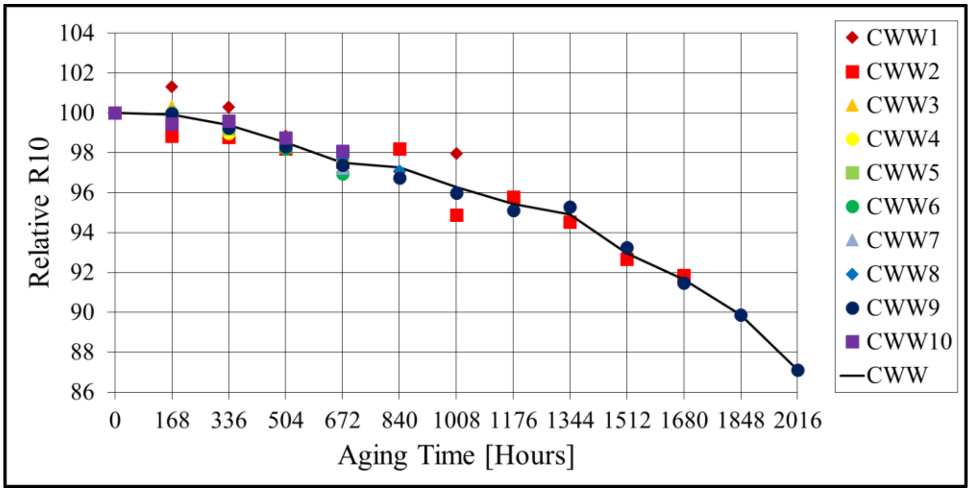


Figure 104: SSLG1 – Relative R10 of CWW at 85°C/85%.

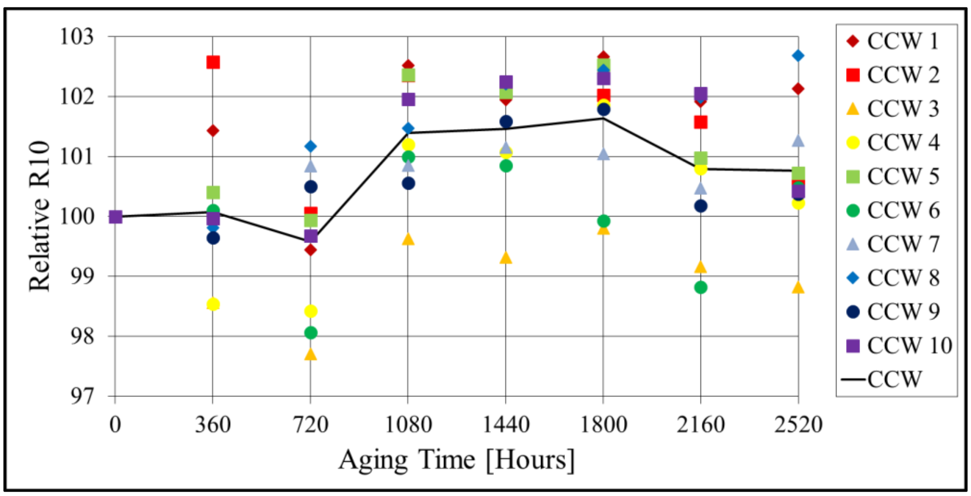


Figure 105: SSLG2 – Relative R10 of CCW at 55°C/65%.

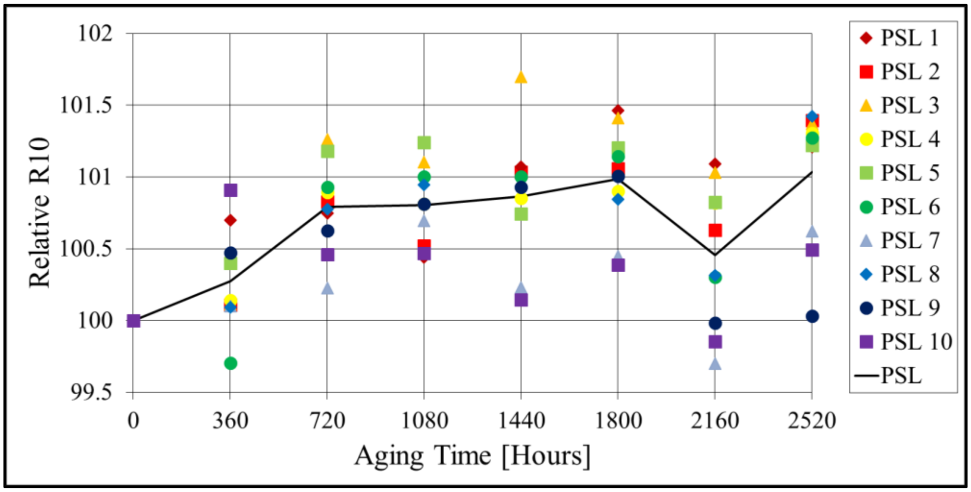


Figure 106: SSLG2 – Relative R10 of PSL at 55°C/65%.

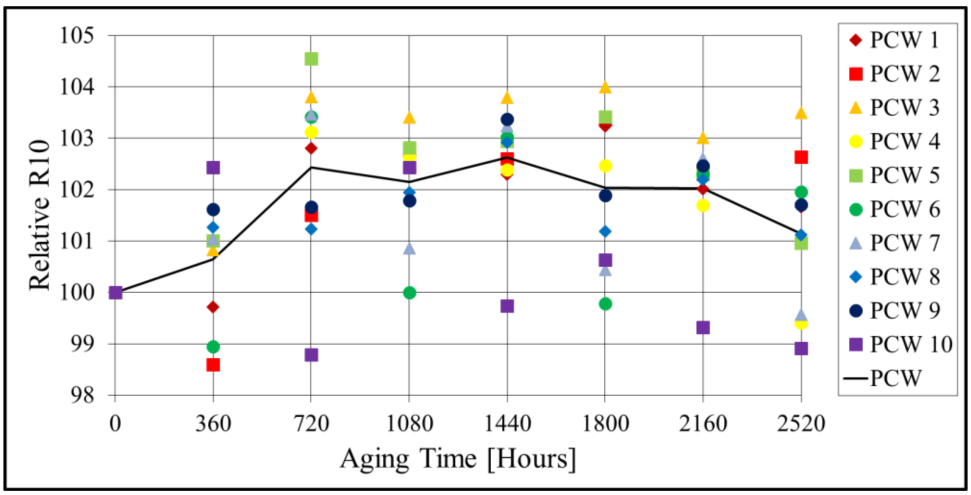


Figure 107: SSLG2 – Relative R10 of PCW at 55°C/65%.

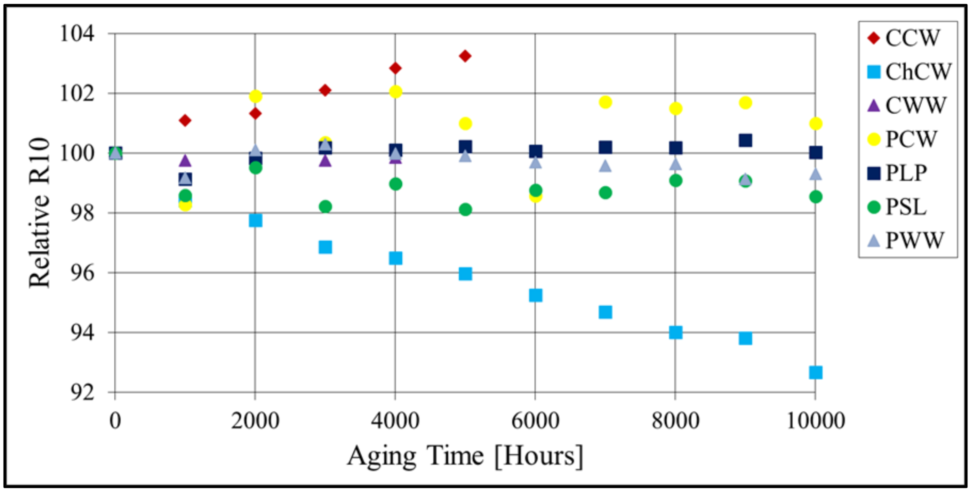


Figure 108: SSLG3 – Relative R10 at 25°C/45%.

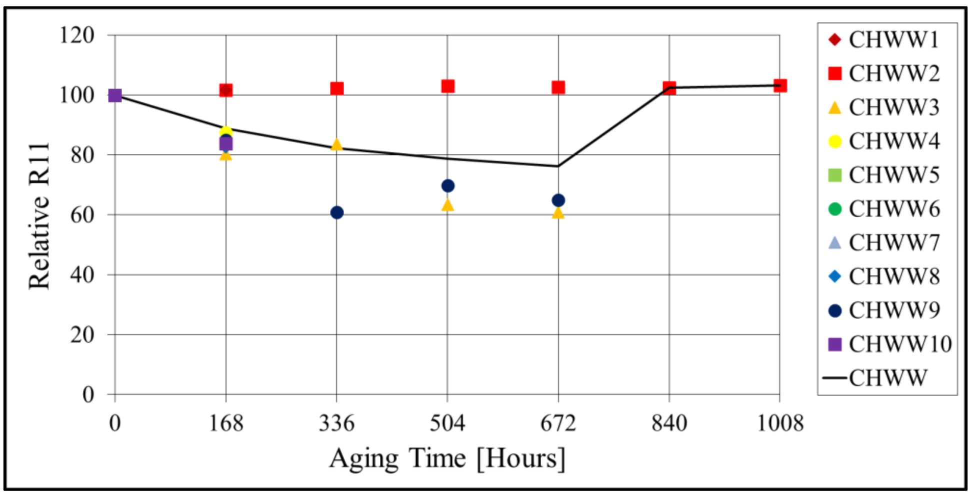


Figure 109: SSLG1 – Relative R11 of CHWW at 85°C/85%.

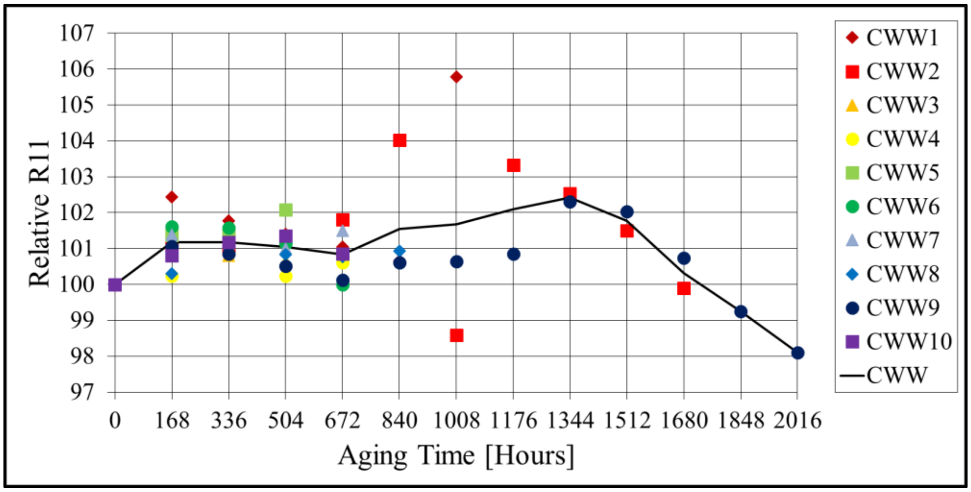


Figure 110: SSLG1 – Relative R11 of CWW at 85°C/85%.

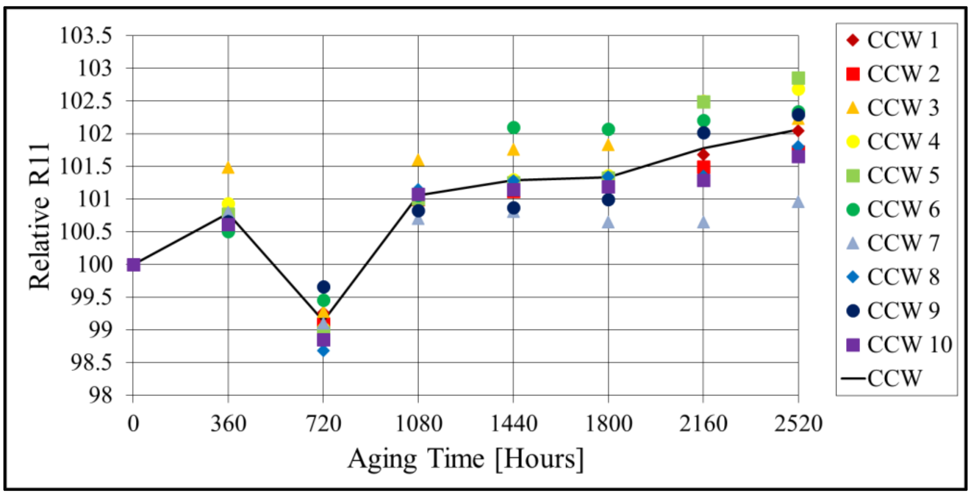


Figure 111: SSLG2 – Relative R11 of CCW at 55°C/65%.

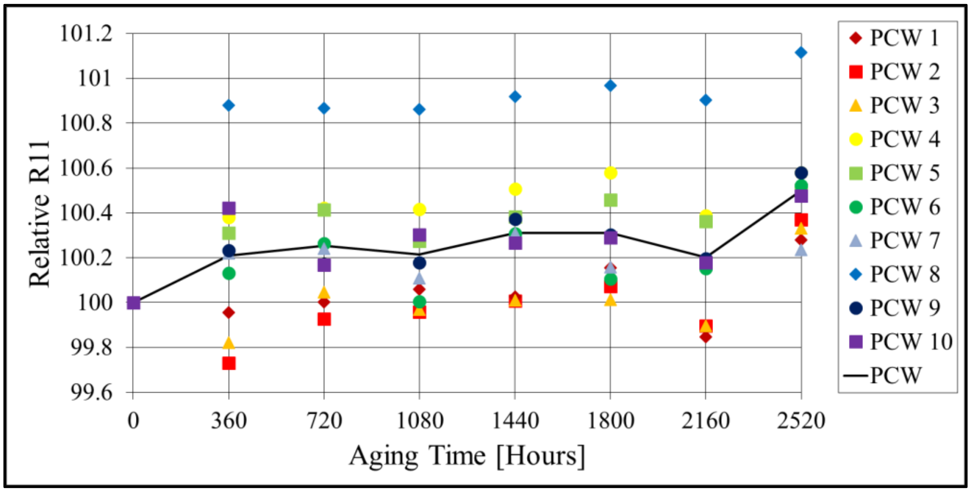


Figure 112: SSLG2 – Relative R11 of PCW at 55°C/65%.

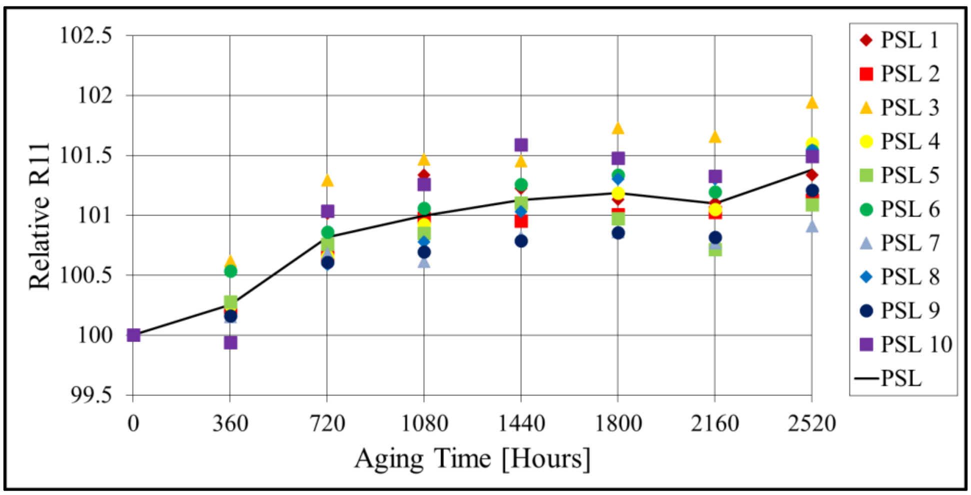


Figure 113: SSLG2 – Relative R11 of PSL at 55°C/65%.

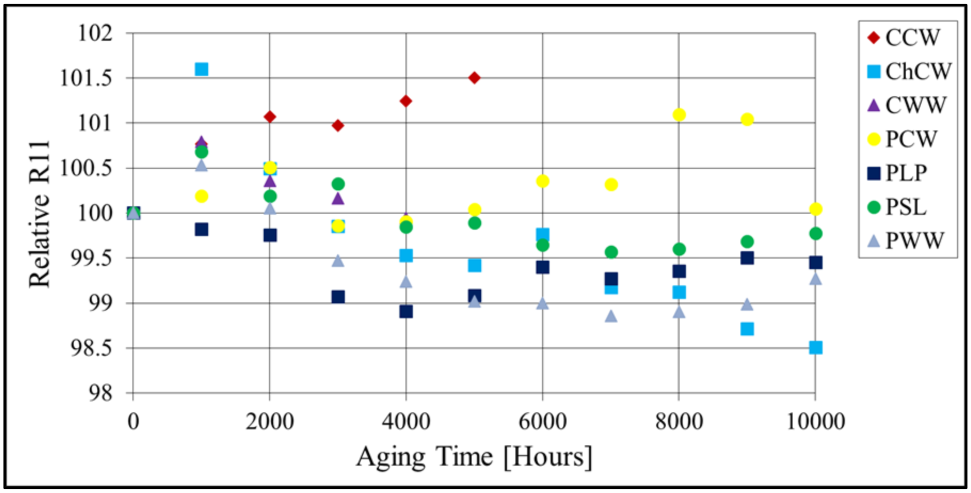


Figure 114: SSLG3 – Relative R11 at 25°C/45%.

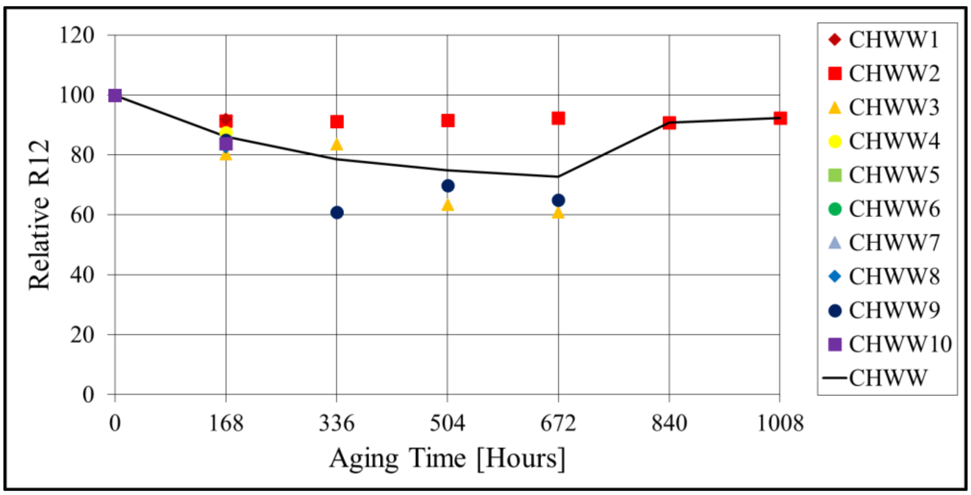


Figure 115: SSLG1 – Relative R12 of CHWW at 85°C/85%.

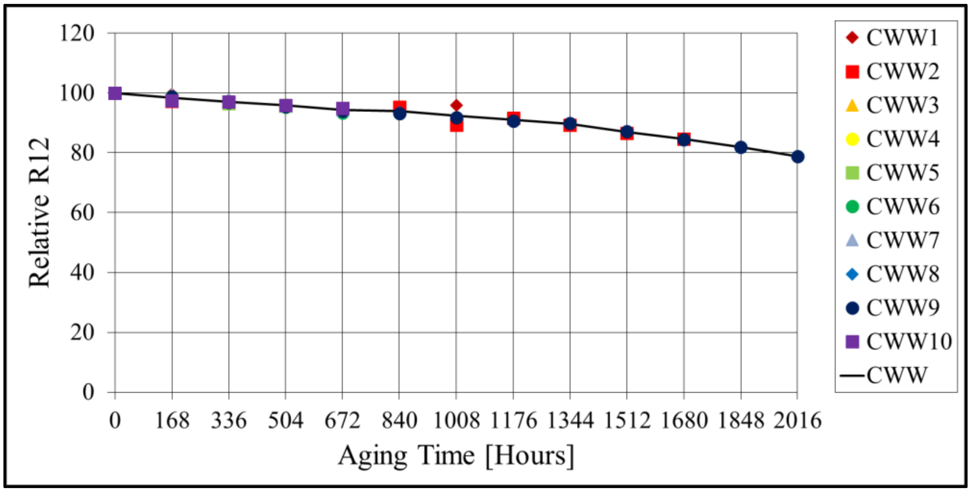


Figure 116: SSLG1 – Relative R12 of CWW at 85°C/85%.

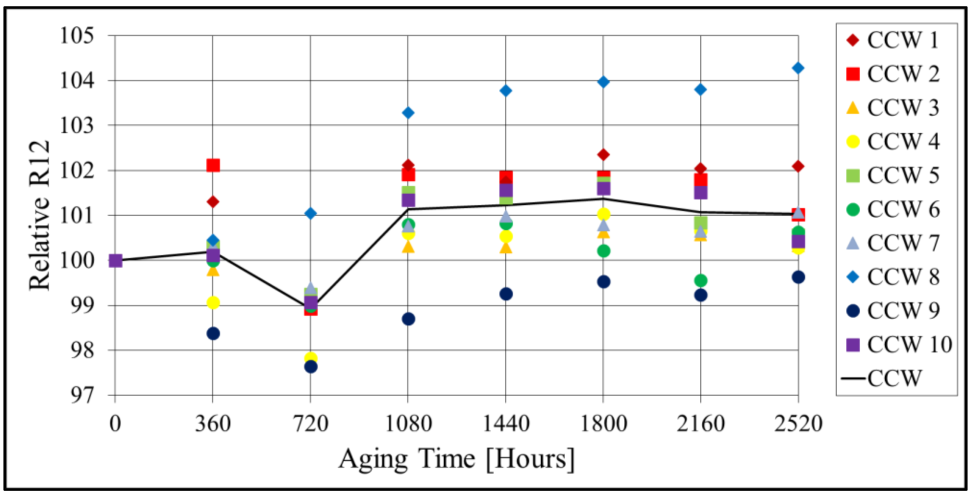


Figure 117: SSLG2 – Relative R12 of CCW at 55°C/65%.

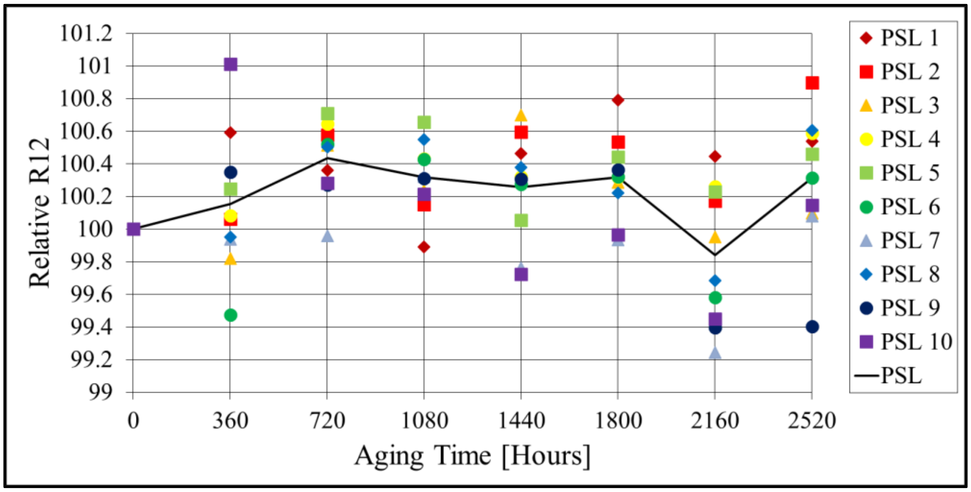


Figure 118: SSLG2 – Relative R12 of PSL at 55°C/65%.

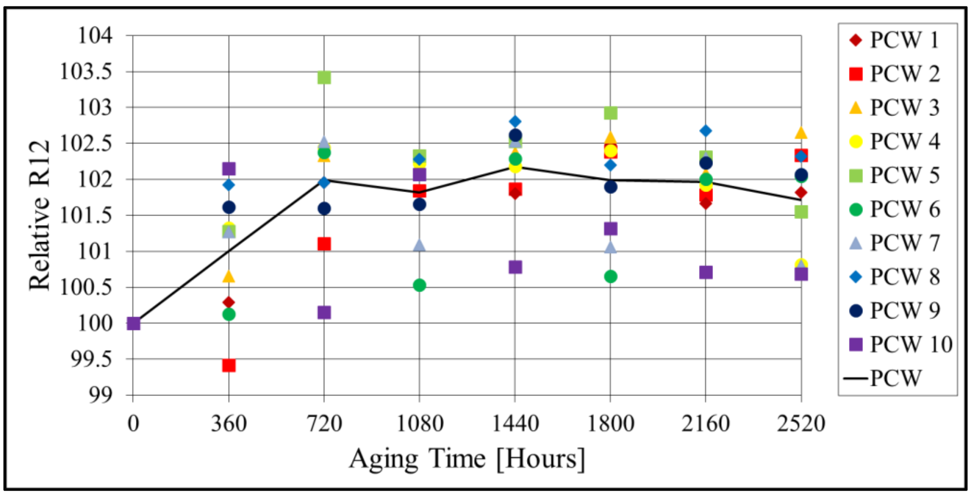


Figure 119: SSLG2 – Relative R12 of PCW at 55°C/65%.

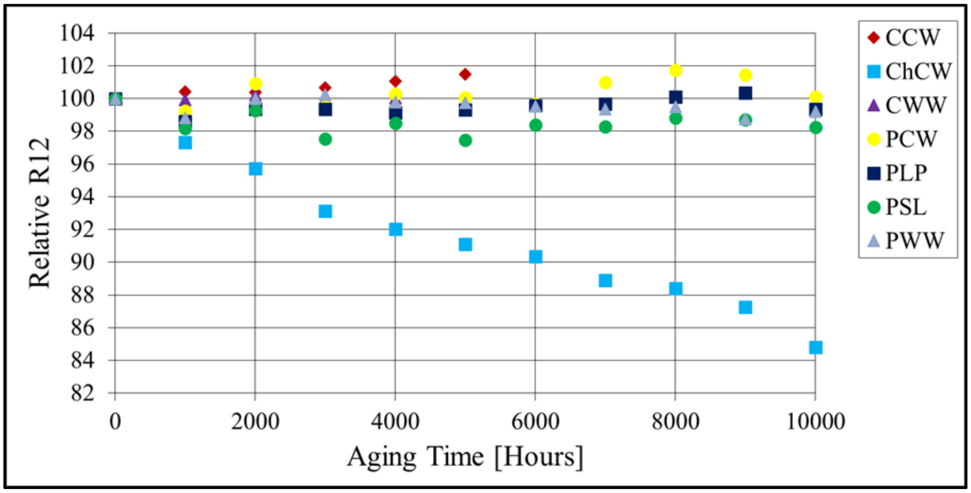


Figure 120: SSLG3 – Relative R12 at 25°C/45%.

Table 22: Rated Parameters of SSL Lamps Used with Peck's Power Law.

| **SSL Lamp** | **CCW** | **CHWW** | **CWW** | **PCW** | **PSL** |
|---|---|---|---|---|---|
| Power [W] | 9 | 9 | 9.5 | 12 | 10.5 |
| Power Factor | 1 | 0.63 | 0.9 | 0.9 | 0.9 |
| Length [mm] | 111.1 | 125 | 112.7 | 104.6 | 111.7 |
| Diameter [mm] | 60.3 | 69.6 | 60.3 | 61.2 | 68.9 |
| Weight [g] | 113 | 148 | 113 | 132 | 56 |
| Efficacy [lm/W] | 88.9 | 88.9 | 84.2 | 69.1 | 76.2 |

The initial function, F (Ψ), used with Peck's Power Law is shown in equation (167), where the parameters c1 – c14 are the unknown powers of each initial term.

$$F(\Psi)=\begin{bmatrix} Power^{c1}\cdot PowerFactor^{c2}\cdot Length^{c3}\cdot Diameter^{c4} \\ \cdot Weight^{c5}\cdot Efficacy^{c6}\cdot\left(\frac{RX_o}{RX_a}\right)^{c7} \\ \cdot\left(\frac{RY_o}{RY_a}\right)^{c8}\cdot\left(\frac{RZ_o}{RZ_a}\right)^{c9}\cdot\left(\frac{Ryb_o}{Ryb_a}\right)^{c10}\cdot\left(\frac{RR9_o}{RR9_a}\right)^{c11}\cdot \\ \left(\frac{RR10_o}{R10_a}\right)^{c12}\cdot\left(\frac{RR11_o}{RR11_a}\right)^{c13}\cdot\left(\frac{RR12_o}{RR12_a}\right)^{c14} \end{bmatrix} \tag{167}$$

Similarly to what was done with the general form of Peck's model, each SSL lamp specific AF has been used with the initial function to investigate a generalized AF model.

The log-linear form of Peck's Power Law from equation (152), along with PCR has been used to determine the unknown parameters in Peck's Power Law model, as well as the unknown values of the proposed function to accurately predict the AFs of the SSL lamps. Figure 121 is the Scree plot used to eliminate the eigenvalues that had the smallest percent contribution in the model.

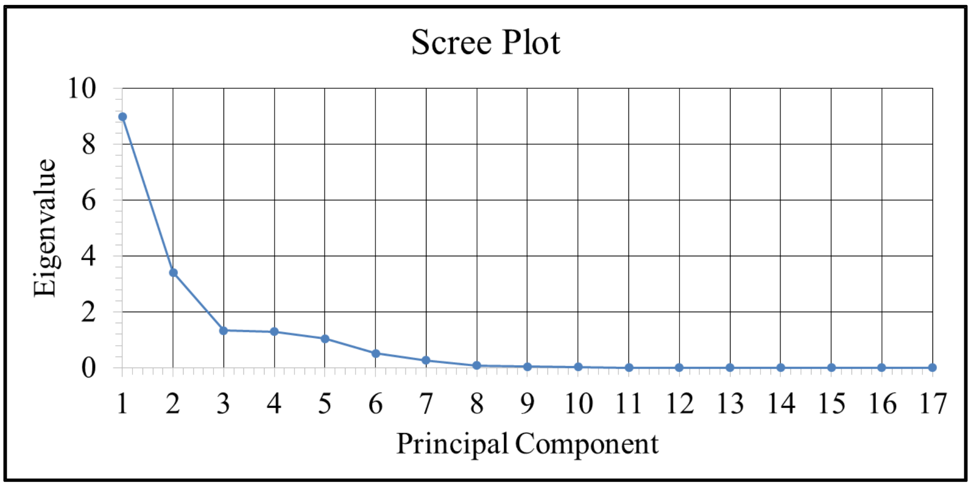


Figure 121: Self-Validation of Peck's Power Law Model.

From the Scree plot, the first seven eigenvalues were chosen for this analysis with these eigenvalues producing 99% of the cumulative percentage contribution. Additionally, the choice of these eigenvalues has eliminated all of the SSL colorimetric parameters leaving only known physical characteristics of each lamp, as well as the temperature and humidity conditions. After the elimination of the eigenvalues, a regression analysis was performed to determine the unknown coefficients in the generalized AF model with the results shown in Table 23. The advantage of having a generalized AF model in this form is no prior knowledge of the luminous flux degradation or degradation from the other colorimetric parameters is necessary.

Table 23: Principal Components Regression Analysis Predictor Variables.

| Principal Components | Parameter | Standard Error | t-statistic | p-value |
|---|---|---|---|---|
| Z1 | -1.99 | 0.00 | -197750390.01 | 0.00 |
| Z2 | 2.72 | 0.00 | 86796749.73 | 0.00 |
| Z3 | -3.18 | 0.00 | -75311389.79 | 0.00 |
| Z4 | 2.18 | 0.00 | 40650978.78 | 0.00 |
| Z5 | 0.00 | 0.00 | NaN | NaN |
| Z6 | 0.00 | 0.00 | NaN | NaN |
| Z7 | 0.00 | 0.00 | NaN | NaN |

After the SSL specific parameters were determined, the principal component values were transformed back into their natural state with the final values shown in Table 24. Compared to the generalized form of Peck's model used to model corrosion of microelectronics, the SSL specific parameter associated with RH, b2, is about 2.66 times larger than the traditional value of 2.7. Also, the SSL activation energy is slightly lower than the range of 0.7 – 0.8 used to analyze corrosion of electronics.

Table 24: Final From of the Generalized AF Parameters.

| Natural Component | Value |
|---|---|
| b0 (Const.) | -52.78 |
| b1 (Ea/kb) | 7534.03 |
| b2 (-N) | -7.17 |
| c1 (Power) | 3.81 |
| c2 (Power Factor) | 0.93 |
| c3 (Length) | 0.25 |
| c4 (Diameter) | 9.26 |
| Ea | 0.65 |

The self-validation of the generalized AF model is shown in Figure 122 and illustrates a perfect match between the predicted and actual AFs with the final form of the generalized acceleration model for SSL lamps shown in equation (168).

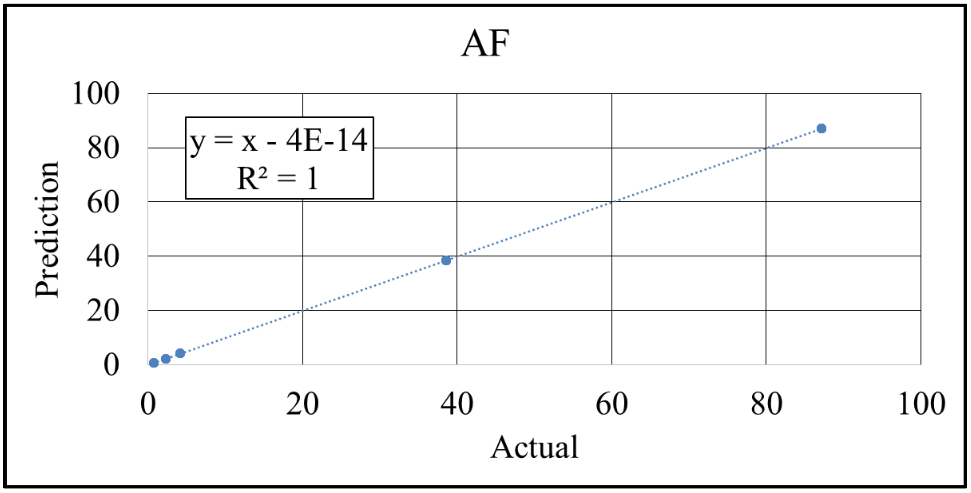


Figure 122: Self-Validation of the Generalized AF Model.

$$AF = \left\{ \begin{array}{l} \left(\frac{RH_o}{RH_a}\right)^{-7.17} \cdot \exp\left(7534.03 \cdot \left(\frac{1}{T_o} - \frac{1}{T_a}\right)\right) \cdot Power^{3.81} \\ \cdot PowerFactor^{0.93} \cdot Length^{0.25} \cdot Diameter^{9.26} \end{array} \right\} \tag{168}$$

A change in diameter will produce the largest change of an AF compared to the other manufacturer specified parameters, such as a change in length which will have the lowest effect. Using this generalized AF model, one would be able to construct an SSL lamp with a specific AF performance criteria as the goal.

To validate the robustness of the generalized predictive model, the physical characteristics of SSLG1 – PWW, which was not used in the development of the AF model, and its ALT condition was used with equation (168) to determine the percentage error between the actual and predicted AF. The parameters used in the AF model and the results are shown in Table 25.

Table 25: Cross Validation of the Generalized AF Model.

| Lamp | $T_{acc}$[°C] | $RH_{acc}$% | P | Pf | L | D | **AF Actual** | **AF Predicted** | **% Error** |
|---|---|---|---|---|---|---|---|---|---|
| PWW | 85 | 85 | 11 | 0.7 | 105 | 60 | **46.40** | **50.02** | **7.81** |

An AF of 50.02 was predicted for SSLG1 – PWW and its actual AF is 46.40. The generalized AF model produce a percentage error of **7.81%**. Therefore, this proposed generalized AF model has the potential to produce meaningful lifetime predictions of an SSL lamp at any operating condition with only knowledge of “failure” at a single ALT condition.

$$AF = \frac{\alpha_{acc}}{\alpha_{op}} = \frac{t_{f_{op}}}{t_{f_{acc}}} \Rightarrow t_{f_{op}} = t_{f_{acc}} \cdot AF \tag{169}$$

### 4.1.3. SSL Failure Analysis

Each SSL lamp from group SSLG1 catastrophically failed. Continuity and diode testing, using a handheld digital multimeter, has been performed on the electrical drivers of each lamp in this group to determine the location of the failure modes. The components used to verify continuity in CHWW is depicted in Figure 123 with the results tabulated in Table 26.

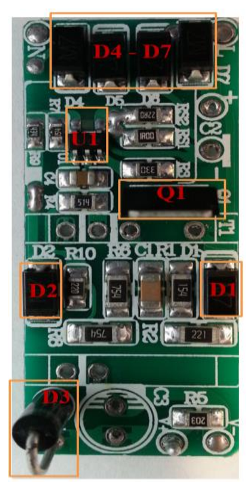


Figure 123: Electrical Driver of CHWW.

Table 26: Failure Analaysis of CHWW.

| Symbol | CHWW 1 | CHWW 2 | CHWW 3 | CHWW 4 | CHWW 5 | CHWW 6 | CHWW 7 | CHWW 8 | CHWW 9 | CHWW 10 |
|---|---|---|---|---|---|---|---|---|---|---|
| D1 | Pass | Pass | Pass | Pass | Pass | Pass | Pass | Pass | Pass | Pass |
| D2 | Pass | Pass | Pass | Pass | Pass | Pass | Pass | Pass | Pass | Pass |
| D3 | Pass | Pass | Pass | Pass | Pass | Pass | Pass | Pass | Pass | Pass |
| D4 | Pass | Pass | Pass | Pass | Pass | Pass | Pass | Fail | Fail | Pass |
| D5 | Pass | Pass | Pass | Fail | Pass | Pass | Pass | Pass | Pass | Fail |
| D6 | Pass | Pass | Pass | Pass | Pass | Pass | Pass | Pass | Fail | Pass |
| D7 | Pass | Pass | Pass | Fail | Pass | Pass | Pass | Pass | Pass | Fail |
| Q1 | Pass | Pass | Pass | Pass | Pass | Pass | Pass | Pass | Pass | Pass |
| U1 | Fail | Pass | Pass | Fail | Pass | Fail | Fail | Fail | Fail | Fail |

From the continuity analysis, the majority of the test vehicles in this group experienced failure in the IC controller, U1, with short circuiting as the predominant failure mechanism. The cause of this catastrophic failure mechanism is an electrical surge due to the ingress of moisture in the SSL lamps. Additional failure modes for some of the SSL lamps are shown in Figure 124 - Figure 128.

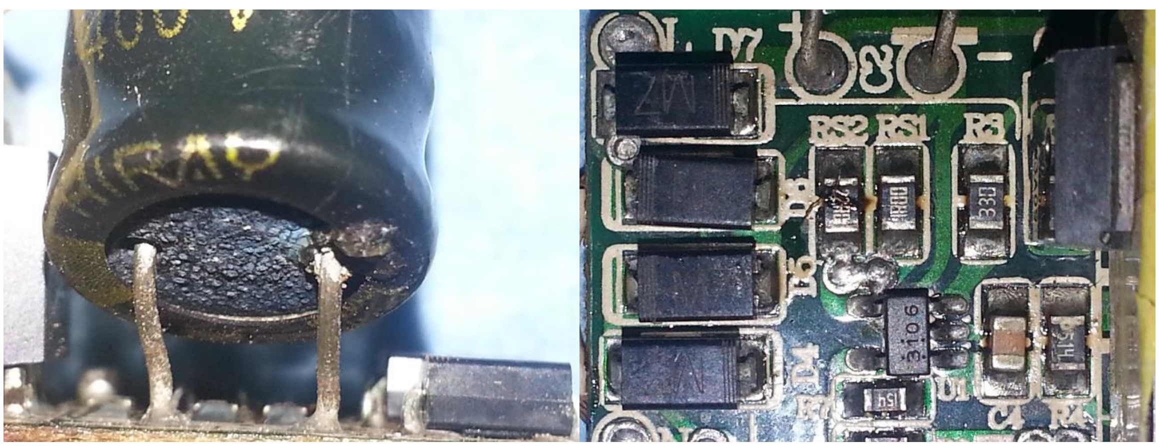


Figure 124: Failure Modes of CHWW 2 – Degradation of Surface Mount Components and the Aluminum Electrolytic Capacitor.

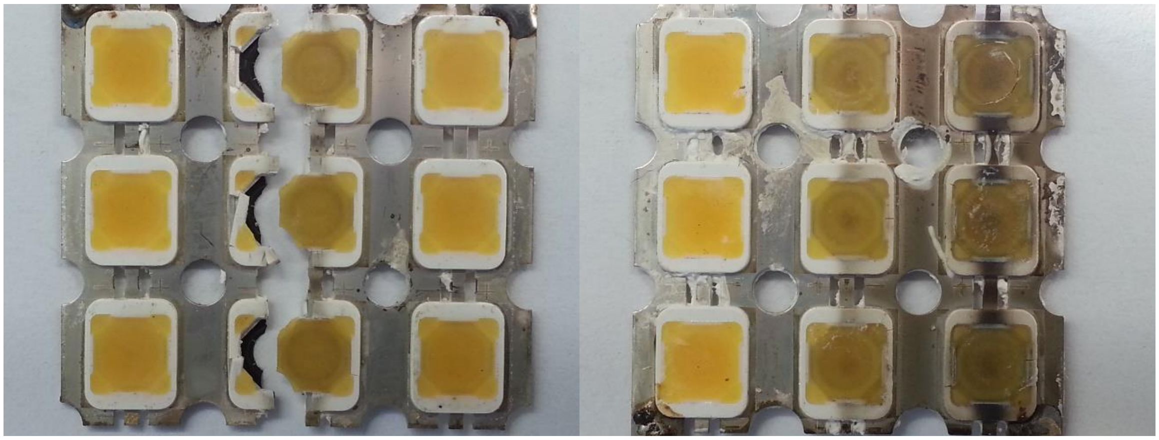

Figure 125: Failure Mode of CHWW 3 (Left) and CHWW 5 (Right) – LED Array Cracked Down the Center Producing an Open Circuit.

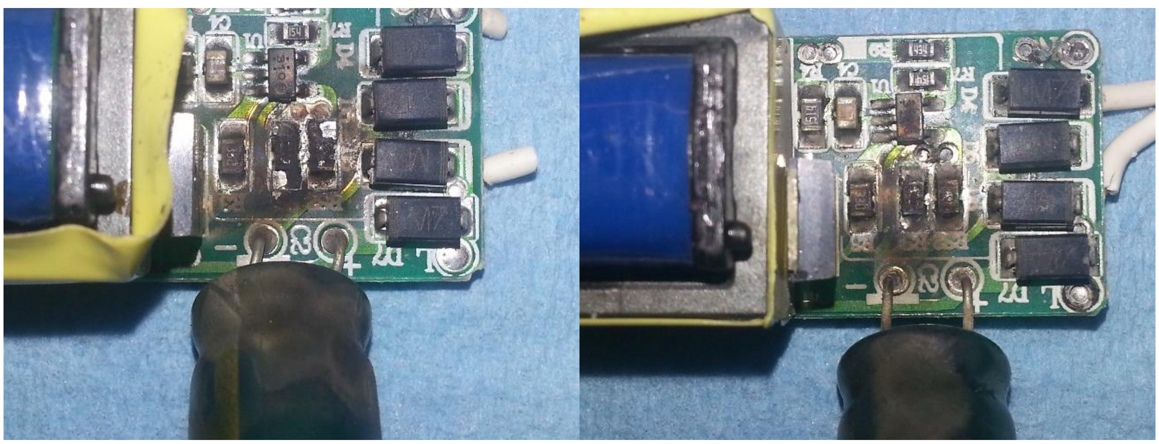

Figure 126: Failure Modes of CHWW 6 (Left) and CHWW 8 (Right) – Catastrophic Degradation of Surface Mount Components and the Aluminum Electrolytic Capacitor.

Figure 127: Failure location of CHWW 7 – Degradation of Surface Mount Components.

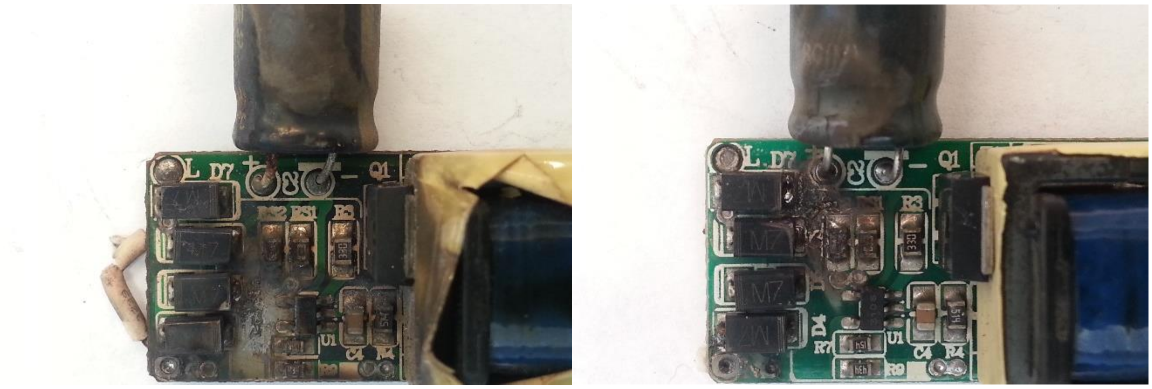

Figure 128: Failure Modes of CHWW 9 (Left) and CHWW 10 (Right) – Catastrophic Degradation of Surface Mount Components and the Aluminum Electrolytic Capacitor Due to an Electrical Fire.

Continuity and diode testing of CWW indicated failure in four SSL lamps as the fuse with the other components of the electrical driver experiencing no failure. The components used to verify continuity in CWW is depicted in Figure 129 with the results tabulated in Table 27.

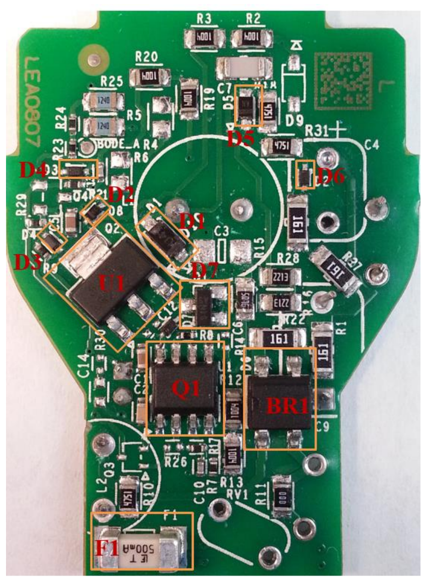


Figure 129: Electrical Driver of CWW.

Table 27: Failure Analaysis of CWW.

| Symbol | CWW 1 | CWW 2 | CWW 3 | CWW 4 | CWW 5 | CWW 6 | CWW 7 | CWW 8 | CWW 9 | CWW 10 |
|---|---|---|---|---|---|---|---|---|---|---|
| D1 | Pass | Pass | Pass | Pass | Pass | Pass | Pass | Pass | Pass | Pass |
| D2 | Pass | Pass | Pass | Pass | Pass | Pass | Pass | Pass | Pass | Pass |
| D3 | Pass | Pass | Pass | Pass | Pass | Pass | Pass | Pass | Pass | Pass |
| D4 | Pass | Pass | Pass | Pass | Pass | Pass | Pass | Pass | Pass | Pass |
| D5 | Pass | Pass | Pass | Pass | Pass | Pass | Pass | Pass | Pass | Pass |
| D6 | Pass | Pass | Pass | Pass | Pass | Pass | Pass | Pass | Pass | Pass |
| D7 | Pass | Pass | Pass | Pass | Pass | Pass | Pass | Pass | Pass | Pass |
| BR1 | Pass | Pass | Pass | Pass | Pass | Pass | Pass | Pass | Pass | Pass |
| Q1 | Pass | Pass | Pass | Pass | Pass | Pass | Pass | Pass | Pass | Pass |
| F1 | Pass | Pass | Pass | Fail | Fail | Fail | Pass | Fail | Pass | Pass |

The exact open circuit failure for CWW 1, CWW 3 and CWW 10 is presently unknown. The remaining SSL lamps that passed the continuity test experienced degradation in the heatsink causes the lamps to “fall apart” as shown in Figure 132.


Figure 130: Failure Mode of CWW 3 (Top-Left), CWW 7 (Top-Right) and CWW 9 (Bottom) –Degradation of the Aluminum Heatsink Due to the Exposure to Moisture.

Continuity and diode testing of PWW indicated catastrophic failure in multiple components of the electrical driver. The components used to verify continuity in PWW is depicted in Figure 131 with the results tabulated in Table 28.

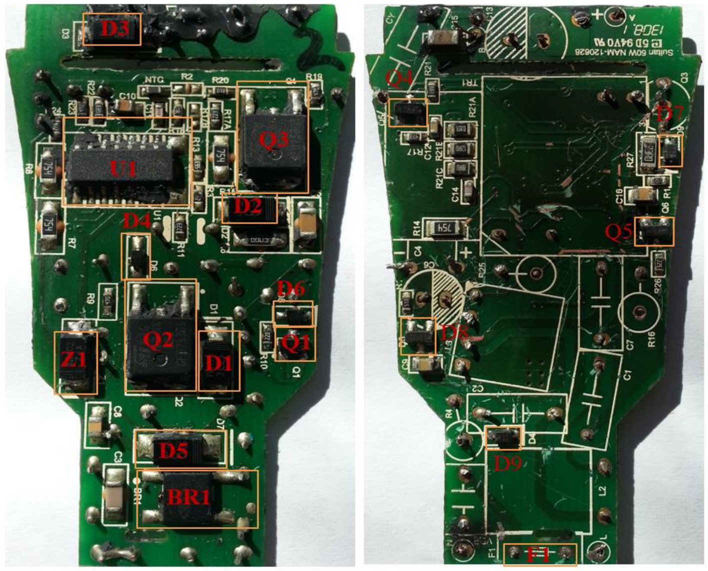


Figure 131: Electrical Driver of PWW.

Table 28: Failure Analaysis of PWW.

| Symbol | PWW 1 | PWW 2 | PWW 3 | PWW 4 | PWW 5 | PWW 6 | PWW 7 | PWW 8 | PWW 9 | PWW 10 |
|---|---|---|---|---|---|---|---|---|---|---|
| D1 | Pass | Pass | Pass | Pass | Pass | Pass | Pass | Pass | Pass | Pass |
| D2 | Pass | Pass | Pass | Pass | Pass | Pass | Pass | Pass | Pass | Pass |
| D3 | Pass | Pass | Pass | Pass | Pass | Pass | Pass | Pass | Pass | Pass |
| D4 | Pass | Fail | Pass | Pass | Pass | Pass | Pass | Fail | Fail | Pass |
| D5 | Pass | Pass | Pass | Pass | Pass | Pass | Pass | Pass | Pass | Pass |
| D6 | Pass | Fail | Pass | Fail | Pass | Fail | Fail | Fail | Fail | Pass |
| D7 | Pass | Fail | Pass | Pass | Fail | Pass | Pass | Pass | Pass | Pass |
| D8 | Pass | Pass | Pass | Pass | Pass | Pass | Pass | Pass | Pass | Pass |
| D9 | Fail | Pass | Pass | Fail | Fail | Fail | Fail | Pass | Pass | Pass |
| BR1 | Pass | Pass | Pass | Pass | Pass | Pass | Pass | Pass | Pass | Pass |
| Z1 | Pass | Pass | Pass | Pass | Pass | Fail | Fail | Fail | Pass | Pass |
| U1 | Pass | Pass | Pass | Pass | Pass | Pass | Pass | Pass | Pass | Pass |
| Q1 | Pass | Fail | Fail | Pass | Pass | Fail | Pass | Fail | Fail | Pass |
| Q2 | Pass | Pass | Pass | Pass | Pass | Pass | Pass | Pass | Pass | Pass |
| Q3 | Pass | Pass | Pass | Pass | Pass | Pass | Pass | Pass | Pass | Pass |
| Q4 | Fail | Pass | Fail | Fail | Fail | Fail | Fail | Fail | Fail | Fail |
| Q5 | Pass | Fail | Fail | Fail | Fail | Pass | Fail | Fail | Fail | Fail |
| F1 | Fail | Fail | Fail | Fail | Pass | Fail | Fail | Fail | Fail | Pass |

From the continuity analysis, the short circuit experienced by each test vehicle is primarily attributed to the failed fuse, F1, and secondarily attributed to the failed diode bridges, Q4 and Q5. Additional failure modes for some of the SSL lamps are shown in Figure 132 - Figure 136.

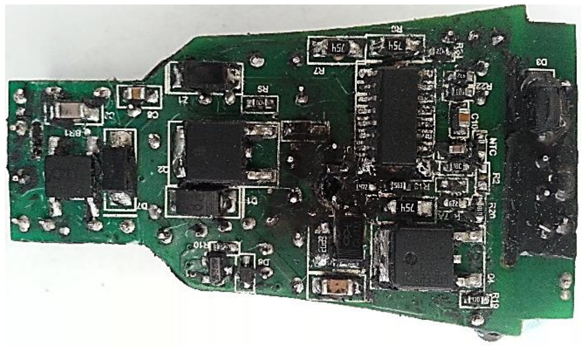

Figure 132: Failure Mode of PWW 1 – Catastrophic Degradation Due to an Electrical Fire that Burned a Hole into the Circuit Board.

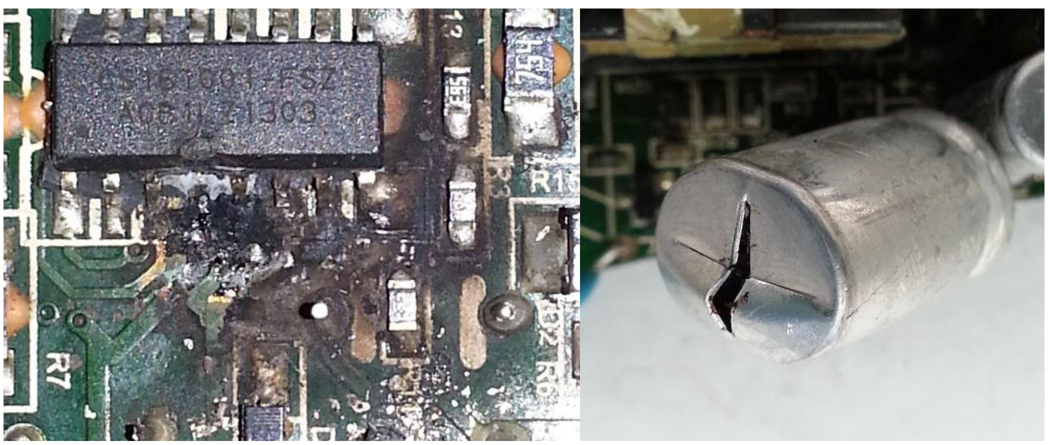

Figure 133: Failure Mode of PWW 2 – Catastrophic Degradation Due to an Electrical Fire that Burned a Hole into the Circuit Board and Catastrophic Failure of an Aluminum Electricalytic Capacitor.

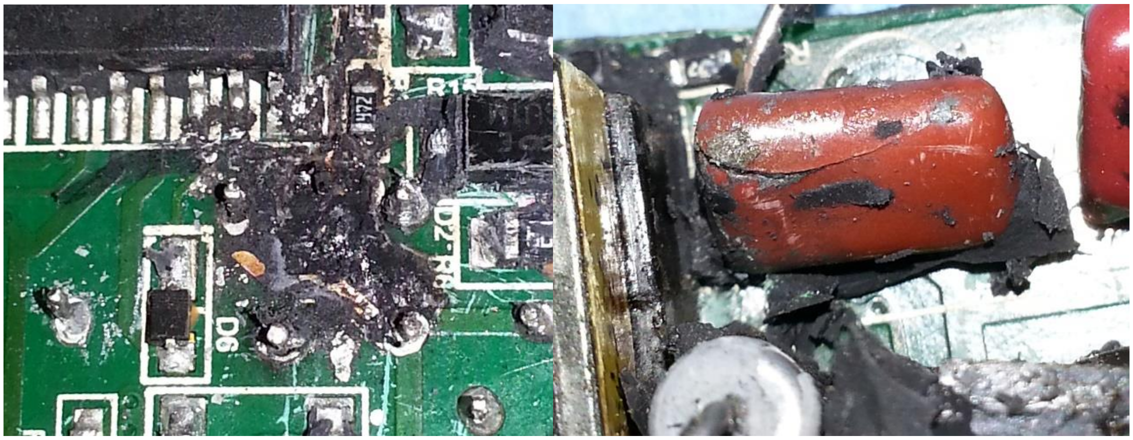


Figure 134: Failure Mode of PWW 4 – Catastrophic Degradation Due to an Electrical Fire that Burned a Hole into the Circuit Board and Catastrophic Failure of a Film Capacitor.

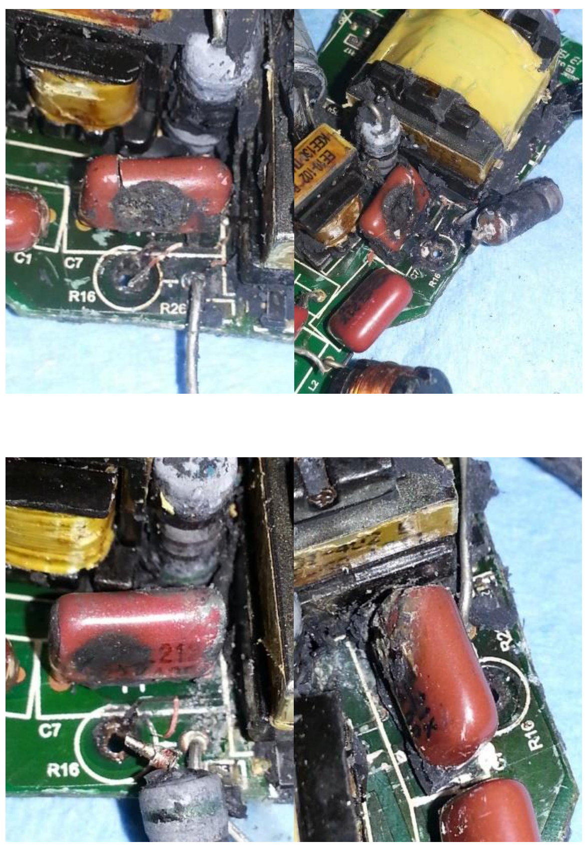


Figure 135: Failure Mode of PWW 5 (Top-Left), PWW 6 (Top-Right), PWW 9 (Bottom Left) and PWW 10 (Bottom-Right) –Degradation of Film Capacitor and Two Through Hole Reistors.

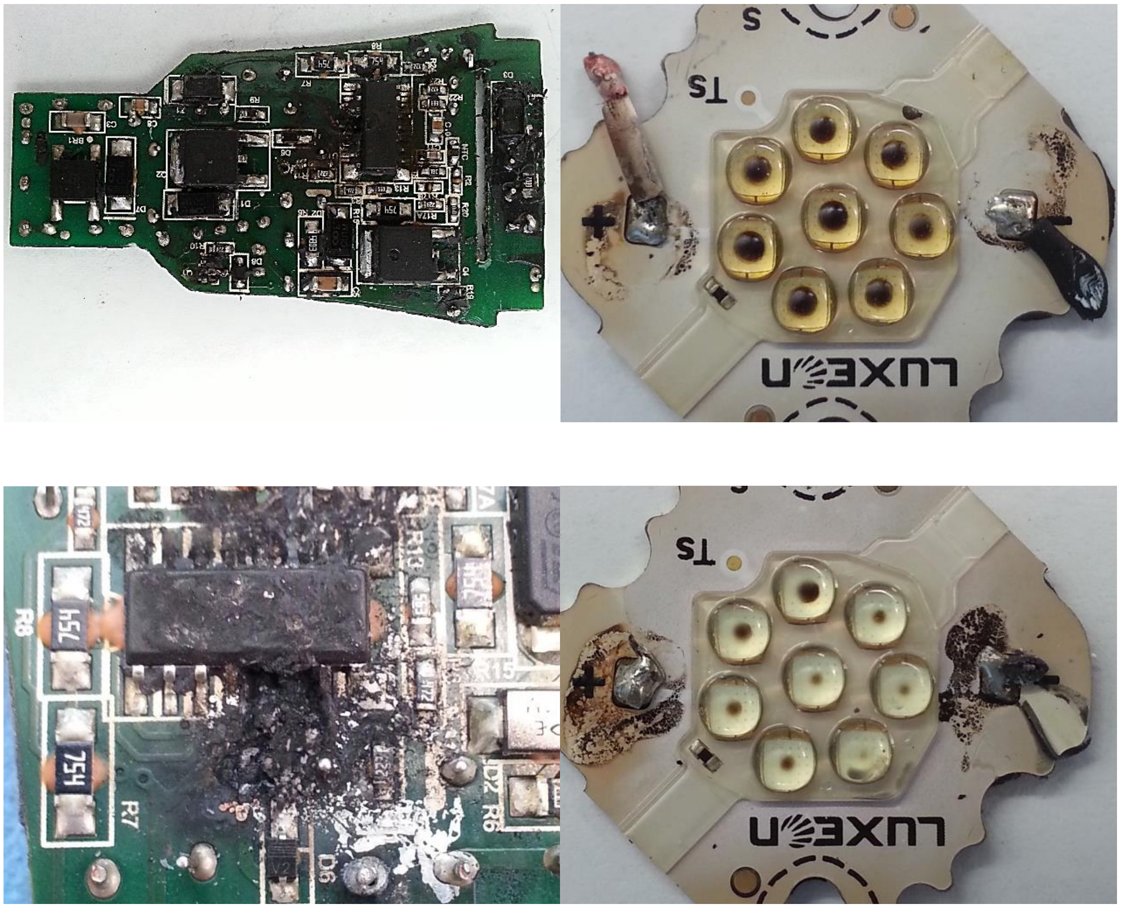

Figure 136: Failure Mode of PWW 7 (Top) and PWW 8 (Bottom) – Catastrophic Degradation Due to an Electrical Fire that Burned a Hole into the Circuit Board and Encapsulant Degradation of the LED Array.

## 4.2. SSL ELECTRICAL DRIVERS

### 4.2.1. EDG1 PHM

The average of each capacitor's relative ESR and relative CAP for EDG1 at an aging time of 2120.33 hours is shown in Figure 137 – Figure 144. The proposed leading indicators of failure, relative CAP and ESR, are trending in the correct direction based off previously reported results in literature (Rubycon Corporation, 2013) (Nichicon Inc., 2002) (Han, 2009) (Harada, 1993) (Gasperi, 1996) (BHC Components, 2002) (Panasonic Industrial Company, 2008) (Cornell Dubilier Electronics Inc., 2000) (Celaya, 2011) (Ma,

2005) (Sankaran, 1997) (Stevens, 2002). The noise threshold has already been eliminated for each data set with the first datum point given a value of 100%.

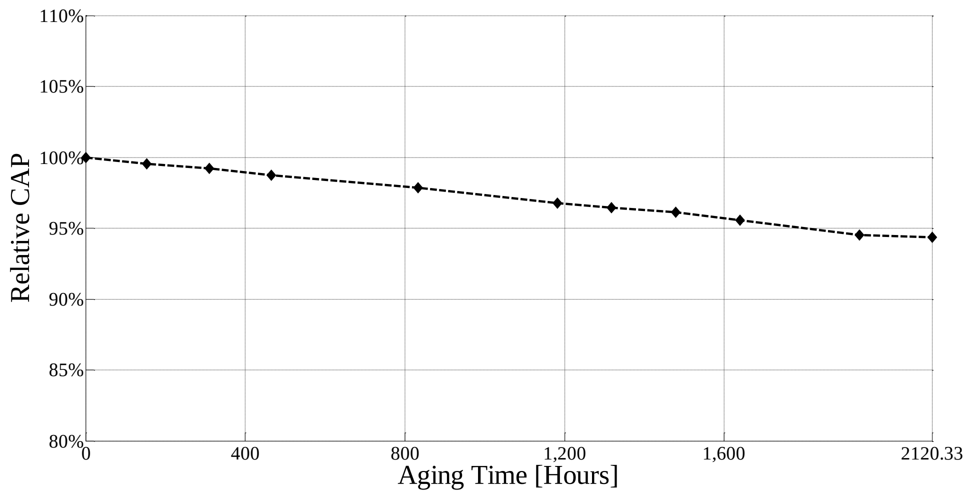


Figure 137: AEC One – Relative CAP of Average EDG1 at 135°C.


Figure 138: AEC One – Relative ESR of Average EDG1 at 135°C.

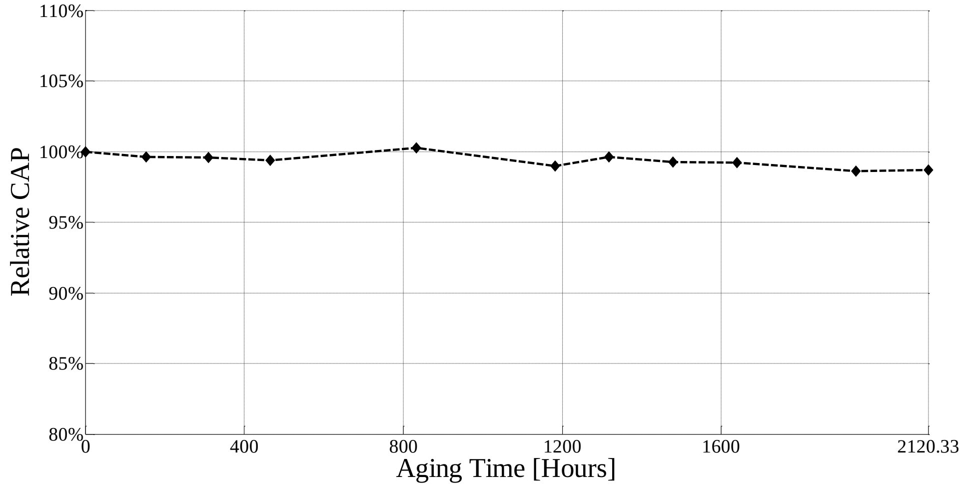


Figure 139: AEC Two – Relative CAP of Average EDG1 at 135°C.

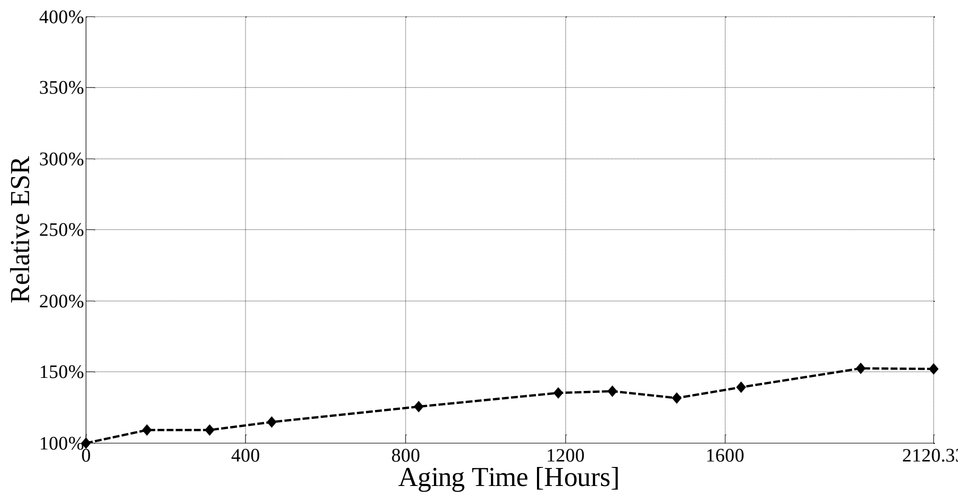


Figure 140: AEC Two – Relative ESR of Average EDG1 at 135°C.

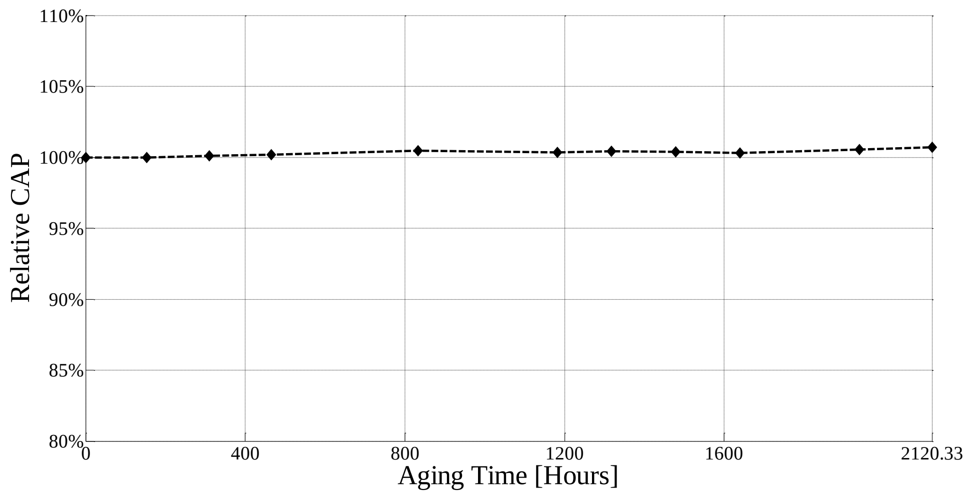


Figure 141: AEC Three – Relative CAP of Average EDG1 at 135°C.

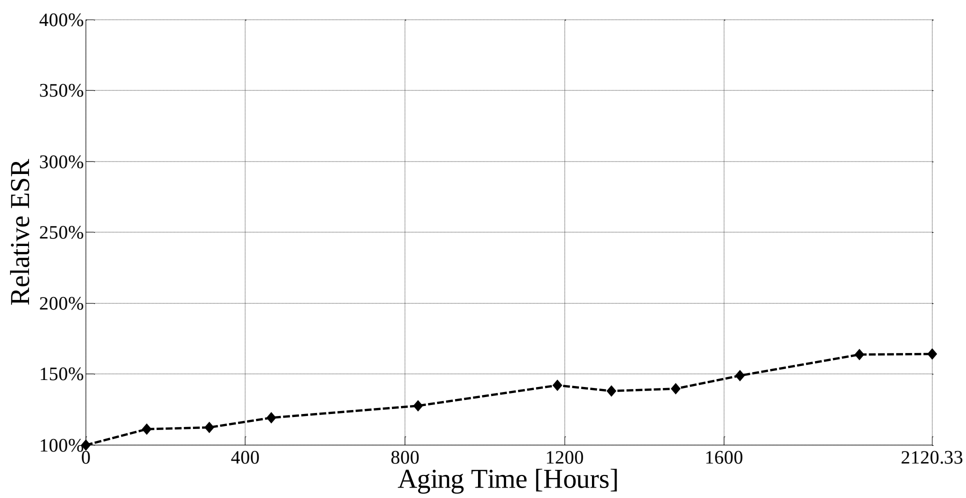


Figure 142: AEC Three – Relative ESR of Average EDG1 at 135°C.

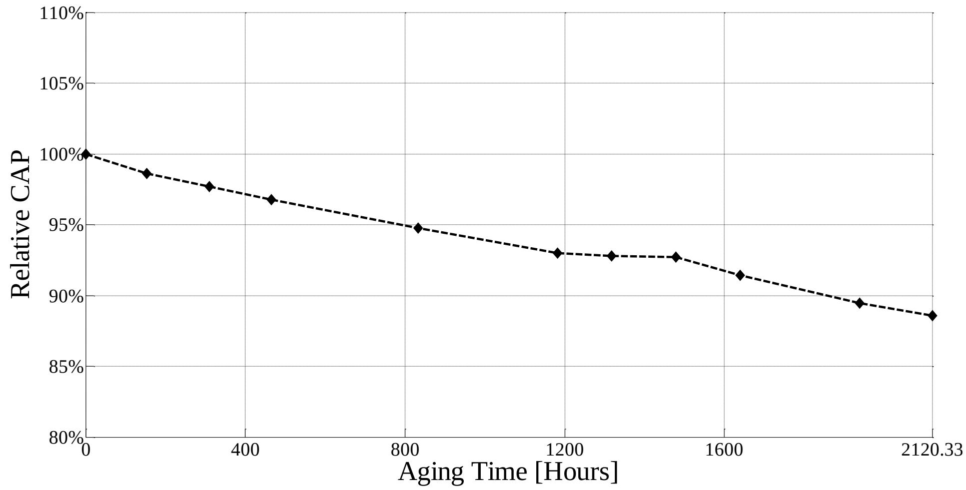


Figure 143: AEC Four – Relative CAP of Average EDG1 at 135°C.

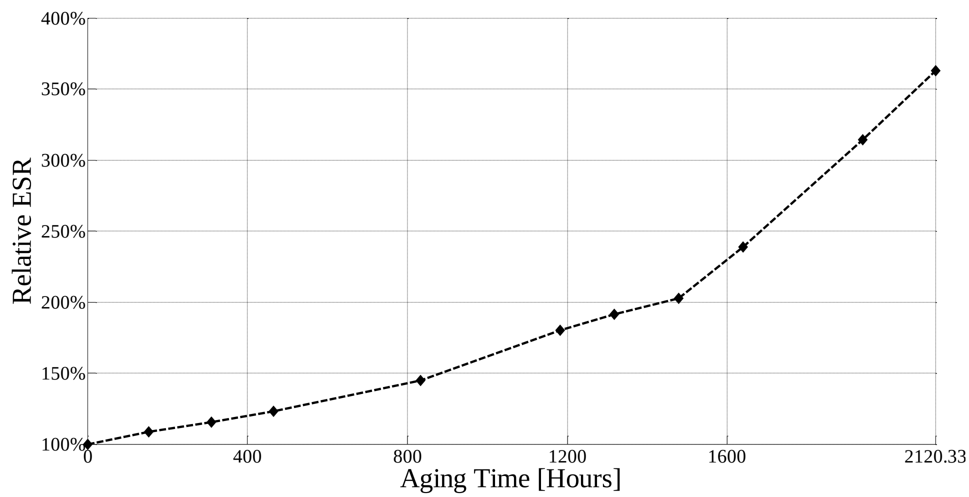


Figure 144: AEC Four – Relative ESR of Average EDG1 at 135°C.

The failure threshold for this work has been taken as 70% of the original luminous flux called L70 (IES, 2008a) (IES, 2008b) (IES, 2011) (IES, 2014a) (IES, 2014b). The pristine luminous flux value of the LE used to monitor the output of the EDs is 2000 lm ± 10%. The L70 value of the LE was not obtained due to the EDs under test delivering the correct voltage output to the LE. The average relative luminous flux value for each measurement time is shown in Figure 145 with the rated pristine luminous flux range and L70 location.

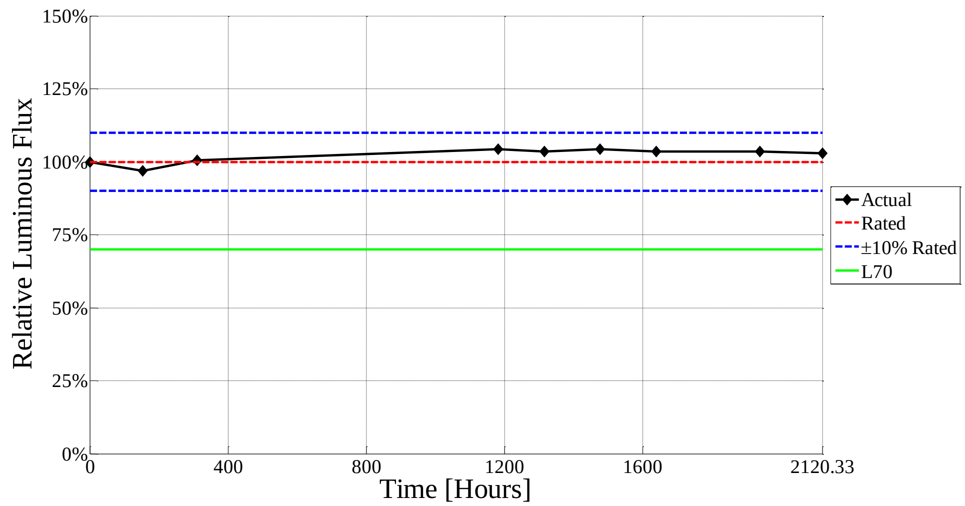


Figure 145: Average RLF of the Pristine Light Engine from EDG1 at 135°C.

From Figure 145, the RLF value of the LE is pristine and well within the pristine boundaries. Therefore, no correlation between the degradation of the AEC values, relative CAP and ESR, and the output of the LE was observed. Since the EDs are still supplying the required voltage to produce a pristine RLF value of the LE, the AECs have not “failed” in a traditional sense even though there is a large amount of degradation occurring within AEC One and AEC Four.

Figure 139 – Figure 142 show little to no change in the relative CAP and ESR measurements of AECs Two and Three. Both of these AECs are reading at approximately 100% at each collected relative CAP value with only a slight change in the relative ESR. This infers that these two AECs have the most impact on the relative luminous flux output of the electrical drivers.

Figure 137 – Figure 138 and Figure 143 – Figure 144 depict a different story. AECs One and Four are trending almost identically producing suitable degradation curves for a data driven approach to train a PHM framework to make RUL predictions. After careful study of the ED's circuit diagram, it has been determined that AEC One is at an optimal location for the possible implementation of a sensor to monitor CAP and ESR change compared to the location of AEC Four. For this reason, AEC One was used to demonstrate the ability of a PHM framework to accurately monitor damage accrual. Since the overall health of the SSL system could not be quantified with RLF degradation, the RUL was quantified using the collected data from AEC One. The RUL predictions were determined using a failure threshold of ten times the length of aging time, 2120.33 hours, due to the exact $t_{eol}$ being unknown. The relative CAP and ESR values for AEC One have been used along with the KF algorithm to track the degradation of the SSL system in order to prognosticate the RUL. Figure 147 and Figure 146 graphically depicts the actual data, the filtered data and the predicted RUL for the relative CAP and ESR, respectively.

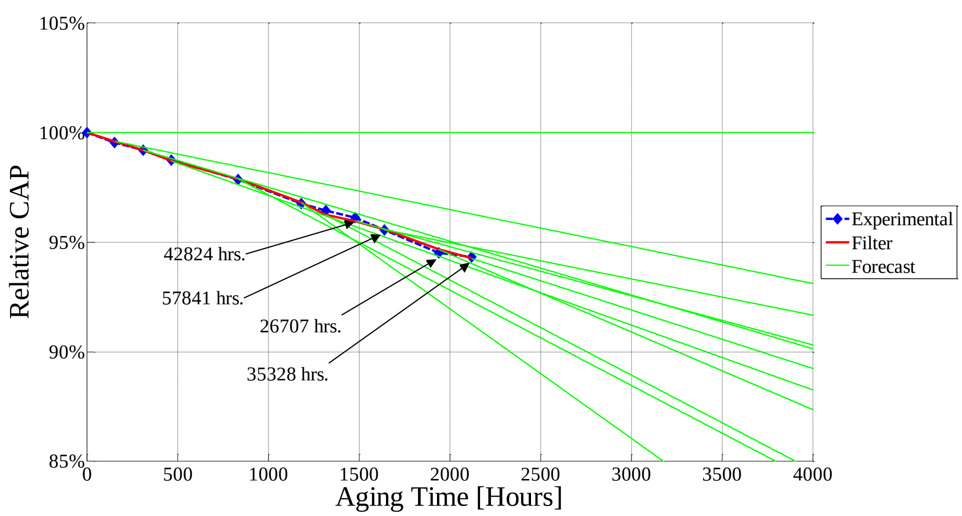


Figure 146: AEC One – KF of Relative CAP from EDG1 Average.

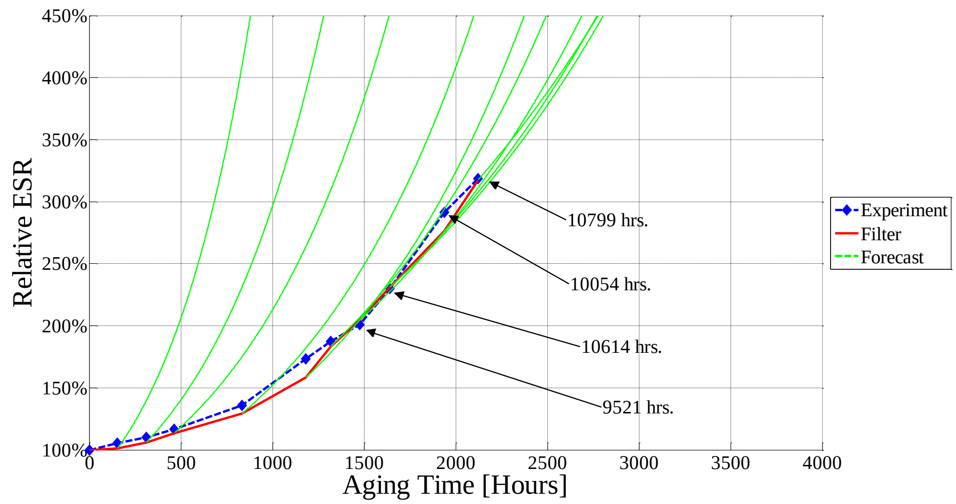


Figure 147: AEC One – KF of Relative ESR from EDG1 Average.

The KF algorithm was trained using a data driven approach using the collected data. The KF tracks the relative CAP and ESR data with a high degree of accuracy as shown in Figure 146 and Figure 147, respectively. The KF model prognosticated the RUL of relative ESR with a higher degree of accuracy than the relative CAP since it began to converge toward a common point at the end of the ESR predictions. This exhibits a well-trained algorithm to prognosticate RUL. Conversely, the forecasted relative CAP still has a lot of variation in the RUL predictions which makes it necessary to collect more data to properly train the model to obtain to accurate predictions.

To validate these claims and evaluate the robustness of the PHM algorithm, the alpha-lambda performance metric was used to compare the actual RUL against the predicted RUL (Saxena A. C., 2008) (Saxena A. C., 2009a) (Saxena A. C., 2009b). This metric demonstrates the robustness of the KF algorithm's RUL predictions. Since $t_{eol}$ was not known prior to this analysis, the last measurement time, 2120.33 hours, was considered a pseudo $t_{eol}$ for the estimation of the RUL for both relative CAP and ESR. Figure 148 and

Figure 149 illustrate the alpha-lambda performance metrics for relative CAP and ESR, respectively.

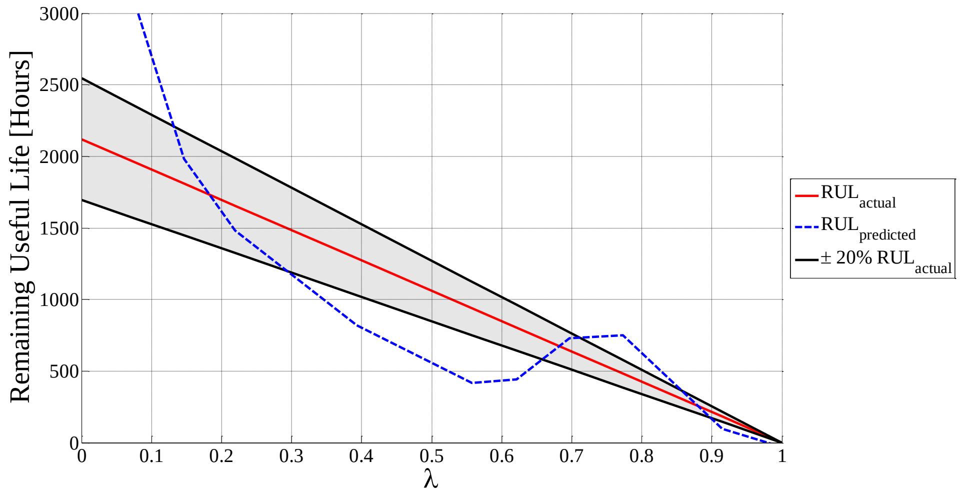


Figure 148: AEC One – α-λ of Relative CAP from EDG1 Average.

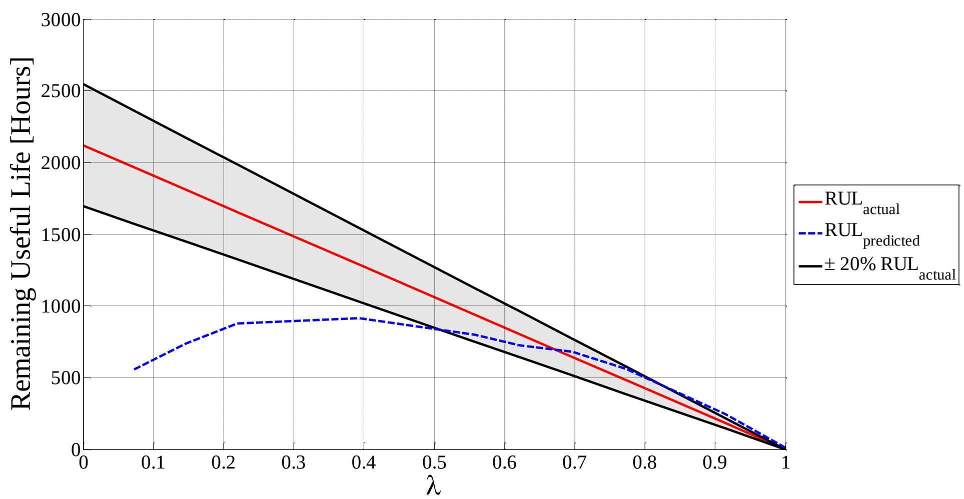


Figure 149: AEC One – α-λ of Relative ESR from EDG1 Average.

The gray shaded area in the alpha-lambda graphs is called the alpha bounds. It provides a region to describe the accuracy of the algorithm and is taken at ± 20 % of the actual RUL. If the predicted RUL falls within the alpha bounds, then it is taken as a correct prediction. Lambda is defined as the time normalized with $t_{eol}$. When lambda equals one, the part has "failed".

Figure 148 demonstrates RUL predictions of relative CAP that oscillate above and below the alpha bounds which requires more data to better train the KF algorithm to fix the overshoot and undershoot of the RUL predictions. The collection of more data will give greater insight as to the usefulness of this proposed leading indicator to monitor the health of the SSL system.

In Figure 149, the KF algorithm under predicted the RUL of the Relative ESR in the beginning and never over predicts the RUL. Typically, it is better to under predict than to over predict. The predicted RUL starts to converge towards the actual RUL and stays within the alpha bounds at about half way through the collected data. This means that the algorithm has sufficiently forecasted the $t_{eol}$ of the relative ESR. This also demonstrates that this proposed leading indication of failure may prove to be useful to monitor the overall health of the SSL system.

Data collection of EDG1 was continued until the ALT experiment was stopped at 7166 hours. The ALT for the AEC's went past that of the EDs to investigate the possibility of thermally activated failure mechanisms present in a high temperature storage condition. This was due to the large differences in the relative CAP and ESR values from the pristine values, as well as the inability to use the EDs to monitor overall health of the SSL system by means of RLF. The plastic interconnects used to attach the ED to the LE and AC power became too degraded to safely connect AC power. Figure 150 - Figure 157 illustrates the entire dataset for EDG1.

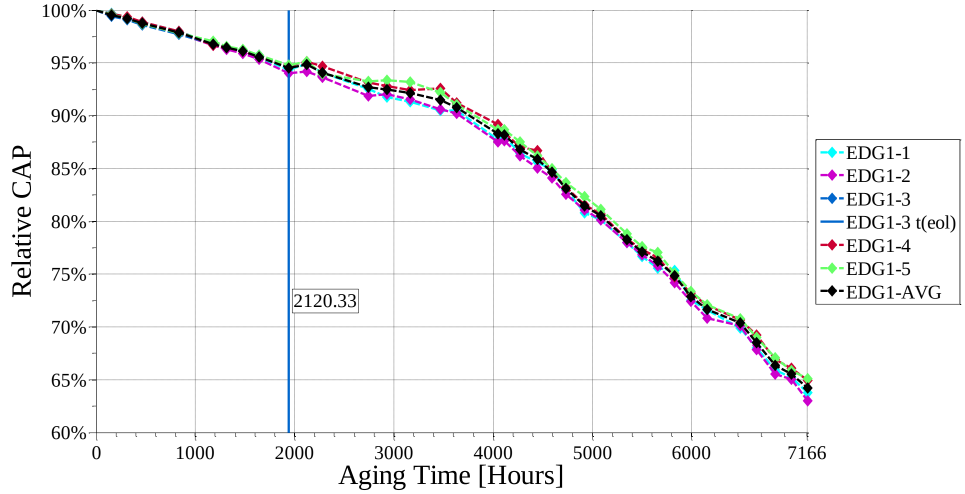


Figure 150: AEC One – Relative CAP of EDG1.

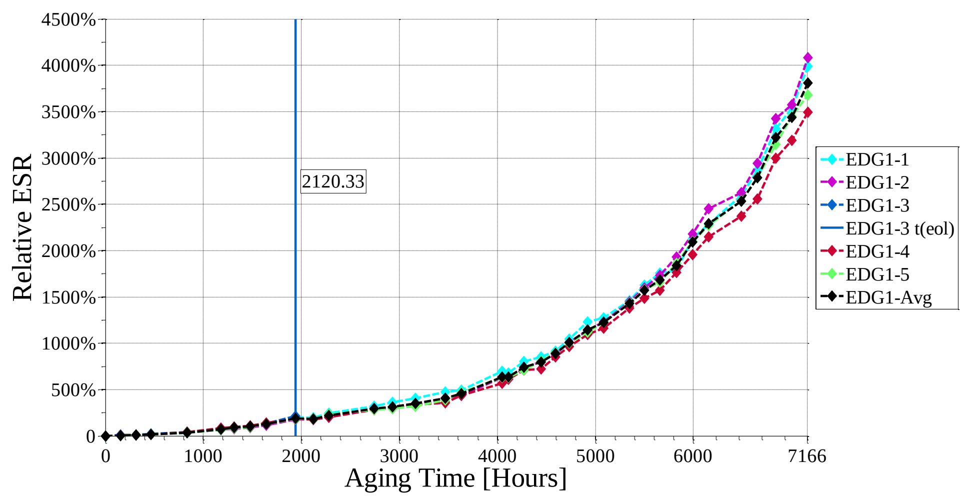


Figure 151: AEC One – Relative ESR of EDG1.

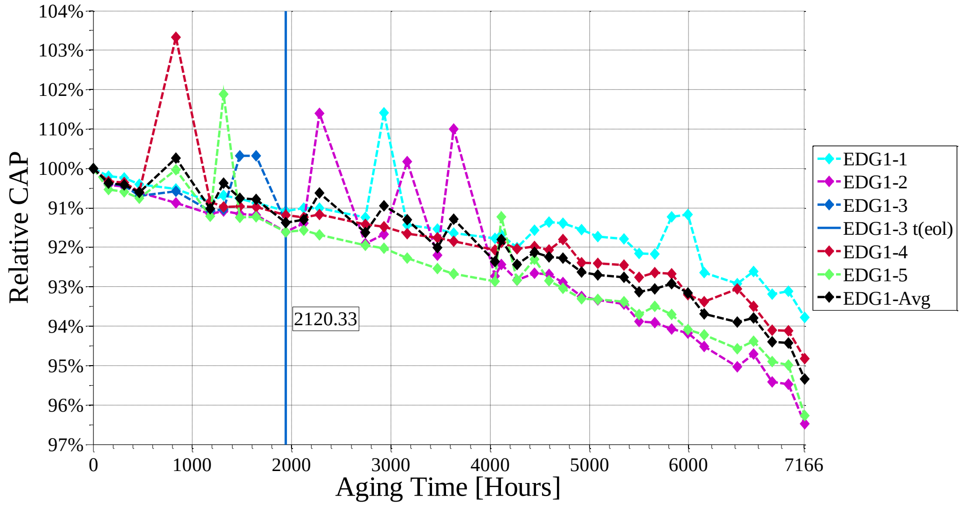


Figure 152: AEC Two – Relative CAP of EDG1.

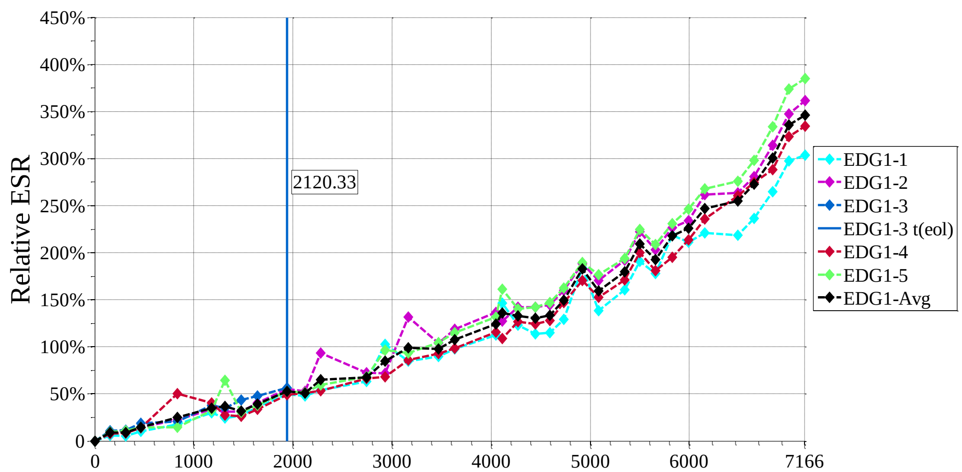


Figure 153: AEC Two – Relative ESR of EDG1.

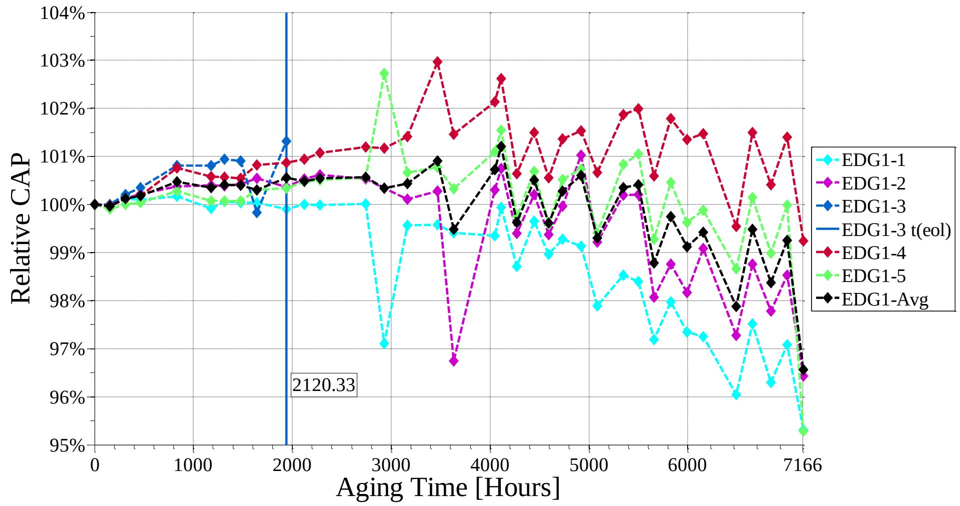


Figure 154: AEC Three – Relative CAP of EDG1.

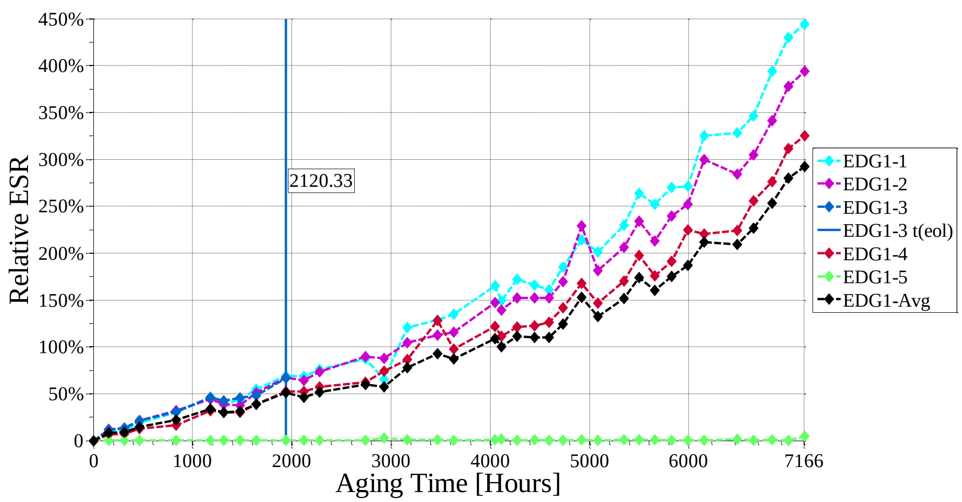


Figure 155: AEC Three – Relative ESR of EDG1.

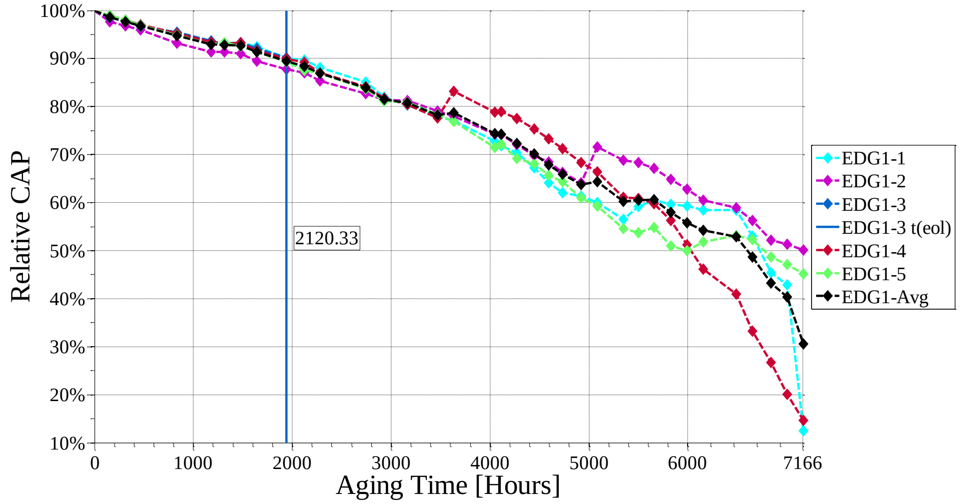


Figure 156: AEC Four – Relative CAP of EDG1.

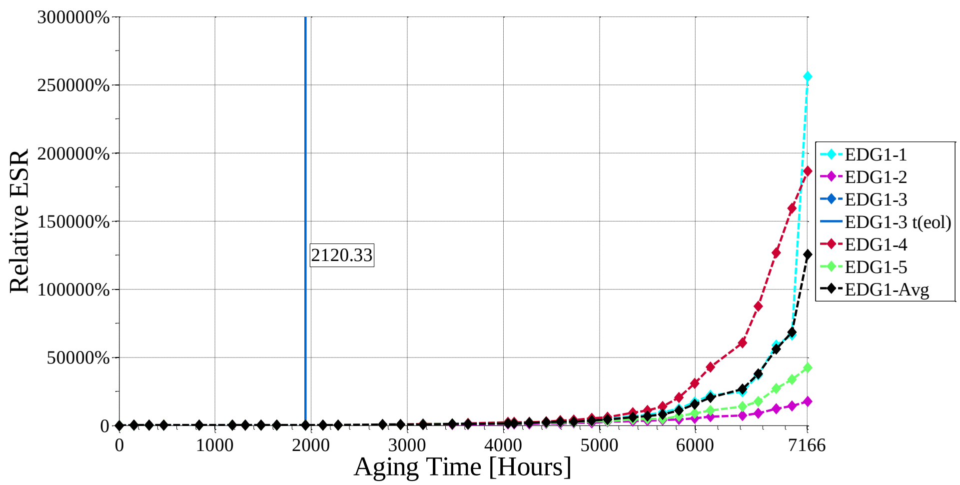


Figure 157: AEC Four – Relative ESR of EDG1.

The average values of CAP and ESR for the complete dataset of AEC One was used with the EKF and KF for the establishment of a PHM framework. The estimated state, the remaining useful life, the beta performance metric and the relative accuracy metric are shown for CAP and ESR in Figure 158 - Figure 165.

A) 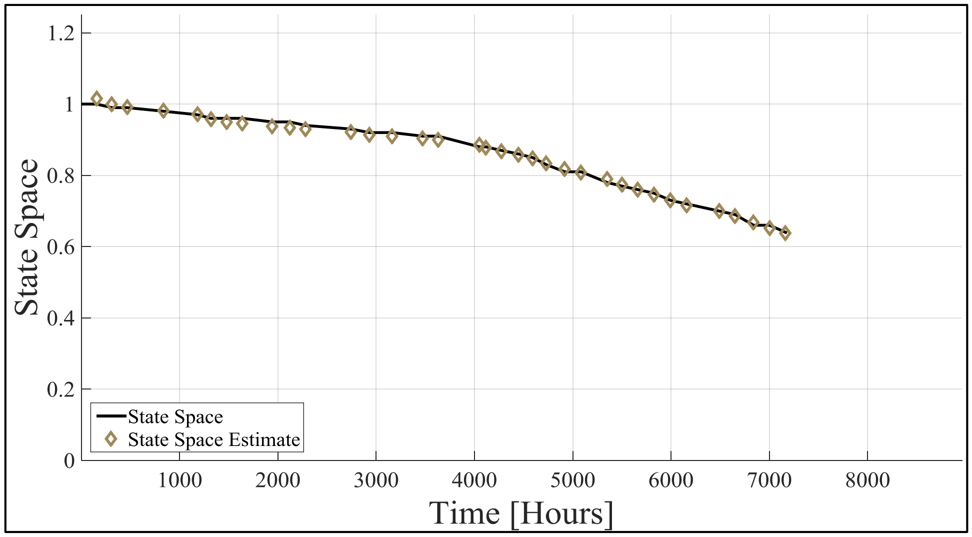


B) 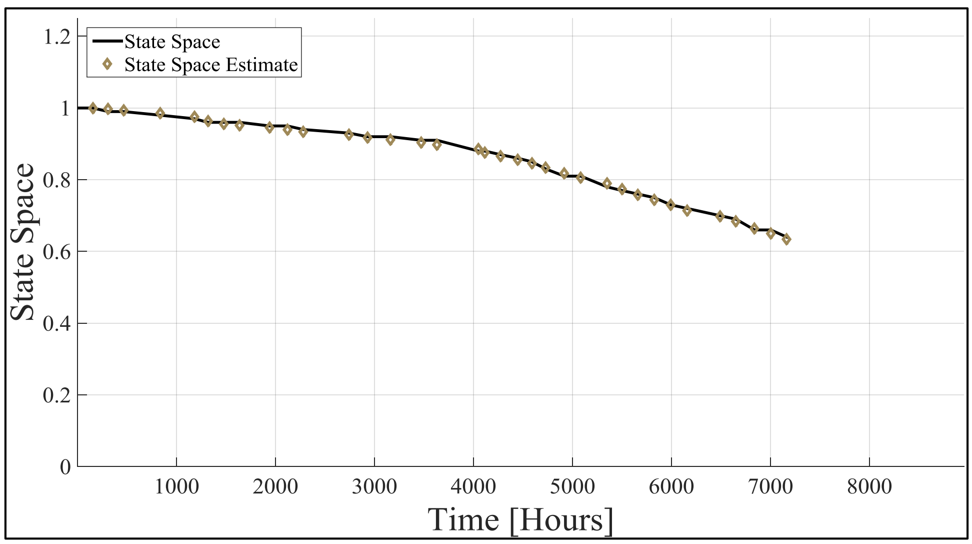


Figure 158: EDG1 – AEC One Relative Capacitance State Space for A) KF and B) EKF.

A)

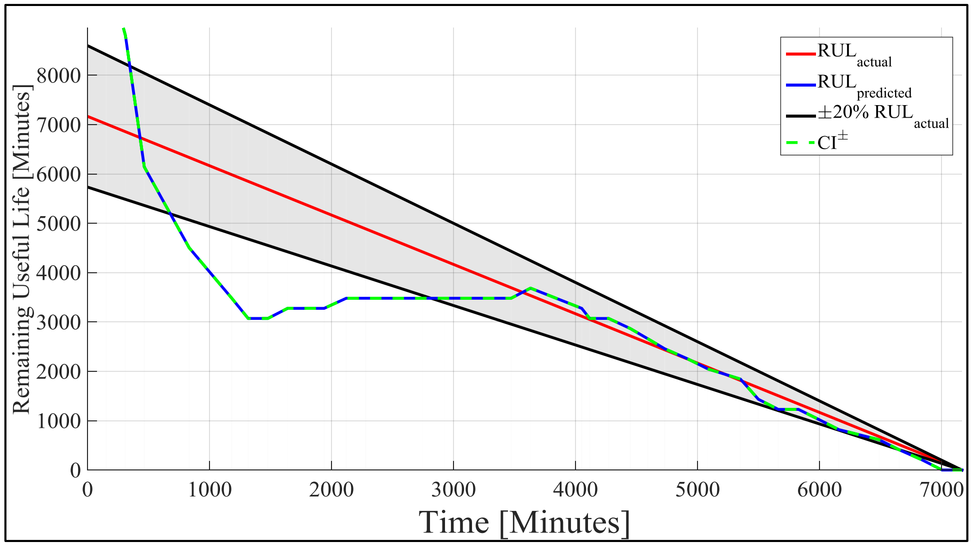


B)

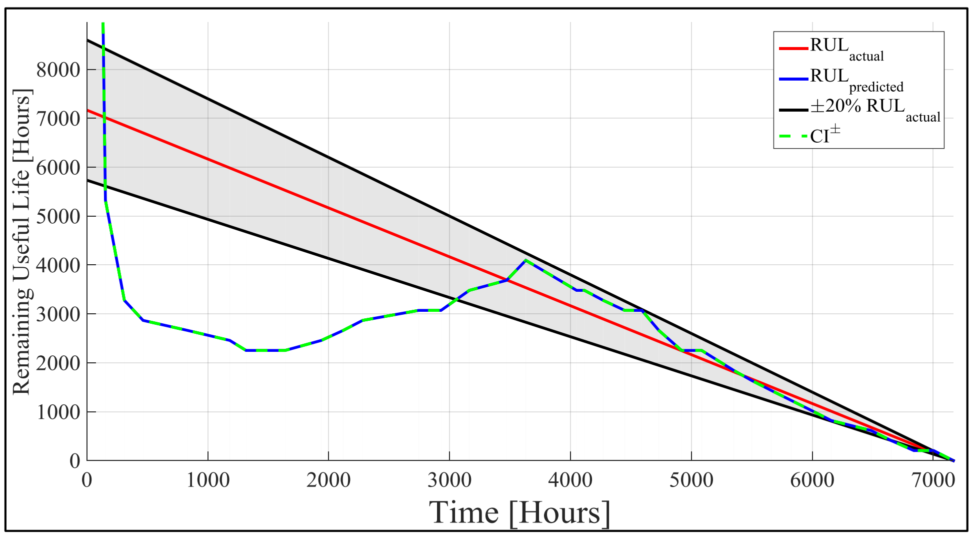


Figure 159: EDG1 – AEC One Relative Capacitance RUL for A) KF and B) EKF.

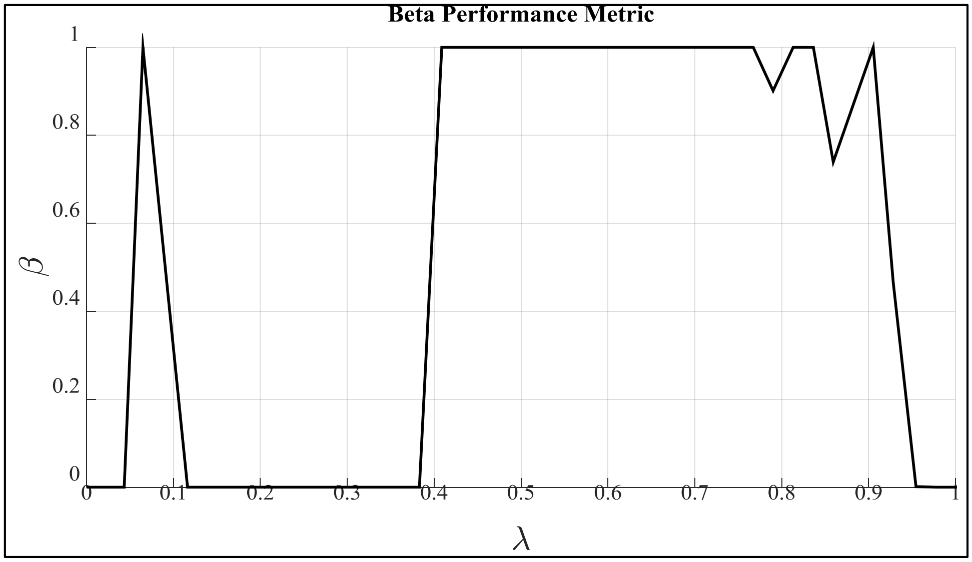


A)

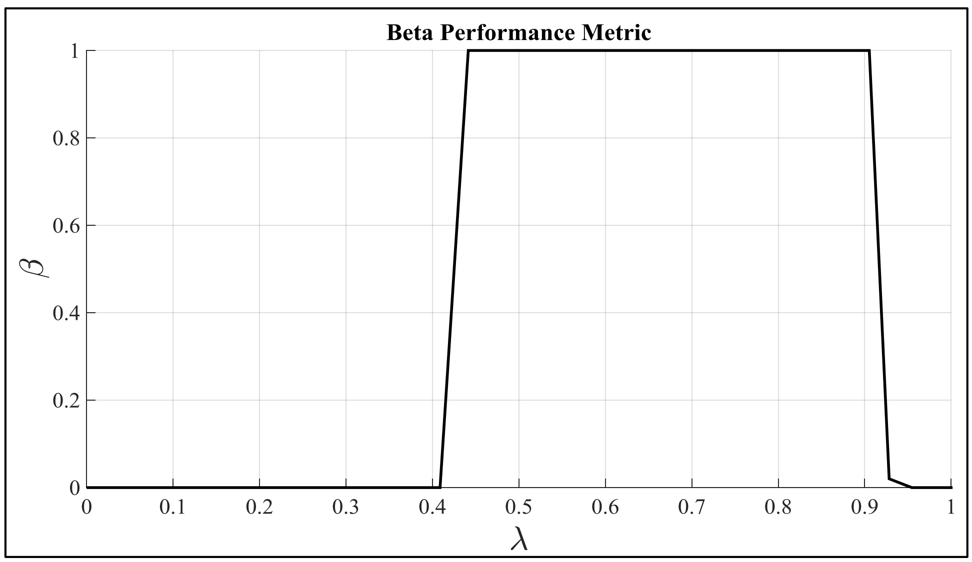


B)

Figure 160: EDG1 – AEC One Relative Capacitance Beta Metric for A) KF and B) EKF.

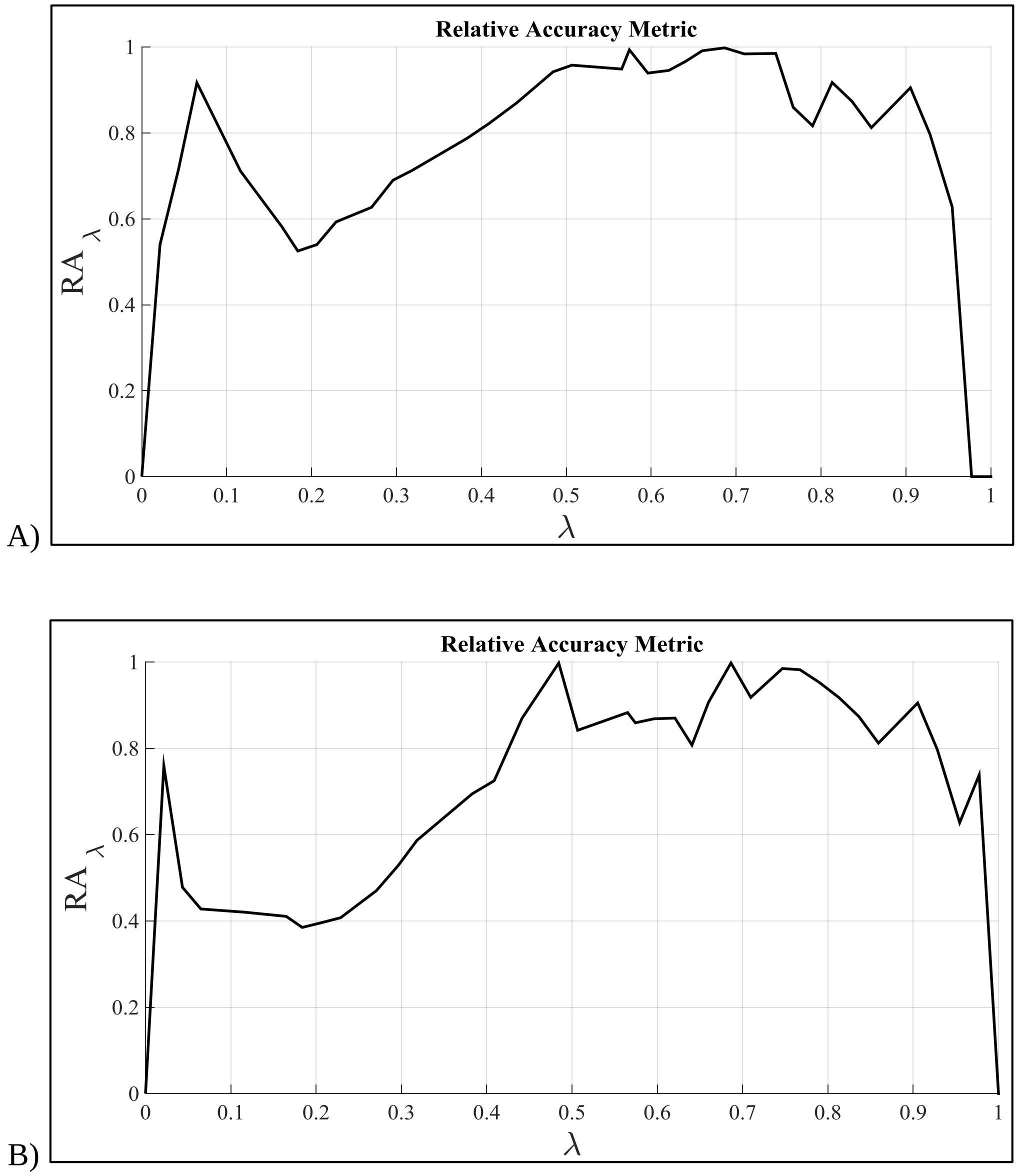


Figure 161: EDG1 – AEC One Relative Capacitance Relative Accuracy Metric for A) KF and B) EKF.

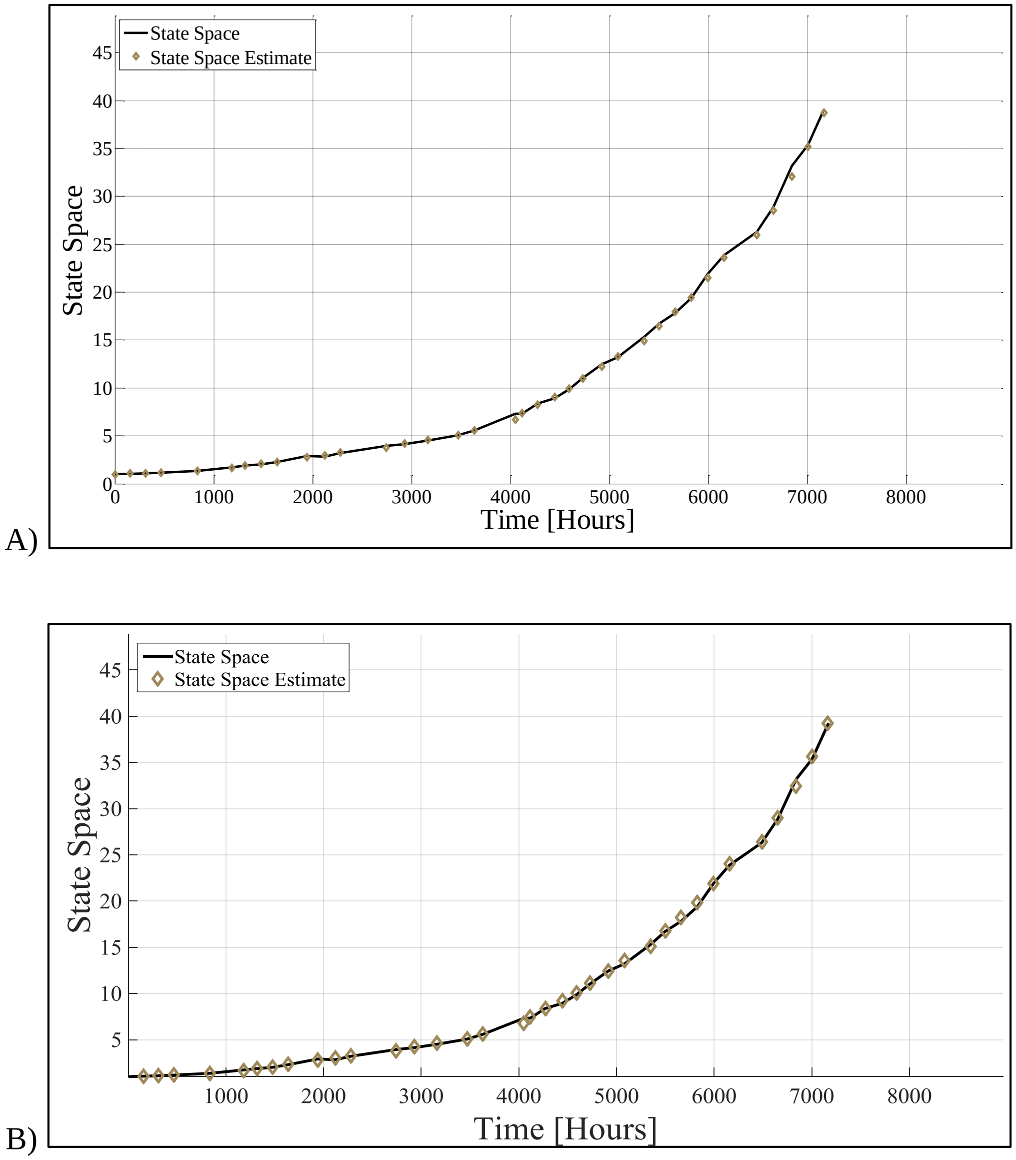


Figure 162: EDG1 – AEC One Relative ESR State Space for A) KF and B) EKF.

A)

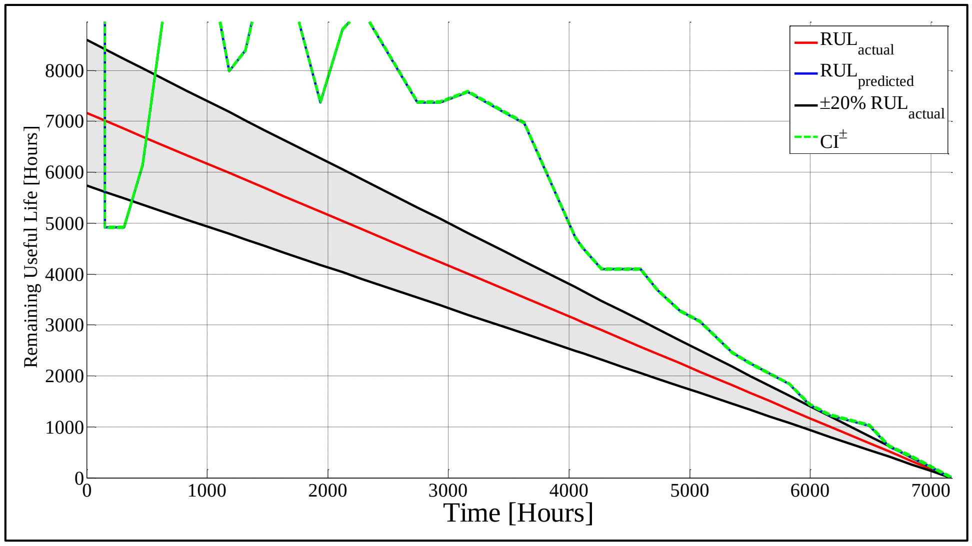


B)

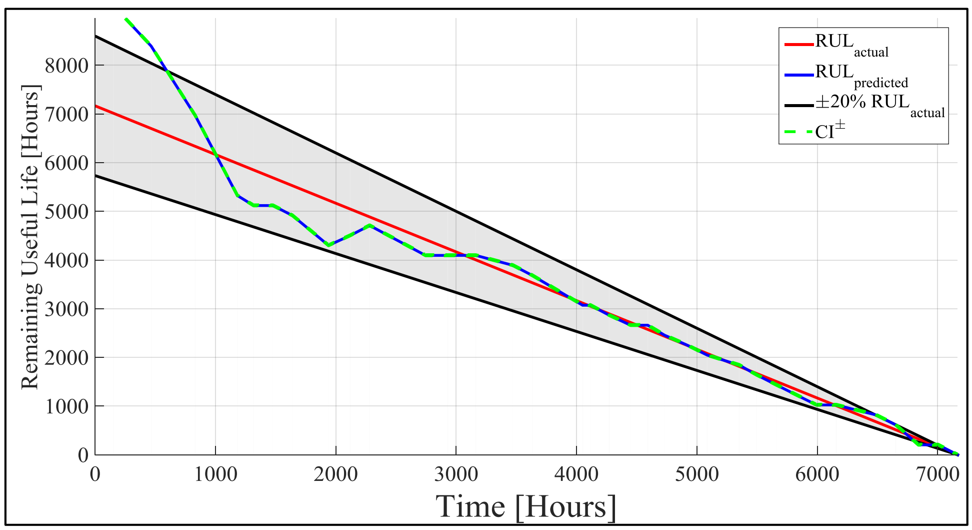


Figure 163: EDG1 – AEC One Relative ESR RUL for A) KF and B) EKF.

A)
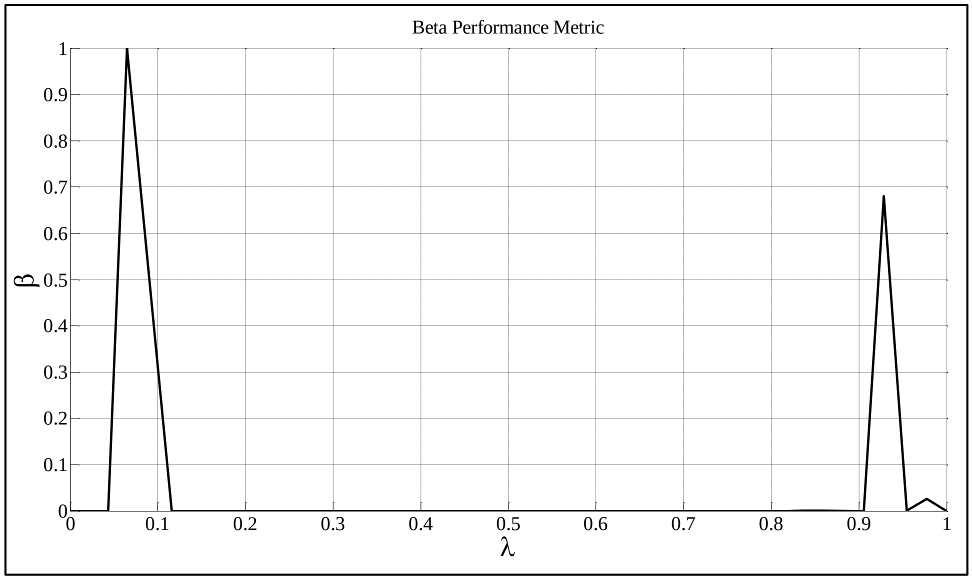


B)
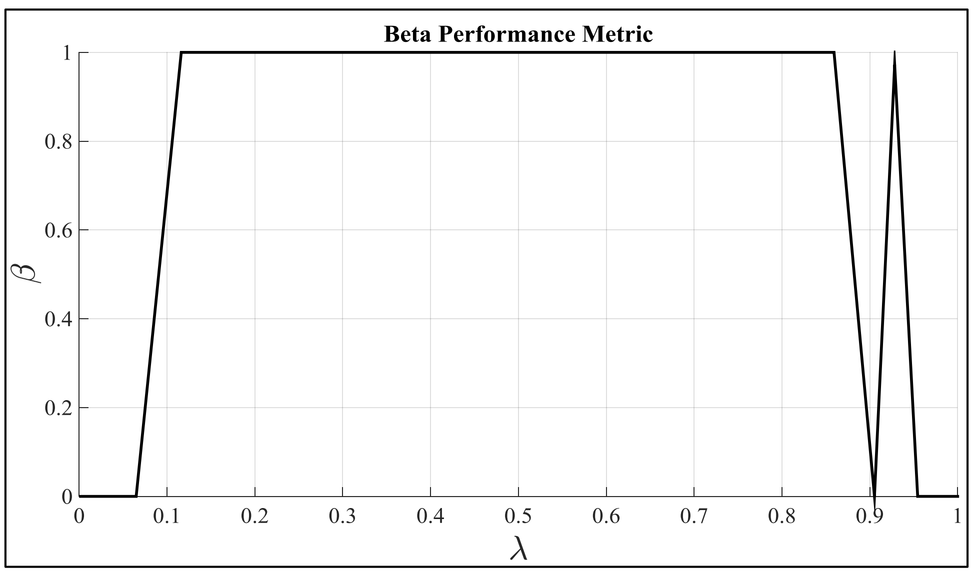


Figure 164: EDG1 – AEC One Relative ESR Beta Metric for A) KF and B) EKF.

A)

B)

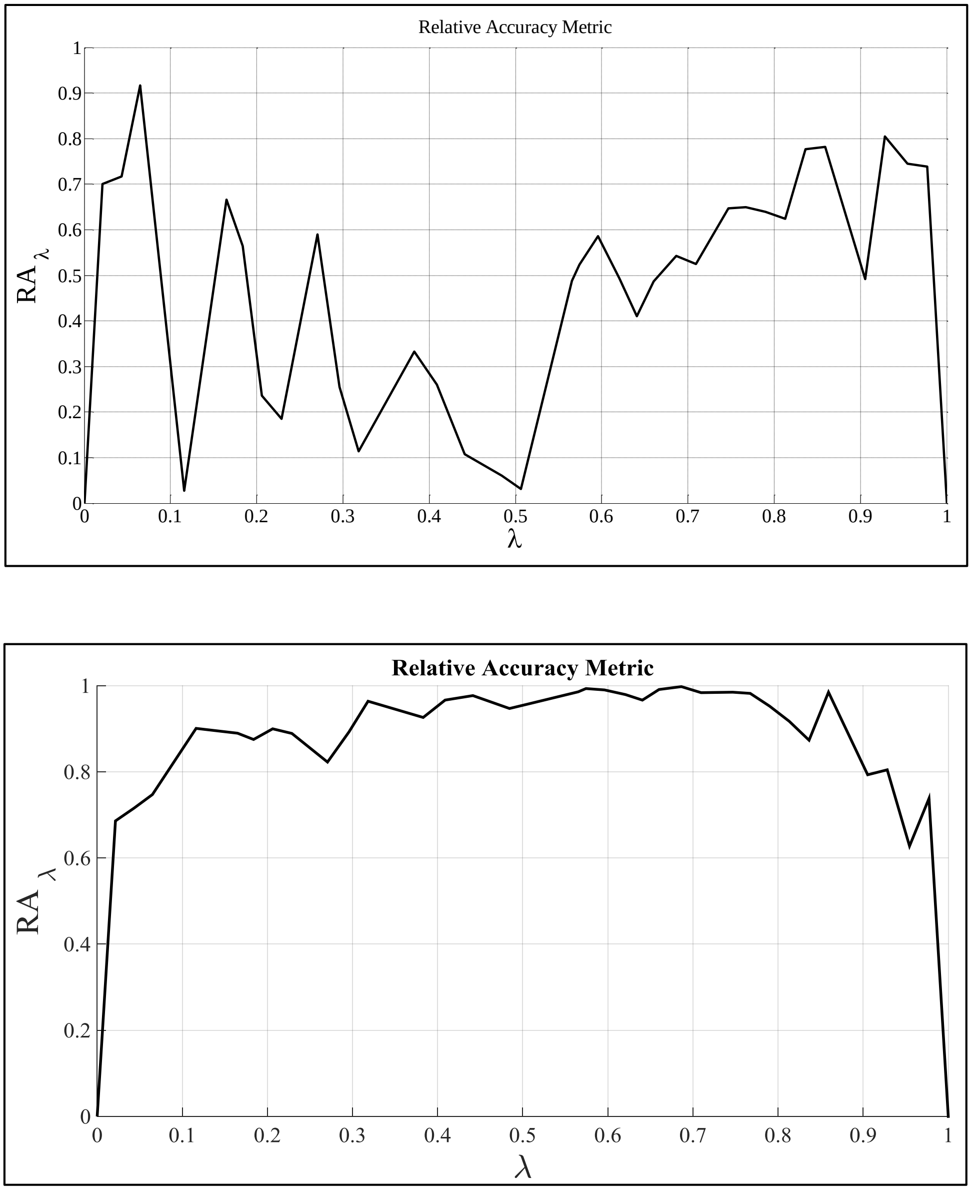


Figure 165: EDG1 – AEC One Relative ESR Relative Accuracy Metric for A) KF and B) EKF.

From the PHM analysis, the relative CAP and ESR was estimated successfully from the EKF and the KF. The relative CAP showed little difference between the performances of the two filters. Both the KF and EKF produced similar RUL predictions and can be effectively used to predict the RUL using relative capacitance as the leading indicator of failure.

However, the performance of the EKF and KF differed drastically when the relative ESR was used as the leading indicator of failure. The KF produced unsuitable RUL predictions, while the EKF produced accurate estimates of the end of life. This is predominantly due to the sensitivity in the selection of the noise parameters. The EKF does not require as much accuracy when estimating the noise parameters, but the KF is highly sensitive to the selection.

The EKF has shown the most promise as a PHM tool for the prediction of the remaining useful life of the AEC using both the relative capacitance and the relative ESR. The KF, while successful with the capacitance, did not prove to be as robust as the EKF and should, therefore, not be used for end of life predictions for AECs in general.

### 4.2.2. EDG1 &EDG2 Comparison

After the data collection of EDG1 was stopped, an investigation into the thermally induced failure modes was conducted. It was observed that the degradation of the plastic interconnects was the primary source of failure. Table 29 details the failure analysis of EDG1.

Table 29: EDG1 Failure Analaysis.

| Driver | Failure Time [Hours] | Failure Site | Failure Mode |
|---|---|---|---|
| EDG1-1 | 3057.58 | Plastic Interconnects | Open Circuit |
| EDG1-2 | 3057.58 | Plastic Interconnects | Open Circuit |
| EDG1-3 | 2120.33 | AEC Two | Short Circuit |
| EDG1-4 | 3682.15 | Plastic Interconnects | Open Circuit |
| EDG1-5 | 3449.83 | Plastic Interconnects | Open Circuit |

Figure 166: Identification of the Failure Modes for EDG1.

The additional group of EDs from EDG2 was aged at 85°C/85% until complete failure occurred with the EDs at approximately 4294 hours as shown in Figure 167. The luminous flux for each ED never deviated outside of the pristine range given by the manufacturer through the course of the ALT experiment. RLF gave no indication of degradation or of the impending failure inside the EDs. Therefore, RLF was not a suitable indicator to describe the degradation of the EDG2. Each ED was tested until a failure mechanism became present rendering the ED inoperable.

The AECs were approximately aged for an additional 1000 hours before ALT was stopped. ALT was stopped due to the negligible change of the relative CAP and ESR, as well as the inability to relate CAP and ESR degradation to the SSL system. Testing was completely stopped for EDG2 at 5351.65 hours. Figure 168 – Figure 175 graphically shows the relative CAP and ESR of each AEC from EDG2. The fluctuations in the ESR values may be attributed to measurement error or a minute amount of atmospheric corrosion occurring on the metallic leads preventing a suitable connection of the measurement probes since corresponding values were closer to the actual pristine value. Additionally, the temperature condition for this test was well below the maximum rated operating temperature for the AECs which proved too small to induce degradation in the form of electrolytic loss. Furthermore, the construction of the AECs did not allow for the ingress of moisture that potentially would dilute the electrolyte producing a decrease in capacitance.

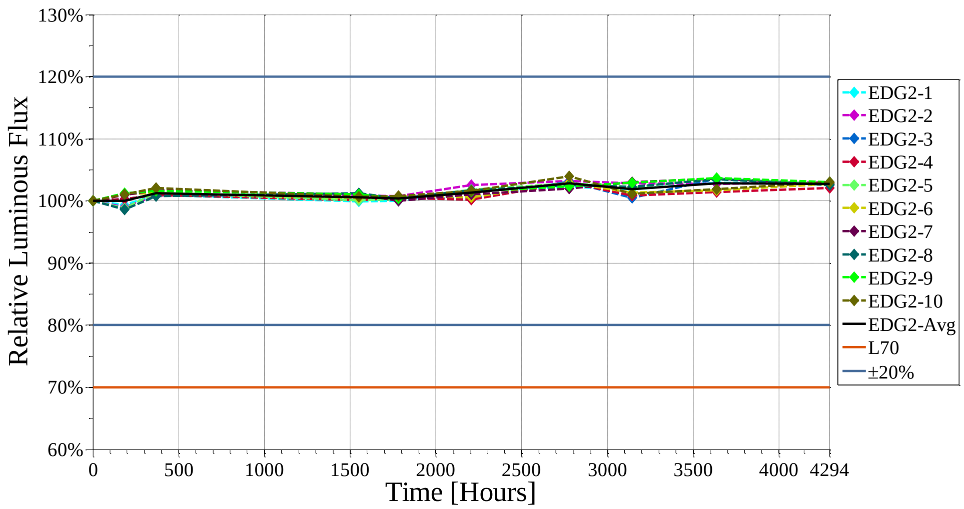


Figure 167: RLF of the Pristine Light Engine from EDG2.

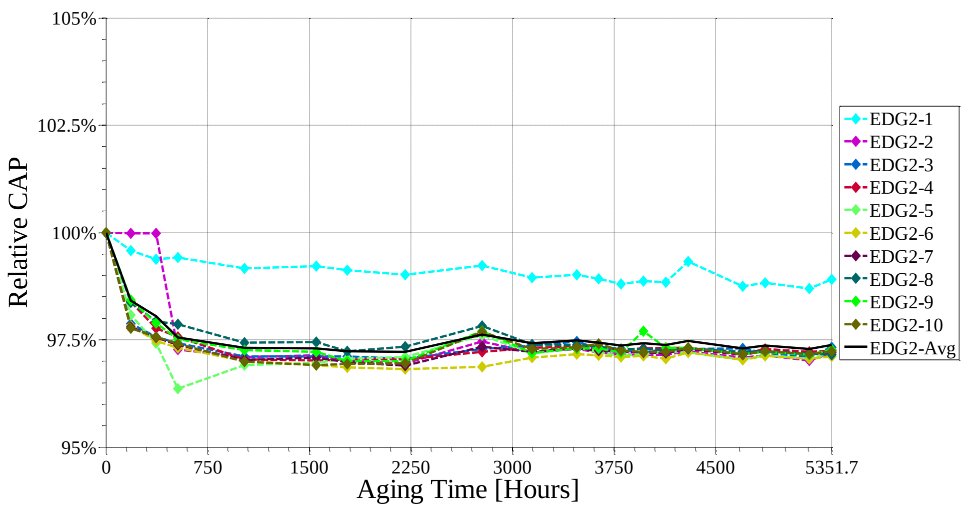


Figure 168: AEC One – Relative CAP of EDG2.

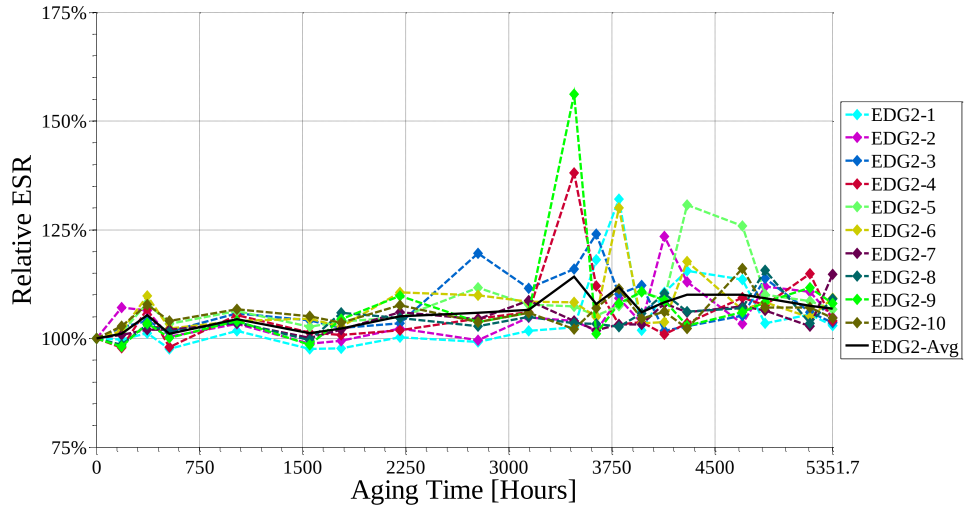


Figure 169: AEC One – Relative ESR of EDG2.

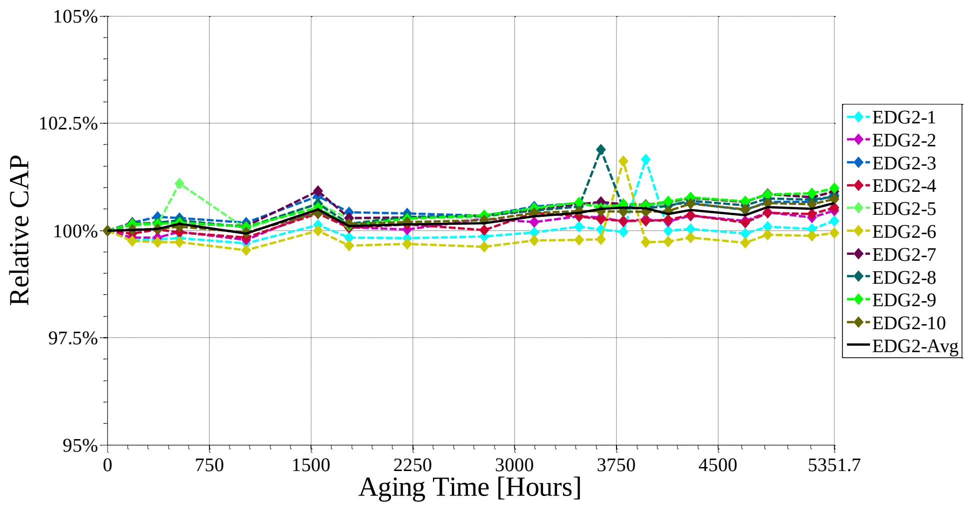


Figure 170: AEC Two – Relative CAP of EDG2.

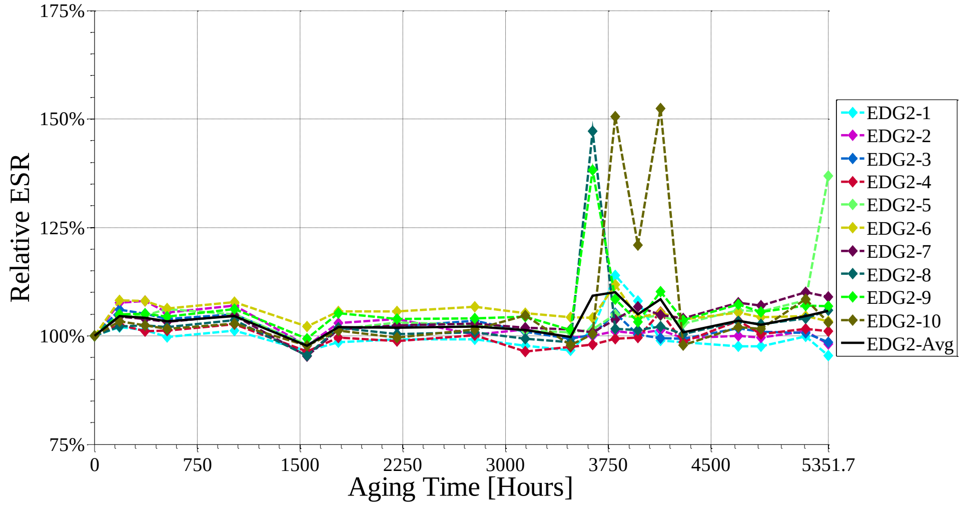


Figure 171: AEC Two – Relative ESR of EDG2.

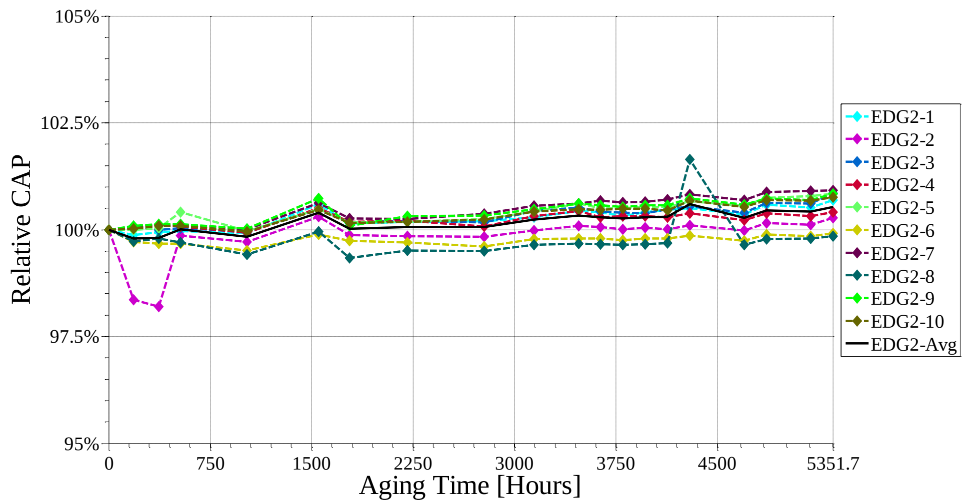


Figure 172: AEC Three – Relative CAP of EDG2.

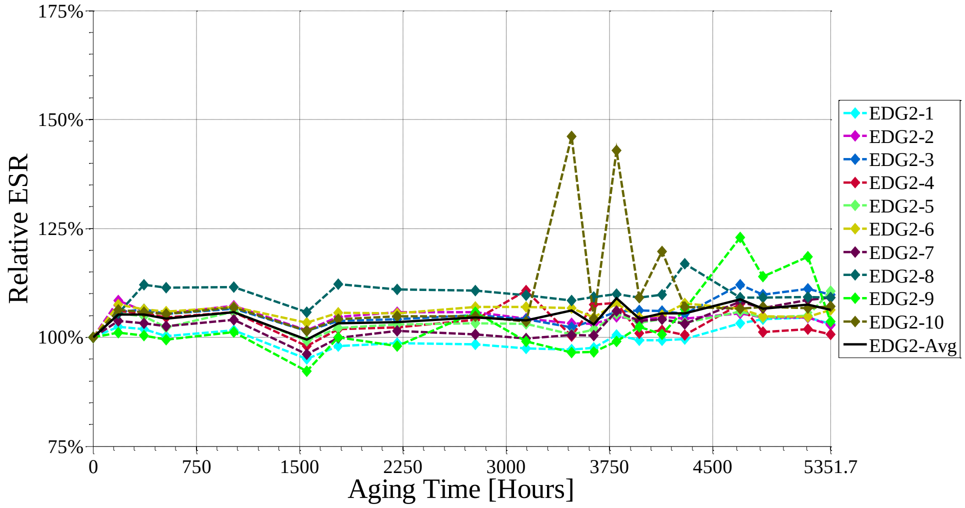


Figure 173: AEC Three – Relative ESR of EDG2.

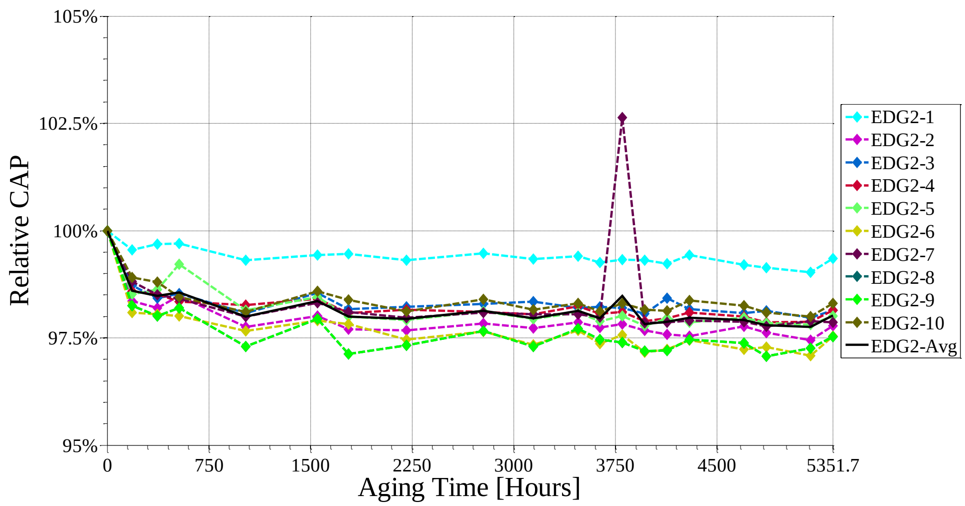


Figure 174: AEC Four – Relative CAP of EDG2.

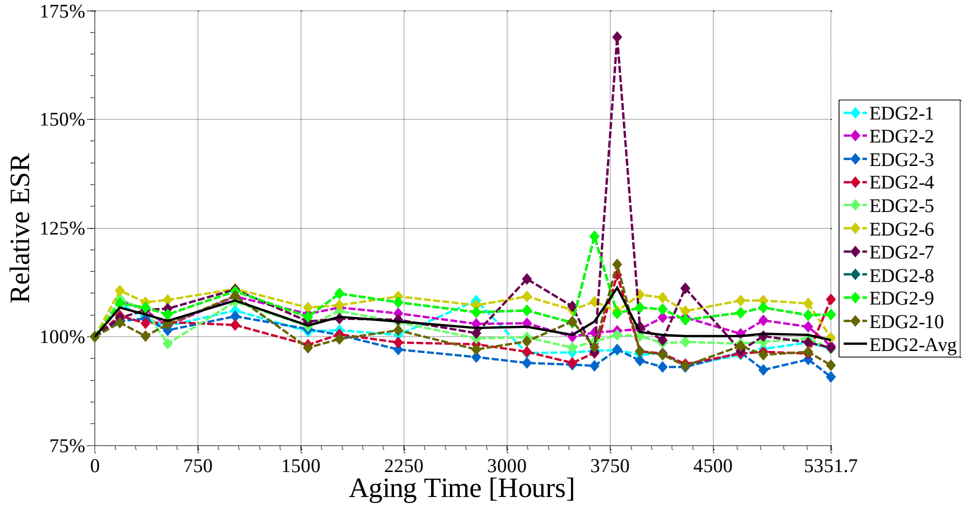


Figure 175: AEC Four – Relative ESR of EDG2.

Since relative CAP and ESR degradation was virtually nonexistent, the collected data from EDG2 was not suitable to use the PHM techniques shown with EDG1. The EDs from EDG2 did experience unforeseen component level failure which rendered each ED useless to some degree. Multiple failure sites have been determined with each ED experiencing only one of the failure sites. Table 30 catalogs the failure sites and failure modes of EDG2.

Table 30: EDG2 Failure Anaalysis.

| **Driver** | **Failure Time [Hours]** | **Failure Site** | **Failure Mode** |
|---|---|---|---|
| EDG2-1 | 333.37 | Gate Driver | Short Circuit |
| EDG2-2 | 0.00 | Unknown | Open Circuit |
| EDG2-3 | 3143.78 | CL21-S PFCAP | CAP Leakage |
| EDG2-4 | 3635.37 | CL21-S PFCAP | CAP Leakage |
| EDG2-5 | 0.00 | SMD-R 1206 | Short Circuit |
| EDG2-6 | 3635.37 | CL21-S PFCAP | CAP Leakage |
| EDG2-7 | 369.12 | Gate Driver | Short Circuit |
| EDG2-8 | 185.15 | SMD-C 1206 | Short Circuit |
| EDG2-9 | 369.12 | Gate Driver | Short Circuit |
| EDG2-10 | 3635.37 | CL21-S PFCAP | CAP Leakage |

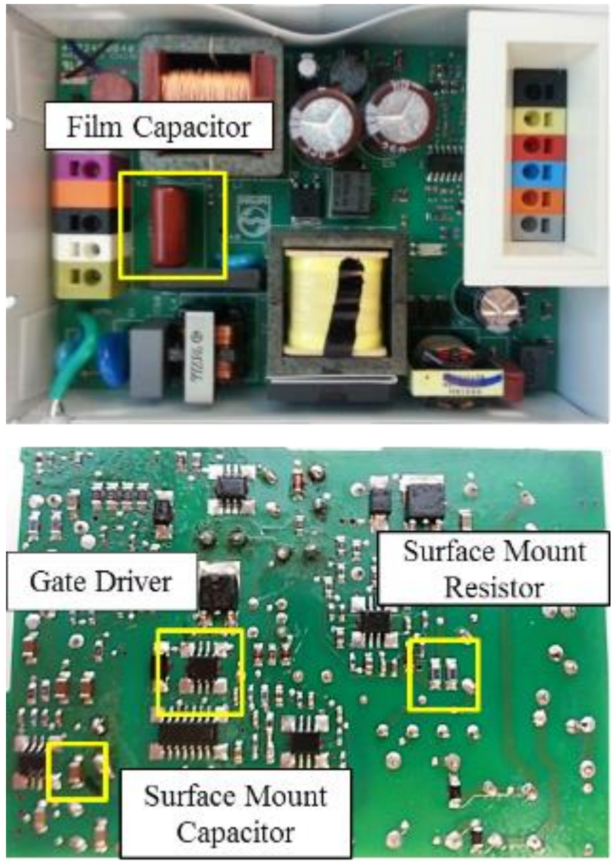


Figure 176: Identification of the Failure Sites for EDG2.

Figure 176 depicts a pristine ED from the top and bottom views to show the placement of each failed component inside the SSL system. The different failure sites detailed in Table 30 have been circled in yellow to show the components in their pristine form and their location inside the ED. Examples of the two predominate failure sites, the MOSFET and film capacitor, which engrossed 70% of the failures EDG2 encountered, is shown in Figure 177.

A)

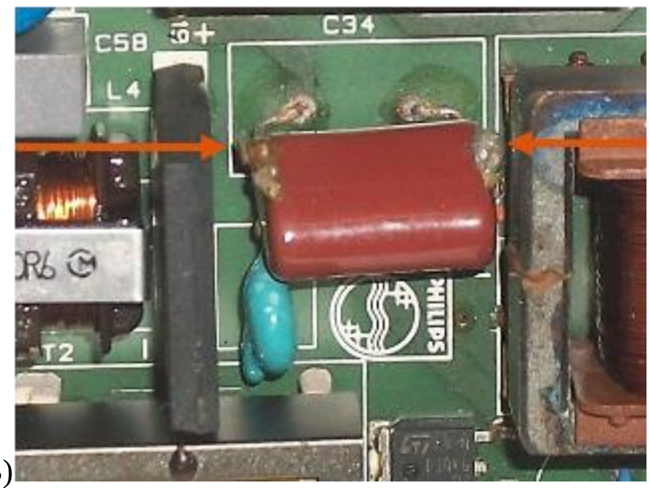


B)

Figure 177: An Example of a failed A) MOSFET and B) Film Capacitor from EDG2.

Since the relative CAP & ESR and the RLF of EDG2 did not give any sign of impending failure, additional photometric parameters were studied as possible leading indicators of failure for the SSL system at this ALT condition. The CCT, CIE 1976 chromaticity color space (u` & v`) and the color shift were calculated to investigate any possible interactions between the EDs and the LE for EDG2. The results are shown below in Figure 178 – Figure 181 with the values of each ED plotted on the same graph.

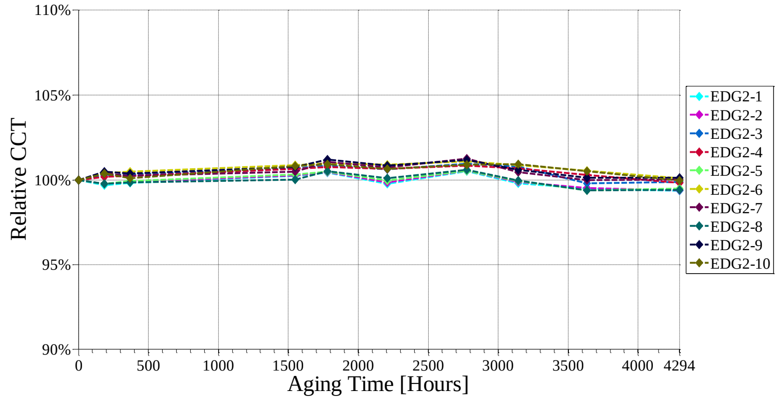


Figure 178: The relative CCT of the pristine LE with EDG2.

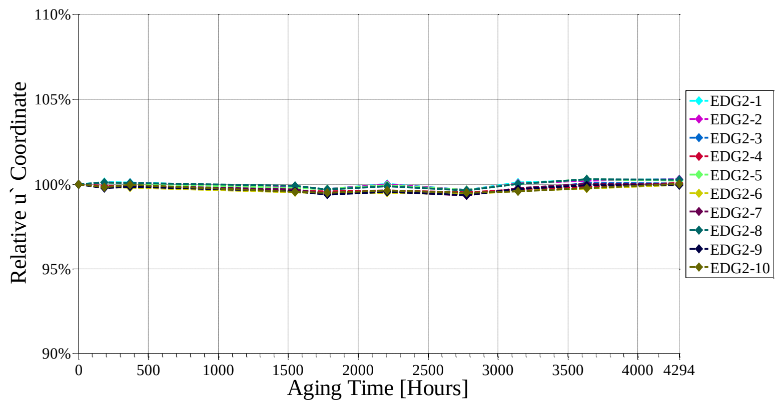


Figure 179: The relative u` from the CIE 1976 color space of the pristine LE with EDG2.

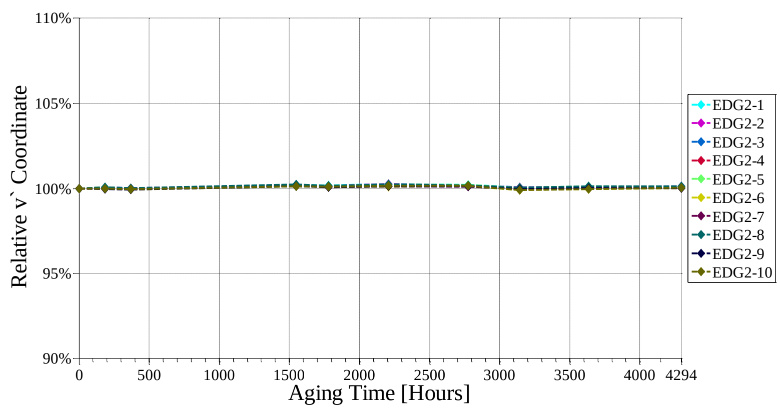


Figure 180: The relative v` from the CIE 1976 color space of the pristine LE with EDG2.

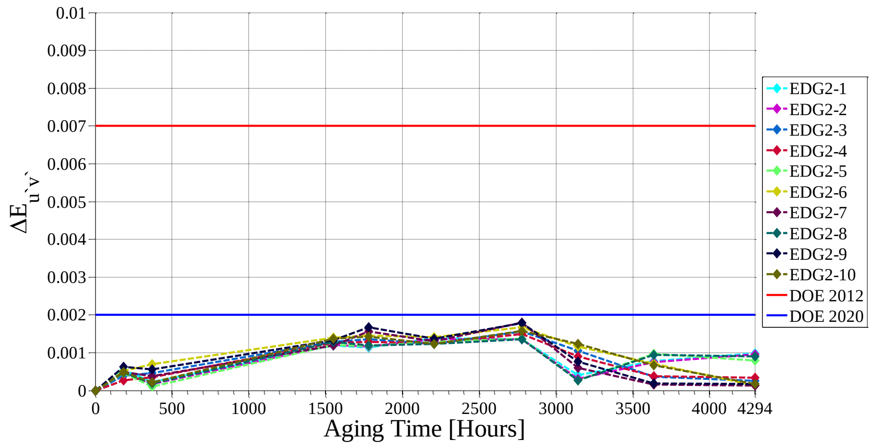


Figure 181: The CIE 1976 coordinate system color shift of the pristine LE with EDG2.

The CCT, u`-coordinate and v`-coordinate are virtually constant throughout the course of this ALT test. These parameters also suggest that the system is healthy with no indication of imminent failure inside the EDs. The color shift of the LE has a minimal to nonexistent change due to measure errors in the data collection. As a point of reference, the DOE's 2012 color shift target of 0.007 after 6000 hours and the 2020 target of 0.002 over the lifetime of the lighting system are given. The color shift for this SSL device stays below both DOE targets. Consequently, color shift did not forecast impending failure inside the EDs. From the photometric analysis, indications of catastrophic failure were not present.

An overall comparison of the AECs from both ALT conditions has been conducted using a normalized time and the natural log of the ESR and CAP and is shown in Figure 182 - Figure 189.

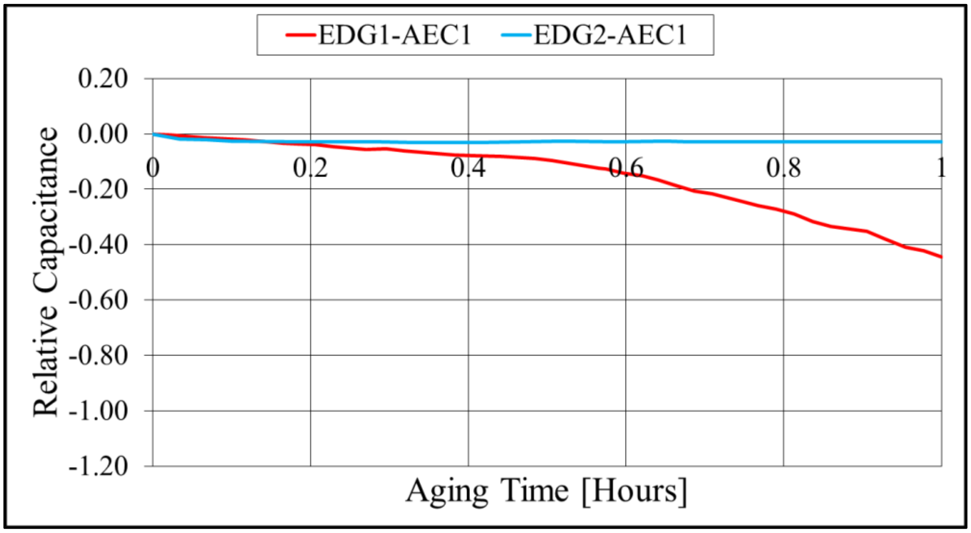


Figure 182: Comparison of the Relative CAP of AEC1 for EDG1 and EDG2.

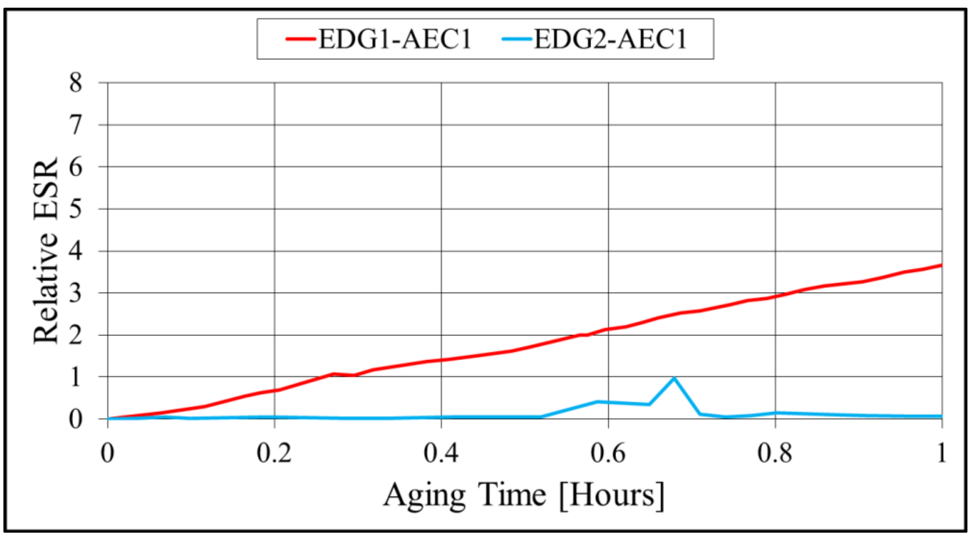


Figure 183: Comparison of the Relative ESR of AEC1 for EDG1 and EDG2.

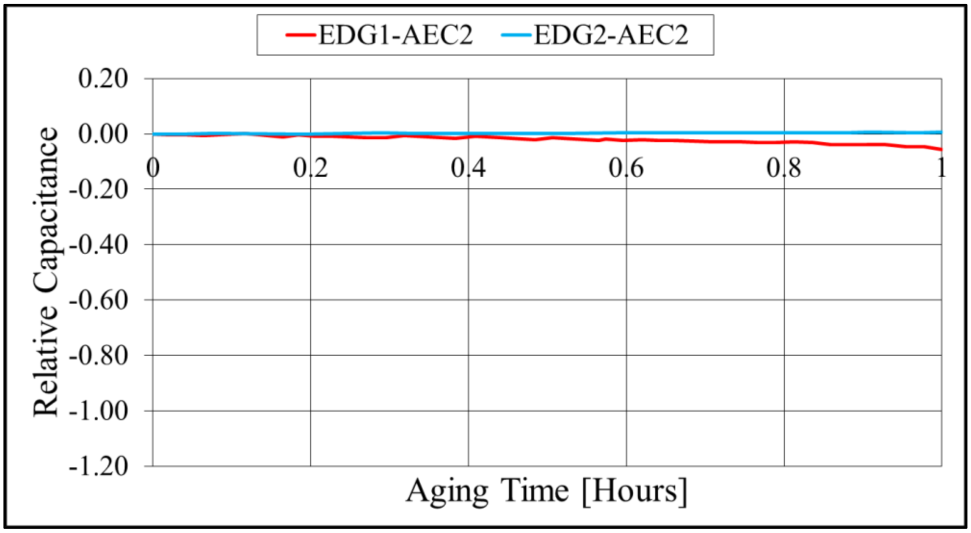


Figure 184: Comparison of the Relative CAP of AEC2 for EDG1 and EDG2.

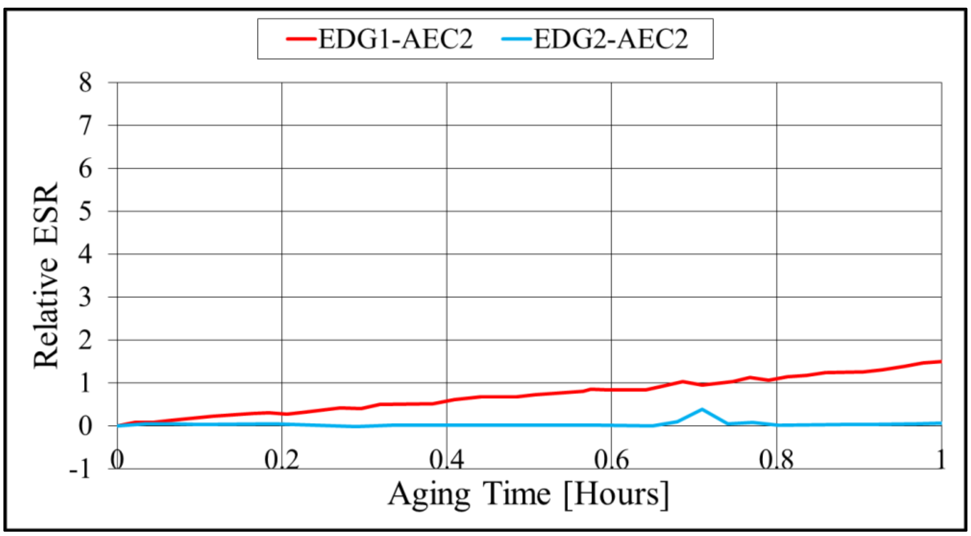


Figure 185: Comparison of the Relative ESR of AEC2 for EDG1 and EDG2.

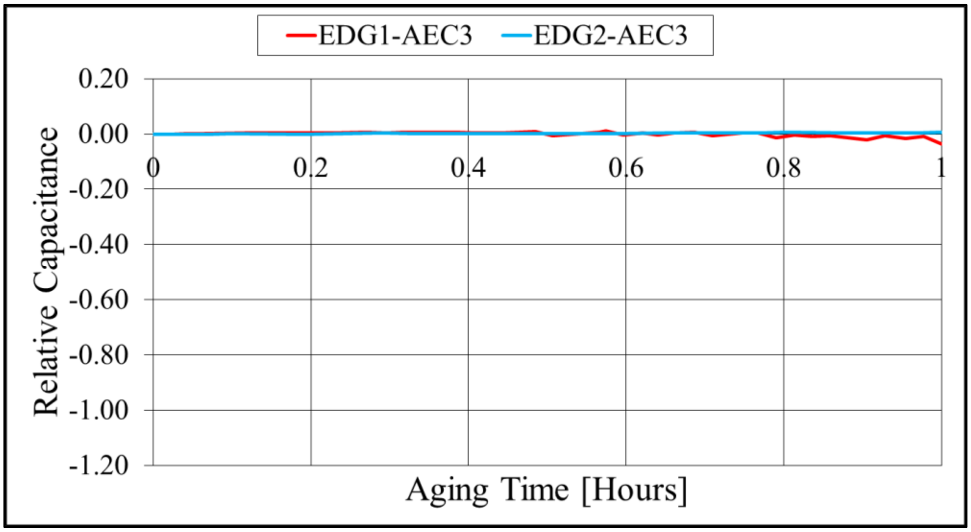


Figure 186: Comparison of the Relative CAP of AEC3 for EDG1 and EDG2.

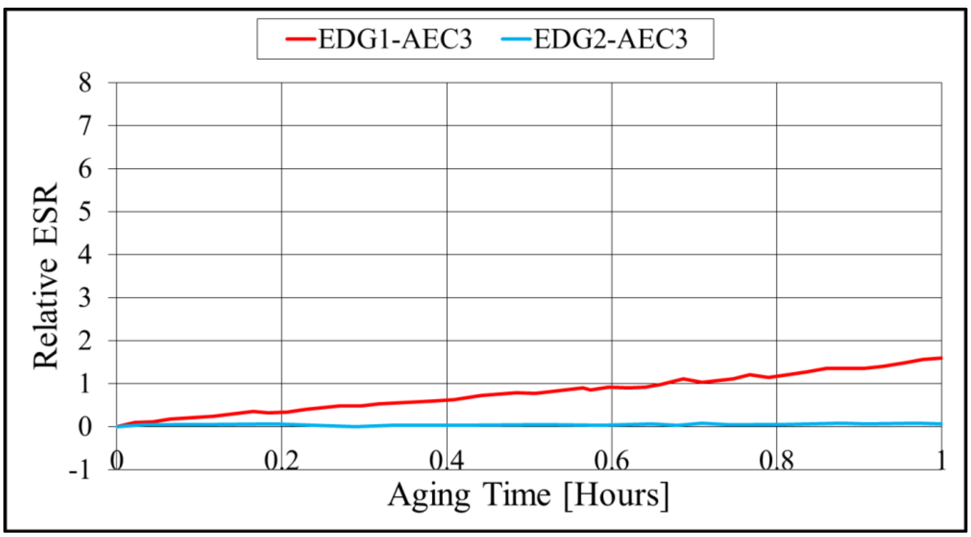


Figure 187: Comparison of the Relative ESR of AEC3 for EDG1 and EDG2.

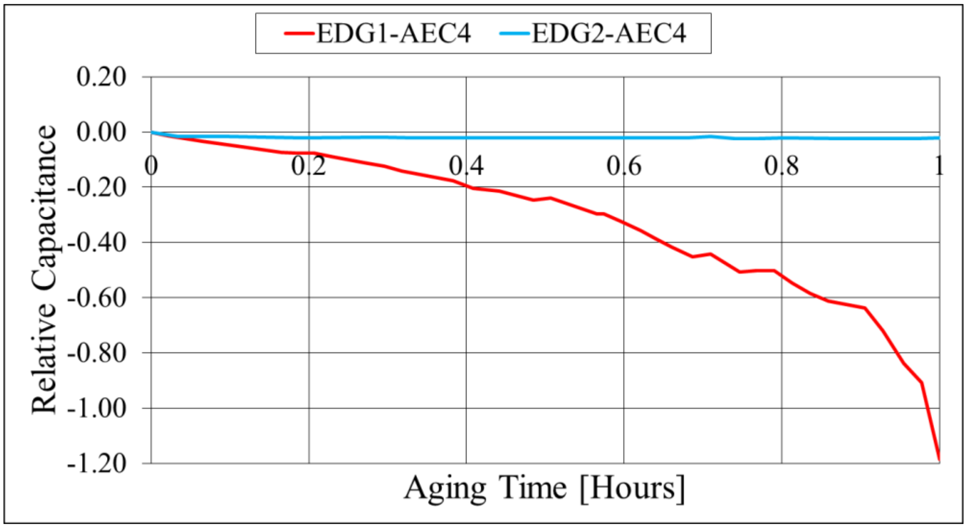


Figure 188: Comparison of the Relative CAP of AEC4 for EDG1 and EDG2.

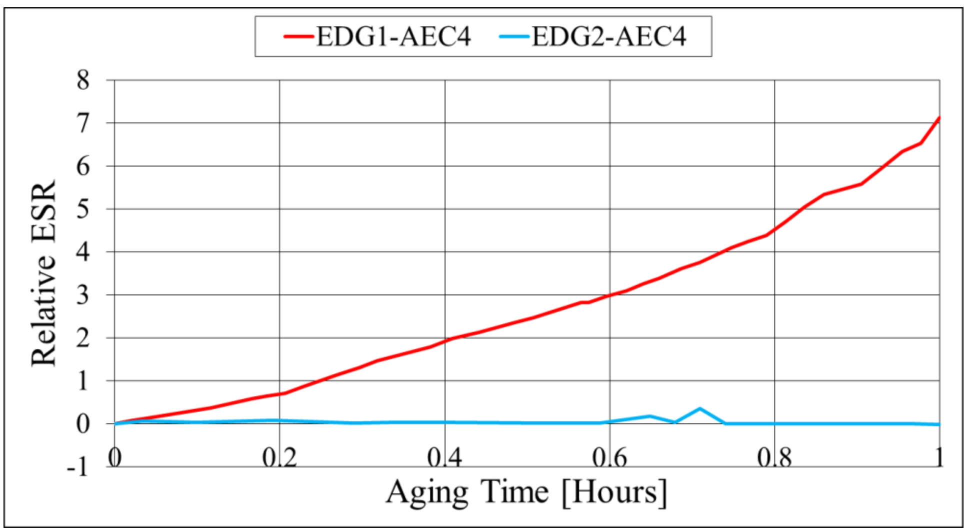


Figure 189: Comparison of the Relative ESR of AEC4 for EDG1 and EDG2.

Since the photometric analysis of EDG2 was inconclusive, a statistical analysis of the photometric quantities was conducted to demonstrate the precision of the data collection for EDG1 and EDG2. Figure 190 and Figure 191 illustrate the univariate distribution of the initial luminous flux and CCT, respectively, as well as tables of the statistical summary and quantiles pertaining to each distribution.

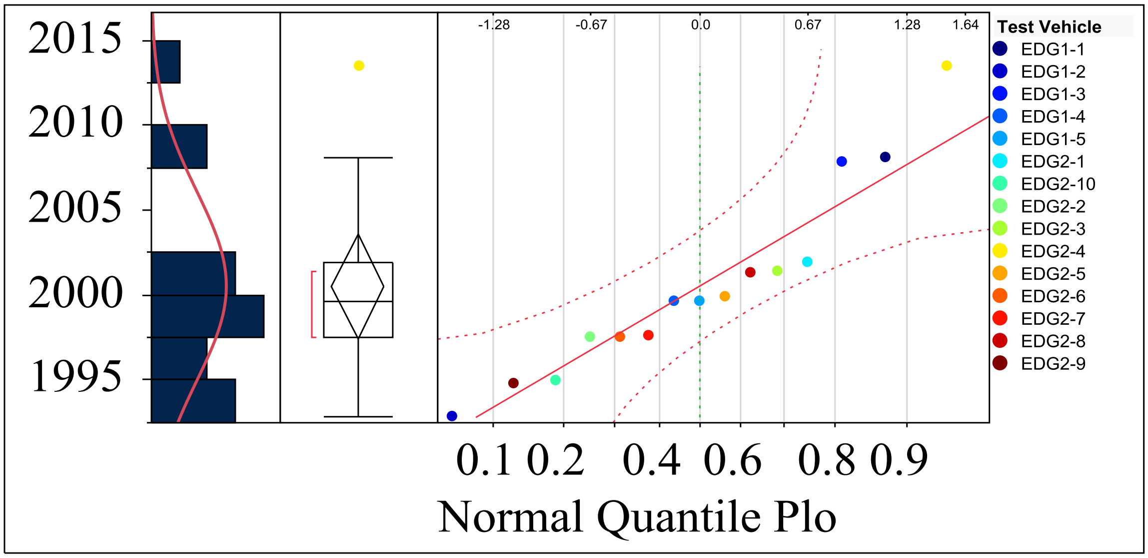


Figure 190: The Initial Luminous Flux [Lumens] of the EDG1 and EDG2.

Table 31: Statistical Summary for Figure 190.

| **Statistic** | **Value [Lumens]** |
|---|---|
| Mean | 2000.5347 |
| Standard Deviation | 5.580083 |
| Standard Error of the Mean | 1.4407712 |
| Upper 95% Mean | 2003.6248 |

Table 32: Quantiles for Figure 190.

| **Percent** | | **Value [Lumens]** |
|---|---|---|
| 100.0% | maximum | 2013.48 |
| 99.5% | | 2013.48 |
| 97.5% | | 2013.48 |
| 90.0% | | 2010.26 |
| 75.0% | quartile | 2001.94 |
| 50.0% | median | 1999.58 |
| 25.0% | quartile | 1997.48 |
| 10.0% | | 1993.97 |
| 2.5% | | 1992.79 |
| 0.5% | | 1992.79 |
| 0.0% | minimum | 1992.79 |

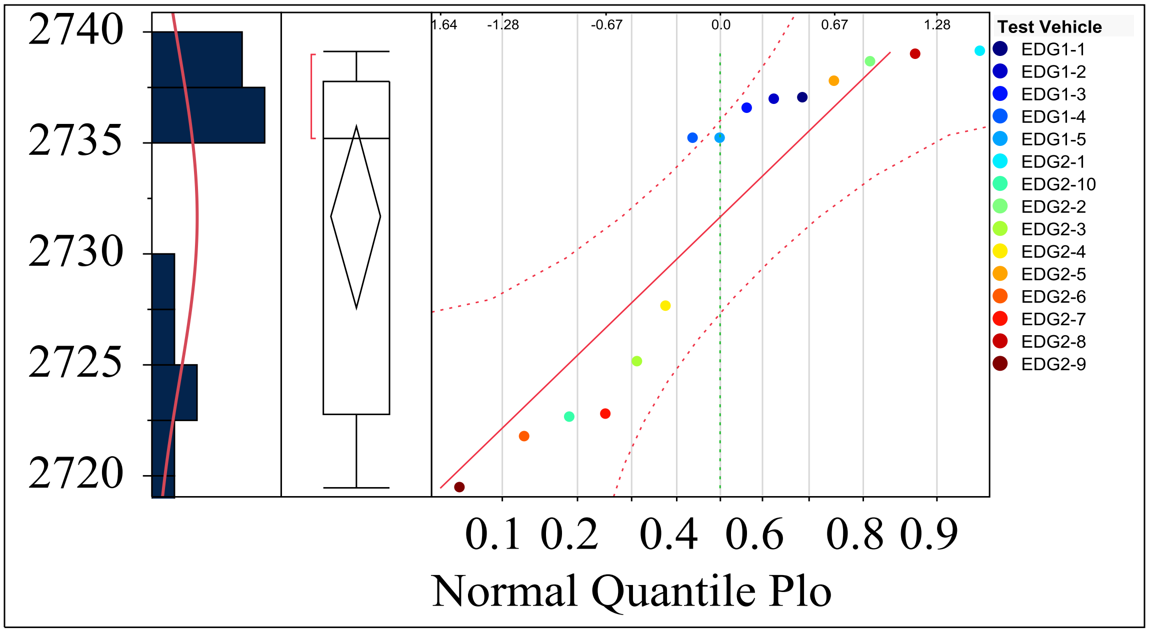


Figure 191: The initial CCT [Kelvin] of of the EDG1 and EDG2.

Table 33: Statistical Summary for Figure 191.

| **Statistic** | **Value [Kelvin]** |
|---|---|
| Mean | 2731.6552 |
| Standard Deviation | 7.4069642 |
| Standard Error of the Mean | 1.9124699 |
| Upper 95% Mean | 2735.757 |

Table 34: Quantiles for Figure 191.

| **Percent** | | **Value [Kelvin]** |
|---|---|---|
| 100.0% | maximum | 2739.1 |
| 99.5% | | 2739.1 |
| 97.5% | | 2739.1 |
| 90.0% | | 2739.03 |
| 75.0% | quartile | 2737.8 |
| 50.0% | median | 2735.21 |
| 25.0% | quartile | 2722.76 |
| 10.0% | | 2720.84 |
| 2.5% | | 2719.43 |
| 0.5% | | 2719.43 |
| 0.0% | minimum | 2719.43 |

The rated luminous flux and CCT values for this SSL system are 2000±10% lumens and 2700 kelvin, respectively. From the univariate distribution of the initial luminous flux, the mean is approximately 2000 lumens with a very small standard deviation of about 5.5 lumens. The single outlier of 2015 lumens is still well within the rated luminous flux value of this SSL system. All of the Quantiles are inside the Lilliefors confidence bounds and closely match the estimation of the expected mean. This validates the precision of the measurement system with the initial luminous flux values from EDG1 and EDG2 statistically equal. Similarly, this is shown in the results for the initial CCT. The estimated mean of the CCT is 2732 Kelvin which is about a 1% difference from the rated value. The Quantiles are inside the Lilliefors confidence bounds except for one data point. However, all the initial CCT values are less than 2% of the rated CCT. Again, this validates the precision of the measurement system with the initial CCT values from EDG1 and EDG2 statistically equal. Since EDG1 and EDG2 have no statistically different initial values, the relative values at any aging times can be compared with a high degree of accuracy. A statistical analysis of EDG1 and EDG2 was completed for an aging time of 3154 hours using the parameters of RLF, relative CCT and color shift.

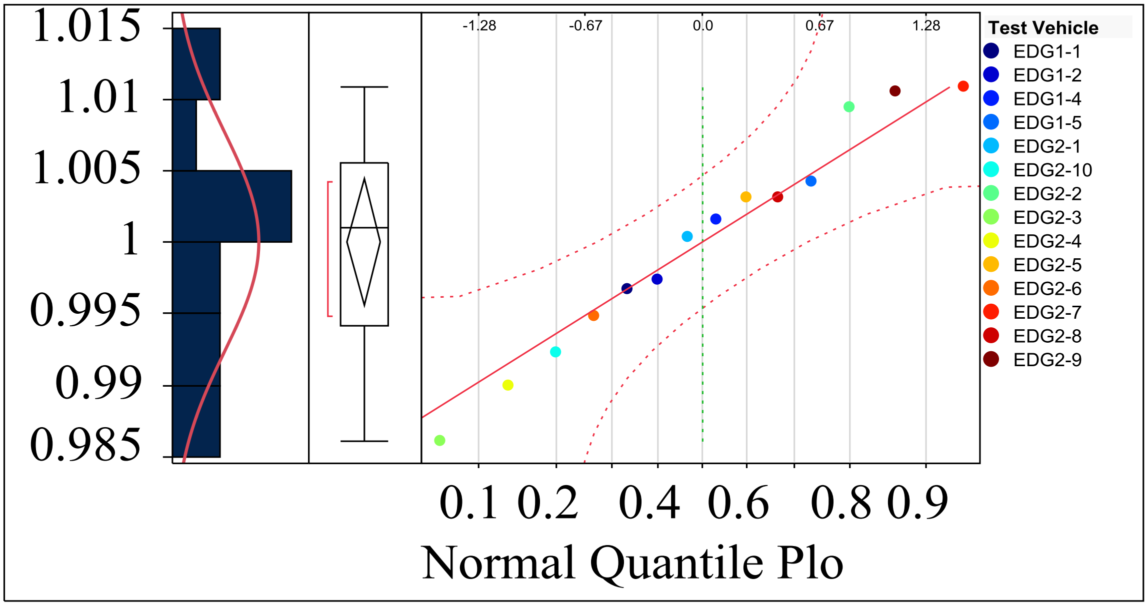


Figure 192: The RLF of the EDG1 and EDG2 at 3154 Hours.

Table 35: Statistical Summary for Figure 192.

| **Stat** | **Value** |
|---|---|
| Mean | 1.0000468 |
| Standard Deviation | 0.0076458 |
| Standard Error of the Mean | 0.0020434 |
| Upper 95% Mean | 1.0044613 |

Table 36: Quantiles for Figure 192.

| **Percent** | | **Value** |
|---|---|---|
| 100.0% | maximum | 1.01089 |
| 99.5% | | 1.01089 |
| 97.5% | | 1.01089 |
| 90.0% | | 1.0107 |
| 75.0% | quartile | 1.00559 |
| 50.0% | median | 1.001 |
| 25.0% | quartile | 0.99415 |
| 10.0% | | 0.98801 |
| 2.5% | | 0.98605 |
| 0.5% | | 0.98605 |
| 0.0% | minimum | 0.98605 |

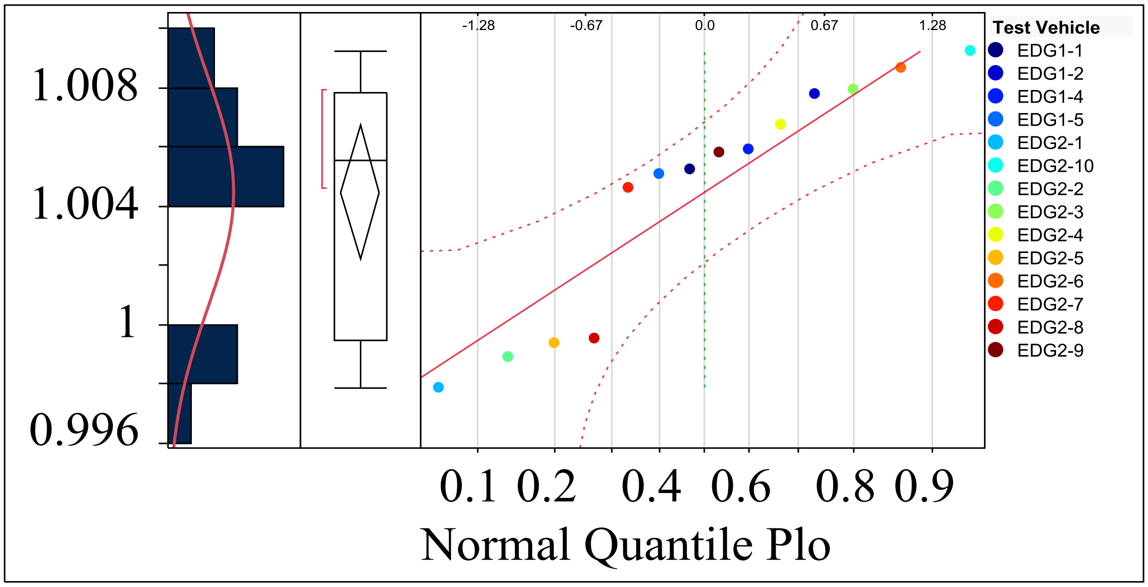


Figure 193: The Relative CCT of the EDG1 and EDG2 at 3154 Hours.

Table 37: Statistical Summary for Figure 193.

| **Stat** | **Value** |
|---|---|
| Mean | 1.0044706 |
| Standard Deviation | 0.0039101 |
| Standard Error of the Mean | 0.001045 |
| Upper 95% Mean | 1.0067282 |

Table 38: Quantiles for Figure 193.

| **Percent** | | **Value** |
|---|---|---|
| 100.0% | maximum | 1.00923 |
| 99.5% | | 1.00923 |
| 97.5% | | 1.00923 |
| 90.0% | | 1.00894 |
| 75.0% | quartile | 1.00781 |
| 50.0% | median | 1.00554 |
| 25.0% | quartile | 0.99948 |
| 10.0% | | 0.99838 |
| 2.5% | | 0.99787 |
| 0.5% | | 0.99787 |
| 0.0% | minimum | 0.99787 |

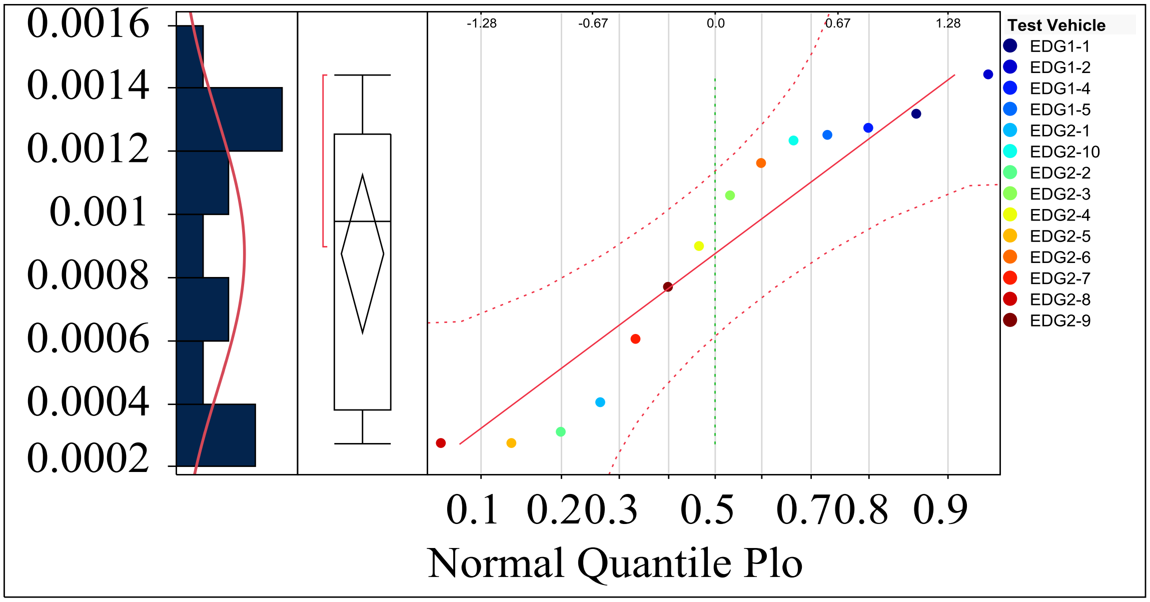


Figure 194: The $\Delta E_{u`v`}$ of the EDG1 and EDG2 at 3154 Hours.

Table 39: Statistical Summary for Figure 194.

| Stat | Value |
|---|---|
| Mean | 0.0008758 |
| Standard Deviation | 0.0004311 |
| Standard Error of the Mean | 0.0001152 |
| Upper 95% Mean | 0.0011247 |

Table 40: Quantiles for Figure 194.

| Percent | | Value |
|---|---|---|
| 100.0% | maximum | 0.00144 |
| 99.5% | | 0.00144 |
| 97.5% | | 0.00144 |
| 90.0% | | 0.00138 |
| 75.0% | quartile | 0.00126 |
| 50.0% | median | 0.00098 |
| 25.0% | quartile | 0.00038 |
| 10.0% | | 0.00027 |
| 2.5% | | 0.00027 |
| 0.5% | | 0.00027 |
| 0.0% | minimum | 0.00027 |

As was previously shown for the initial values of EDG1 and EDG2, all of the Quantiles are inside the Lilliefors confidence bounds and closely match the estimation of the expected mean. There is statistically no difference between EDG1 and EDG2 in the photometric and colorimetric quantities at 3154 hours. Since there was not any statistical differences in the lighting parameters of EDG1 and EDG2, a comparison of the relative CAP and ESR of EDG1 and EDG2 at three similar aging times has been conducted.

EDG1 ALT produced wear-out failures and was beneficial in measuring the leading indicators of CAP and ESR for a PHM framework. Conversely, EDG2 produced catastrophic failures with no noticeable change in the hypothesized leading indicators. The comparative results between EDG1 and EDG2 of relative CAP and ESR for each AEC is shown in Figure 195 – Figure 202.

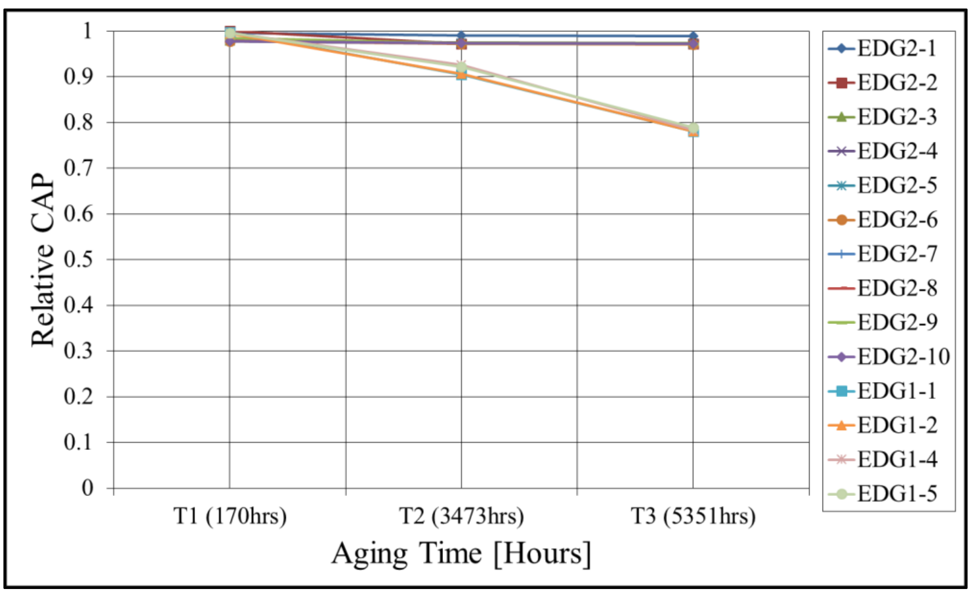


Figure 195: AEC One – ALT Comparison of Relative CAP.

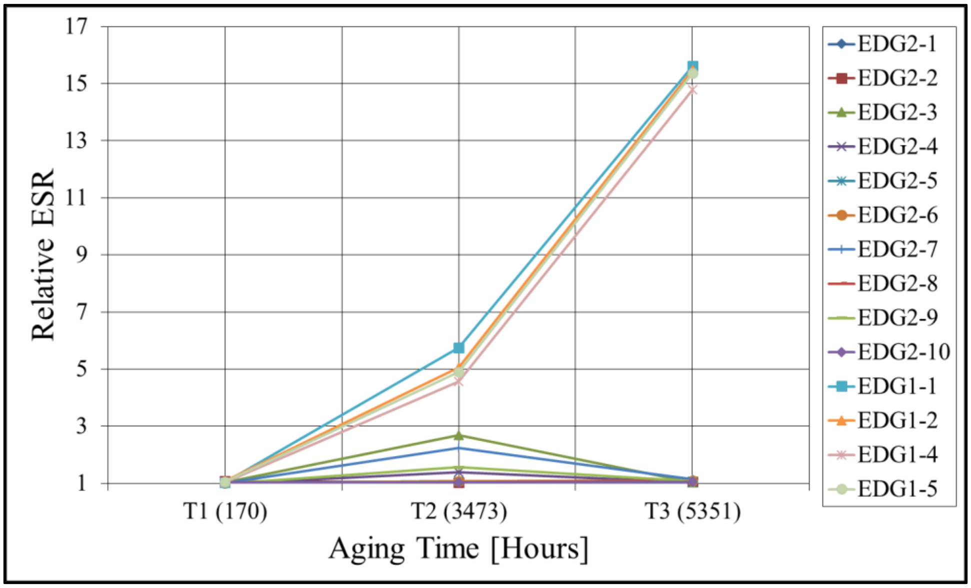


Figure 196: AEC One – ALT Comparison of Relative ESR.

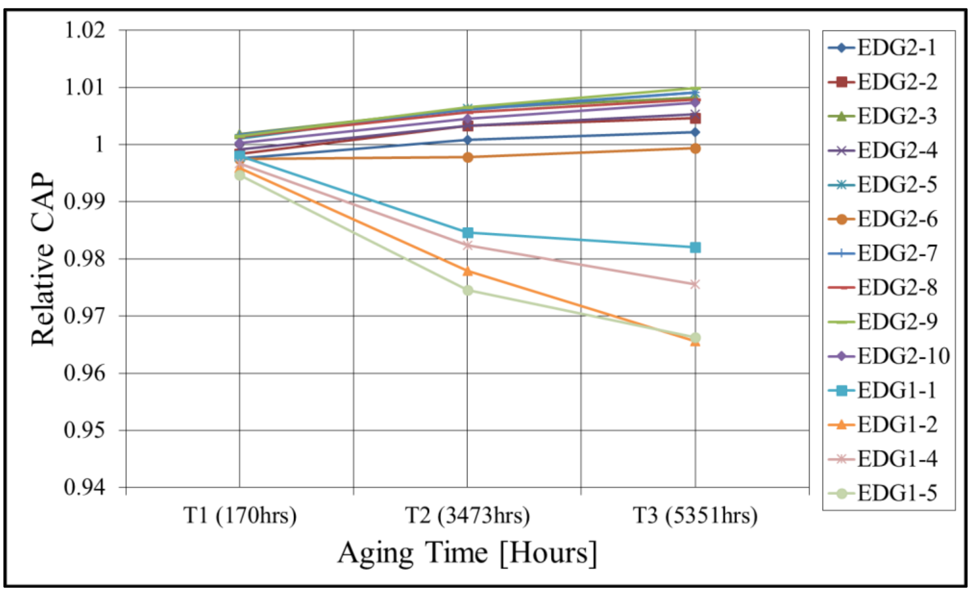


Figure 197: AEC Two – ALT Comparison of Relative CAP.

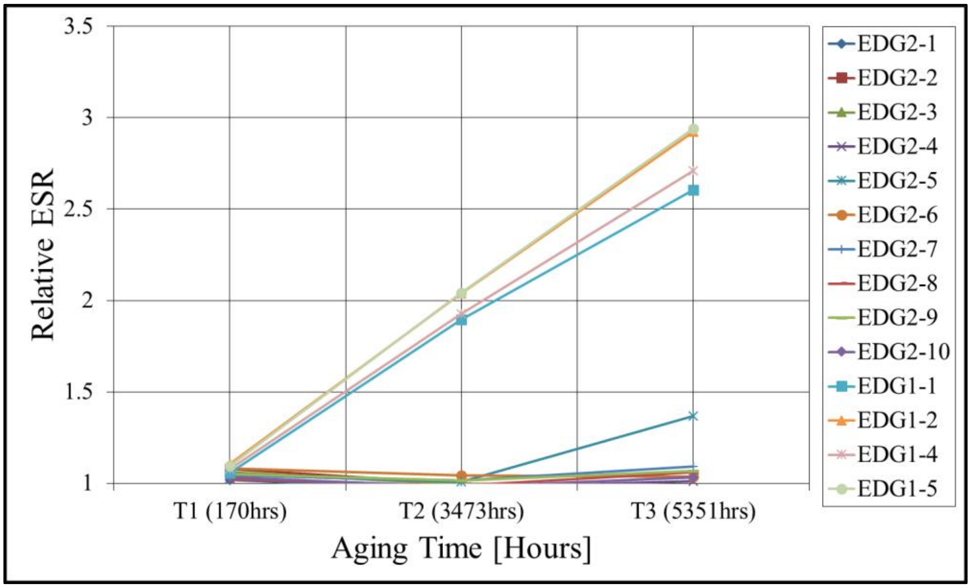


Figure 198: AEC Two – ALT Comparison of Relative ESR.

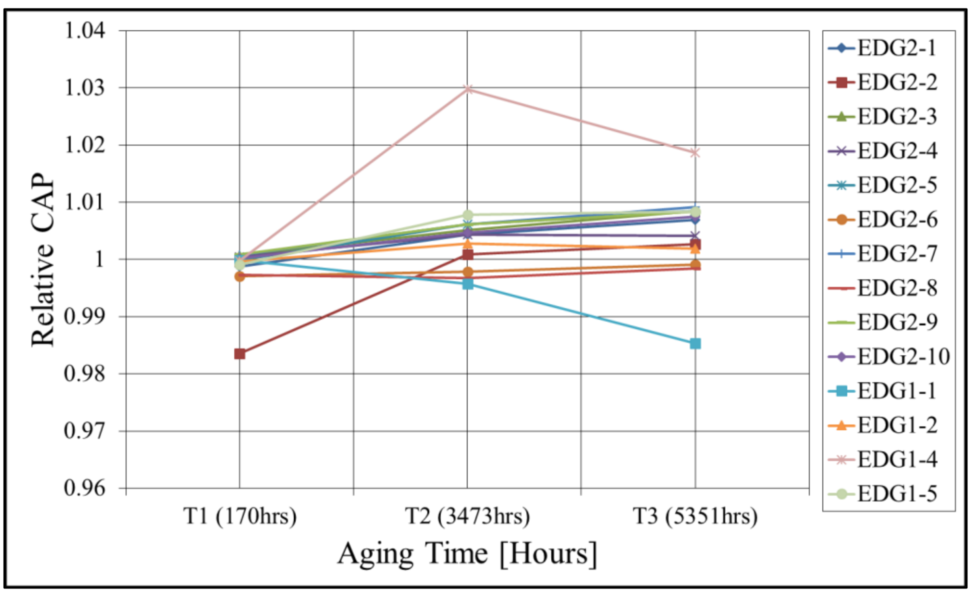


Figure 199: AEC Three – ALT Comparison of Relative CAP.

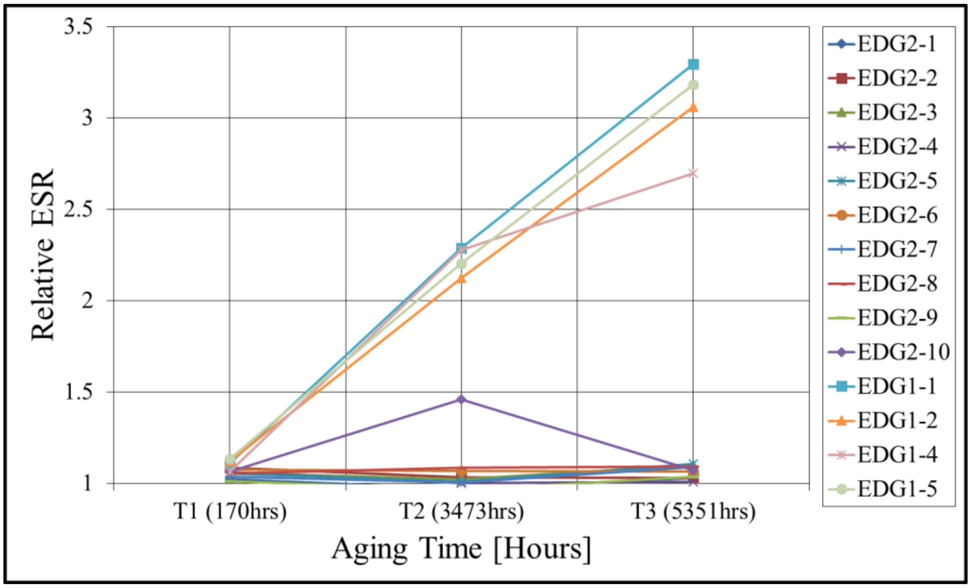


Figure 200: AEC Three – ALT Comparison of Relative ESR.

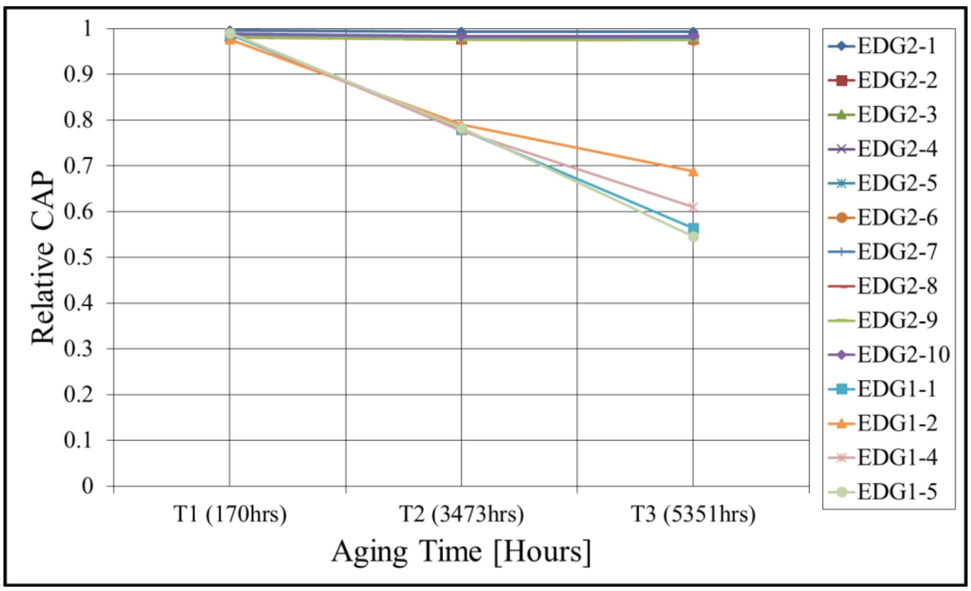


Figure 201: AEC Four – ALT Comparison of Relative CAP.

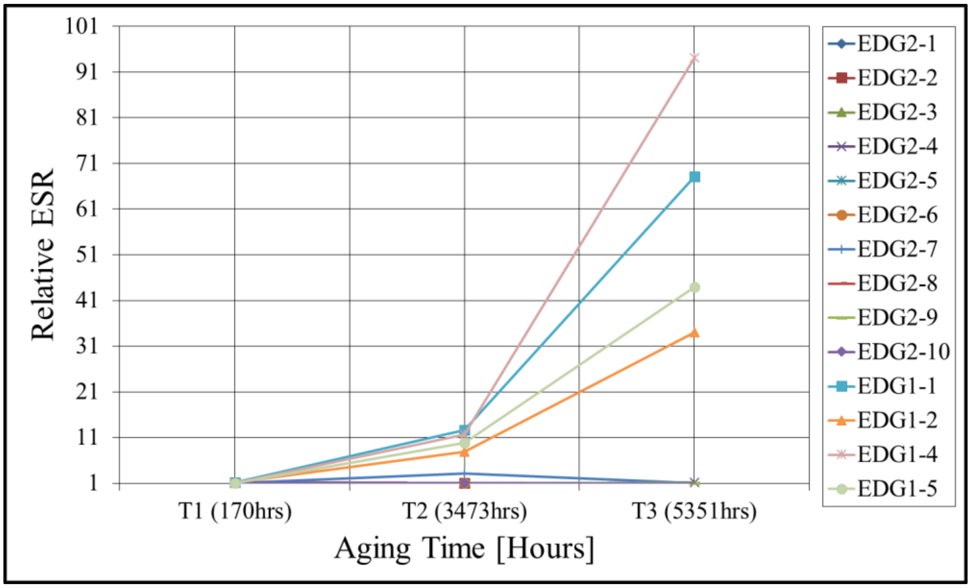


Figure 202: AEC Four – ALT Comparison of Relative ESR.

EDG1 ALT produced degradation in the AECs while EDG2 ALT had a negligible effect on the AECs performance. EDG2 ALT was used to accelerate the ingress of moisture into the AEC, as well as the EDs. Conversely, EDG1 ALT enhanced the degradation due to high thermal stresses. In this case, the lower temperature condition used in EDG2 ALT proved too small to allow moisture to penetrate the external seals of the AECS, however, it did prove sufficient to accelerate the degradation of other unforeseen components inside the ED. The results demonstrate that EDG1 ALT is better suited to induce degradation inside the AECs for the purpose of monitoring ESR and CAP as prognostic indicators

## 4.3. SSL Electrical Connectors

### 4.3.1. PHM

Fretting degradation acceleration was performed on the EC shown in Figure 24. Figure 203 depicts the change of resistance for the length of the ALT experiment.

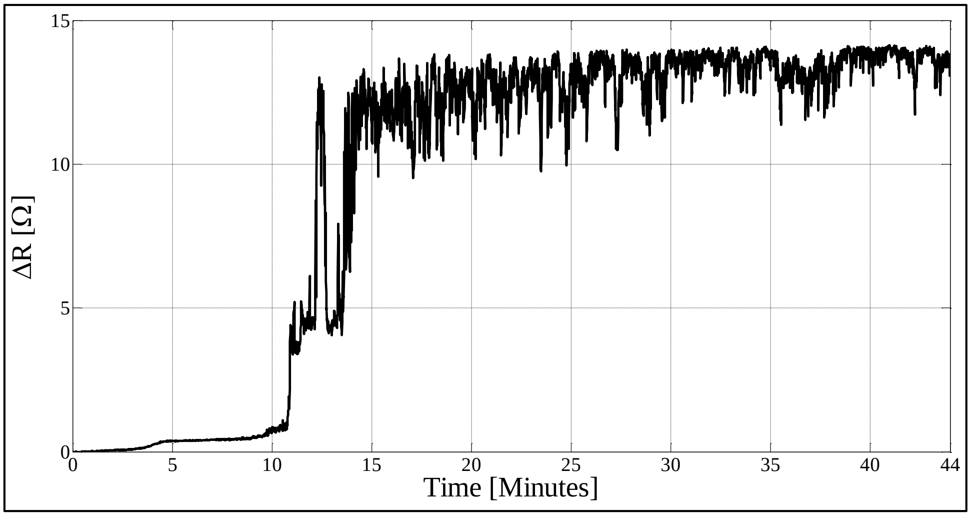


Figure 203: Change in Resistance from Fretting Degradation during ALT.

The failure criterion for this analysis was taken as a change in resistance of 0.3 Ω to coincide with the failure condition used in industry for a "bad" EC. When the connector reached this failure threshold, it was considered no longer operational. The experimental data was truncated to eliminate the data after the failure threshold which was reached at 4.3 minutes, as shown in Figure 204.

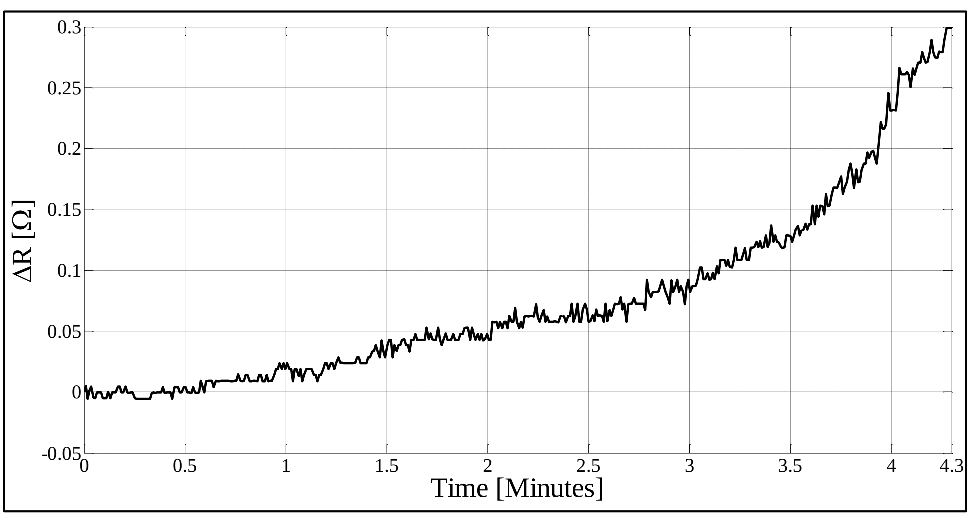


Figure 204 Change in Resistance from Fretting Degradation Truncated to 0.3Ω.

In order to optimally track the degradation using the KF, the resistance change values below the noise floor were eliminated. The noise floor was taken as 10% of the failure criterion or 0.03 Ω in order to eliminate the oscillations about zero due to a lack of fretting occurring. Figure 205 shows the remaining change in resistance data used to train the KF in order to prognosticate RUL. The change in resistance data was filtered using KF in conjunction with Matlab starting at 1.4280 minutes into the experimentation as shown in Figure 205. The filtered change in resistance data has been plotted on top of the raw resistance data to demonstrate the robustness of the KF to track the degradation of the connector as depicted in Figure 206.

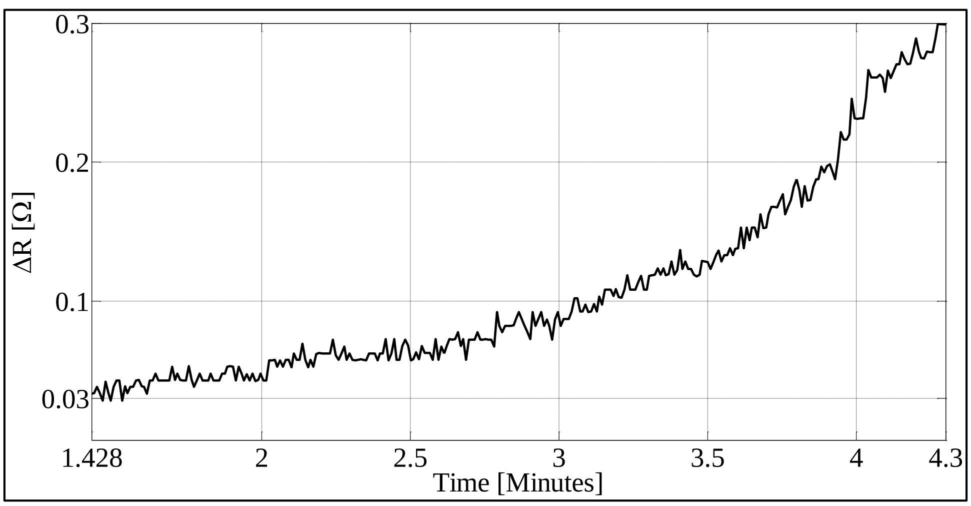


Figure 205: Change in Resistance from Fretting Degradation Truncated to 0.03Ω.

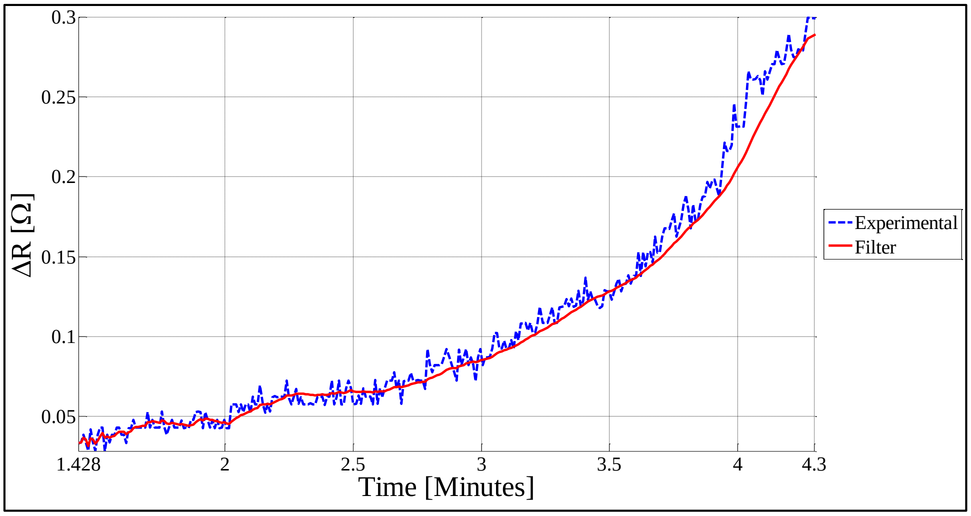


Figure 206: The State Space of the EC Using the KF.

The KF tracks the change in resistance with a high degree of accuracy. The KF was used to make a new prediction on the remaining useful life after every datum point collected. The time it took the connector to "fail" was approximately 4.3 minutes. The predicted remaining useful life has been plotted on top of the actual remaining useful life and is shown in Figure 207. The estimated RUL obtained from the algorithm begins to accurately predict the actual RUL at about 2.3 minutes. The estimated RUL oscillates above the actual RUL before converging towards $t_{eol}$.

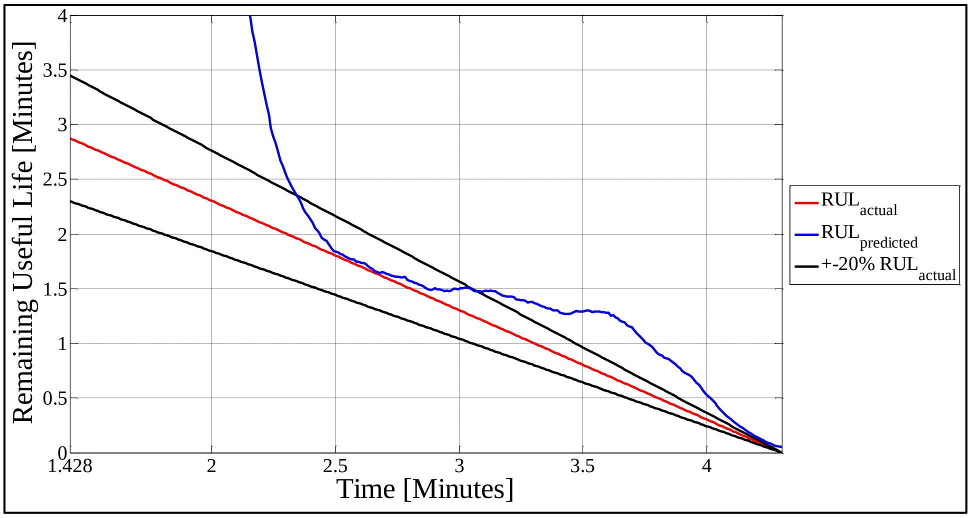


Figure 207: Remaining Useful Life Predictions of EC.

A prognostics metric was performed in order to demonstrate the robustness of the PHM algorithm. The validation process follows the algorithm assessment metrics proposed in literature (Saxena A. C., 2008) (Saxena A. C., 2009a) (Saxena A. C., 2009b). The first metric used to validate the robustness of the PHM algorithm is the alpha-lambda performance shown in Figure 208. It has been calculated to determine the time over which the algorithm successfully predicted the RUL and is similar the RUL estimation in Figure 207 with the inclusion of confidence intervals about the predictions over a normalized time, λ.

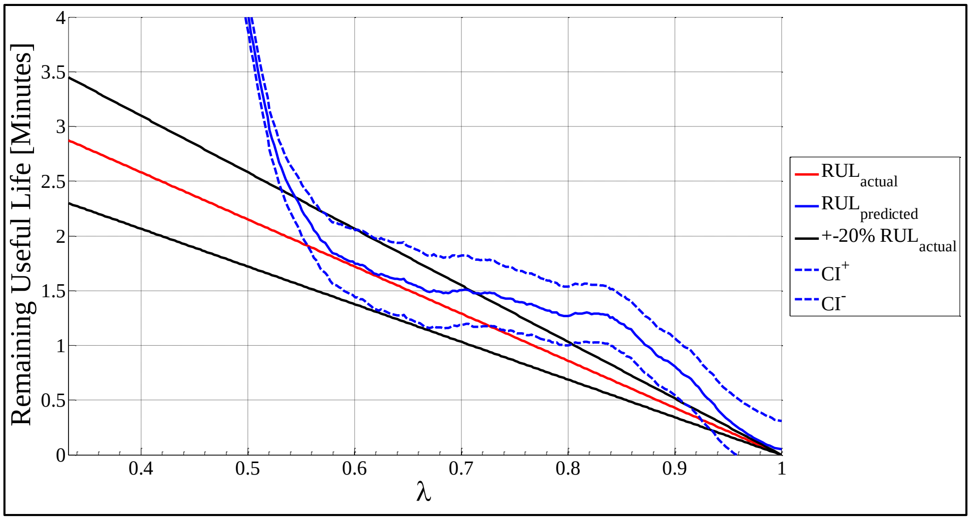


Figure 208: Alpha-Lambda Performance of KF Algorithm.

The actual RUL can only be calculated after the component has failed. The region of an accepted true estimate lies between the alpha bounds which is ± 20% of the actual RUL. If the predicted RUL falls within the alpha bounds, then it is taken as a correct prediction. Lambda is time that has been normalized by $t_{eol}$. When lambda equals one, the part has "failed". (Saxena A. C., 2008) (Saxena A. C., 2009a) (Saxena A. C., 2009b)

The second metric demonstrated is the beta statistic shown in Figure 209. It is used to quantify the precision of the RUL predictions and discriminates against algorithms that have a lot of uncertainty associated with RUL predictions. The beta calculation is defined as the area under the predicted RUL probability density function that falls within the alpha bounds at the specified normalized time, λ, as shown in equation (170) and Figure 209. (Saxena A. C., 2008) (Saxena A. C., 2009a) (Saxena A. C., 2009b)

$$\beta = \int_{-\alpha}^{+\alpha} \phi(x) \cdot dx \qquad (170)$$

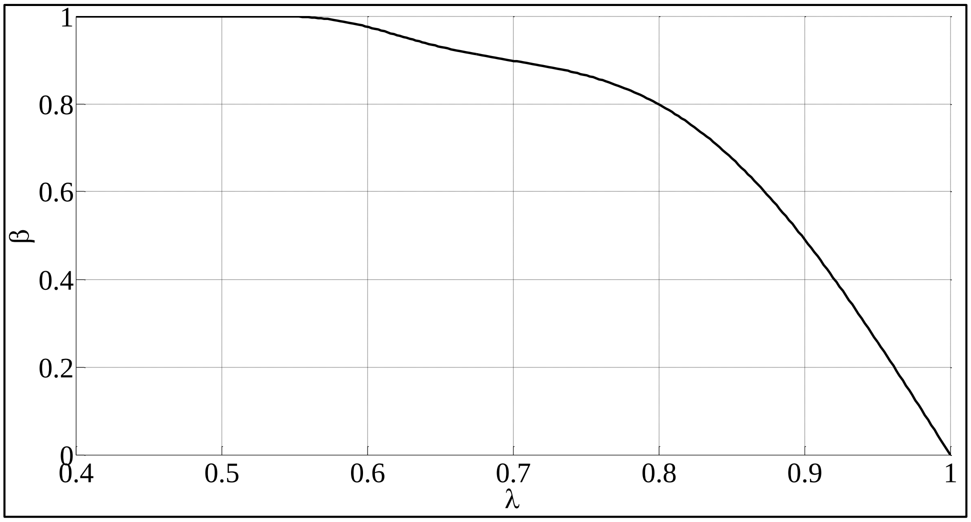


Figure 209: Beta calculation showing area under RUL prediction PDF that falls within the alpha bounds.

A high beta-value value indicates a RUL prediction closer to the actual RUL. This metric becomes biased towards the end of life due to small deviations between the actual and estimated RUL producing large effects on the Beta curve. (Saxena A. C., 2008) (Saxena A. C., 2009a) (Saxena A. C., 2009b)

The third metric is the relative accuracy shown in Figure 210. Relative accuracy has a value of 1 for a perfect predicted value of the RUL and is defined in equation (171).

$$RA_{\lambda} = 1 - \frac{\left| RUL_{actual} - RUL_{predicted} \right|}{RUL_{actual}} \tag{171}$$

Relative accuracy is used to emphasize the prediction errors closer to the actual failure of a component. Larger peaks on the graph indicate a higher accuracy in the prediction. (Saxena A. C., 2008) (Saxena A. C., 2009a) (Saxena A. C., 2009b)


Figure 210: Relative Accuracy of RUL prediction.

Since the KF showed promise for the prediction of remaining useful life of the EC, the EKF was used to add to the PHM framework of SSL devices. The estimated state, the remaining useful life, the beta performance metric and the relative accuracy metric are shown for the same dataset in Figure 205.

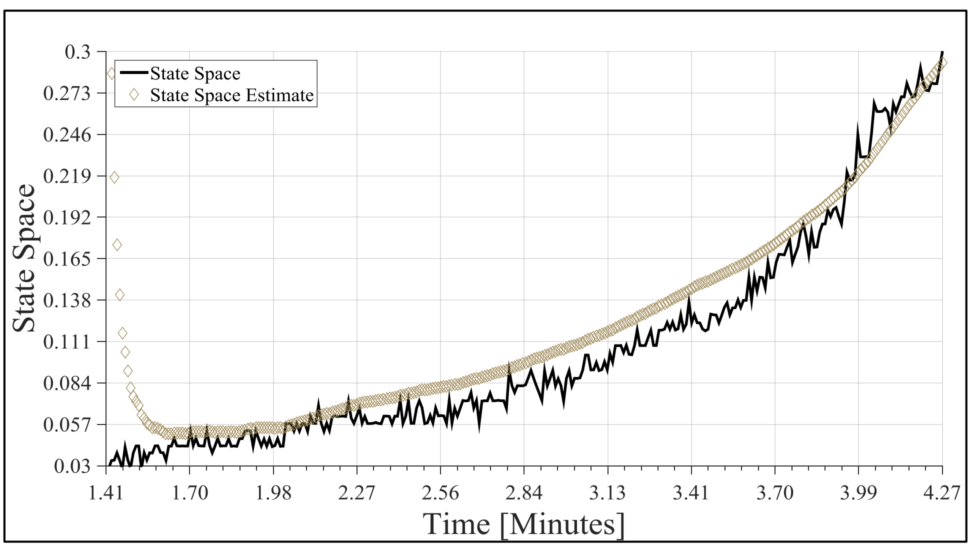


Figure 211: The State Space of the EC Using the EKF.

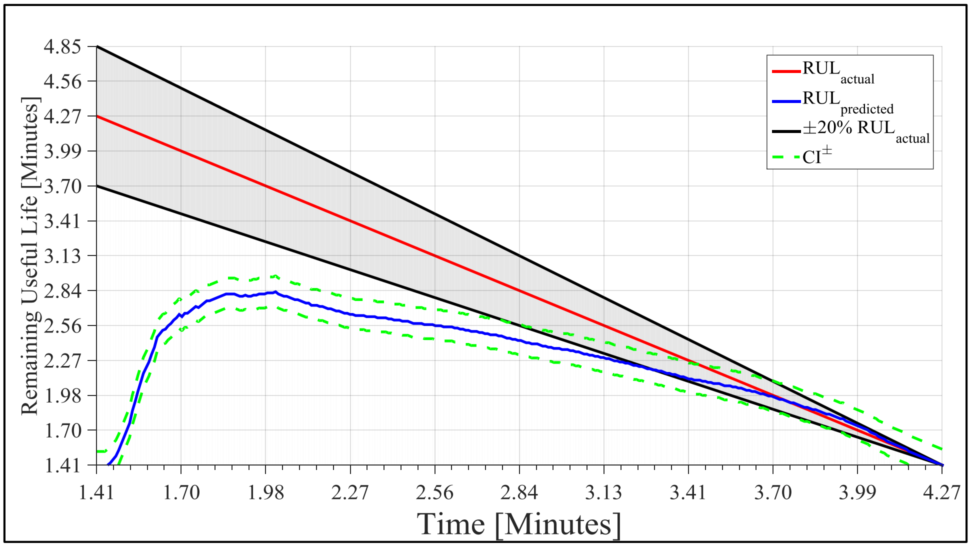


Figure 212: The RUL of the EC Using the EKF.

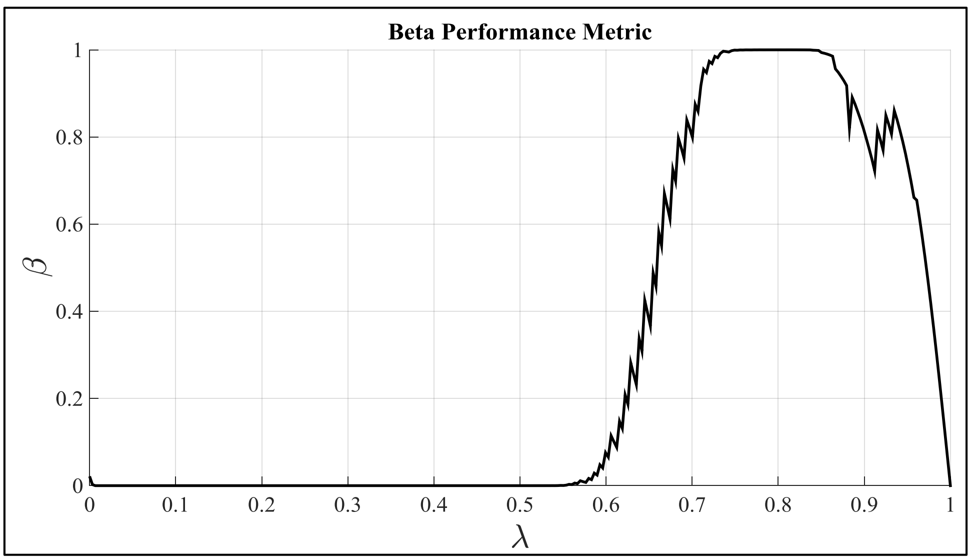


Figure 213: The Beta Metric for the RUL Predictions Using the EKF.

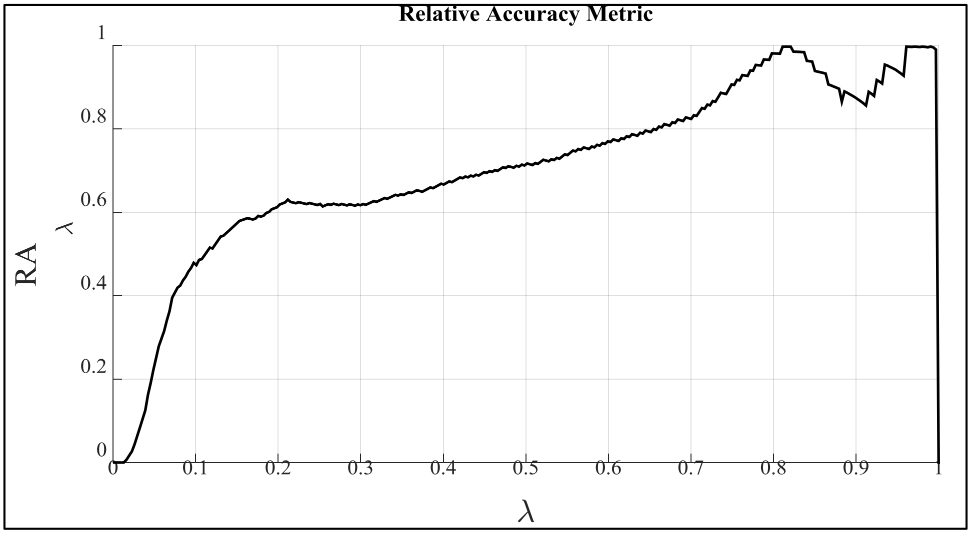


Figure 214: The Relative Accuracy Metric for the RUL Predictions Using the EKF.

From the PHM analysis, the change in resistance of the EC was estimated successfully from the EKF and the KF. However, the performance of the EKF and KF differed drastically. The KF produced "noise" RUL predictions, while the EKF produced accurate estimates of the end of life. This is predominantly due to the sensitivity in the selection of the noise parameters. The EKF does not require as much accuracy when estimating the noise parameters, but the KF is highly sensitive to the selection.

### 4.3.2. FEA ANALYSIS

A simplified 2D pin, spring and housing model was created with ANSYS 13 and was used to perform a finite element analysis to investigate fretting corrosion. The model geometry was created in units of millimeters instead of the default units of meters. This was done to ensure that a proper mesh was created because the smallest dimension is 0.200 mm. Also, the following simplified assumptions have been used for this model: The connector model is in plane stress only; the connector model is perfectly elastic; the connector model is assumed to be in steady-state and static.

The pin and spring both consist of brass as the bulk material with a tin plated surface. The connector housing is constructed out of Nylon. For the FEA, the bulk material property of the pin and spring were used with the tin plated surface finish neglected. Table 41 list the material properties of brass and nylon used in the simulation at a reference temperature of 25°C. Figure 215 shows the completed 2D model consisting of the spring, pin, and housing with the points of contact labeled.

Table 41: Material Properties for the Electrical Connector Assembly

| **Property** | **Brass** | **Nylon** |
|---|---|---|
| Modulus of Elasticity [$N/mm^2$] | 1.06E5 | 2.45E3 |
| Poisson's Ratio | 0.33 | 0.4 |
| Coefficient of Thermal Expansion [$°C^{-1}$] | 2.24E-5 | 5.98E-5 |
| Thermal Conductivity [W/(mm·K)] | 9.25E-2 | 1.45E-4 |
| Electrical Resistivity [Ω·mm] | 1.64E-4 | 4.85E16 |

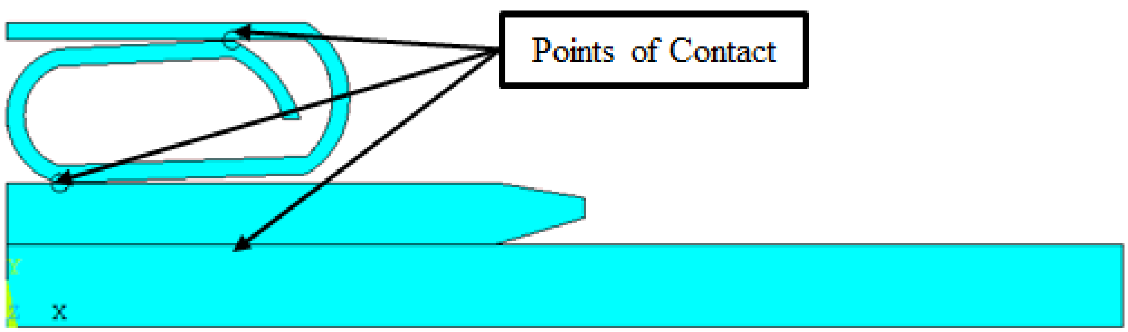


Figure 215: Electrical Pin and Spring Finite Element Model

Additional areas were added at the two points of contact encountered by the spring to assist in the convergence of the contact pairs. No additional areas were needed for the contact of the pin and the housing because of the large contact area. The contact pairs for the regions of contact were created using the Contact Manager panel. This created a contact element (CONTA172) and a target element (TARGE169) for each of the three contact pairs.  The contact element was considered to be the top contact with the target element as the bottom contact. ANSYS coupled the mechanical, electrical and thermal equations together to perform the analysis using the Couple Field Element type Quad 8 Node 223 (PLANE223 Element) (ANSYS).

The model was first meshed using the Mesh Tool with triangular elements and the ANSYS meshing defaults.  The mesh was refined four additional times in order to ensure that the model had converged towards the correct solution. A total of five simulations were carried out.  The final mesh was used to acquire the plots.  Figure 216 illustrates the final mesh used in the FEA with the boundary conditions labeled.

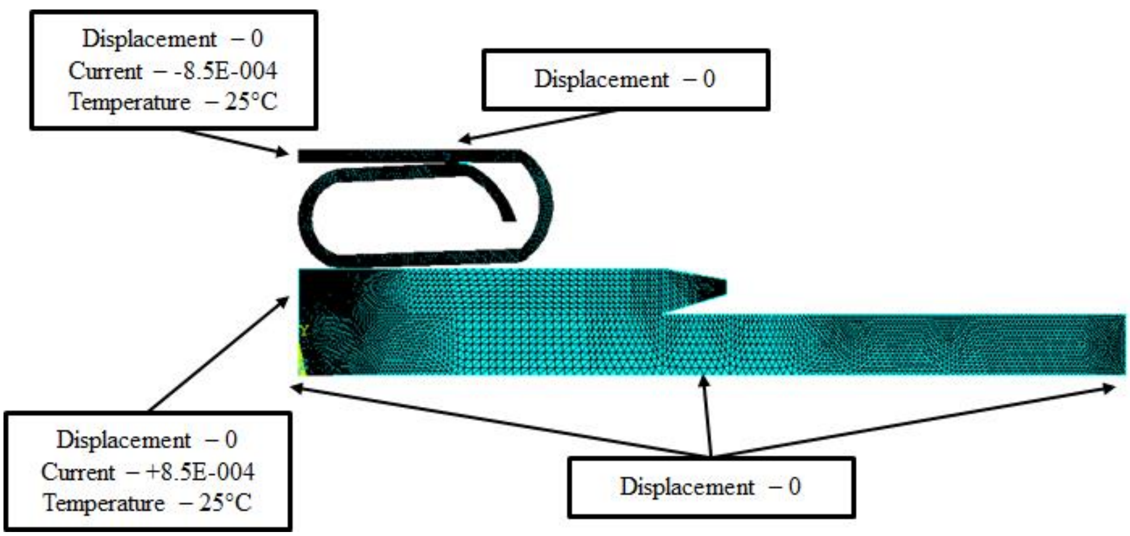


Figure 216: Meshed Model with Boundary Conditions.

The construction of the connector assembly proved to be rather challenging.  The first approach was to construct the spring completely compressed against the pin surface. Figure 217  illustrates the first approach.

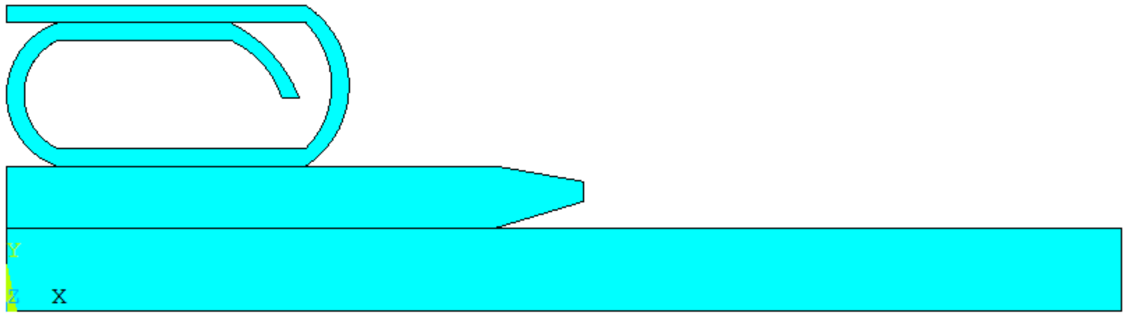


Figure 217: The Initial 2D Drawing.

This 2D sketch is an unrealistic drawing of what the model actually looks like. This approach was original used because of the unknown location of points on the spring after the insertion of the pin. This model wouldn’t converge when the ANSYS simulation was run. In order to acquire a converged solution, the model was changed.

The new location of the spring was arbitrarily chosen because the exact placement of the spring is unknown. The previous location was offset by 0.1 mm with the motion of the spring taken into account. Figure 218 shows the final sketch of the spring used with FEA.

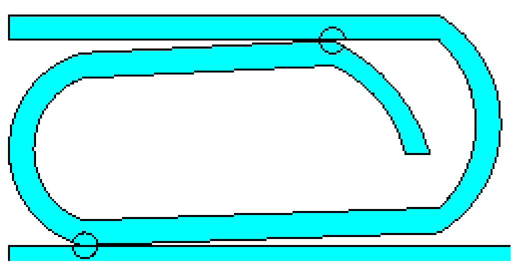

Figure 218: Final Spring Sketch.

Using the 2D sketch in Figure 215, a mesh convergence was carried out to determine the appropriate number of nodes needed to run the FEA properly. The change in electrical potential was the criteria used to check for mesh convergence. Table 42 lists the change in the electrical potential, the number of nodes and the percent error from the previous value. Figure 219 graphically shows the change in electrical potential against the number of nodes.

Table 42: Mesh Convergence Table

| Change in Electrical Potential [V] | Number of Nodes | Percent Error |
|---|---|---|
| 3.96E-006 | 1083 | NA |
| 4.04E-006 | 3918 | 1.98% |
| 4.11E-006 | 8529 | 1.70% |
| 4.18E-006 | 14904 | 1.67% |
| 4.21E-006 | 58044 | 0.71% |

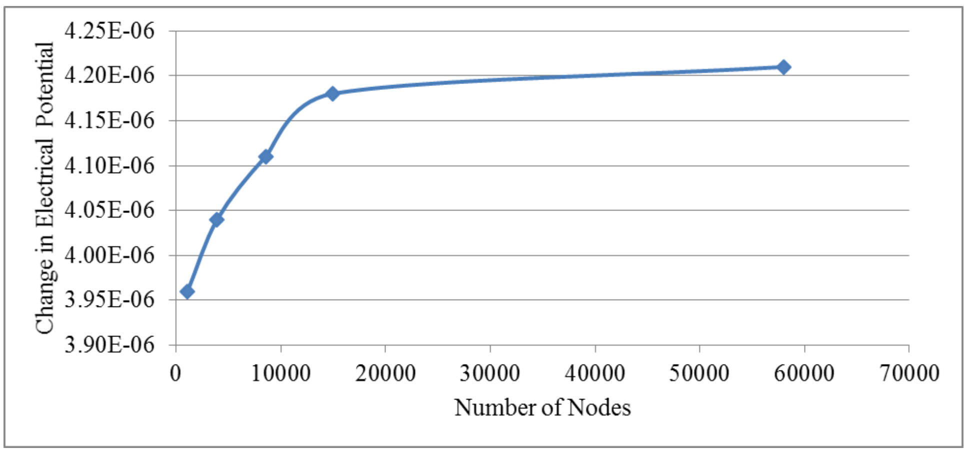


Figure 219: Electrical Potential versus Number of Nodes.

The last FEA simulation had a percent error of less than one percent. This was the best one out of the five and was used to perform the rest of the analysis. In Figure 220, the maximum displacement occurs between the spring and pin contacts and at a spot on the nylon housing.

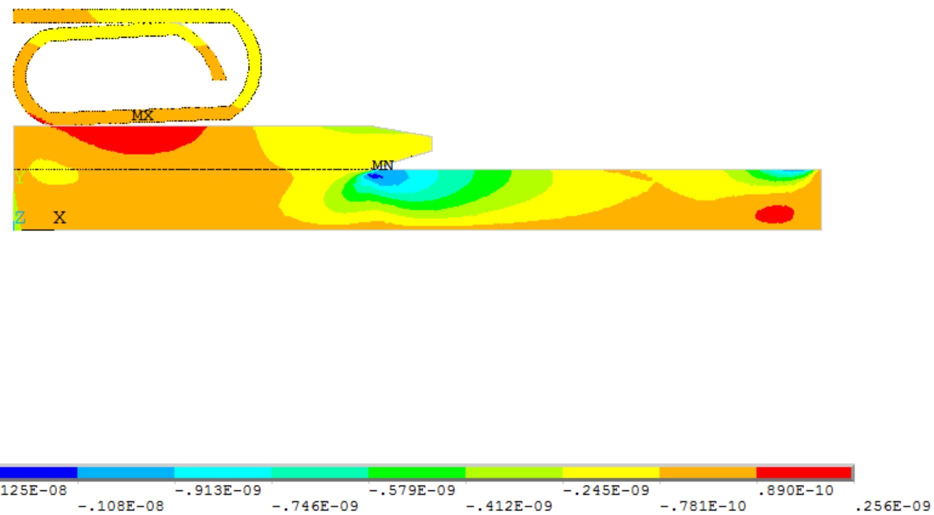


Figure 220: Displacement.

The stress and strain in Figure 221 and Figure 222 both have maximums located at the corner where the end of the pin meets the housing. This is mostly due to the shape of the pin because the pin doesn't sit in direct contact with the housing through the entire length of the pin.

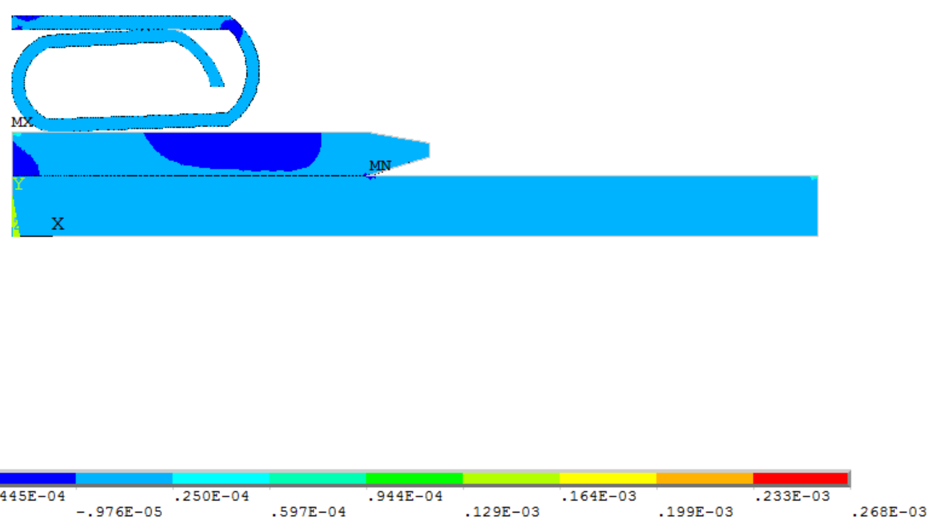


Figure 221: Stress.

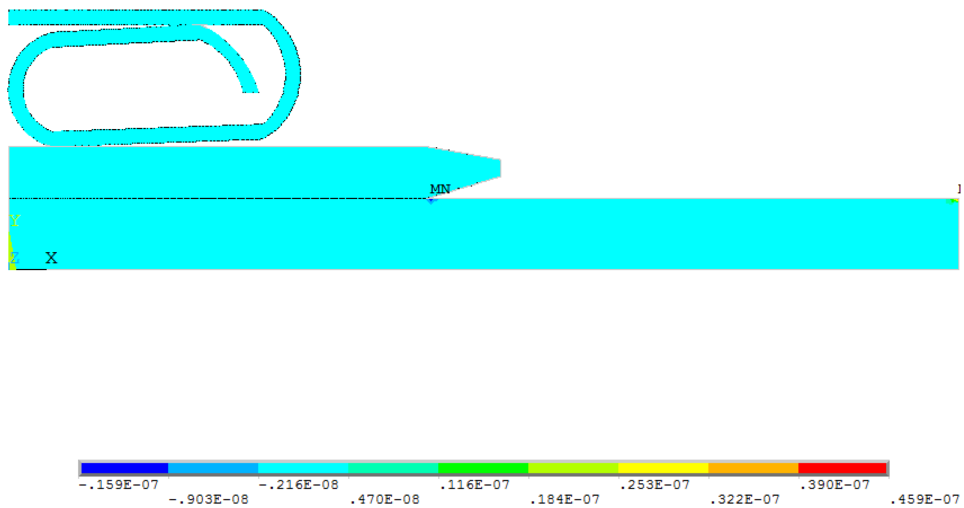


Figure 222: Strain.

The electrical potential in Figure 223 shows the maximum drop occurs where the current leaves the assembly. Unfortunately, this model predicts the electrical potential to be zero through the length of the pin.  Further investigation needs to occur to correct this mistake.

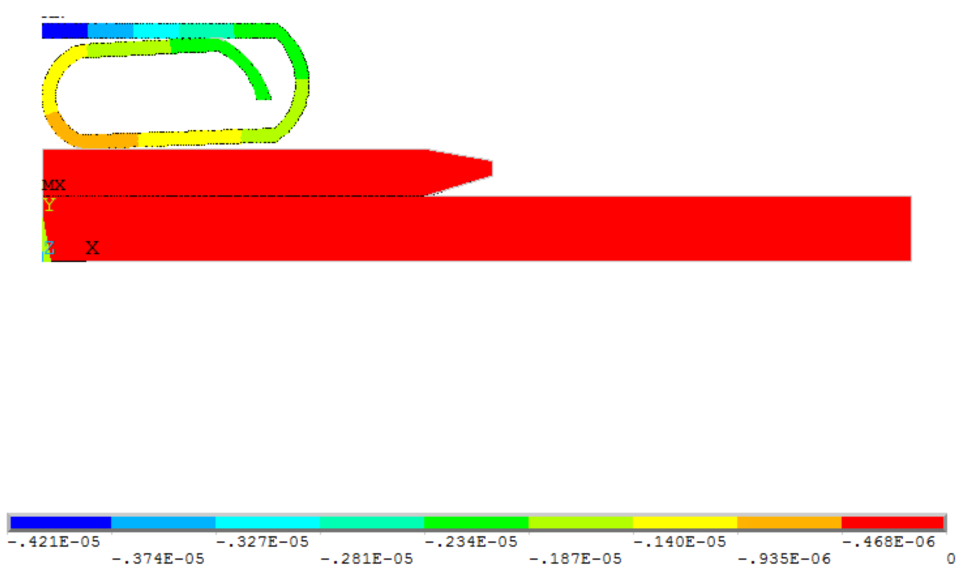


Figure 223: Electrical Potential.

The von Mises stress distribution in Figure 224 predicts a maximum at the top left corner pin, the bottom left corner where the pin and the housing meet and the bottom right corner where the pin and housing meet.

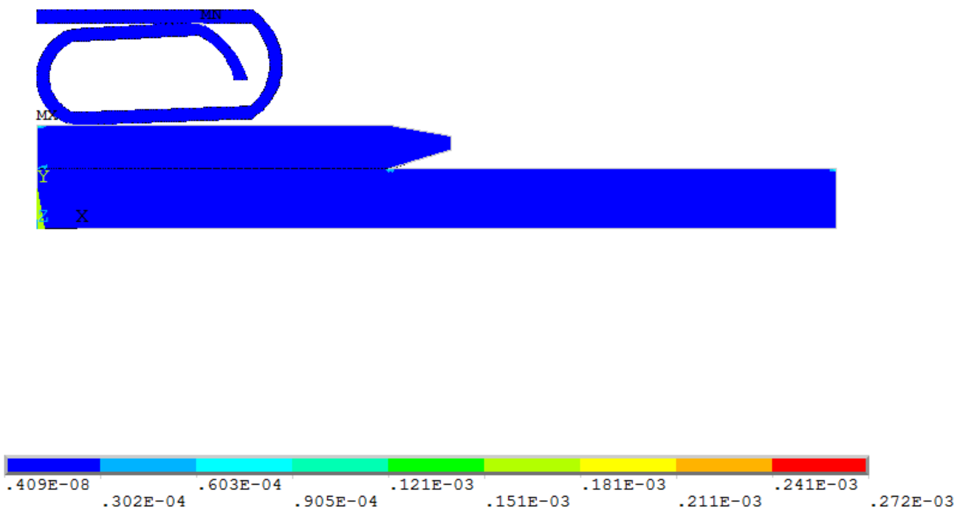


Figure 224: von Mises Stress Distribution.

.

# 5. Summary & Conclusions

Since the passing of the Energy Independence and Security Act of 2007, the U.S. government has mandated greater energy independence which has acted as a catalyst for accelerating and facilitating research efforts toward the development and deployment of market-driven solutions for energy-saving homes, buildings and manufacturing, as well as sustainable transportation and renewable electricity generation. As part of this effort, an emphasis toward advancing solid-state lighting technology through research, development, demonstration, and commercial applications is assisting in the phase out of the common incandescent light bulb, as well as develop a more economical lighting source that is less toxic than compact fluorescent lighting. This has led lighting manufacturers to pursue SSL technologies for a wide range of consumer lighting applications.

One method for the characterization of an SSL luminaire's lifetime is in terms of lumen maintenance life. Lumen maintenance or lumen depreciation is the percentage decrease in the relative luminous flux from that of the original, pristine luminous flux value. Lumen maintenance life is the estimated operating time, in hours, when the desired failure threshold is projected to be reached at normal operating conditions. The failure threshold of SSL luminaires in this work was lumen maintenance of 70% -- a 30% reduction in the light output of the luminaire. Currently, there are no industry accepted standards to estimate the time to failure of an SSL luminaire in ALT conditions with TM28 only allowing for projections based off of nominal use.

TM28 utilizes the Arrhenius equation to determine SSL device specific reaction rates from thermally driven failure mechanisms used to characterize a single failure mode – the relative change in the luminous flux output or “light power” of the SSL luminaire. TM28 requires a minimum of 6000 hours of testing with a recommended sampling period less than or equal to 1000 hours. Additionally, it necessitates two different temperature conditions, 25°C and 45°C are suggested, to determine the SSL lamp specific activation energy.

One principal issue with TM28 is the lack of additional stresses or parameters needed to characterize non-temperature dependent failure mechanisms. Another principal issue with TM28 is the assumption that lumen maintenance or lumen depreciation gives an adequate comparison between SSL luminaires. Additionally, TM28 has no process for the determination of acceleration factors or lifetime estimations. The use of TM28 yields lumen maintenance projections that can be useful in the determination of acceleration factors, as shown in this work.

Currently, a literature gap exists for established accelerated test methods for SSL devices to assess quality, reliability and durability before being introduced into the marketplace. Furthermore, there is a need for Physics-of-Failure based approaches to understand the processes and mechanisms that induce failure for the assessment of SSL reliability in order to develop generalized acceleration factors that better represent SSL product lifetime. This validates the reasoning behind the development of acceleration techniques to quantify SSL reliability under a variety of environmental conditions. The ability to assess damage accrual and investigate reliability of SSL components and systems is essential to understanding the life time of the SSL device itself.

Three distinct categories of test vehicles have been detailed for the investigation of component and system reliability of SSL devices. The first test vehicles discussed were a SSL lamps that consisted of different sizes, manufacturers and rated characteristics. The next set of test vehicles discussed was an off-the-shelf SSL device that had the LE and ED housed separately with a focus on the aluminum electrolytic capacitors inside the ED. The last test vehicles discussed were tin coated, rectangular-pin and socket ECs used to connect an SSL LE and its accompanying ED.

The group of SSL lamps consisted of warm-white and cool-white lamps, remote phosphor and proximate phosphor lamps, as well as different shapes, sizes, packaging designs, and rated values. To bolster the claim of insufficiency, a comparison was done on lamps that underwent 85°C with bias, 85°C/85% with bias and 85°C/85% without bias. The largest take away from this is that additional failure modes other than thermally driven failures, used with the TM28 standard, must be accounted for when evaluating the lifetime of SSL devices.

The SSL lamps underwent a steady-state temperature humidity bias life test of 85°C/85%, 55°C/65% and 25°C/45% with one hour cycles of electrical bias. Some useful photometric and colorimetric characteristics were demonstrated and used, along with the physical parameters of the SSL lamps, to produce a generalized acceleration model suitable for any SSL lamp. Peck's Power Law and principal component regression was used to produce the generalized acceleration factor model for lifetime predictions. PCR was used to remove any linear dependency produced from combining different populations with repeated observations. The final form of the generalized acceleration model utilized physical parameters, temperature and humidity only. This eliminates the need for degradation knowledge, such as lumen maintenance, that is required to use the TM28 standard. The model was successfully cross-validated with an SSL lamp set not used to develop the model producing an error between the predicted and actual acceleration factor of 7.81%.

The EDs were divided into two categories, EDG1 and EDG2. EDG1 underwent a high temperature storage life profile of 135°C and EDG2 underwent a steady-state temperature-humidity soak profile of 85°C & 85% relative humidity. The equivalent series resistance and capacitance of the aluminum electrolytic capacitors were measured directly at each test interval prior to being reconnected to the EDs. The overall health of the SSL system was monitored as the output of the ED by means of the luminous flux output of its accompanying pristine LE. The two profiles were compared to investigate which accelerated condition is better suited for this test vehicle. The relevant equivalent series resistance and capacitance of AEC One from EDG1 was used with the EKF and KF to produce meaningful lifetime predictions toward the development of a prognostic framework for aluminum electrical capacitors. This analysis demonstrated that the EKF is best suited to predict the remaining useful life of the AECs in terms of both leading indications of failure, relative CAP and relative ESR.

An EC underwent accelerated vibration testing to induce fretting degradation. Resistance spectroscopy and phase sensitive detection were used to capture minute changes in voltage across a modified Wheatstone bridge to determine the change in contact resistance. The contact resistance was used with the KF and EKF to accurately produce remaining useful life predictions for the implementation of a prognostic and health management framework. Both filters were demonstrated to be successful at predicting the remaining useful life of the ECs using the leading indicator of resistance change.

The deficiencies in TM28 validate the need behind the development of acceleration techniques to quantify SSL reliability under a variety of environmental conditions. The ability to assess damage accrual and investigate reliability of SSL components and systems is essential to understanding the life time of the SSL device itself. The methodologies developed in this work increases the understanding of SSL devices through the investigation of component and device reliability under a variety of accelerated test conditions. The approaches for suitable lifetime predictions through the development of novel generalized acceleration factors, as well as a prognostics and health management framework, will greatly reduce the time and effort needed to produce SSL acceleration factors for the development of lifetime predictions

## 5.1. FUTURE WORK

This work can be expanded beyond what has been demonstrated. The generalized acceleration model can be used as a starting point to produce a more accurate lifetime prediction model that utilizes non-thermally driven failure modes. Additional test conditions for each SSL lamp and the inclusion of additional SSL lamps will give valuable luminous flux degradation data to determine decay rates. This will allow for a curve-fit of decay rate versus temperature/humidity to produce a generalized decay rate model. With the addition of more ALT conditions and test vehicles, the collected degradation data and the generalized acceleration model can be used towards the achievement of a robust lifetime model for all SSL devices.

## Works Cited


Abdennadher, K. V. (2010). A Real-Time Predictive-Maintenance System of Aluminum Electrolytic Capacitors Used in Uninterrupted Power Supplies. *IEEE Transactions on Industry Applications*, *46*(4), 1644-1652.

Albertsen, A. (2012). *Electrolytic capacitor lifetime estimation.* Jianghai Europe GmbH.

Angadi, S. V. (2008). A Multi-Physics Finite Element Model of an Electrical Connector Considering Rough Surface Contact. *Proceedings of the 54th IEEE Holm Conference on Electrical Contacts.*

ANSYS. (n.d.). *Coupled-Field Analysis Guide.* ANSYS Inc.

Baillot, R. D. (2010). Effects of silicone coating degradation on GaN MQW LEDs performances using physical and chemical analysis. *Microelectronics Reliability*, *50*, 1568-1573.

Balakrishnan, A. V. (1987). *Kalman Filtering Theory (Series in Communication and Control Systems)1987.* New York: Optimization Software.

BHC Components. (2002). *Aluminum Electrolytic Capacitor Application Notes.*

Bryant, M. D. (1994). Resistance Buildup in Electrical Connectors Due to Fretting Corrosion of Rough Surfaces. *IEEE Transactions on Components, Packaging and Manufacturing Technology – Part A*, *17*(1), 86-95.

Buggy, M. C. (2004). Material selection in the design of electrical connectors. *Journal of Materials Processing Technology, 153-154*, 213-218.

Cartwright, R. P. (2011). Long term wear of complete contacts subject to fretting. *Wear, 271*, 2821-2825.

Celaya, J. R. (2011). A model-based prognostics methodology for electrolytic capacitors based on electrical overstress accelerated aging. *Proceedings of the Annual Conference of the Prognostics and Health Management Society*, (pp. 31-39). Montreal, Quebec Canada.

Chang, M.-H. D. (2012). Light emitting diodes reliability review. *Microelectronics Reliability, 52*, 762-782.

Choi, Y. S. (2011, June). Electrical contact resistance of multi-contact connector in semi-retractable current lead. *IEEE Transactions on Applied Superconductivity, 21*(3), 1050-1053.

CIE. (1995). *Method of Measuring and Specifying Colour Rendering Properties of Light Sources.* 13.3-1995.

CIE. (2004a). *Colorimetry.* 15-2004.

CIE. (2004b). *A Review of Chromatic Adaptation Transforms.* TC-152.

Congress, U. (2007, December 19). Energy Independence and Security Act. *Pub. L. no. 110-140.* Washington D.C.

Cornell Dubilier Electronics Inc. (2000). *Application Guide: Aluminum Electrolytic Capacitors.*

CREE. (2013). *LED Color Mixing: Basics and Backgrounds.* CLD-AP38 REV 1.

Daniel, C. M. (2004). Electrical behavior of periodically microstructered Sn/CuSn4 contact models under fretting conditions. *Wear, 257*, 266-270.

DeCusatis, C. (1997). *Handbook of Applied Photometry.* New York: AIP Press.

DOE EERE. (2013c). *Gateway Demonstrations: Demonstration of LED Street Lighting.* Kansas City, Missouri: DOE.

DOE: EERE. (2012). *Solid-State Lighting Multi-Year Market Development Support Plan.* Building Technologies Program: Solid-State Lighting Program.

DOE: EERE. (2013a). *Hammer Testing Findings for Solid-State Lighting Luminaires.* DOE.

DOE: EERE. (2013b). *Gateway Demonstrations: Demonstration Assessment of LED Parking Structure Lighting.* Washington D.C.: DOE.

DOE: EERE. (2013d). *Subjective Evaluation of Beam Quality, Shadow Quality, and Color Quality for LED PAR38 Lamps.* Richland, Washington: PNNL.

DOE: EERE. (2014a). *Gateway Demonstrations: Long-Term Testing of LED Luminaires.* Minneapolis, Minnesota: DOE.

Dow Corning Corporation. (1997). *Silicone Chemistry Overview*. Midland, MI: Dow Corning Corporation.

EERE. (2006). *Office of Energy Efficiency & Renewable Energy*. Retrieved January 12, 2015, from http://energy.gov/eere

Everitt, B. S. (1992). *Applied Multivariate Data Analysis.* New York: Oxford University Press.

Fan, J. Y. (2011). Physics-of-failure based prognostics and health management for high power white light-emitting diode lighting. *IEEE Transactions on Device and Materials Reliability, 11*(3), 407-416.

Fekedulegen, B. D. (2002). *Coping with Multicollinearity: An Example on Application of Principal Components in Dendroecology.* Newtown Square, PA: United States Department of Agriculture Forest Service.

Flowers, G. T. (2004). Vibration thresholds for fretting corrosion in electrical connectors. *IEEE Transactions on Components and Packaging Technology, 27*(1), 583-590.

Flowers, G. T. (2005). Modeling early stage fretting of electrical connectors subjected to random vibration. *IEEE Transactions on Components and Packaging Technology, 28*(4), 721-727.

Flowers, G. T. (2006). A study of the physical characteristics of vibration-induced fretting corrosion. *IEEE Transactions on Components and Packaging Technology, 29*(24), 318-325.

Fouvry, S. J. (2011). Introduction of an exponential formulation to quantify the electrical endurance of micro-contacts enduring fretting wear: Application to Sn, Ag and Au coatings. *Wear, 271*, 1524-1534.

Frank, R. F. (2007). Comparative corrosion and current burst testing of copper and aluminum electrical power connectors. *IEEE Transactions on Industry Applications, 43*(2), 462-468.

Gasperi, M. L. (1996). Life prediction model for aluminum electrolytic capacitors. *IEEE Industrial Applications Society, 3*, 1347-1351.

Georgiev, A. M. (1945). *The Electrolytic Capacitor.* New York: Murray Hill Books.

Goodman, D. V. (2005). Practial Applications of PHM/Prognostics to COTS Power Converters. *IEEE Aerospace Conference* (pp. 3573-3578). Big Sky, MT: IEEE.

Grewal, M. S. (2001). *Kalman Filtering: Theory and Practice Using MATLAB* (2nd ed.). New York: John Willy & Sons Inc.

Hallberg, O. a. (1991). Recent Humidity Accelerations, A Base for Testing Standards. *Quality and Reliability Engineering International, 7,* 169-180.

Hambley, A. R. (2005). *Electrical Engineering Principles and Applications.* Upper Saddle River, New Jersey: Pearson Education Inc.

Han, L. N. (2009). Developing an accelerated life test method for LED drivers. *Proceedings of the 9th International Conference on Solid State Lighting.* SPIE.

Harada, K. K. (1993). Use of ESR for deterioration diagnosis of electrolytic capacitor. *IEEE Transactions on Power Electronics, 8*(4), 355-361.

Hernandez-Andres, J. L. (1999). Calculating correlated color temperatures across the entire gamut of daylight and skylight chromaticities. *Journal of Applied Optics, 38*(27), 5703-5709.

Hewlett Packard. (1997). *Reliability of precision optical performance AllnGaP LED lamps in traffic signals and variable message signs.* Application Brief I-004.

Hsieh, Y. F.-Y. (2012). Determination of optimal converting point of color temperature conversion complied with ANSI C78.377 for indoor solid-state lighting and display applications. *Journal of Optics Express, 20*(18), 20059-20070.

Hsu, Y. L. (2008). Failure mechanisms associated with lens shape of high-power LED modules in aging test. *IEEE Transactions on Electronic Devices, 55*(2), 689-694.

IES. (2005). *Nomenclature and Definitions for Illuminating Engineering.* RP-16-05.

IES. (2008a). *IES LM-79-08 Approved Method: Electrical and Photometric Measurements of Solid-State Lighting Products.* New York: Illuminating Engineering Society.

IES. (2008b). *IES LM-80-08 Approved Method: Measuring Lumen Maintenance of LED Light Sources.* New York: Illuminating Engineering Society.

IES. (2011). *IES TM-21-11 Projecting Long Term Lumen Maintenance of LED Light Sources.* New York: Illuminating Engineering Society.

IES. (2014a). *IES LM-84-14 Approved Method for Measuring Luminous Flux and Color Maintenance of LED Lamps, Light Engines, and Luminaires.* New York: Illuminating Engineering Society.

IES. (2014b). *IES TM-28-14 Projecting Long Term Luminous Flux Maintenance of LED Lamps and Luminaires.* New York: Illuminating Engineering Society.

Imam, A. M. (2005). Condition monitoring of electrolytic capcitor in power electronic circuits using adaptive filter modeling. *IEEE 36th Power Electronics Specialists conference* (pp. 601-607). Recife, Brazil: IEEE.

Jackson, R. L. (2007). The effect of Initial Connector Insertions on Electrical Contact Resistance. *Proceedings of the 53th IEEE Holm Conference on Electrical Contacts.*

JEDEC. (2006). *Failure Mechanisms and Models for Semiconductor Devices.* JEDEC.

JEDEC. (2009). *JEDEC Steady State Temperature Humidity Bias Life Test Standard.* JESD22-A101C.

JEDEC. (2010). *JEDEC High Temperature Storage Life Standard.* JESD22-A103D.

Jedrzejczyk, P. F. (2009). A fast methodology to quantify electrical-contact behavior under fretting loading conditions. *Wear, 267*, 1731-1740.

Kleinbaum, D. G. (1978). *Applied Regression Analysis and Other Multivariable Methods.* Boston, MA: Duxbury Press.

Krzanowski, W. J. (2000). *Principles of Multivariate Analysis: A User's Perspective.* New York: Oxford University Press.

Kulkarni, C. S. (2012). Accelerated aging experiments for capacitor health monitoring and prognostics. *2012 IEEE AUTOTESTCON* (pp. 356-361). Anaheim, CA: IEEE.

Kulkarni, C. S. (2012). Physics based electrolytic capacitor degradation models for prognostic studies under thermal overstress. *1st European Conference of the Prognostics and Health Management Society*, (pp. 156-164). Dresden, Germany.

Lakshmanan, A. K. (2011, May). Synthesis, photoluminescence and thermal quenching of YAG:Ce phosphor for white light emitting diodes. *Indian Journal of Pure & Applied Physics, 49*, 303-307.

Lall, P. B. (2008d). Interrogation of system state for damage assessment in lead-free electronics subjected to thermo-mechanical loads. *IEEE Proceedings of the 58th Electronic Components and Technology Conference* (pp. 918-929). Orlando, Florida: IEEE.

Lall, P. C. (2006a). Health monitoring for damage initation & pregression during mechanical shock in electronic assemblies. *Proceedings of the 56th Electronics Components and Technology Conference* (pp. 85-94). San Diego, California: IEEE.

Lall, P. C. (2007a). Statistical pattern recognition and built in reliability test for feature extraction and health monitoring of electronics under shock loads. *Proceedings of the 57th Electronics Components and Technology Conference* (pp. 1161-1178). Reno, Nevada: IEEE.

Lall, P. C. (2008a). Health monitoring for damage initiation and progression during mechanical shock in electronic assemblies. *IEEE Transactions on Components and Packaging Technologies, 31*(1), 173-183.

Lall, P. G. (2007b). Solder-joint reliability in electronics under shock and vibration using explicit finite element sub-modeling. *IEEE Transactions on Electronic Packaging Manufacturing, 30*(1), 74-83.

Lall, P. H. (2006b). Feature extraction and damage data for prognostication of leaded and leadfree electronics. *Proceedings of the 56th Electronics Components and Technology Conference* (pp. 718-727). San Diego, California: IEEE.

Lall, P. H. (2007c). Prognostics health monitoring (PHM) for prior-damage assessment in electronics equipment under thermo-mechanical loads. *Proceedings of the 57th Electronics Components and Technology Conference* (pp. 1097-1111). Reno Nevada: IEEE.

Lall, P. H. (2007e). Feature extraction and damage-precursors for prognostication of lead-free electronics. *Microelectronics reliability, 47*, 1907-1920.

Lall, P. H. (2008c). Algorithms for prognostication of prior damage and residual life in lead-free electronics subjected to thermo-mechanical loads. *IEEE Proceedings of the 10th Intersociety Thermal and Thermo-mechanical Phenomena* (pp. 638-651). Orlando, Florida: IEEE.

Lall, P. I. (2004a). Leading indicators-of-failure for prognosis of electronic and MEMS packaging. *Proceedings of the 54th Electronics Components and Technology Conference.* Las Vegas, Nevada: IEEE.

Lall, P. I. (2004b). Damage mechanics of electronics on metal-backed substrates in harsh environments. *Proceedings of the 54th Electronics Components and Technology Conference.* Las Vegas, Nevada: IEEE.

Lall, P. I. (2004c). Model for BGA and CSP reliability in automotive underhood applications. *IEEE Transactions on Components and Packaging Technologies, 27*(3), 585-593.

Lall, P. I. (2005a). Prognostication and health monitoring of leaded and lead free electronic and MEMs packages in harsh environments. *Proceedings of the 55th Electronics Components and Technology Conference* (pp. 1-9). Orlando, Florida: IEEE.

Lall, P. I. (2006c). Prognostics and health management of electronic packaging. *IEEE Transactions on Components and Packaging Technologies, 29*(3), 666-677.

Lall, P. I. (2006d). Damage mechanics of electronics on metal-backed substrates in harsh environments. *IEEE Transactions on Components and Packaging Technologies, 29*(1), 204-212.

Lall, P. I. (2008f). Design envelopes and optical feature extraction techniques for survivability of SnAg leadfree packaging architectures under shock and vibration. *IEEE Proceedings of the 58th Electronic Components and Technology Conference* (pp. 1036-1047). Orlando, Florida: IEEE.

Lall, P. L. (2009a). Prognostication Based On Resistance-Spectroscopy for High Reliability Electronics under Shock-Impact. *ASME International Mechanical Engineering Conferance & Exposition.*

Lall, P. L. (2009b). Resistance spectroscopy-based condition monitoring for prognostication of high reliability electronics under shock-impact. *Proceedings of the 59th Electronic Components and Technology Conference.* IEEE.

Lall, P. L. (2010a). Prognostics Using Kalman-Filter Models and Metrics for Risk Assessment in BGAs under Shock and Vibration Loads. *Proceedings of the 60th Electronic Components and Technology Conference.* IEEE.

Lall, P. L. (2010b). Use of Prognostics in Risk-Based Decision Making for BGAs under Shock and Vibration Loads. *11th IEEE Intersociety Conference on Thermal and Thermomechanical Phenomena in Electronic Systems.* IEEE.

Lall, P. L. (2011a). Extend Kalman Filter Models and Resistance Spectroscopy for Prognostication and Health Monitoring of Lead-free Electronics under Vibration. *IEEE Conference on Prognostics and Health Management.*

Lall, P. L. (2011b). Particle Filter Models and Phase Sensitive Detection for Prognostication and Health Monitoring of Lead-free Electronics under Shock and Vibration. *Proceedings of the 61st Electronic Components and Technology Conference.*

Lall, P. L. (2011c). PHM of Lead-free Interconnects using Resistance Spectroscopy Based Particle Filter Models for Shock and Vibration Environments. *Proc. Of ASME 2011 Technical Confernce & Exposition On Packaging and Integration of Electronics and Photonic Systems.* ASME.

Lall, P. P. (2004d). Models for reliability prediction of fine-pitch BGAs and CSPs in shock and drop-impact. *Proceedings of the 54th Electronics Components and Technology Conference* (pp. 1296-1303). Las Vegas, Nevada: IEEE.

Lall, P. P. (2005b). Failure-envelope approach to modeling shock and vibration survivability of electronic and MEMs packaging. *Proceedings of the 55th Electronics Components and Technology Conference* (pp. 480-490). Orlando, Florida: IEEE.

Lall, P. P. (2006e). Models for reliability prediction of fine-pitch BGAs and CSPs in shock and drop-impact. *IEEE Transactions on Components and Packaging Technologies, 29*(3), 464-474.

Lall, P. P. (2007d). Smeared property models for shock-impact reliability of area-array packages. *ASME Journal of Electronic Packaging, 129*, 373-381.

Lall, P. P. (2008b). Failure-envelope approach to modeling shock and vibration survivability of electronic and MEMs packaging. *IEEE Transactions on Components and Packaging Technologies, 31*(1), 104-113.

Lall, P. S. (2008e). Principal component regression models for life prediction of plastic ball grid arrays on copper-core and no-core assemblies. *IEEE Intersociety conference on Thermal and Thermo-mechanical Phenomena in Electronic Systems* (pp. 770-785). Orlando, FL: IEEE.

Lall, P. S. (2012b). Leading Indicators for Prognostic Health Management of Electrical Connectors Subjected to Randaom Vibration. *IEEE Intersociety conference on Thermal and Thermo-mechanical Phenomena in Electronic Systems.* San Diego, CA: IEEE.

Lall, P. S. (2013a). Prognostics of damage accrual in SSL luminaires and drivers subjected to HTSL accelerated aging. *Proceedings of the ASME 2013 International Technical*

*Conference and Exhibition on Packaging and Integration of Electronic and Photonic Microsystems.* Burlingame, CA: ASME. doi:10.1115/IPACK2013-73250

Lall, P. S. (2014). Reliability of solid-state lighting electrical drivers subjected to WHTOL accelerated aging. *14th IEEE Inter-Society Conference on Thermal and Thermomechanical Phenomena in Electonic Systms* (pp. 1164-1170). Lake Buena Vista, FL: IEEE.

Lall, P. W. (2012a). Comparison of Kalman-filter and extended Kalman-filter for the PHM of Electronics. *IEEE Intersociety conference on Thermal and Thermo-mechanical Phenomena in Electronic Systems.* San Diego: IEEE.

Lall, P. Z. (2013b). Assessment of Lumen Degradation and Remaining Life of LEDs using Particle Filter. *Proceedings of the ASME 2013 International Technical Conference and Exhibition on Packaging and Integration of Electronic and Photonic Microsystems.* Burlingame, CA: ASME.

Lam, L. M. (2006). Temperature, humidity and pressure measurements on automotive connectors. *IEEE Transactions on Components and Packaging Technology, 29*(2), 333-340.

Lan, S. T. (2012). Reliability study of LED driver - A case study of black box testing. *Microelectronics Reliability, 52,* 1940-1944.

Lin, Y. T. (2006). Materials challenges and solutions for the packaging of high power LEDs. *IEEE International Microsystems, Packaging, Assembly Conference* (pp. 1-4). Taipei, Taiwan: IEEE.

Lu, G. M. (2015). Color Shift Investigations for LED Secondary Optical Designs: Comparison between BPA-PC and PMMA. *Optical Materials, 45*, 37-41.

Lunia, A. K. (2014). Theoretical analysis of blue to white down conversion for light-emitting diode light with yttrium aluminum garnet phosphor. *Journal of Photonics for Energy, 4*, 043596-1- 043596-11.

Luo, X. W. (2010). Effects of moist environments on LED module reliability. *IEEE Transactions on device and materials reliability, 10*(2), 182-186.

Ma, H. W. (2005). Fault Diagnosis and Failure Prediction of Aluminum Electrolytic Capacitors in Power Electronic Converters. *31st Annual Conference of IEEE Industrial Electronics Society.* IEEE.

McCluskey, P. M. (2000). Reliability of commercial plastic encapsulated microelectronics at temperatures from 125C to 300C. *IEEE Aerospace Conference* (pp. 445-450). Big Sky, MT: IEEE.

McCluskey, P. M. (2000). Reliable use of commercial technology in high temperature environments. *Microelectronics Reliability, 40*, 1671-1678.

Mehr, M. Y. (2013a). Lifetime assessment of Bisphenol-A Polycarbonate (BPA-PC plastic lens, used in LED-based products. *Microelectronics Reliability*.

Mehr, M. Y. (2013b). Photodegradation of bisphenol A polycarbonate under blue light radiation and its effect on optical properties. *Optical Materials, 35*, 504-508.

Meneghini, M. T. (2008, June). A review on the reliability of GaN-based LEDs. *IEEE Transactions on Device and Materials Reliability, 8*(2), 323-331.

Miller, N. K. (2014a). *LED Lighting in a Performing Arts Building at the University of Florida.* Gainsville, Florida: PNNL.

Miller, N. M. (2013). *Pedestrian Friendly Outdoor Lighting.* Richland, Washington: PNNL.

Mukhopadhyay, P. (2009). *Multivariate Statistical Analysis.* Singapore: Word Scientific Printers.

Narendran, N. G. (2004). Solid-state lighting: failure analysis of white LEDs. *Journal of Crystal Growth*, *268*, 449-456.

Nelson, W. (1982). *Applied Life Data Analysis.* New York: John Wiley & Sons, Inc.

Nelson, W. (1990). *Accelerated Testing: Statistical Models, Test Plans, and Data Analysis.* New York: John Wiley & Sons.

Nguyen, X. L. (2010). The fabrication of GaN-based light emitting diodes (LEDs). *Advances in Natural Science: Nanoscience and Nanotechnology*, *1*, 1-5. doi:10.1088/2043-6254/1/2/025015

Nichicon Inc. (2002). *General Descriptions of Aluminum Electrolytic Capacitors.* Technical Notes CAT.810E.

Nippon Chemi-Con. (2013). *Miniature Aluminum Electrolytic Capacitors.* Specification Sheet.

Noel, S. C. (2011). Fretting behavior of various intermetallic compounds in electrical contacts: Influence on reliability. *Wear*, *271*, 1515-1523.

Oh, J. R. (2010). Full down-conversion of amber-emitting phophor-converted light-emitting diodes with powder phosphors and a long-wave pass filter. *Optics Express*, *18*(11), 11063-11072.

Ohno, Y. (2014). Practical Use and Calculation of CCT and Duv. *The Journal of the Illuminating Engineering Society of North America*, *10*, 47-55.

Ohring, M. (1998). *Reliability and Failure of Electronic Materials and Devices.* San Diego: Academic Press.

Panasonic Industrial Company. (2008). *Aluminum Electrolytic Capacitors.*

Park, Y. W. (2008). Fretting corrosion of tin-plated contacts. *Tribology International*, *41*, 616-628.

Park, Y. W. (2010). Effect of intermittent fretting on corrosion behavior in electrical contact. *Wear, 268,* 353-360.

Peck, D. S. (1986). Comprehensive Model for Humidity Testing Correlation. *IEEE-IRPS*, 44-50.

Philips Lumileds Lighting Company. (2006). *Luxeon Reliability.* Luxeon Reliability Datasheet RD25.

Rawlings, J. (1988). *Applied Regression Analysis.* Pacific Grove, CA: Wadsworth & Brooks.

Rubycon Corporation. (2013). *Technical Notes for Electrolytic Capacitor.*

Sankaran, V. R. (1997). Electrolytic capacitor life testing and prediction. *IEEE Industrial Applications Society*, *2*, 1058-1065.

Saxena, A. C. (2008). Metrics for Evaluating Performance of Prognostic Techniques. *International Conferance on Prognostics and Health Management.*

Saxena, A. C. (2009a). Evaluating Algorithm Performance Metrics Tailored for Prognostics. *IEEE Aerospace Conference.* IEEE.

Saxena, A. C. (2009b). On Applying the Prognostics Performance Metrics. *Annual Conference of the PHM Society.*

Schanda, J. (2007). *Colorimetry: Understanding the CIE System.* Hoboken: John Wiley & Sons Inc.

Schubert, E. F. (2006). *Light-Emitting Diodes.* Cambridge, UK: Cambridge University Press.

Stanford Research Systems. (n.d.). *About Lock-In Amplifiers.* Stanford Research Systems Application Notes.

Stevens, J. L. (2002). The service life of large aluminum electrolytic capacitors: Effects of construction and application. *IEEE Transactions on Industry Applications*, *38*(5), 1441-1446.

Sutharssan, T. B. (2011). Prognostics and Reliability Assessment of Light Emitting Diode Packaging. *IEEE International Conference on Electronic Packaging Technology & High Density Packaging.* IEEE.

Swingler, J. (2009). Enhancing connector reliability by using conducting polymer materials to minimize contact fretting. *Materials and Design, 30*, 3935-3942.

Swingler, J. L. (2010). Study of temperature change and vibration induced fretting on intrinsically conducting polymer contact systems. *IEEE Transactions on Components and Packaging Technology, 33*(2), 409-415.

Viswanadham, P. a. (1998). *Failure Modes and Mechanisms in Electronic Packages.* New York: Chapman & Hall.

Westland, S. a. (2004). *Computational Colour Science Using Matlab.* Hoboken, New Jersy: John Wiley & Sons, Inc.

Wyszecki, G. a. (1982). *Color Science: Concepts and Methods, Quantitative Data and Formulae* (2nd ed.). New York: John Wiley & Sons.

Xie, F. (2007). *A study of vibration-induced fretting corrosion for electrical connectors.* Auburn University.

Xie, F. F. (2009). Analysis and prediction of vibration-induced fretting motion in blade/receptacle connector pair. *IEEE Transactions on Components and Packaging Technology, 32*(3), 583-590.

Xie, R. J. (2007). Silicon-based oxynitride and nitride phosphors for white LEDs - A review. *Science and Technology of Advanced Materials, 8*, 588-600.

Zarchan, P. M. (2000). *Fundamentals of Kalman Filtering: A Practical Approach* (Vol. 190). Virginia: Progress in Astronautics and Aeronautics.

Zhang, T. M. (2011). Computational study on the effect of contact geometry on fretting behavior. *Wear, 271*, 1462-1480.

Zhang, T. M. (2011). Computational study on the effect of contact geometry on fretting behaviour. *Wear*, *271*, 1462-1480.

Zhou, Y. L. (2012). A Remaining Useful Life Prediction Method Based on Condition Monitoring for LED Driver. *IEEE Prognostics & System Health Management Conference*. IEEE.

Zukauskas, A. S. (2002). *Introduction into Solid-State Lighting*. New York: John Wiley & Sons Inc.